Sheffield Hallam University

A Sheffield Hallam University thesis
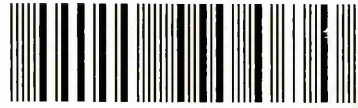
ProQuest Number: 10700907

ProQuest 10700907

INSTRUMENTATION OF PARTICLE CONVEYING

USING ELECTRICAL CHARGE TOMOGRAPHY

by

MOHD FUA'AD RAHMAT
B.E.Eng.(Hons)(UTM)
MSc(Control Eng.)(Sheffield)

A thesis submitted to
Sheffield Hallam University
for the degree of Doctor of Philosophy
in the School of Engineering

November 1996

Dedication

Dengan nama Allah yang Maha Pengasih lagi Maha Penyayang

To my respected parents,

      Tuan Haji Rahmat bin Haji Ali and Puan Hajjah Zainun binti Haji Jaafar

To my beloved wife,

      Norazizah binti Haji Ahmad

To my dearest daughters,

      Maryam Syuhaidah and Mastura Nabilah

To my brothers and sisters,

      Fazidah, Syukur, Hannan and Mohd Farid

Thank you for being very patient and understanding during my research and study at Sheffield Hallam University. May Allah reward them for their constant prayers for me towards success.

Acknowledgements

ABSTRACT

This thesis presents an investigation into the application of electrodynamic sensors to a tomographic imaging system.

Several sensing mechanisms for measurement using non-intrusive techniques are discussed and their relevance to pneumatic conveying considered. Electrical charge tomography systems are shown to be worthy of investigation. Electrodynamic sensors are inherently low cost and simple in concept. This sensor is used to detect the inherent charge on dry, moving solids. Models are developed to predict the sensitivity of circular and rectangular electrodes. The spatial filtering effect of these sensors is investigated. Cross correlation is briefly reviewed and a software program is presented and tested. For tomographic imaging the forward problem for the individual sensors is modelled, used to solve the inverse problem and derive the linear back projection and filtered back projection algorithms.

The design of the electronic circuitry which forms the transducer is presented. The gravity drop flow rig is described and the relationship between sand flow and plastic bead flow relative to the flow indicator setting determined. The dual 16-channel sensor array measurement section is described. Flow models are developed and used to predict the relative output voltage profiles expected from the sensor arrays.

The linearity and frequency bandwidth of the sensor electronics is measured. The effect of sensor size on sensitivity and spatial filtering are investigated for circular and rectangular electrodes.

Estimates of the solid concentration of flowing particles are made using individual sensors. Concentration profiles are generated and compared with predicted values. Peripheral velocities of the flowing material are determined from transit times calculated by cross correlation of upstream and downstream sensor signals.

Concentration profiles are calculated using linear back projection and filtered back projection algorithms from data measured by the sensor arrays. Velocity profiles are obtained by cross correlation of upstream and downstream pixel concentration values. Estimates of the mass flow rate are obtained by combining concentration and velocity profiles.

Suggestions for further work on electrodynamic sensors and tomographic measurements are made.

Contents

CHAPTER 1

Introduction

1.1 An overview of process tomography

Tomography is an interdisciplinary field concerned with obtaining cross-sectional, two-dimensional images of three-dimensional objects (Scott 1995). The word tomography can be defined briefly as a slice of a picture. The Helicon encyclopaedia defines tomography as the obtaining of plane section images, which show a slice through an object. In this project, the objective is to use arrays of electrodynamic sensors as the primary sensors to make tomographic measurements in pneumatic conveyors transporting dry powders. The measured data will be processed to generate, off-line, an image which displays the concentration and velocity profile over a cross-section of the conveyor.

The tomographic imaging of objects offers a unique opportunity to unravel the complexities of structure without the need to invade the object (Beck and Williams 1996). The development of tomographic instrumentation, started in the 1950s, has led to the widespread availability of body scanners, which are so much a part of modern medicine. Nowadays there is an increasing need to know more about the exact way the internal flows in process equipment are behaving. These needs occur because industry is under pressure to utilise resources more efficiently and to satisfy demand and legislation for product quality and reduced environmental emissions. Tomographic instrumentation offers non-invasive techniques and robust sensors to solve industrial needs. It also includes tomographic imaging methods to manipulate the data from

1

remote sensors in order to obtain precise quantitative information from inaccessible locations (Dickin *et al* 1991 a).

The basic idea of process tomography is to install a number of sensors around the pipe or vessel to be imaged. The sensor output signals depend on the position of the component boundaries within their sensing zones. The output signals are conditioned and input to a computer which is used to reconstruct a tomographic image of the cross section being observed by the sensors. These images have the potential to provide information on concentration, velocity, component volume flow rate and particle size measurements.

Process tomography essentially evolved during the mid-1980s (Beck and Williams 1996). A number of applications of tomographic imaging of process equipment were described in the 1970s, but generally these involved using ionising radiation from x-ray or isotope sources (Beck and Williams 1996). They were not satisfactory for the majority of process applications on a routine basis because of the high cost involved and safety constraints.

In the 1980s work started at UMIST, England on electrical capacitance tomography for imaging multi-component flows from oil wells and in pneumatic conveyors (Beck and Williams 1996). At the same time at the Morgantown Energy Technology Centre USA, a capacitance tomography system were designed for measuring the void distribution in gas fluidized beds (Beck and Williams 1996). Also in the mid-1980s medical scientists started to realise the potential of electrical impedance tomography (measuring electrical resistance) as a safe, low-cost method for imaging the human body. This work was

done at the Sheffield University Royal Hallamshire Hospital in the UK and Rensselaer Polytechnic Institute in the USA (Beck and Williams 1996).

In 1988 work started at UMIST on the development of electrical impedance tomography (EIT) for imaging vessels containing electrically conducting fluids (Beck and Williams 1996). The difference between medical EIT and process EIT is medical EIT measures the location of objects in space, whereas process EIT needs to measure both the location and the velocity of movement (Beck and Plaskowski 1987).

By 1990, process tomography was maturing as a potentially useful technique for application to industrial process design and operation. Therefore a four year programme was established called the European Concerted Action on Process Tomography with aims to organise workshops on tomography. The ECAPT workshops (Manchester 1992, Karlshrue 1993, Porto 1994 and Bergen 1995) reported new sensing techniques, new algorithms and began to address the fundamental challenges such as spatial resolution, speed of acquisition, quality of information and other factors that are essential to make the technology acceptable to industrial practice.

1.2 Pneumatic conveying

Pneumatic conveying is utilised extensively to transport dry powders and granular materials (Brown *et al* 1996). Materials handled by this means in industry range from lumps of coal and crushed ores in the mining industries to pellets and fine powders of polyethylene, PVC and polypropylene in the chemical industries (Brown *et al* 1996). Pneumatic conveying systems are in concept quite simple and are eminently suitable for the transporting of materials in factory, site and plant situations. The basic system requirements are a compressor, a device for entraining the conveyed material, the

3

conveying pipeline and a receiver to disengage the conveyed material and carrier gas.

The capability of a system for conveying material depends upon the pipeline geometry, the conveying parameters and the properties of the conveyed material (Brown *et al* 1996). Some of the conveying parameters of importance are the flow velocity, the distribution of gas/solid fraction, drag factor, particle shape, particle density and the pressure gradient distribution of the material.

These may all contribute to the different flow characteristics or regimes in the conveying pipeline, and thus effect the efficiency of energy consumption (Beck 1986) or cause blockage and damage to pipes.

In horizontal pneumatic conveying, the flow regimes generated depend primarily upon the conveying gas velocity. In dense phase transport, where the conveying gas velocity is relatively low, the distribution of solid particles tend to become non-uniform and form a moving bed on the base of the pipeline.

In discussing sensors for light phase conveying the author has assumed that the solids are generally dispersed through the conveyor, but uniformity is not implied as shown in figure 1.1.

Dispersed homogeneous flow   Dispersed non-homogeneous flow

Roping flow
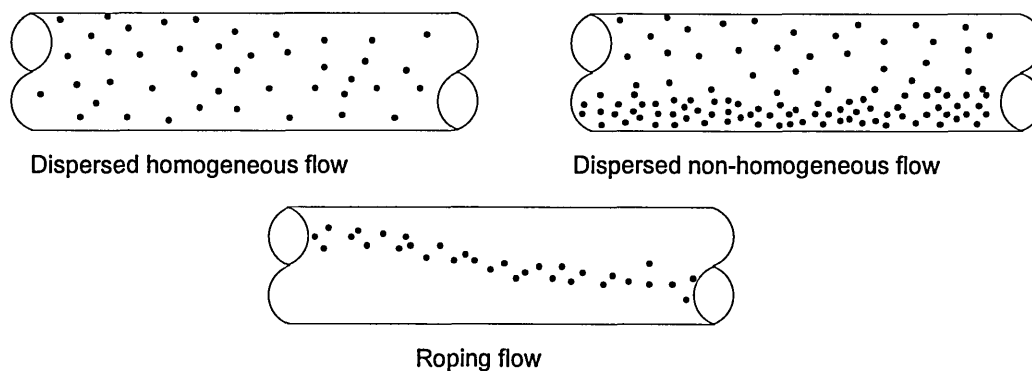
Figure 1.1. Light phase conveying

The solids phase density is defined by any of the following:

- The ratio of gas volume to solids volume is greater than to 20:1 V/V

- which corresponds to a solids concentration or loading of up to 5%.

- or ratio of the mass of solids to the mass of gas is up to 50:1 kg/kg

Another type of conveyor is the gravity drop feeder. It is a form of conveyor where gravity produces the movement of the particles and is used in the work presented in this thesis.

1.3 Aims and objectives of the thesis

The aim of the thesis is to investigate the feasibility of using electrodynamic sensors for concentration measurement, velocity measurement and tomographic imaging of solids/gas flows.

The specific objectives of this thesis are to :

1. Become familiar with the concepts of process tomography, associated sensor technology and the electrodynamic sensor.

2. Investigate design parameters associated with using electrodynamic sensors and produce a model of an electrodynamic concentration measurement system.

3. Design and test an electrodynamic sensor which will detect dry flowing powders.

4. Design and implement two arrays of electrodynamic sensors, upstream and downstream around a measurement section.

5. Design and implement an electronic measurement system which will provide data from the electrodynamic sensors in a form suitable for processing to produce concentration profiles, tomographic images and particle velocity determination.

6. Develop a reconstruction algorithm enabling data from the electrical charge measurement system to be processed and displayed to show concentration profiles and tomographic images.

7. Investigate the use of cross correlation of pixels of upstream and downstream concentration profiles to determine the velocity profile.

8. Test the complete system on a gravity drop conveyor using a range of dry materials.

9. Investigate the calculation of mass flow rate based on concentration and velocity information.

10. Consider the work presented in this thesis and make suggestions for further work.

1.4 Organisation of the thesis

Chapter one presents an introduction to process tomography.

Chapter two presents an overview of several sensing mechanisms for measurement of pneumatically conveyed dry solids such as capacitance, optical fibre, ultrasonic and electrodynamic.

Chapter three consists of two parts. The first part describes modelling to predict the electrodynamic sensor output voltage profiles arising from different, artificially produced flow regimes. The second part describes an image reconstruction method for electrical charge tomography.

Chapter four discusses the complete electrical charge tomographic measurement system, including sensor design, sensor array configuration, data acquisition system, the flow rig and artificial flow baffles.

Chapter five presents experiments on sensitivity and spatial filtering effect and results of electrodynamic sensor performance.

Chapter six presents results of concentration and velocity measurements

Chapter seven presents results of concentration profiles, velocity profiles and tomographic images.

Chapter eight presents mass flow rate calculations.

Lastly chapter nine discusses the conclusions to be drawn from this work and makes suggestions for future work.

CHAPTER 2

Review of Sensors in Pneumatic Conveying

Chapter summary

Four type of sensors suitable for tomographic imaging of pneumatically conveyed dry powders are reviewed. The types of sensor are capacitance, optical fibre, ultrasonic and electrical charge/electrodynamic.

2.1 Introduction

This chapter provides an overview of measurement systems for process tomography applications. A basic system for process tomography is shown in figure 2.1.
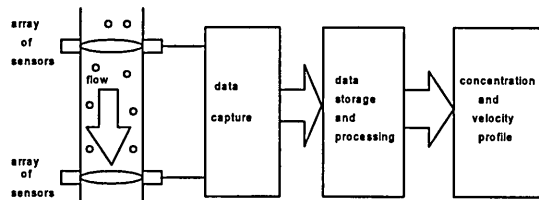
Figure 2.1 : Process Tomography System.

Three basic components in a process tomography system are :-

(a). The sensors

(b). The data acquisition system

(c). The image reconstruction system and display.

2.2 Tomography sensors

Sensor technology is the most essential and critical part of any measurement system (Dickin *et al* 1991a). The sensors in a tomography system are usually placed in a circular array around the circumference of the process vessel. This is to provide multiple projections of the object or event being measured. The main advantage derived

from such a configuration is multi-component spatial distributions can be obtained through image reconstruction techniques (Dickin *et al* 1991 a). The following subsection provides a short review of several process tomography systems currently being investigated.

2.2.1 Electrical Capacitance Tomography (ECT)

Electrical capacitance tomography (ECT) systems have been developed at UMIST (Huang *et al* 1991) based on transducers developed by Huang (Huang *et al* 1988). Huang's capacitance measuring circuit is based on the charge transfer principle. A number of capacitance electrodes is mounted on the circumference of a flow pipe and interrogated in turn by electronic control. Measurements are based on changes in capacitance values between electrodes due to the variations in permittivities of the flowing material.

Capacitance systems are suitable for medium to high solid loading in process conveyors (Isaksen and Nordtvedt 1992). However, as the solids loading decreases the systems fail to produce meaningful images because of the relatively low signal to noise ratio of the capacitance to voltage transducer and non-uniform sensing fields (Xie 1993). The existing ECT systems are unsuitable for light phase pneumatic conveying systems. At present ECT is not at all suitable for light phase pneumatic conveying for solid concentrations below 10:1 V/V. Also the relatively low spatial bandwidth of ECT system restricts their application in velocity determination.

2.2.2 Optical fibre tomography

Optical fibre sensors can be applied in process tomography to produce concentration profiles for solids transported both by gas and liquid (Green *et al* 1995). This paper

investigates the use of a single optical fibre transducer (which is part of a 16 x 16 tomographic sensor array) to measure cross sectional variations in bulk concentration due to flowing solids and one aspect of the dynamic response of the sensor by determining the spatial filtering effect (Hammer and Green, 1983) of a range of multimode plastic fibres. Optical fibres exhibit high linearity when used to measure solid flow rates and show good agreement between predicted and measured values for the spatial filtering effect. These results demonstrate the suitability of low cost optical fibre sensors for monitoring flowing materials. In particular, optical fibre frequency bandwidth, when used to measure passing objects is very high (Ghassemlooy 1992), typically tens of kilohertz. This high bandwidth makes them suitable for velocity measurement using cross correlation techniques (Yan *et al* 1995a).

Optical fibre can be used as a process tomography sensor to view the cross section of a process and provide information relating to the materials distribution (Abdul Rahim *et al* 1996). This involves taking measurements from sensors placed around the section of the process being investigated and processing the data to reconstruct an image. The optical sensor model (Abdul Rahim 1996) is based on path length and predicts the expected sensor output voltage profiles arising from different, artificially produced flow regimes. These artificial flow regimes are created by placing a shaped obstruction inside a gravity drop conveyor in the path of the flowing solids. An image reconstruction algorithm for optical tomography based on the back projection (Nordin 1995) between view lines algorithm is used to generate tomographic images as a representation of the data on concentration measurement. The disadvantages of the optical system are dust that blocks the beam and the high cost needed to construct the system.

2.2.3 Ultrasonic tomography

Instrumentation systems employing a variety of ultrasonic techniques have been applied to a wide range of measurements in the chemical and process industries (Asher 1983). Ultrasonic sensors can be applied for process tomography in pneumatic conveying due to the successful application within the fields of non-destructive testing and medical diagnosis (Brown *et al* 1996). A tomographic technique is being developed for imaging gas-solid flow distributions in pneumatic conveying pipelines. The technique utilises ultrasonic transmission-mode measurements constrained to the megahertz region. Image reconstruction is performed by an efficient back projection method implemented with a standard graphic algorithm. Key issues in the application of ultrasound to gas-solids flow can be identified by considering some fundamentals of pipeline and flow medium characteristics. A brief summary of these issues is given below.

(i). The mismatch between the low acoustic impedance of the continuous (gaseous) component of the flow and conventional piezoceramic material results in greatly reduced transducer performance (Reilly *et al* 1994).

(ii). The dynamic nature of the flow and the relatively low propagation velocity of sound impose demanding temporal constraints on data acquisition because flow characterisation should be performed at a fast rate relative to the changes within the flow (Brown *et al* 1995).

(iii). Ultrasonic measurement of the solids distribution is dependent on complex interactions between the transmitted ultrasound and the flow (Brown *et al* 1995).

2.3 Electrical charge tomography

Electrical charge tomography is a technique based on using electrodynamic sensors. A non-intrusive electrodynamic transducer can measure phase density and velocity on industrial pneumatic conveying systems where the solids/gas ratio is low and the solids turbulently conveyed (Shackleton 1982). Shackleton surveyed several different methods of mass flow rate measurement and discusses the limitations associated with these methods. She also studied the relationship between mass flow rate to streaming charge and derived a mathematical model relating the turbulence of the conveying air to the changes in charge detected by the sensing electrode. In her experimental work, Shackleton used two types of sensor, the ring electrode and the probe electrode.

Beck (1986) used electrodynamic transducers for cross correlation velocity measurement of solids in pneumatic conveyors. Beck's project relates to an instrumentation and control system which provides minimum cost conveying for a variable solids feed rate and composition, in a lean phase vertical pneumatic conveyor.

Gregory (1987) applied electrodynamic sensors to measure the velocity of shot leaving the nozzle of a commercial shot peening machine. Gregory used two axially spaced electrodynamic sensors to detect electrostatic variations within the flow. The sensors are used to sense the random changes in induced charge (shot charge inherent in the mechanical acceleration process) arising from the turbulent nature of pneumatic conveying. The electrical charges induced into the electrodes are amplified. The velocity of the shot is determined by cross-correlating the signals from the two sensors, which yields the shot flow transit time, T, between them. This time delay, T, is then related to the shot velocity by $v = s/T$ where s is the axial separation of the two

electrodynamic sensors. High speed cine photography was used for calibrating shot velocities using the measurement system, and has shown both methods for determining the velocity of shot leaving the nozzle to be in agreement.

Bidin (1993) investigates four techniques of characterising particulate processes using electrical charge tomography. These techniques are the multi-sensing of electrical charge in a cross-section, a neural network based classifier for flow regime identification, cross correlation based velocity determination and spectral analysis of electrodynamic signals. Bidin in his thesis developed single charged-particle, two charged-particles and multi charged particles models to simulate the induction effect on a sensor by charge. His tomographic measurement system consists of sixteen sensors equally spaced around the boundary of a circular 81 mm inside diameter pipe. This is a single slice tomographic measurement. The flowing material in his conveying system is a sand consisting mainly of 600 micron sized particles which are used for measurements of the induced voltages due to different flow regimes. The voltage profile from the sixteen sensors gives spatial information about the flow regime and after normalisation, the profile is fed to a Kohonen neural network which classifies the data and provides flow regime identification.

The electrodynamic sensor has a high spatial filtering bandwidth (section 5.3), which makes it a very useful for velocity determination (Shackleton 1982). It has limitations which arise because of the tribo electrification phenomena (Shackleton 1982) so that the level of charge on a particle can vary depending upon material, size, shape, humidity etc. However, it is interesting to investigate its use and limitations as a sensor for measurement of concentration, velocity and volume flow rates in a tomographic system, which is the subject of this dissertation.

CHAPTER 3

Mathematical Modelling

Chapter summary

Models are developed to predict the sensitivity of circular and rectangular electrodes. The spatial filtering effect of these sensors is investigated. Cross correlation is briefly reviewed and a software program is presented and tested. For tomographic imaging the forward problem for the individual sensors is modelled, used to solve the inverse problem and derive the linear back projection and filtered back projection algorithms.

3.1 Introduction

This chapter consists of four parts. The first part describes the sensor design in terms of sensitivity and spatial filtering. The second part describes the cross correlation function. The third part describes modelling to predict the sensor output voltage profiles arising from different artificially produced flow regimes. The method used to produce the flow regimes is described. The fourth part describes the back projection algorithm used for tomographic image reconstruction in chapter seven.

3.2 Sensor design

In this section, sensor design is based on two important characteristics i.e. sensitivity and the spatial filtering effect.

3.2.1 Sensitivity

Sensitivity can be defined as the change in output of the transducer due to a change in the mass flow rate and the unit of the sensitivity is volts/gram/second.

3.2.1.1 The induction model

For a single charged particle, q, the field E is uniformly radial over its surface (Duckworth 1960),

$$E = \frac{q}{4\pi\varepsilon_0 R^2} \qquad (3.1)$$

where ε_0 is the permittivity of free space (8.854e-12 F/m) and air (relative permittivity 1) is the dielectric medium. It is assumed in this model that the field results in a charge appearing on the surface of an electrode used to sense the change in potential at a point on the wall of a non-conducting or dielectric pipe. Based on figure 3.1 and equation (3.1), the flux at PQ is given by,

$$E = \frac{q}{4\pi\varepsilon_0 (PQ)^2} \qquad (3.2)$$
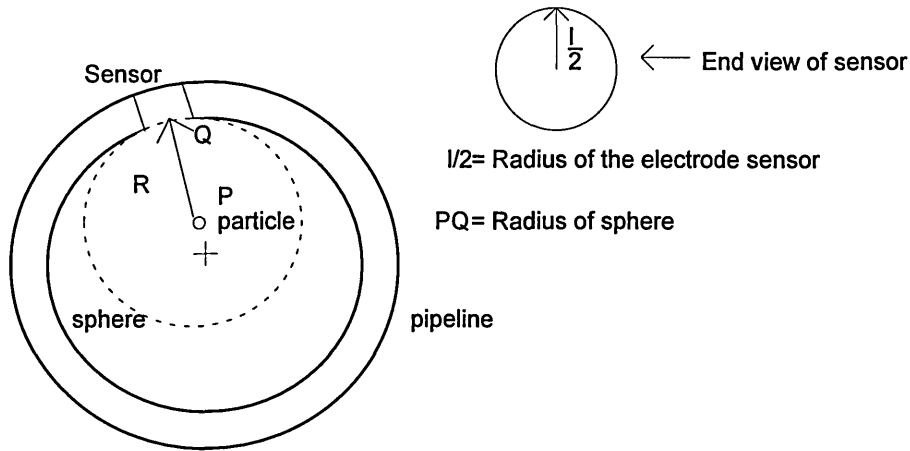
Figure 3.1 : Plan view of the model of a charged particle in the sensing volume

This view of the model is compatible with both circular and rectangular electrodes. However further detailed analysis depends upon electrode shape.

3.2.1.2 The response to a moving particle (flat ended, circular electrode)

Consider a particle p, carrying a charge q, travelling at a uniform velocity V, constrained to pass a conducting circular, flat ended electrode (figure 3.2) along a path which is perpendicular to the vertical axis of the electrode.
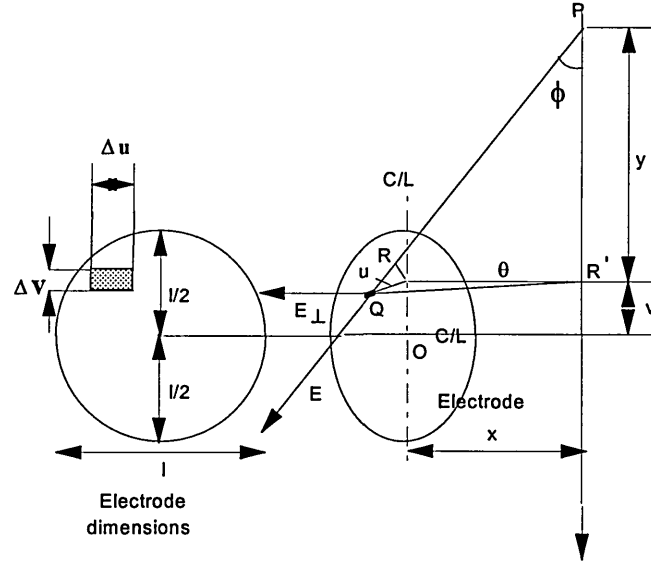
Figure 3.2. Isometric view of a charged particle approaching a flat ended, circular electrode

The electric field, E, due to the charged particle at a distance PQ is

$$E = \frac{q}{4\pi\varepsilon_o (PQ)^2} \tag{3.2}$$

The component of this field normal to the sensor at this point, $E_\perp$, is

$$E_\perp = E \sin\phi \cos\theta \tag{3.3}$$

where angle QRR' = 90° and RR' is normal to electrode.

$$\therefore \sin\phi = \frac{QR'}{QP} \quad \text{and} \quad \cos\theta = \frac{x}{QR'} \tag{3.4}$$

$$E_\perp = E \cdot \frac{QR'}{QP} \cdot \frac{x}{QR'}$$

16

$$E_\perp = E \cdot \frac{x}{QP}$$

Substituting from equation (3.2),

$$E_\perp = \frac{q}{4\pi\varepsilon_o (QP)^2} \cdot \frac{x}{(QP)} \tag{3.5}$$

From figure 3.2,

$$(QP)^2 = (y - v)^2 + (QR')^2 \tag{3.6}$$

$$(QR')^2 = u^2 + x^2 \tag{3.7}$$

$$\therefore E_\perp = \frac{qx}{4\pi\varepsilon_o (QP)^3} = \frac{qx}{4\pi\varepsilon_o \left\{ (y-v)^2 + u^2 + x^2 \right\}^{\frac{3}{2}}} \tag{3.8}$$

The charge induced into a small element of the electrode of area δs is, (Yan *et al* 1995a)

$$dq' = -\varepsilon_o E_\perp \delta s \tag{3.9}$$

substituting for $E_\perp$,

$$dq' = -\varepsilon_o \frac{qx}{4\pi\varepsilon_o \left\{ (y-v)^2 + u^2 + x^2 \right\}^{\frac{3}{2}}} \cdot \Delta u \cdot \Delta v \tag{3.10}$$

Equation 3.10 must be integrated over the whole circular cross section of the sensor to determine the induced charge total as shown in equation (3.11).

$$q' = -\frac{qx}{2\pi} \cdot \int_{\frac{-l}{2}}^{\frac{l}{2}} dv \cdot \int_{u=0}^{\sqrt{\frac{l^2}{4} - v^2}} \frac{du}{\left\{ (y-v)^2 + u^2 + x^2 \right\}^{\frac{3}{2}}} \tag{3.11}$$

$$q' = -\frac{qx}{2\pi} \int_{\frac{-l}{2}}^{\frac{l}{2}} \frac{\sqrt{l^2 - 4v^2} \cdot dv}{(x^2 + (y-v)^2) \cdot (4x^2 + 4y^2 - 8vy + l^2)} \tag{3.12}$$

Equation (3.12) cannot be solved implicitly. However it can be evaluated by substituting numerical values for x, l, q, and y using DERIVE software to give an

17

induced charge signal as shown in figure 3.3. From equation (3.12), the current, i' is given by

$$i' = \frac{dq'}{dt} \text{ where } y = Vt \tag{3.13}$$

The variation in current signal, $|\,i'\,|$ due to the position of the charged particle p is shown in figure 3.4, assuming q = 1 coulomb, l = 10 mm and x = 10 mm.
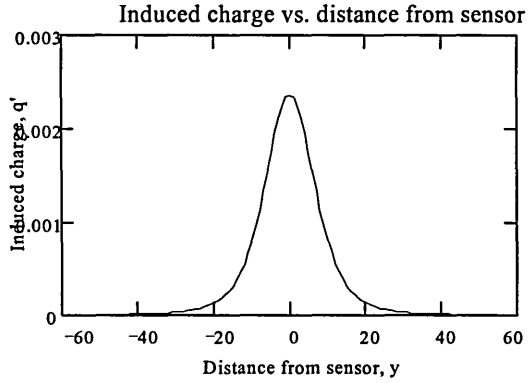
Figure 3.3. Induced charge vs. distance from sensor for a circular sensor of diameter 10 mm.
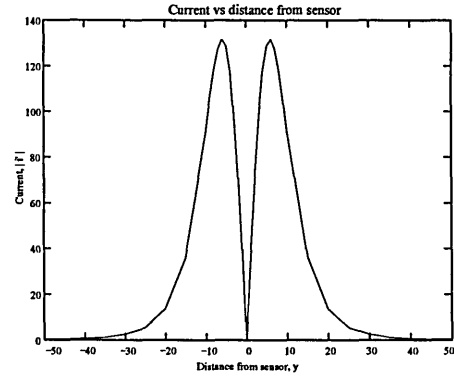
Figure 3.4. Current vs. distance from sensor for a circular sensor of diameter 10 mm

3.2.1.3 The response to a moving particle (rectangular sensor)

Consider a particle p, carrying a charge q, travelling at a uniform velocity V, constrained to pass a conducting rectangular electrode (figure 3.5) along a path which is perpendicular to the vertical axis of the electrode.

18
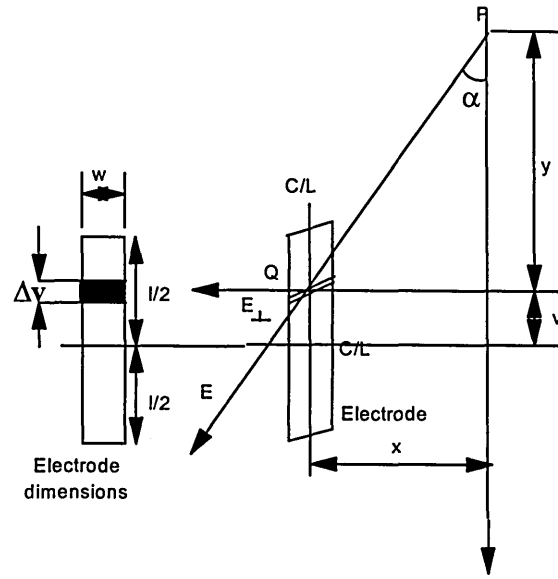
Figure 3.5. Isometric view of a charged particle approaching a rectangular electrode

The electric field, E, due to the charged particle at a distance PQ is

$$E = \frac{q}{4\pi\varepsilon_0(PQ)^2} \qquad (3.2)$$

The component of this field normal to the sensor at this point, $E_\perp$, is

$$E_\perp = \frac{q}{4\pi\varepsilon_0(PQ)^2}\sin\alpha \qquad (3.14)$$

The charge induced into a small element of the electrode of area δs is, (Yan *et al* 1995a)

$$dq' = -\varepsilon_0 E_\perp \delta s \qquad (3.15)$$

substituting from equation (3.14),

$$dq' = -\varepsilon_0 \frac{q}{4\pi\varepsilon_0} \frac{1}{(PQ)^2}\sin\alpha.w\Delta v \qquad (3.16)$$

but $\sin\alpha = \dfrac{x}{(PQ)} \qquad (3.17)$

$$\therefore dq' = -\frac{qx}{4\pi} \cdot \frac{w}{(PQ)^3} \cdot \Delta v \qquad (3.18)$$

19

From figure 3.5,

$$(PQ)^2 = (y - v)^2 + x^2 \qquad (3.19)$$

Therefore the charge induced into the element δs is

$$dq' = -\frac{qxw}{4\pi} \cdot \frac{\Delta v}{\{(y - v)^2 + x^2\}^{\frac{3}{2}}} \qquad (3.20)$$

Therefore the total charge induced into the sensor is given by

$$q' = -\frac{qxw}{4\pi} \cdot \int_{-\frac{l}{2}}^{\frac{l}{2}} \frac{dv}{\{(y - v)^2 + x^2\}^{\frac{3}{2}}} \qquad (3.21)$$

This has been integrated using DERIVE software giving,

$$q' = -\frac{qxw}{4\pi} \cdot \left[\frac{1}{x^2} \left\{ \frac{(y + \frac{l}{2})}{\left[y^2 + yl + \frac{l^2}{4} + x^2 \right]^{\frac{1}{2}}} - \frac{(y - \frac{l}{2})}{\left[y^2 - yl + \frac{l^2}{4} + x^2 \right]^{\frac{1}{2}}} \right\} \right] \qquad (3.22)$$

For the rectangular electrodes investigated in section 3.2.2.2, w = 10 mm, x = 10 mm

and l is varied from 20 mm to 300 mm. From equation (3.22), the current, I' is given by

$$i' = \frac{dq'}{dt} \text{ where } y = Vt \qquad (3.23)$$

This has been solved using DERIVE software giving,

$$i' = \frac{8.V.a.b.[(x^2 - y.c).b - (x^2 + y.d).a] - y.(4.x^2 - l^2 + 4.y^2).(c.b + d.a)}{x^2.a^3.b^3} \qquad (3.24)$$

where

$$a = \sqrt{4.x^2 + l^2 - 4.l.y + 4.y^2} \qquad (3.25)$$

$$b = \sqrt{4.x^2 + l^2 + 4.l.y + 4.y^2} \qquad (3.26)$$

$$c = 1 - 2.y \qquad (3.27)$$

$$d = 1 + 2.y \qquad (3.28)$$

Results for this case have been evaluated for V= 5000 mm/s, q = 1, x = 10 mm and w = 10 mm. The results for l = 20 mm are shown graphically in figures 3.6 and 3.7.
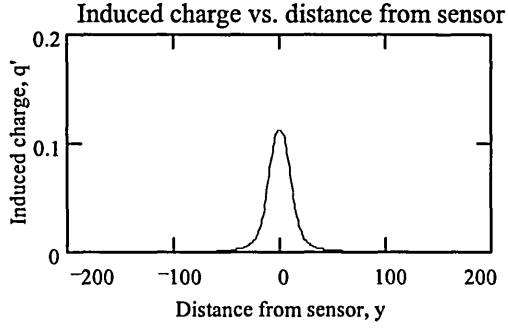
Figure 3.6. Induced charge vs. distance from sensor for rectangular electrode length 20 mm
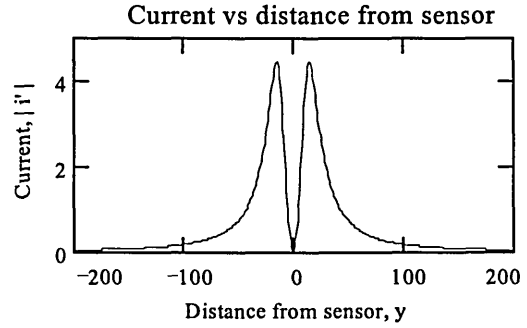
Figure 3.7. Current vs. distance from sensor for rectangular electrode length 20 mm

The results for l = 300 mm are shown graphically in figures 3.8 and 3.9.
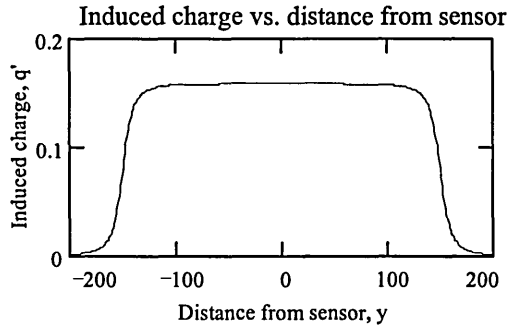
Figure 3.8. Induced charge vs. distance from sensor for rectangular electrode length 300 mm
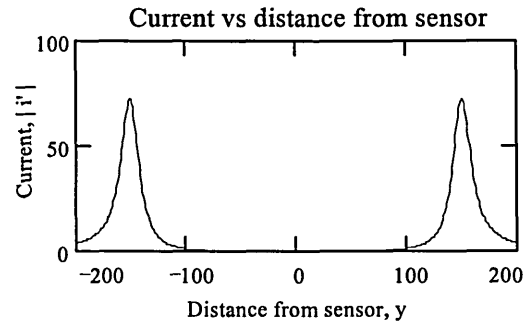
Figure 3.9. Current vs. distance from sensor for rectangular electrode length 300 mm

3.2.2 Spatial filtering effect

The spatial filtering effect can be defined as the relationship between sensor size and the frequency bandwidth of the transducer determined from the frequency response obtained during a pulse which corresponds to a detectable particle.

3.2.2.1 The flat ended, circular electrode

Assume that a charge in the form of a pulse $\rho(t)$ of the conveyed component (termed a concentration pulse) passes the electrode, of length d with velocity υ as shown in figure 3.10 (Harmer and Green 1983).
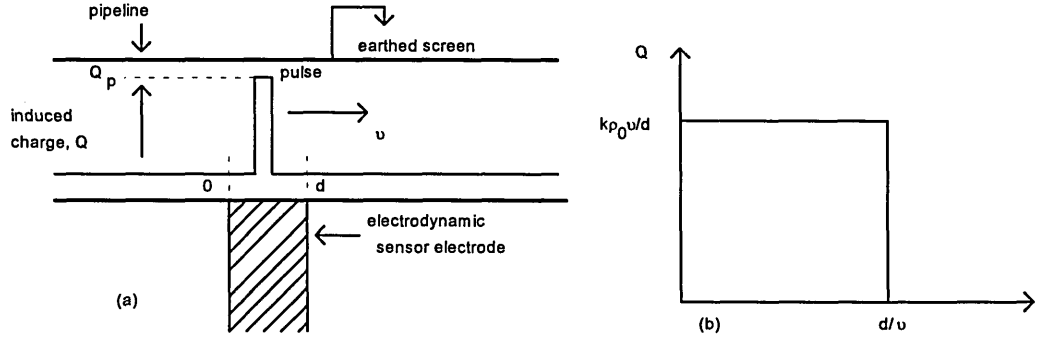
Figure 3.10 : Time history of concentration pulse

If the electrostatic field between the sensor and screen are homogeneous and non fringing, the charge pulse will create a change in the charge induced in the sensor which can be described by a rectangular pulse of duration $\dfrac{d}{\upsilon}$ (figure 3.10 (b)). The amplitude of the charge pulse can be determined from

$$\Delta Q_p = k\frac{\upsilon}{d}\int_0^\infty \rho_p(t)dt \tag{3.29}$$

where k is a constant of proportionality with appropriate dimensions. If the pulse of concentration is short compared to $\dfrac{d}{\upsilon}$ it can be regarded as a Dirac pulse :

$$\rho_p(t) = \rho_0\delta(t) \tag{3.30}$$

where $\int_0^\infty \delta(t)dt = 1$ and ρ_0 is the amplitude of the concentration pulse.

The corresponding amplitude of the change in charge is

$$\Delta Q_p = \frac{k\rho_0\upsilon}{d} \tag{3.31}$$

22

and the charge response may be described by the following equation

$$\Delta Q_p(s) = (\frac{k\rho_0 \upsilon}{ds}).(1 - \exp(-\frac{ds}{\upsilon})) \qquad (3.32)$$

where s is the Laplace variable = $\sigma + j\omega$. Hence the electrode transfer function is

$$h(s) = (\frac{1}{\rho_0}).\Delta Q_p(s) = (\frac{k\upsilon}{ds}).(1 - \exp(-\frac{ds}{\upsilon})) \qquad (3.33)$$

This may be transformed into the frequency domain by replacing s with $j\omega$. Hence

$$h(j\omega) = (\frac{k\upsilon}{dj\omega}).(1 - \exp(-\frac{dj\omega}{\upsilon})) \qquad (3.34)$$

Equation (3.34) may be rewritten :

$$h(j\omega) = \frac{k\upsilon}{d}[\sin(\frac{\omega d}{\upsilon}) - j(1 - \cos(\frac{\omega d}{\upsilon}))] \qquad (3.35)$$

and the amplitude frequency response for the transfer function between ρ_0 and ΔQ_p is

$$|h(j\omega)| = \left|\frac{\Delta Q_p}{\rho_0}\right| = k\left|\frac{\sin(\frac{\omega d}{2\upsilon})}{\frac{\omega d}{2\upsilon}}\right| \qquad (3.36)$$

This transfer function is plotted in figure 3.11. Equation (3.36) enables the transfer function between conveyed component concentration and electrode sensor to be measured by recording the response generated by a travelling pulse of concentration passing between the electrodes provided that the pulse length is short compared to the electrode length.

The transfer function minima occur when $sin(\frac{\omega d}{2\upsilon}) = 0$. Therefore $\frac{\omega d}{2\upsilon} = \pi$, 2π, 3π,........

and minima when $\frac{\upsilon}{d} = \frac{\omega}{2\pi}, \frac{\omega}{4\pi}, \frac{\omega}{6\pi}$........
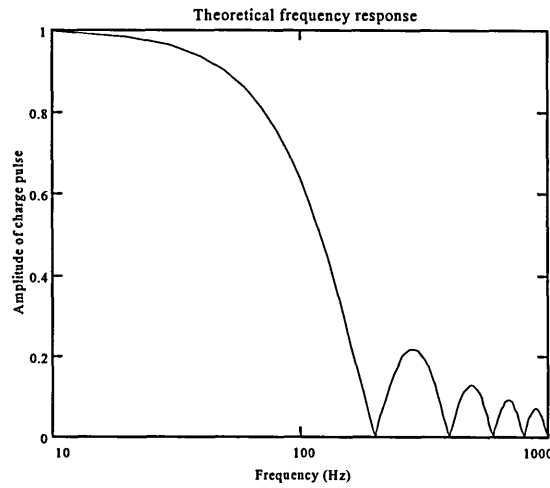
Figure 3.11 : Theoretical transfer function, υ = 2 m/s, d = 0.01 m and f_0 = 200 Hz

3.2.2.2 The rectangular electrode

The rectangular electrodes are much longer than the flat ended, circular electrodes and recordings of the voltage from the sensor, taken when investigating the spatial filtering effect, are slightly different to those obtain from the flat ended, circular electrodes (section 3.2.2.1). The analysis referred to above requires modifying in order to determine the spatial filtering characteristics of long rectangular sensors.

In the experimental verification of this analysis (section 5.6, figure 5.18), the long electrodes of length d are curved to approximately the same radius as the charged bead moves along to ensure the bead to electrode gap remains constant as the bead passes the electrode. In this case the charged bead is passing the electrode for a longer period than for the flat ended, circular sensor. The charge and discharge currents are noticeably spaced in time, as are the corresponding rectified voltages (figure 3.12). The spatial filtering effect for this system is calculated by considering the system as consisting of two impulses with a time delay separating them. If the pulse durations are short compared with d/v they may be regarded as two Dirac pulses.
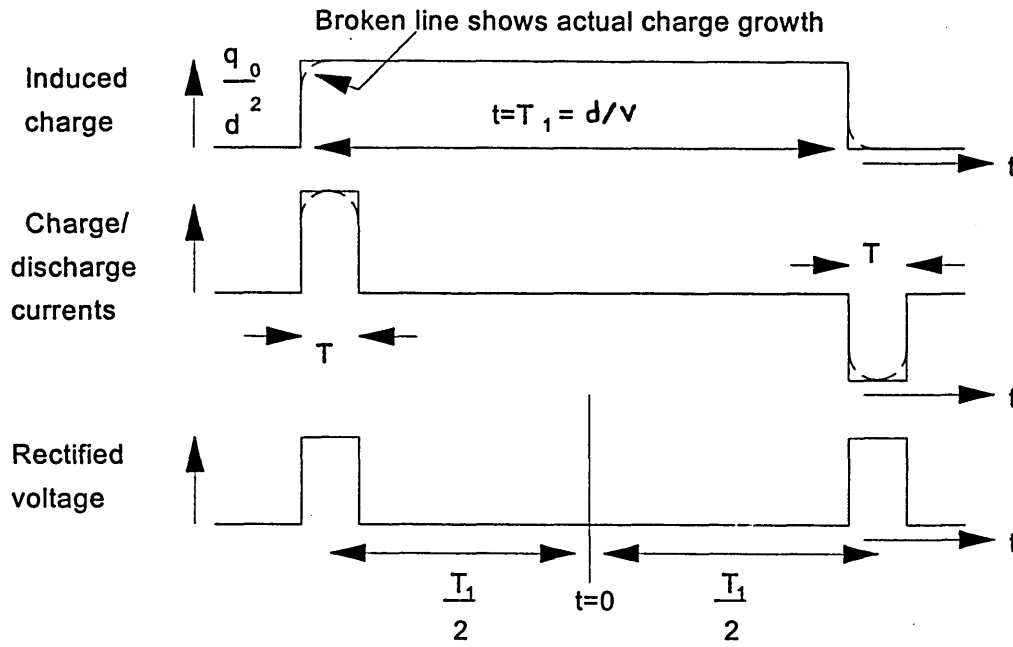
Figure 3.12 : Idealised induced charge and corresponding voltages for the rectangular electrode.

Then the transducer response may be written

$$V_i(\omega) = \int_{-\frac{T_1}{2}-\frac{T}{2}}^{-\frac{T_1}{2}+\frac{T}{2}} k \frac{q_o}{d^2} e^{j\omega t} dt + \int_{\frac{T_1}{2}-\frac{T}{2}}^{\frac{T_1}{2}+\frac{T}{2}} k \frac{q_o}{d^2} e^{j\omega t} dt \qquad (3.37)$$

where T is the time taken to charge and discharge the electrode. After integration and expansion equation (3.37) gives

$$\frac{V_i}{q_0} = \frac{4k}{d^2\omega} \cos\frac{\omega T_1}{2} \sin\frac{\omega T}{2} \qquad (3.38)$$

which may be written in the frequency domain.

The modulus of equation 3.38 is given by

$$\left|\frac{V_i}{q_0}\right| = \frac{2k}{d^2} \left|\cos\frac{\omega d}{2v}\right| \left|\frac{\sin\frac{\omega T}{2}}{\frac{\omega}{2}}\right| \qquad (3.39)$$

and the effect of d and v on the modulus shown graphically in figure 3.13.

25
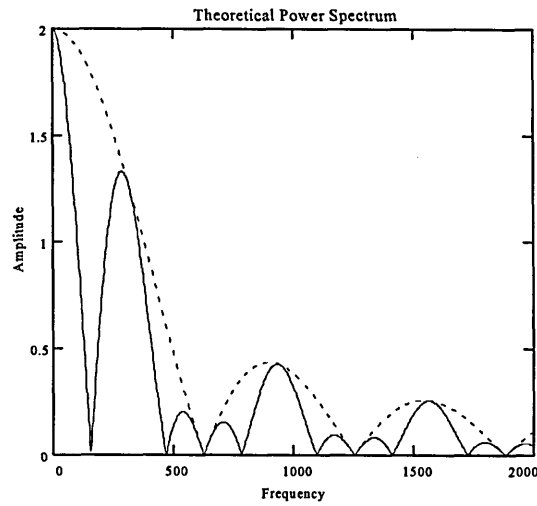
Figure 3.13 : Predicted spatial frequency response for the rectangular electrode.
The dotted line represents (2k/d^2).| sin (ωT/2)/(ω/2) | and the solid line represents
(2k/d^2).| cos(ωd/2v) |.| sin(ωT/2)/(ω/2) |

3.3 Cross correlation

Correlation analysis is a process to quantify the degree of interdependence of one process upon another, or to establish the similarity between one set of data and another (Ifeachor and Jervis, 1993). Application of correlation analysis can be found in many fields based on the following examples :-

(a). Image processing for robotics vision - data from different images are compared

(b). Remote sensing by satellite - data from different images are compared

(c). Radar and sonar systems for range and position - transmitted and reflected wave forms are compared.

(d). Detection and identification of signals in noisy environments

(e). Control engineering - to observe the effects of inputs and outputs in the presence of noise

Correlation analysis can be divided into two parts:-

(a). Auto correlation

The process of auto correlation establishes the relationship between the signal and a time-shifted version of itself. The auto correlation function is a graph of correlation coefficients relating two versions of the same signal plotted against a shift in time. The instrument which measures the auto correlation function of a signal is called an autocorrelator.

(b). Cross correlation

Cross correlation is a process of comparing one signal with another by multiplication of corresponding instantaneous values and taking the average. The cross correlation function is a graph of the value of the cross correlation coefficient against parametric time shift. This graph will measure the similarity and relationship between two different signals. The maximum value of the cross correlation function means that two different signals are more nearly the same for that particular time delay.

3.3.1 Cross correlation sequences

The cross correlation function relating two continuous signals x(t) and y(t) may be defined as (Beck and Plaskowski 1987)

$$R_{xy}(\tau) = \lim_{T \to \infty} \frac{1}{T} \int_0^T x(t)y(t+\tau)dt \qquad (3.40)$$

where τ is a time shift imposed upon one of the signals.

Consider two digital signal sequences x(n) and y(n). The cross correlation of x(n) and y(n) is a sequence $R_{xy}(\tau)$, which in discrete time intervals is defined as

$$R_{xy}(\tau) = \sum_{n=-\infty}^{\infty} x(n)y(n-\tau), \qquad \tau = 0, \pm 1, \pm 2, \qquad (3.41)$$

or equivalently, as

$$R_{xy}(\tau) = \sum_{n=-\infty}^{\infty} x(n+\tau)y(n), \qquad \tau = 0, \pm 1, \pm 2, \qquad (3.42)$$

27

The index τ is the time shift parameter and the subscripts xy on the cross correlation sequence $R_{xy}(\tau)$ indicate the sequences being correlated. The order of the subscripts, with x preceding y , indicates the direction in which one sequence is shifted relative to the other. From equation (3.23), the sequence x(n) is unshifted and y(n) is shifted by lag units in time, to the right for τ positive and to the left for τ negative. Shifting x(n) to the left by τ units relative to y(n) is equivalent to shifting y(n) to the right by τ units relative to x(n). Computations (3.23) and (3.24) give an identical cross correlation sequences. If we reverse the roles of x(n) and y(n) in (3.23) and (3.24) and hence reverse the order of the indices xy, we obtain the cross correlation sequence

$$R_{yx}(\tau) = \sum_{n=-\infty}^{\infty} y(n)x(n-\tau) \tag{3.43}$$

or equivalently

$$R_{yx}(\tau) = \sum_{n=-\infty}^{\infty} y(n+\tau)x(n) \tag{3.44}$$

By comparing (3.2.3) with (3.2.5) or (3.2.4) with (3.2.6), we conclude that

$$R_{xy}(\tau) = R_{yx}(-\tau) \tag{3.45}$$

$R_{yx}(\tau)$ is the folded version of $R_{xy}(\tau)$, where the folding is done with respect to $\tau = 0$.

Hence $R_{yx}(\tau)$ provides exactly the same information as $R_{xy}(\tau)$ about the similarity of x(n) to y(n).

3.3.2 Normalised cross correlation

The cross correlation function $R_{xy}(n)$ between two data sequences x(n) and y(n) each containing N data can be written as

$$R_{xy}(\tau) = \sum_{n=0}^{N-1} x(n)y(n-\tau) \tag{3.46}$$

This definition of cross correlation, however, produces a result which depends on the number of sampling points taken. This is corrected for by normalising the result to the number of points by dividing by N. This can be regarded as averaging the sum of the products. Thus, an improved definition of cross correlation is

$$R_{xy}(\tau) = \frac{1}{N}\sum_{n=0}^{N-1} x(n)y(n-\tau) \tag{3.47}$$

$$R_{xy}(-\tau) = \frac{1}{N}\sum_{n=0}^{N-1} x(n+\tau)y(n) \tag{3.48}$$

It is often necessary to measure cross correlation according to the fixed scale between (-1) and (+1). This can be achieved by normalising the values by an amount depending on the energy content of the data. The normalising factor for $R_{xy}(\tau)$ can be written as

$$\sqrt{[\frac{1}{N}\sum_{n=0}^{N-1}x^2(n).\frac{1}{N}\sum_{n=0}^{N-1}y^2(n)]} = \frac{1}{N}\sqrt{[\sum_{n=0}^{N-1}x^2(n).\sum_{n=0}^{N-1}y^2(n)]} \tag{3.49}$$

The normalised expression for $R_{xy}(\tau)$ then becomes

$$\rho_{xy}(\tau) = \frac{R_{xy}(\tau)}{\frac{1}{N}\sqrt{[\sum_{n=0}^{N-1}x^2(n).\sum_{n=0}^{N-1}y^2(n)]}} \tag{3.50}$$

where $R_{xy}(\tau) = \frac{1}{N}\sum_{n=0}^{N-1}x(n)y(n-\tau)$

$\rho_{xy}(\tau)$ is known as the normalised cross correlation coefficient. Its value always lies between -1 and +1. +1 means 100% correlation in the same sense, -1 means 100% correlation in the opposing sense. A value of 0 signifies zero correlation. This means the signals are completely independent.

3.3.3 Velocity measurement by cross correlation

Velocity measurement of particles moving in a pipe using cross correlation can be realised in hardware (cross correlator) and software (computer programming). Both methods can be used on-line and off-line to the measurement system.

3.3.3.1 The cross correlator

Cross-correlation flow meters measure the transit time of a tagging signal (turbulence, clumps of particles, etc.) in the flow between two axially spaced sensors (Beck 1981a). The above technique is suitable for process industries which handle solids and fluids in pipelines. A correlator can be realised from the above method by using large-scale integrated circuits and microprocessors (Browne etc al 1982). Figure 3.14 below illustrates the concept of flow measurement by cross-correlation. The cross-correlation function is defined to be :

$$R_{xy}(\tau) = x(t-\tau)y(t)dt \tag{3.51}$$

This function has a maximum value when the cross-correlation lag τ is equal to the transit time τ_d of the tagging signals. Hence the velocity υ is given by

Flow velocity = Sensor spacing / Time delay

$$\upsilon = \frac{L}{\tau_d} \tag{3.52}$$

where L is the distance between the upstream sensor and downstream sensor. Both sensors result in a pseudo random electrical wave form if there is flow inside the pipeline. For example if sand is flowing inside the pipeline, electrodynamic transducers will sense charge and convert these physical signals to analogue voltages. Cross correlation between the upstream and downstream signals will give a cross correlation function. The position of the maximum value of the cross correlation coefficient will give the time delay between the wave forms.
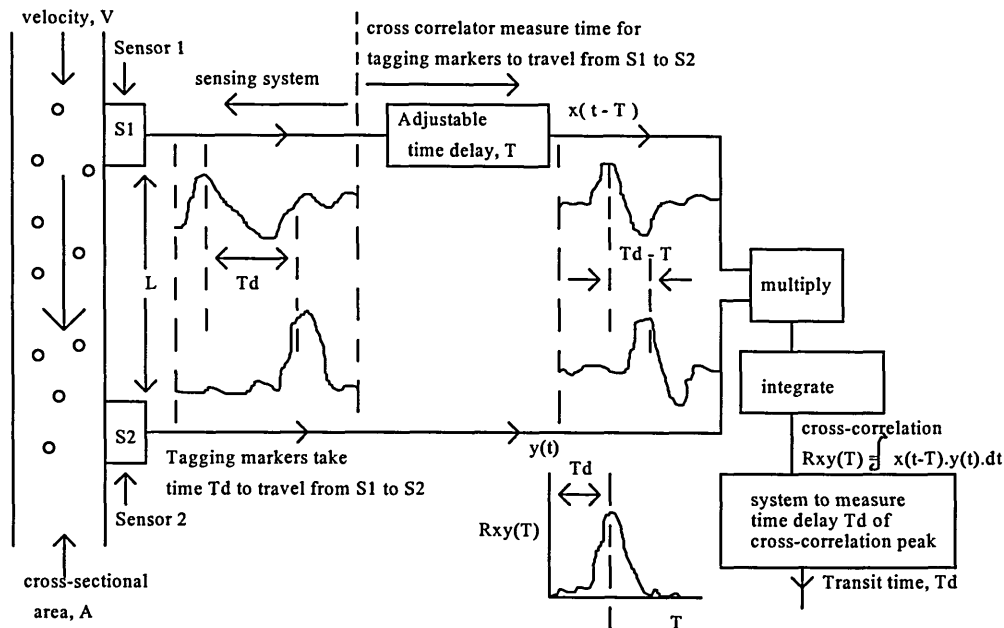
Figure 3.14 : Basic principle of cross-correlation flow meter

3.3.3.2 Software for cross-correlation

A program has been designed that can analyse two different data sets to determine the cross correlation as shown in List 1. This program was written in MATLAB (by Dr. Ken Dutton). Experiments have been carried out to capture data from the electrodynamic sensors using the data acquisition system and the data is processed using off line analysis to obtain the cross correlation function. The computer program, called KXCORR.M, requires two sets of data as inputs to obtain the cross correlation.

```
List 1
function x=kxcorr(u,y)
if nargin~=2,
   error('kxcorr must have two arguments')
end
L=length(u);
if length(y)~=L,
   error('kxcorr - arguments are not the same length')
end
for i=1:L,
   if i==1,
      ushft=u;
   else
      ushft=[ushft(L,1); ushft(1:L-1,1)];
   end
   x(i)=sum(y.*ushft)/L;
```

31

end

plot(x)

In the above program listing, u is an [LX1] matrix consisting of measured data from the upstream sensor and y is an [LX1] matrix from the downstream sensor. The length, L, of both matrices must be the same and x is the cross correlation function. The method used to calculate the cross correlation function is a point to point method. In order to calculate the cross correlation function in the above program, the value of both matrices must be entered and the function x=kxcorr(u,y) called. The maximum value of matrix x is found by using the command [z,j]=max(x) where z is the value of the maximum cross correlation coefficient and j is the index time correspond to the z value.

3.3.3.3 Verification of software correlation programme

A typical wave form from the upstream and downstream sensors for the first 312 samples is shown in figure 3.15.
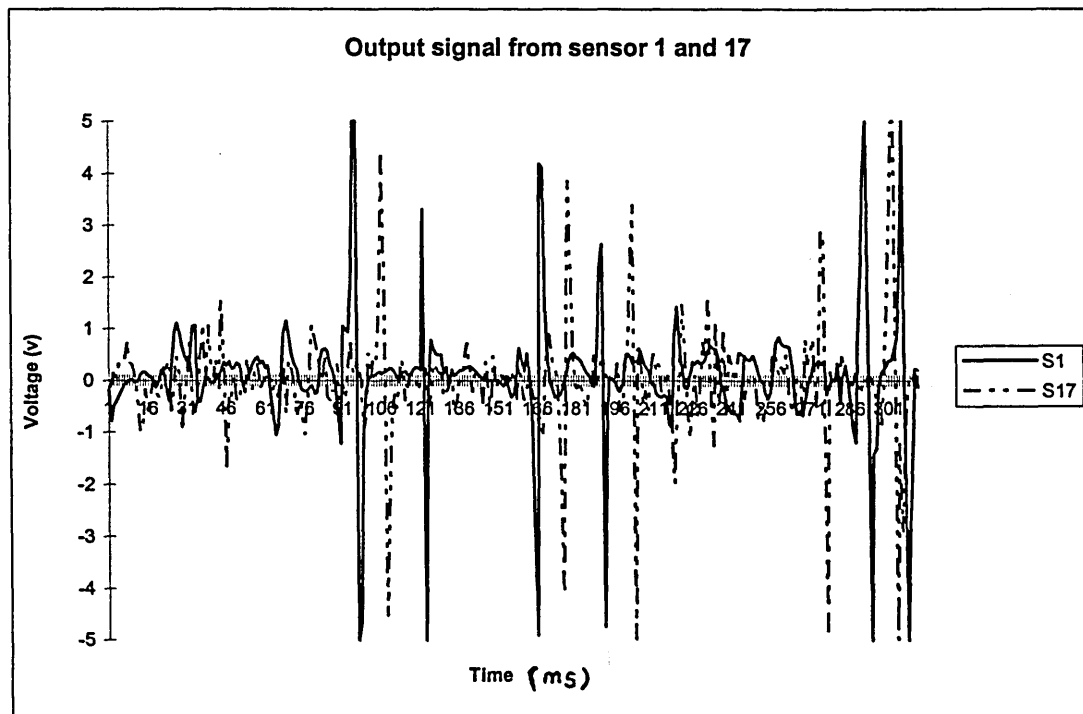
Figure 3.15 : Signal from sensor 1(upstream) and sensor 17(downstream); sampled at 1 kHz.

The locations of sensors 1 and 17 are shown in figure 4.8 section 4.5. The data have been processed using the program listing List 1 to obtain the cross correlation of the two signals using off-line analysis. The result of the cross-correlation is shown in figure 3.16.
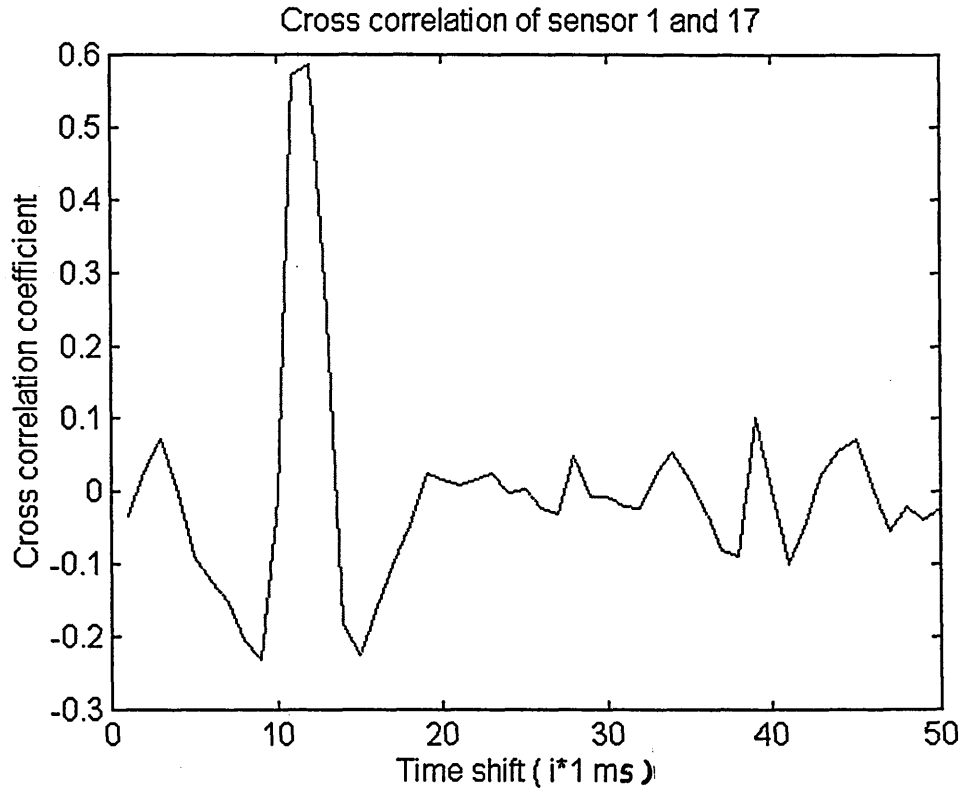
Figure 3.16 : Cross correlation function

The cross-correlation shown in figure 3.16 is for full flow. The first major peak on the graph gives a transit time of 12 ms. From the transit time, the velocity is calculated,

$$\upsilon = \frac{L}{\tau_d} = 0.05 / (12*1 \text{ ms}) = 4.2 \text{ m/s}$$

3.4 Tomographic imaging

In this work tomographic images are derived using a back projection algorithm. In order to derive this algorithm which provides the solution to the inverse problem, the forward problem must be solved.

3.4.1 The forward problem

The forward problem determines the theoretical output of each of the sensors when the sensing area is considered to be two dimensional and contains a uniformly distributed charge of σ coulombs per square metre. The cross-section of the pipe is mapped onto a nine by nine rectangular array consisting of 81 pixels as shown in figure 3.17.
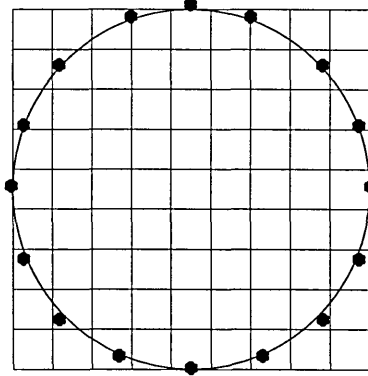
Figure 3.17. 9x9 rectangular array consists of 81 pixels

Each sensor is considered separately and the effect on it due to the uniform surface charge, σ coulombs m^{-2}, on each pixel determined. To minimise boundary problems the sensor is placed 0.5 mm outside the pipe wall. Each pixel is considered in turn. The sensitivity map is generated by calculating the charge which a chosen pixel would induce into the sensor.

Calculation of the sensitivity map for sensors one, two and three are outlined in the following section.

3.4.1.1 Sensor 1 sensitivity map

The centre of the pipe is defined as (0,0) as shown in figure 3.18. The pipe diameter is 81 mm and each pixel is 9x9 mm.

Figure 3.18. Sensitivity model for sensor 1

The general sensitivity equation corresponding to sensor 1 is,

$$I_1 = \iint \frac{\sigma}{r^2} dA = \int_x dx \int_y \frac{\sigma}{x^2 + (41-y)^2} dy \qquad (3.53)$$

where (x,y) are the co-ordinates of the part of the pixel contributing to the sensor output, r is the distance of the charge to the sensor and the inverse square law is obeyed. The total induced charge for sensor 1 when σ is assumed to be 1 Cm^{-2} is,

$$I_1 = \int_{-40.5}^{40.5} dx. \int_{-\sqrt{40.5^2-x^2}}^{\sqrt{40.5^2-x^2}} \frac{1}{x^2 + (41-y)^2} dy \approx 11.75 \text{ coulombs}$$

However the sensitivity map requires the contribution from each pixel to be evaluated separately. Each pixel is identified numerically, the first number is the column number, the second number is the row number starting with 11 for the top left hand pixel. Three examples of the sensitivity calculation are shown below.

$$Pixel51 = \int_{-4.5}^{4.5} dx. \int_{31.5}^{40.5} \frac{1}{x^2 + (41-y)^2} dy \approx 6.20$$

$$Pixel59 = \int\limits_{-4.5}^{4.5} dx. \int\limits_{-40.5}^{-31.5} \frac{1}{x^2 + (41-y)^2} dy \approx 0.01$$

$$Pixel31 = \int\limits_{-22.5}^{-13.5} dx. \int\limits_{31.5}^{\sqrt{40.5^2 - x^2}} \frac{1}{x^2 + (41-y)^2} dy \approx 0.13$$

This calculation is repeated for all the pixels. Complete pixels and parts of pixels outside the pipe contribute zero induced charge to the sensor and so have a sensitivity value of zero i.e. pixel 11, 12, 21, 81, 91, 92, 18, 19, 29, 89, 98 and 99. However, pixels intersected by the pipe boundary have a contribution to the induced charge from the fraction of the pixel within the conveyor. The resulting sensitivity map for sensor 1 is shown in numerical form in figure 3.19(a) below.

0	0	0.13	0.78	6.20	0.78	0.13	0	0
0	0.07	0.16	0.31	0.44	0.31	0.16	0.07	0
0.02	0.06	0.10	0.14	0.16	0.14	0.10	0.06	0.02
0.03	0.05	0.06	0.07	0.08	0.07	0.06	0.05	0.03
0.03	0.03	0.04	0.05	0.05	0.05	0.04	0.03	0.03
0.02	0.02	0.03	0.03	0.03	0.03	0.03	0.02	0.02
0.01	0.02	0.02	0.02	0.02	0.02	0.02	0.02	0.01
0	0.01	0.02	0.02	0.02	0.02	0.02	0.01	0
0	0	0.01	0.01	0.01	0.01	0.01	0	0

Figure 3.19(a). Sensitivity map for sensor 1

Figure 3.19(b). Sensitivity map in 3D for sensor 1

The sensitivity map for sensor 1 is plotted in three dimensions as shown in figure 3.19(b), where (x,y) represent the pipe cross-section and the z-axis is the sensitivity. This shows the significant localised sensitivity of the sensor.

3.4.1.2 Sensor 2 sensitivity map

The sensitivity map for sensor 2, co-ordinates (-15.7,37.9) in similar to that of sensor 1 (section 3.4.1.1) as shown in figure 3.20.
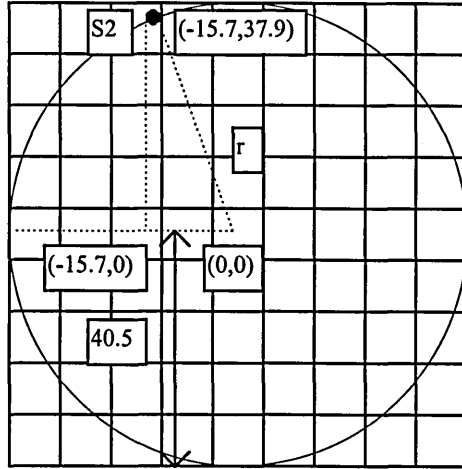
Figure 3.20. Sensitivity model for sensor 2

The general sensitivity equation corresponding to sensor 2 is,

$$I_2 = \iint \frac{\sigma}{r^2} dA = \int_x dx. \int_y \frac{\sigma}{(15.7 + x)^2 + (37.9 - y)^2} dy \qquad (3.54)$$

where the variables have the same definition as for sensor 1. The total induced charge for sensor 2 when σ is assumed to be 1 Cm^{-2} is,

$$I_2 = \int_{-40.5}^{40.5} dx. \int_{-\sqrt{40.5^2 - x^2}}^{\sqrt{40.5^2 - x^2}} \frac{1}{(15.7 + x)^2 + (37.9 - y)^2} dy \approx 11.71 \text{ coulombs}$$

Three examples of the sensitivity calculation are shown below.

$$Pixel31 = \int_{-22.5}^{-13.5} dx. \int_{31.5}^{\sqrt{40.5^2 - x^2}} \frac{1}{(15.7 + x)^2 + (37.9 - y)^2} dy \approx 4.73$$

$$Pixel55 = \int_{-4.5}^{4.5} dx. \int_{-4.5}^{4.5} \frac{1}{(15.7 + x)^2 + (37.9 - y)^2} dy \approx 0.05$$

$$Pixel95 = \int_{31.5}^{40.5} dx. \int_{-4.5}^{4.5} \frac{1}{(15.7 + x)^2 + (37.9 - y)^2} dy \approx 0.02$$

37

This is repeated for all pixels. The resulting sensitivity map for sensor 2 is shown in numerical format in figure 3.21(a).

0	0	1.73	1.80	0.34	0.12	0.04	0	0
0	0.28	0.73	0.54	0.23	0.11	0.06	0.03	0
0.08	0.16	0.21	0.19	0.13	0.08	0.05	0.04	0.04
0.06	0.08	0.10	0.10	0.08	0.06	0.04	0.03	0.02
0.04	0.05	0.06	0.06	0.05	0.04	0.03	0.02	0.02
0.03	0.04	0.04	0.03	0.03	0.03	0.02	0.02	0.02
0.01	0.02	0.03	0.03	0.02	0.02	0.02	0.02	0.02
0	0.02	0.02	0.02	0.02	0.02	0.02	0.01	0
0	0	0.01	0.01	0.01	0.01	0.01	0	0

Figure 3.21(a). Sensitivity map for sensor 2
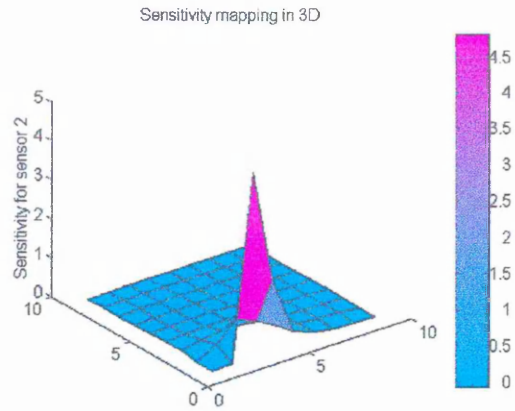
Figure 3.21(b). Sensitivity map in 3D for sensor 2

The sensitivity map for sensor 2 is plotted in three dimensions figure 3.21(b).

3.4.1.3 Sensor 3 sensitivity map

The sensitivity map for sensor 3 is calculated in a similar manner to sensor 1 (section 3.4.1.1) and sensor 2 (section 3.4.1.2) as shown in figure 3.22.
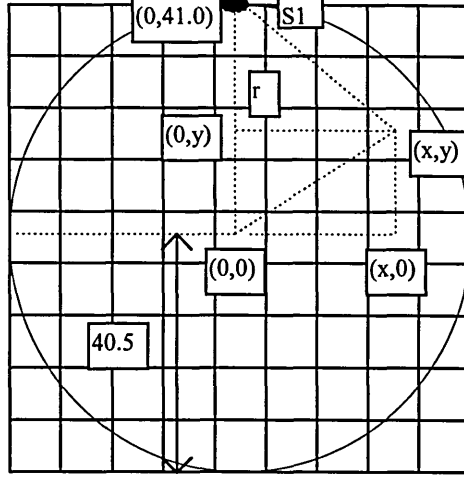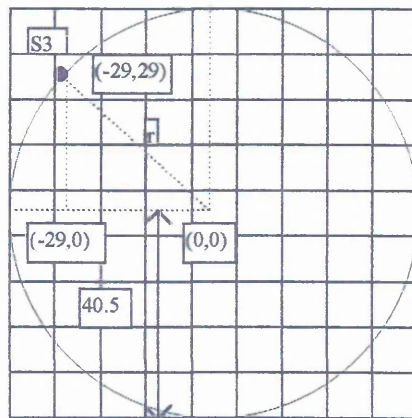

Figure 3.22. Sensitivity model for sensor 3

The general sensitivity equation correspond to sensor 3 is,

$$I_3 = \iint \frac{\sigma}{r^2} dA = \int_x dx . \int_y \frac{\sigma}{(29+x)^2 + (29-y)^2} dy \qquad (3.55)$$

and the total induced charge for sensor 3 when σ is assumed to be 1 Cm^{-2} is,

$$I_3 = \int\limits_{-40.5}^{40.5} dx. \int\limits_{-\sqrt{40.5^2-x^2}}^{\sqrt{40.5^2-x^2}} \frac{1}{(29+x)^2 + (29-y)^2} dy \approx 11.72 \text{ coulombs}$$

However the sensitivity map requires the contribution from each pixel to be evaluated.

Three examples of the sensitivity calculation are shown below.

$$Pixel22 = \int\limits_{-31.5}^{-25.5} dx. \int\limits_{22.5}^{\sqrt{40.5^2-x^2}} \frac{1}{(29+x)^2 + (29-y)^2} dy + \int\limits_{-25.5}^{-22.5} dx. \int\limits_{22.5}^{31.5} \frac{1}{(29+x)^2 + (29-y)^2} dy$$

$$Pixel22 \approx 6.00$$

$$Pixel26 = \int\limits_{-31.5}^{-22.5} dx. \int\limits_{-13.5}^{-4.5} \frac{1}{(29+x)^2 + (29-y)^2} dy \approx 0.06$$

$$Pixel79 = \int\limits_{13.5}^{22.5} dx. \int\limits_{-\sqrt{40.5^2-x^2}}^{-31.5} \frac{1}{(29+x)^2 + (29-y)^2} dy \approx 0.01$$

This is repeated for all pixels. The resulting sensitivity map for sensor 3 is shown in figure 3.23(a).
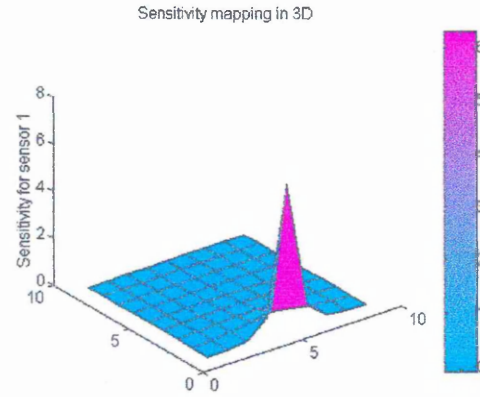

Figure 3.23(a). Sensitivity map for sensor 3
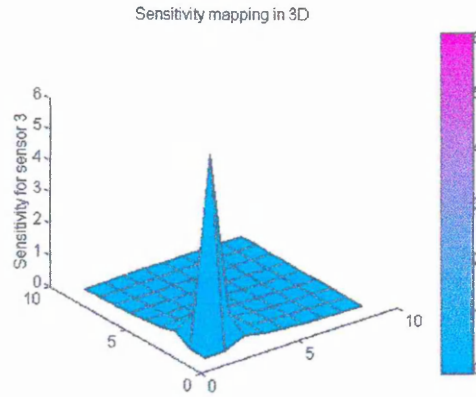
Figure 3.23(b). Sensitivity map in 3D for sensor 3

The sensitivity map for sensor 3 is plotted in three dimensions as shown in figure 3.23(b).

Sensors 4 to 16 sensitivity mappings are obtained by moving the maps for sensor 1 to 3 as shown in table 3.1.

Sensor number	Sensitivity mapping
S4	Mirror of sensor 6 sensitivity map
S5	Rotate sensor 1 sensitivity map 45° anticlockwise
S6	Rotate sensor 2 sensitivity map 45° anticlockwise
S7	Rotate sensor 3 sensitivity map 45° anticlockwise
S8	Mirror of sensor 10 sensitivity map
S9	Rotate sensor 1 sensitivity map 180° anticlockwise
S10	Rotate sensor 2 sensitivity map 180° anticlockwise
S11	Rotate sensor 3 sensitivity map 180° anticlockwise
S12	Mirror of sensor 14 sensitivity map
S13	Rotate sensor 1 sensitivity map 270° anticlockwise
S14	Rotate sensor 2 sensitivity map 270° anticlockwise
S15	Rotate sensor 3 sensitivity map 270° anticlockwise
S16	Mirror of sensor 2 sensitivity map

Table 3.1. Sensitivity map for sensor 4 to 16

3.4.2 The Inverse Problem

The solution of the inverse problem aims to provide an image of the charge concentration distribution within the conveyor, which would result in the measured sensor outputs.

3.4.2.1 Basic back projection

A linear back projection algorithm is used (Abdullah, 1993). The back projection algorithm combines each sensor reading with its sensitivity map to generate the charge concentration map within the pipe, which would provide these readings assuming all

particles carry the same charge. The procedure is to multiply each sensor voltage reading by its sensitivity map to produce sixteen 9x9 matrices. The corresponding individual elements from the 16 matrices are summed to produce a single matrix i.e. the concentration matrix.

The theoretical charge concentration profile has been calculated assuming all the sensors are reading 1 Volt. The charge concentration matrix is shown in figure 3.24(a) with the relative position of the pipe mapped onto it. Figure 3.24(b) displays the result as a coloured tomogram, where the colour relates to charge concentration.

0	0	5.38	3.15	7.32	3.15	5.38	0	0
0	6.9	2.12	1.56	1.41	1.56	2.12	6.9	0
5.38	2.12	1.29	1.03	0.97	1.03	1.29	2.12	5.38
3.15	1.56	1.03	0.86	0.82	0.86	1.03	1.56	3.15
7.32	1.41	0.97	0.82	0.77	0.82	0.97	1.41	7.32
3.15	1.56	1.03	0.86	0.82	0.86	1.03	1.56	3.15
5.38	2.12	1.29	1.03	0.97	1.03	1.29	2.12	5.38
0	6.9	2.12	1.56	1.41	1.56	2.12	6.9	0
0	0	6.38	3.15	7.32	3.15	5.38	0	0

Figure 3.24(a). Theoretical numerical charge concentration distribution when all sensors set to 1 volt (linear back projection algorithm)
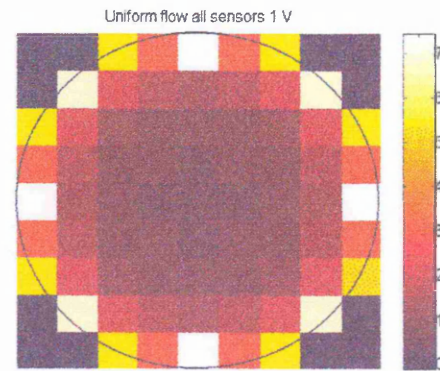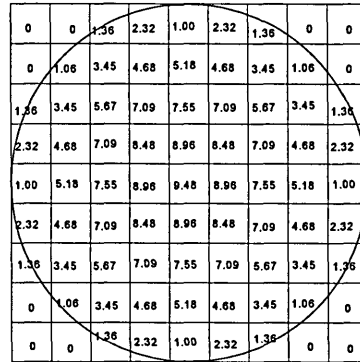
Figure 3.24(b). Theoretical image of charge concentration distribution when all sensors is 1 volt (linear back projection algorithm)

Figures 3.24(a) and 3.24(b) identify the limitation of the simple linear back projection algorithm; the low estimation of charge at the centre of the conveyor. This problem may be reduced by using a filtered back projection algorithm.

3.4.2.2 Filtered back projection

The major limitation of the linear back projection algorithm arises due to the non-linear sensing mechanism of the electrical charge transducer. When the conveyor has a uniformly distributed solids flow, the resulting charge concentration matrix calculated

41

using the linear back projection algorithm, is not uniform at 7.32 units per pixel, but shows lower values as the centre of the pipe is approached, reaching 0.77 units at the centre (figure 3.24a). However a filter can be determined, which, combined with the back projection algorithm, provides a filtered linear back projection algorithm (Barber and Brown 1984). This filter provides weighting to individual pixels to provide a uniform charge concentration profile when all the sensors have equal outputs. The coefficients of the filter are obtained by assuming all the sensors have an output of 1 volt and using these values to calculate the charge concentration matrix described in section 3.5.1. The expected result is a uniform charge concentration matrix with each value being 7.32 units per pixel. The filter matrix is obtained by taking the maximum value of 7.32 units per pixel which is then divided by each value of pixel within the pipe mapping. The resulting filter is shown in figure 3.25.

0	0	1.36	2.32	1.00	2.32	1.36	0	0
0	1.06	3.45	4.68	5.18	4.68	3.45	1.06	0
1.36	3.45	5.67	7.09	7.55	7.09	5.67	3.45	1.36
2.32	4.68	7.09	8.48	8.96	8.48	7.09	4.68	2.32
1.00	5.18	7.55	8.96	9.48	8.96	7.55	5.18	1.00
2.32	4.68	7.09	8.48	8.96	8.48	7.09	4.68	2.32
1.36	3.45	5.67	7.09	7.55	7.09	5.67	3.45	1.36
0	1.06	3.45	4.68	5.18	4.68	3.45	1.06	0
0	0	1.36	2.32	1.00	2.32	1.36	0	0

Figure 3.25. Full flow filter mask

Mathematically, this filter is only applicable to full flow. Similar filters should be calculated for different flow patterns. However to be useful, this requires the flow regime or flow pattern with the conveyor to be known. Flow regimes have been identified using an array of electrodynamic sensors placed around the circumference of a conveyor (Cottam 1994).

Several filter masks for specific non-uniform flows have been developed and are shown in figures 3.26 to figure 3.30. These filters have been derived by assuming separated flow and idealised conditions. For example with half flow, half the pipe is assumed to be completely empty of charged particles and the other half has a uniform charge per unit area over its total area. The filter is then developed from the full flow filter by replacing elements of the matrix by zero if they map to the empty section of the cross-section. Derivation of the other filter masked follows the same procedure.
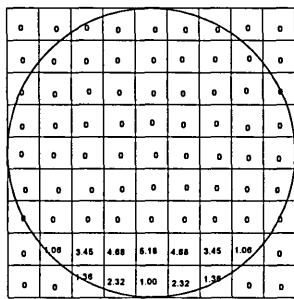
Figure 3.26. Quarter flow filter mask
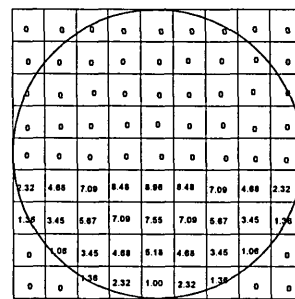
Figure 3.27. Half flow filter mask
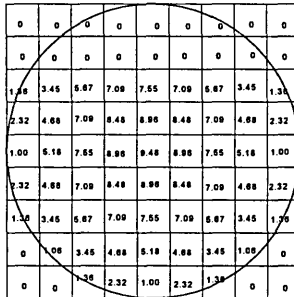
Figure 3.28. Three quarter filter mask
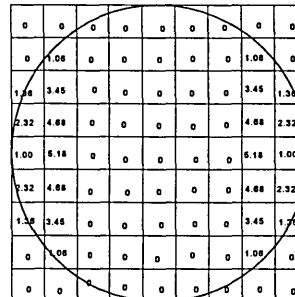
Figure 3.29. Stratified (1) filter mask
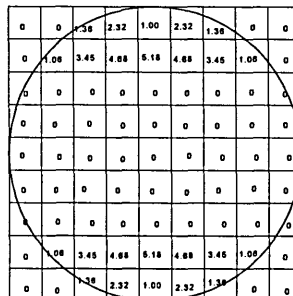
Figure 3.30. Stratified (2) filter mask

CHAPTER 4

The Measurement System

Chapter summary

The design of the electronic circuitry which forms the transducer is presented. The gravity drop flow rig is described and the relationship between sand flow and plastic bead flow relative to the flow indicator setting determined. The dual 16-channel sensor array measurement section is described. Flow models are developed and used to predict the relative output voltage profiles expected from the sensor arrays.

4.1 Introduction

This chapter describes the design of the individual components which combine to form an electrical charge tomography system.

4.2 Electrodynamic transducer

Whenever solid particles are entrained in a flowing stream of gas or air in a conveyor, an electrostatic charge accumulates on the particles. The magnitude of the charges depends on many factors such as the physical properties of the particles, including shape, size, density, conductivity, permittivity, humidity and composition (Shackleton 1982). The pipe wall roughness, pipe diameter, pipe length traversed by the particles, solids velocity and concentration also are major factors contributing to the magnitude of the charges (Williams *et al* 1991). This electrostatic charge can be detected using electrodes or plates and converted into a voltage by the electrodynamic transducer. The voltage is amplified by an AC

amplifier and the output can be cross correlated to give the flow velocity of the solids.

The transducer consists of two basic elements, the electrode or sensing device and the associated electronics (Shackleton 1982). The sensing device consists of a conductor, insulated from the conveyor, which may take a variety of different shapes and sizes. Two types of electrode have found particular application to electrodynamic transducers. The ring electrode illustrated in figure 4.1 (a) has the advantage of averaging the flow velocity near to the pipe wall. An even simpler arrangement is to use pin electrodes, as shown in figure 4.1 (b), which will not average the velocity over the whole pipe wall, but will give the same result as ring electrodes if the flow is axisymmetric (Beck and Plaskowski 1987).
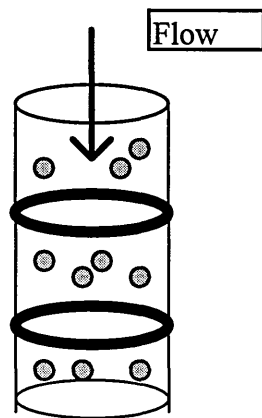
Figure 4.1 (a). Electrodynamic sensing ring electrodes
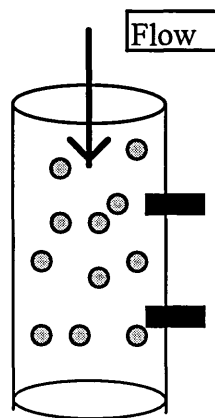
Figure 4.1 (b). Electrodynamic sensing pin electrodes

The associated electronics consist of a circuit for signal conditioning i.e. amplifier and filter. The input of the sensor is a physical signal i.e. electrical charge while the output of the sensor is an electric signal consisting of rectified voltage and averaged voltage as shown in figure 4.2.

Physical Signal

Electrical Charge, Q

Electrodynamic

Transducer

Electrical Signal

Rectified voltage

Averaged voltage

-15V   0V   +15V
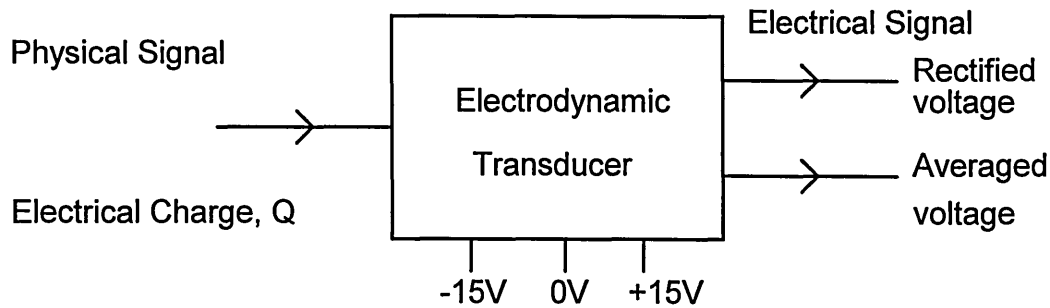
Figure 4.2. Electrodynamic Transducer

The complete circuit of the electrodynamic transducer is shown in figure 4.3.

The electrode (P_2) consists of a metal conductor, which is electrically insulated

from the surrounding metallic conveyor and provides a capacitance to earth. This

capacitance, C_e is not very well defined due to the way it is formed, but it has a

value of approximately 1 pF. In order that measurements are made with similar

capacitance the input circuit consists of a capacitor, C_1, connected between input

and earth. The value of C_1 is 4.7 pF, so the input capacitance is $C_i = (C_e + C_1)$

which has an approximately value of 5.5 to 5.7 pF. The passing charged particles

induce charge, Q_i , into the electrode resulting in a voltage V_i. The input resistor,

R_3 (figure 4.3) provides a path for current to flow into and out of the capacitance

C_i formed between the electrode and ground (section 3.2.1). The current flow

through the input resistor results in the voltage which provides the input to an

integrated circuit amplifier (IC1) connected as a non-inverting voltage follower.

The value of the gain for IC1 is 1 and the bandwidth is 3 Mhz (data sheet for

TL084). The output of the follower is used as a guard voltage for the input

circuit, to minimise stray capacitance of the input circuitry and is ac coupled to

the input to the second stage non-inverting voltage amplifier (IC2). The pair of

back to back zener diodes is an attempt to prevent large voltage discharges which

occur in pneumatic conveyors, from damaging the transducer amplifiers. The

time constant of the coupling circuit in second stage is 1 s, providing a high pass network with a lower cut off frequency of 0.167 Hz. The amplifier has a midband gain 455. The upper cut off frequency is gain bandwidth limited to 6.6 kHz. The output of this stage is available as O/P1, which is used for cross correlation measurements (section 6.4.1) and as the input to the following stage. The third stage of the circuit is precision rectifier composed of two operational amplifiers (IC3 and IC4) ac coupled to the preceding amplifier. This ac coupling removes any long term drift in amplifier IC2 arising for example from changes in the input bias current with age and temperature. The rectifier provides a nominal gain of 1 so that an input sine wave of 2 V peak to peak results in a rectified but unsmoothed output of 1 V peak. The summing amplifier, IC4, has a capacitance, C_{14}, connected across its feedback resistor (R_7). This low pass filter attempts to make the rectified voltage pulses have the same waveform as the induced charge when performing the spatial filtering tests (section 5.6.1). The output of this stage O/P2 is available for the spatial filtering test and as the directly coupled input to the low pass filter circuit IC5, which has an upper cut off frequency of 0.167 Hz. This circuit provides smoothing for the preceding stage and its output, O/P3, is termed the averaged output. A variable resistor, R_5, is used to offset any bias voltage so that the output is zero volts for zero input. The noise output voltage at this point in the circuit is typically 0.353 mV (averaged from 32 sensors when there is no solids flow) .
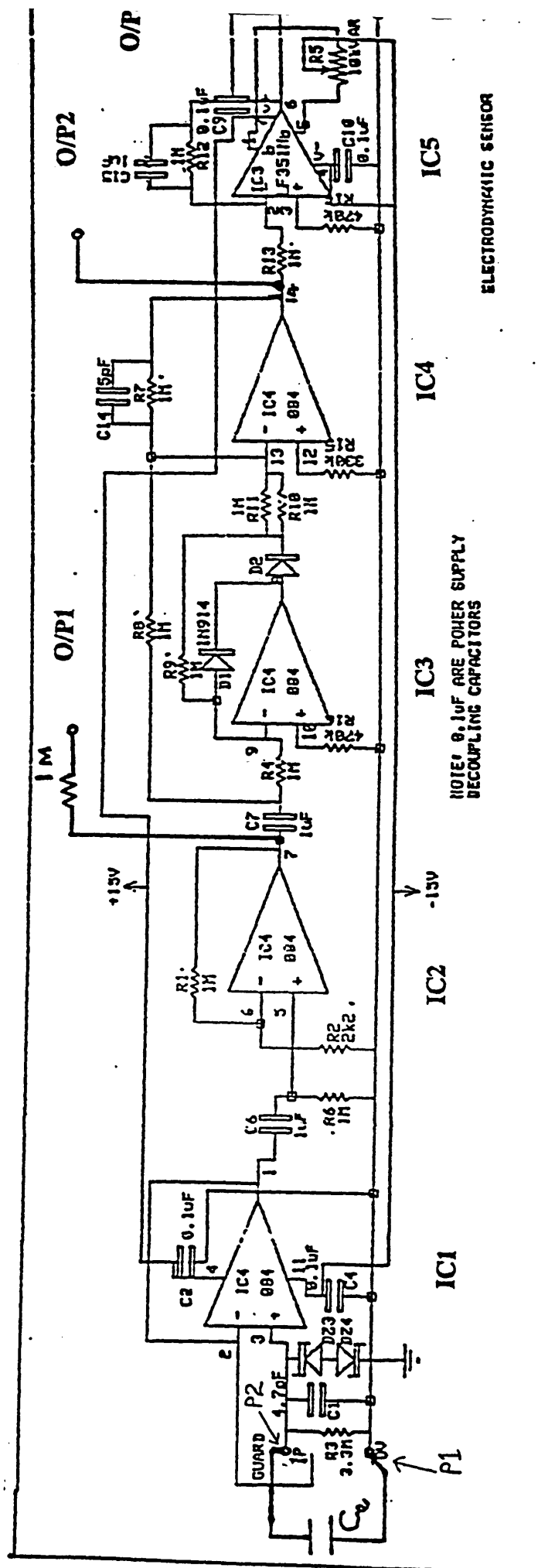
Figure 4.3. Electrodynamic transducer circuit

4.3 The data acquisition system (DAS)

The data acquisition system used in this project is the Keithley Instruments DAS-1801, which is a high performance data acquisition board for the IBM PC. The features of this system are listed in Appendix A.

For concentration measurements (chapter 6 and 7) the band pass amplifier of the transducer system has a cut off frequency of 1 Hz. So a sampling frequency of 5 Hz per channel is chosen. This enables 312 data points to be collected for each of the 32 channels, which enables sixty seconds of flow data to be obtained. For velocity measurements (chapter 6 and 7), the sampling frequency must be fast enough (1 kHz to 5 kHz) to record the transit time between upstream and downstream sensors.

4.4 The flow rig

In order to control the flow of material and enable repeatable solid concentrations and distributions to be provided to the measurement system a gravity drop flow rig is used as shown in figure 4.4.
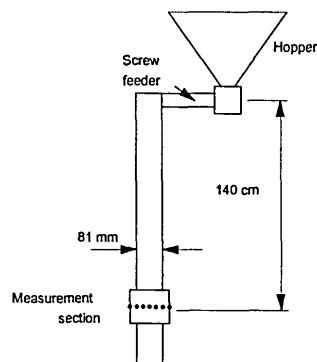
Figure 4.4. The gravity flow rig

The flow rig can be divided into three subsystems i.e. :-

(a). The storage hopper

(b). The screw feeder

(c). The vertical pipe section

This flow rig is a batch conveying system. Sand or plastic granules are used as the conveyed material. The mean particle size of the sand used is 600 micron and the mean particle size of the plastic granules is 3 mm. The relatively low volume of material stored in the hopper provides one restriction on the duration of a flow test.

The flowrate is controlled by a screw feeder positioned at the bottom of the hopper, whose speed of rotation is set by a control unit. The position of the screw feeder is shown in figure 4.5. A vertical pipe, of length 1.4 m and internal diameter 0.081 m, is positioned on the outlet of the screw feeder.

S1, S17

Baffle inserted in this direction

S5, S21

S13, S29

S9, S25

Screw feeder

Screw feeder anticlockwise (seen from this direction)
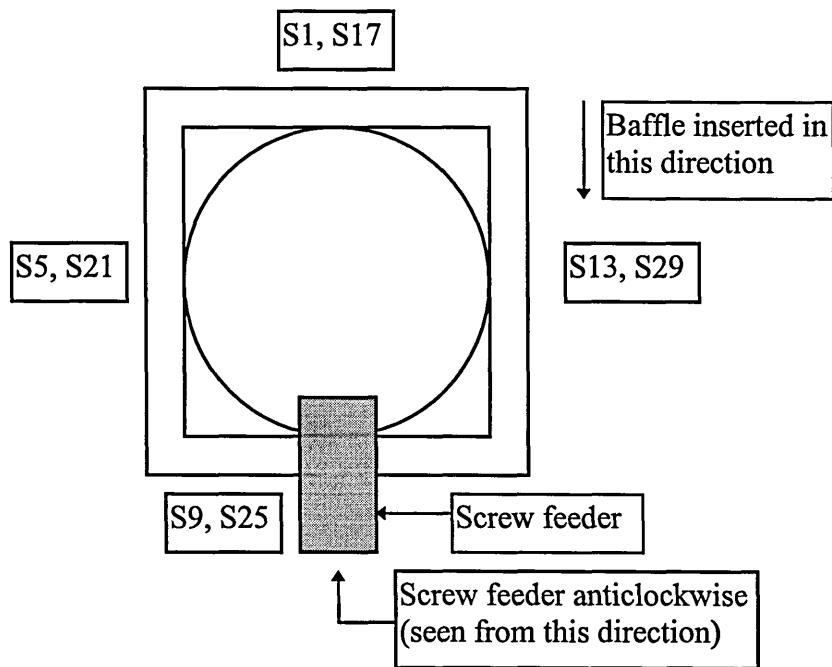
Figure 4.5. Plan view of the flow rig

A calibration relating the solid mass flowrate and the screw feeder set rate is established by the collection of flowing material over recorded time (i.e. 30 s). The result of the calibrations are shown in figure 4.6 and 4.7.
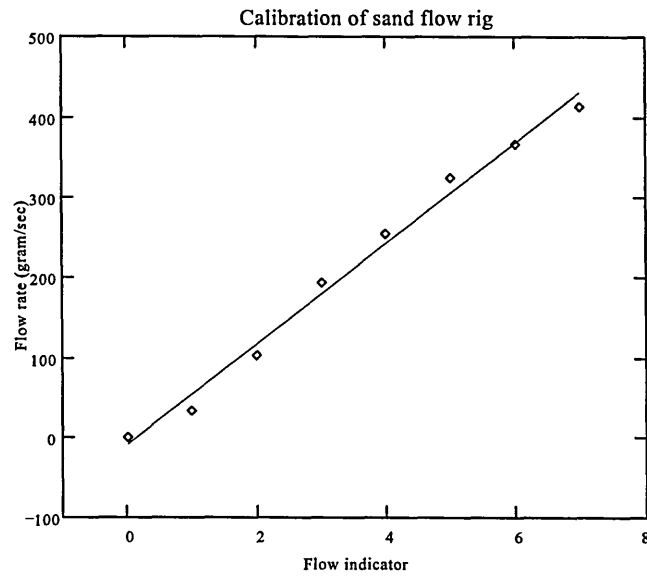
Figure 4.6. Mass flow rate vs. flow indicator for sand

The points in figure 4.6 are data from the experiment. A linear regression line is fitted to the data with a correlation coefficient of 0.99. The slope of the graph is 62.83 and the intercept value is -9.41. The equation of the regression line is

$$\text{mass flow rate} = \frac{dm}{dt} = [62.83 \times \text{Flow indicator setting} - 9.41]\ g/s \qquad (4.1)$$
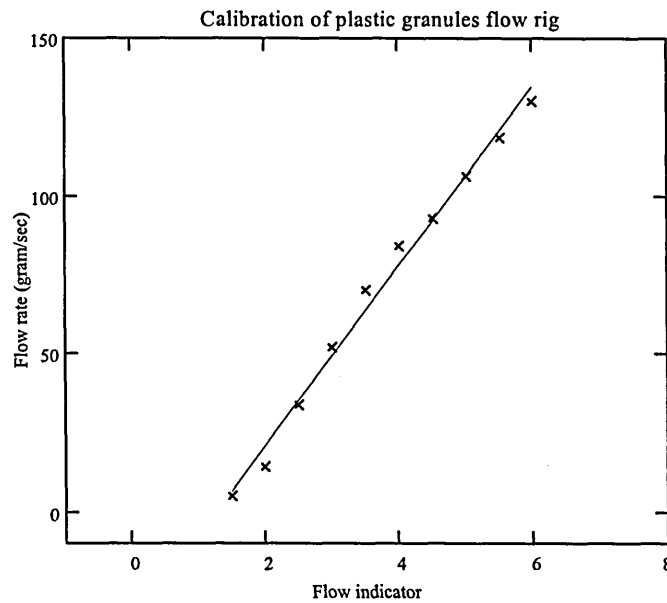
Figure 4.7. Mass flow rate vs. flow indicator for plastic bead

The points in figure 4.7 are data from the experiment. A linear regression line is fitted to the data and the value of the correlation coefficient is 0.99. The

51

relationship between mass flow rate and flow indicator setting is given by equation 4.2.

$$\text{mass flow rate} = \frac{dm}{dt} = [28.51 \text{xFlow indicator setting} - 36.32] \text{ g/s} \qquad (4.2)$$

4.5 Dual 16-channel sensor array

Small electrodes, apart from being cheap and simple to construct, give discrete data from points around the circumference of the conveyor. Sixteen upstream electrodes and sixteen downstream electrodes are used in the measurement system (figure 4.8). The data sampling has to be fast in order to determine simultaneously the boundary voltages on all the sensors, due to the charge on the flowing particles before the flow pattern changes relative to one of the measurement sections. The system samples 32 channels sequentially. The sampling sequence for any specified channel is repeated after a time 32τ, where τ is the sampling time. To ensure that the solid particles are detected the sampling time is adjusted so that the particle is still within the sensing zone of the electrode being used. Most tests for concentration and velocity used 3 mm diameter electrodes. The velocity of the particles through the measurement section was between 4.5 and 5.0 m/s. The required sampling time is

$$t = s / \upsilon = 0.003 / 5 = 0.0006 \text{ s}$$

$$32\tau = 0.0006$$

$$\tau = 18.75 \text{ } \mu s$$

sampling equivalent to frequency of 53 kHz. The sampling frequencies that were used in the velocity measurement tests were 32, 64, 96, 128 and 160 kHz (1, 2, 3,

52

4 and 5 kHz per channel). For some of the concentration measurements (section 6.3 and 6.4) the averaged transducer outputs, o/p 3 (figure 4.3) were monitored, but these results were sampled at 160 Hz (5 Hz per channel) because of the relatively long smoothing time constant.

In order to determine the velocity of the travelling particles, a cross correlation technique is adopted. By having two sensor arrays, one upstream and the other downstream, separated by a half a pipe diameter, it is possible to determine the correlation between the two sets of signals. The time delay between the signals from the two sensors is the time for the source of the signal to travel from the upstream to the downstream one. Since the distance and time are known, the velocity can be determined (Beck and Plaskowski, 1987).
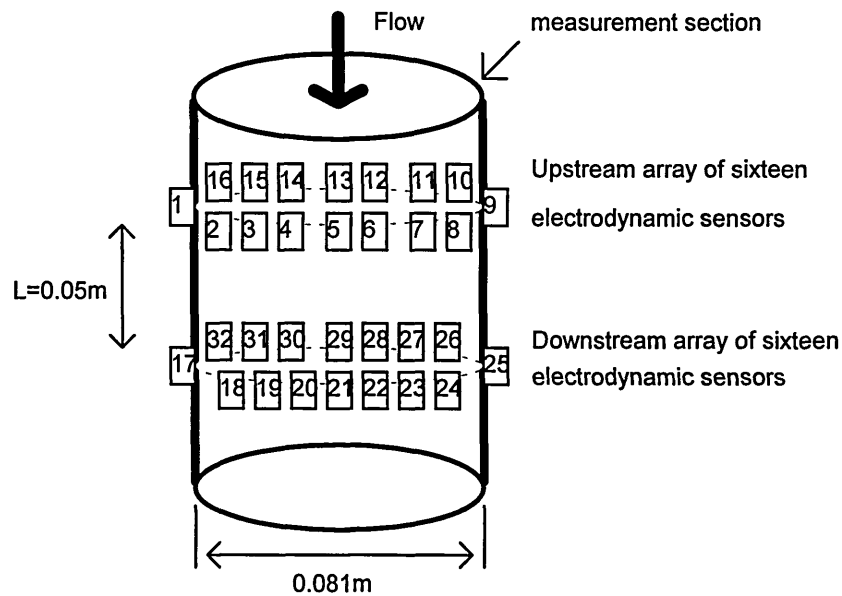
Figure 4.8. Dual sixteen channel sensor array

4.6 The flow models

The flow rig is a gravity drop batch conveyor with a limited range of flow distributions. In order to investigate a wider range of flows and investigate limitations of the electrodynamic sensor a technique to artificially create flow regimes is devised by placing various shaped baffles in the path of the oncoming solid material (figure 4.9 to figure 4.18). These baffles are effectively obstacles and are inserted 5 cm above the upstream sensors. The colour of the baffle in figures 4.9 to figure 4.18 is black and the solid material is grey.

The regimes created and used for tests on the measurement system are :

1. Full flow

This is generated by not putting any obstacle in the pipe so that the solid material is relatively uniformly distributed over the measurement cross-section (figure 4.9).
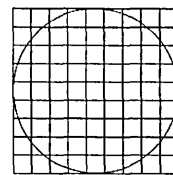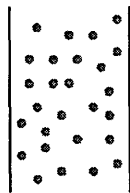
Figure 4.9(a). Side view for full flow   **Figure 4.9(b). Top view for full flow**

2. Three quarter flow

This is created by the baffle blocking a quarter of the pipe diameter and leaving the other three quarters clear for flow of the solid material (figure 4.10). The baffle is a piece of 16 SWG (Standard Wire Gauge) aluminium sheet.
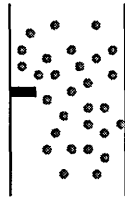
Figure 4.10(a). Side view for three quarter flow
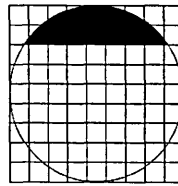
Figure 4.10(b). Top view for three quarter flow

3. Half flow

This is created by a similar baffle to that used in 2, which blocks half the pipe diameter and leaves the other half clear for the flow (figure 4.11).
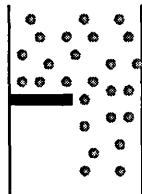
Figure 4.11(a). Side view for half flow
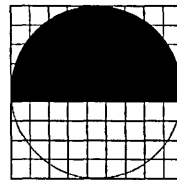
Figure 4.11(b). Top view for half flow

4. Quarter flow

In this case the aluminium baffle is extended to block three quarters of the pipe diameter, leaving only a quarter clear for solid material to flow through (figure 4.12).
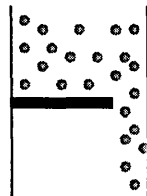
Figure 4.12(a). Side view for quarter flow
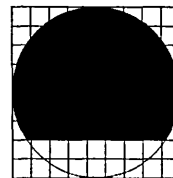
Figure 4.12(b). Top view for quarter flow

5. Stratified (1) flow

This is created by the baffle blocking the middle of the pipe diameter and leaving the left and right (relative to a picture of the measurement cross-section) clear for sand flow (figure 4.13). A pyramid shaped baffle splits the pipe cross-section into two regions with flow on both sides but not through the middle, creating a pseudo-stratified flow regime.

Figure 4.13(a). Side view for stratified (1) flow
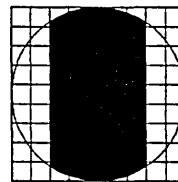
Figure 4.13(b). Top view for stratified (1) flow

6. Stratified (2) flow

This regime is the same as number 5 (stratified (1) flow) but rotated 90° about a vertical axis as shown in figure 4.14.

Figure 4.14(a). Side view for stratified (2) flow
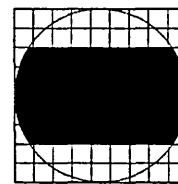
Figure 4.14(b). Top view for stratified (2) flow

7. Channel (1) flow

This is created by placing two pyramid shaped baffles in parallel which splits the flow path into three regions (figure 4.15).
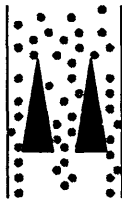
Figure 4.15(a). Side view for channel (1) flow
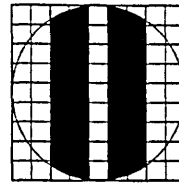
Figure 4.15(b). Top view for channel (1) flow

8. Channel (2) flow

This is similar to number 7 (channel (1) flow) with the baffles rotated by 90° about the pipe axis as shown in figure 4.16.
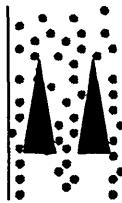
Figure 4.16(a). Side view for channel (2) flow
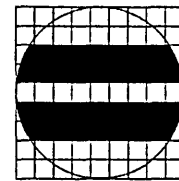
Figure 4.16(b). Top view for channel (2) flow

9. Annular flow

This is created by placing a cone shaped baffle in the middle of the flow path which allows the solid material to flow between the baffle and the pipe generating an annular flow (figure 4.17).

Figure 4.17(a). Side view for annular flow (ring)
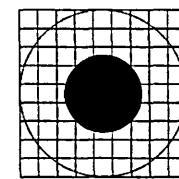
Figure 4.17(b). Top view for annular flow

This is the inverse case of the annular flow in that the solid material is restricted to the middle of the pipe by placing a funnel in the flow path (figure 4.18).
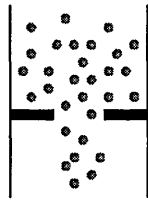
Figure 4.18(a). Side view for core flow
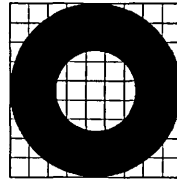
Figure 4.18(b). Top view for core flow

4.7 Predicted response of electrodynamic sensor arrays to artificial flow regimes

Assuming that the solids drop vertically downwards after passing the baffle, i.e. the flow pattern is the same as the baffle shape and the solid material is uniformly distributed throughout the section not shielded by the baffle, the relative measurements to be expected from the sensor array may be predicted. The predicted values are compared with the measured values in section 6.1.

4.7.1 Full flow

No baffle is involved for full flow and a uniform distribution of particles within the conveyor is assumed (figure 4.19).
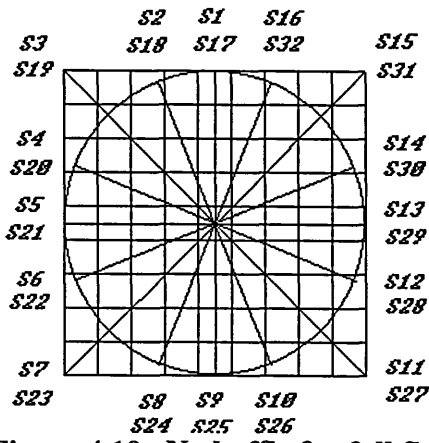
Figure 4.19. No baffle for full flow

Using the results of the forward problem calculation (section 3.4.1.1), which are
summarised in table 4.1, the relative output voltages to be expected from the
individual sensors may be calculated.

Sensor number	Angle of sensor to datum	Relative voltage
S1, S17	0	11.75
S2, S18	22.5	11.71
S3, S19	45	11.72
S4, S20	67.5	11.71
S5, S21	90	11.75
S6, S22	112.5	11.71
S7, S23	135	11.72
S8, S24	157.5	11.71
S9, S25	180	11.75
S10, S26	202.5	11.71
S11, S27	225	11.72
S12, S28	247.5	11.71
S13, S29	270	11.75
S14, S30	292.5	11.71
S15, S31	315	11.72
S16, S32	337.5	11.71

Table 4.1.

The result is shown in figure 4.20 in the form of a relative voltage profile. The
shape of this profile is independent of solids flow rate as the only assumption is
for a uniform solids distribution. However the amplitude of the output does

depend on the flow rates but the graph can be scaled for any desired flow rate by

multiplying each reading by a suitable scaling factor.
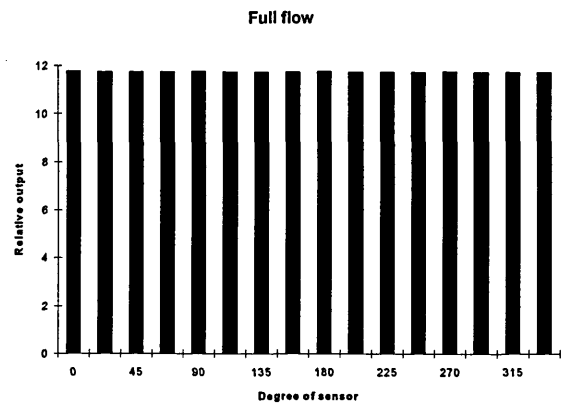
Figure 4.20. Predicted output relative voltage profile for full flow

4.7.2 Three quarter flow

The calculation outlined in section 4.7.1 is repeated for three quarter flow. Figure

4.21 shows the position of the baffle relative to the electrodynamic transducers

and mapped onto the 9x9 pixel array.
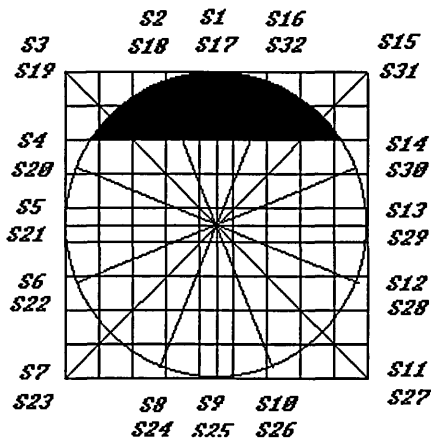
Figure 4.21. Position of the quarter baffle for three quarter flow

All the uncovered pixels are assumed to have a uniform charge density. These

charge densities have been combined with the relevant sensor sensitivity maps to

calculate the expected relative sensor outputs. The results are shown in table 4.2

and graphically in figure 4.22.

Sensor number	Angle of sensor to datum	Relative voltage
S1, S17	0	1.43
S2, S18	22.5	1.56
S3, S19	45	2.08
S4, S20	67.5	5.82
S5, S21	90	10.82
S6, S22	112.5	11.18
S7, S23	135	11.29
S8, S24	157.5	11.35
S9, S25	180	11.42
S10, S26	202.5	11.35
S11, S27	225	11.29
S12, S28	247.5	11.18
S13, S29	270	10.82
S14, S30	292.5	5.82
S15, S31	315	2.06
S16, S32	337.5	1.56

Table 4.2
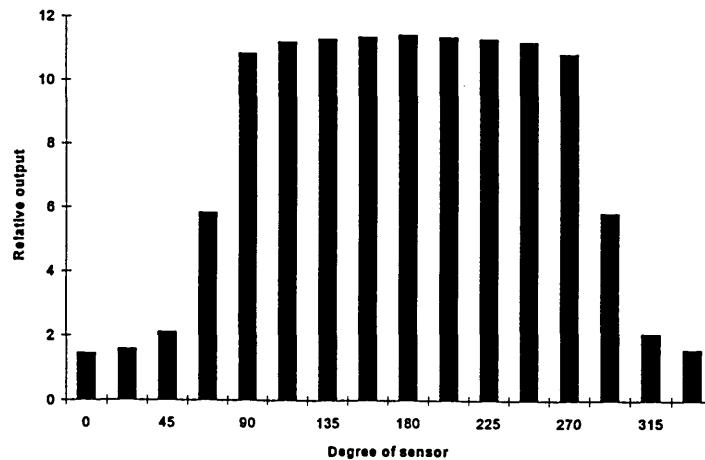
Figure 4.22. Predicted output relative voltage profile for three quarter flow

4.7.3 Half flow

The calculation outlined in section 4.7.1 is repeated for half flow. Figure 4.23 shows the position of the baffle relative to the electrodynamic transducers. The result is shown in table 4.3 and graphically in figure 4.24.
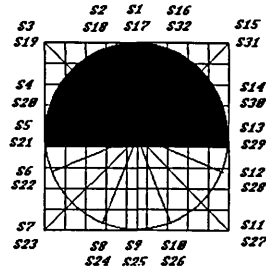
Figure 4.23. Position of the half baffle for half flow

Sensor number	Angle of sensor to datum	Relative voltage
S1, S17	0	0.56
S2, S18	22.5	0.62
S3, S19	45	0.75
S4, S20	67.5	1.02
S5, S21	90	1.91
S6, S22	112.5	9.79
S7, S23	135	10.48
S8, S24	157.5	10.72
S9, S25	180	10.84
S10, S26	202.5	10.85
S11, S27	225	10.46
S12, S28	247.5	9.79
S13, S29	270	1.91
S14, S30	292.5	1.02
S15, S31	315	0.75
S16, S32	337.5	0.62

Table 4.3.
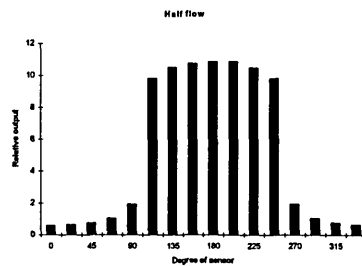
Figure 4.24. Predicted output relative voltage for half flow

4.7.4 Quarter flow

The calculation outlined in section 4.7.1 is repeated for quarter flow with the baffle positioned as shown in figure 4.25. The results are shown in table 4.4 and graphically in figure 4.26.
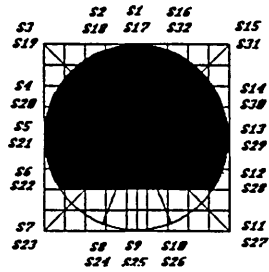
Figure 4.25. Position of the three quarter baffle for quarter flow

Sensor number	Angle of sensor to datum	Relative voltage
S1, S17	0	0.17
S2, S18	22.5	0.18
S3, S19	45	0.2
S4, S20	67.5	0.24
S5, S21	90	0.38
S6, S22	112.5	0.83
S7, S23	135	7.95
S8, S24	157.5	9.22
S9, S25	180	9.5
S10, S26	202.5	9.22
S11, S27	225	7.94
S12, S28	247.5	0.83
S13, S29	270	0.38
S14, S30	292.5	0.24
S15, S31	315	0.2
S16, S32	337.5	0.18

Table 4.4
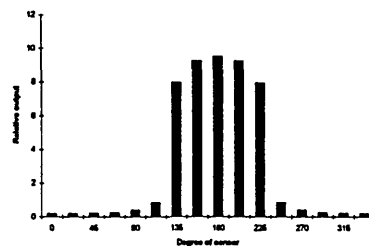
Figure 4.26. Predicted output relative voltage for quarter flow

4.7.5 Stratified (1) flow

The calculation outlined in section 4.7.1 are repeated for stratified (1) flow with

the baffle position shown in figure 4.27. The results are tabulated in table 4.5 and

shown graphically in figure 4.28.
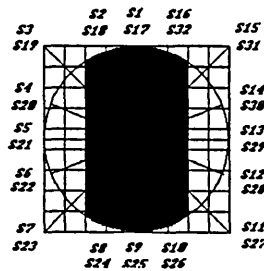
Figure 4.27. Position of the stratified (1) baffle

Sensor number	Angle of sensor to datum	Relative voltage
S1, S17	0	0.76
S2, S18	22.5	1.07
S3, S19	45	8.15
S4, S20	67.5	9.4
S5, S21	90	9.67
S6, S22	112.5	9.4
S7, S23	135	8.14
S8, S24	157.5	1.08
S9, S25	180	0.76
S10, S26	202.5	1.07
S11, S27	225	8.14
S12, S28	247.5	9.4
S13, S29	270	9.67
S14, S30	292.5	9.4
S15, S31	315	8.14
S16, S32	337.5	1.07

Table 4.5
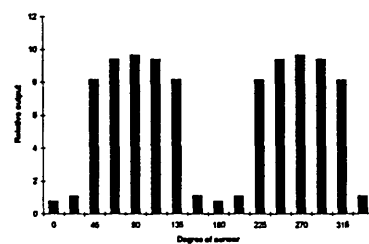
Figure 4.28. Predicted output relative voltage for stratified (1) flow

64

4.7.6 Stratified (2) flow

The calculation outlined in section 4.7.1 are repeated for stratified (2) flow with the baffle position shown in figure 4.29. The result is shown in table 4.6 and graphically in figure 4.30.
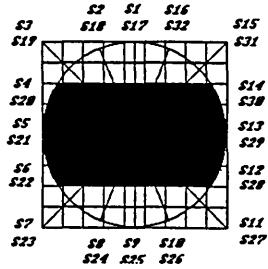
Figure 4.29. Position of the stratified (2) baffle

Sensor number	Angle of sensor to datum	Relative voltage
S1, S17	0	9.67
S2, S18	22.5	9.4
S3, S19	45	8.14
S4, S20	67.5	1.07
S5, S21	90	0.76
S6, S22	112.5	1.07
S7, S23	135	8.15
S8, S24	157.5	9.4
S9, S25	180	9.67
S10, S26	202.5	9.4
S11, S27	225	8.14
S12, S28	247.5	1.07
S13, S29	270	0.76
S14, S30	292.5	1.07
S15, S31	315	8.13
S16, S32	337.5	9.4

Table 4.6
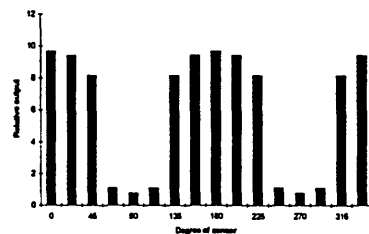
Figure 4.30. Predicted output relative voltage for stratified (2) flow

4.7.7 Channel (1) flow

The calculation outlined in section 4.7.1 are repeated for channel (1) flow with the baffle position shown in figure 4.31. The result is shown in table 4.7 and graphically in figure 4.32.
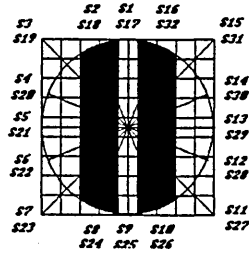
Figure 4.31. Position of the channel (1) baffle

Sensor number	Angle of sensor to datum	Relative voltage
S1, S17	0	7.236
S2, S18	22.5	1.186
S3, S19	45	1.167
S4, S20	67.5	7.46
S5, S21	90	8.411
S6, S22	112.5	7.457
S7, S23	135	1.167
S8, S24	157.5	1.186
S9, S25	180	7.236
S10, S26	202.5	1.186
S11, S27	225	0.903
S12, S28	247.5	7.46
S13, S29	270	8.411
S14, S30	292.5	7.46
S15, S31	315	1.167
S16, S32	337.5	1.186

Table 4.7
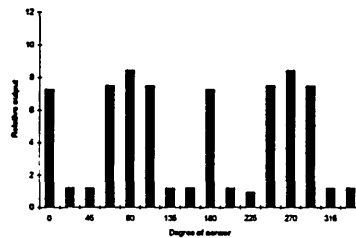
Figure 4.32. Predicted output relative voltage for channel (1) flow

4.7.8 Channel (2) flow

The calculation outlined in section 4.7.1 are repeated for channel (2) flow with the baffle position shown in figure 4.33. The result is shown in table 4.33 and graphically in figure 4.34.
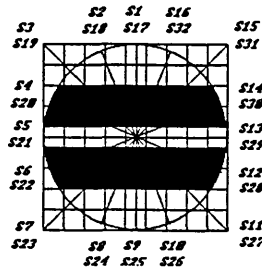
Figure 4.33. Position of channel (2) baffle

Sensor number	Angle of sensor to datum	Relative voltage
S1, S17	0	8.411
S2, S18	22.5	7.46
S3, S19	45	1.168
S4, S20	67.5	1.186
S5, S21	90	7.236
S6, S22	112.5	1.186
S7, S23	135	1.168
S8, S24	157.5	7.46
S9, S25	180	8.411
S10, S26	202.5	7.46
S11, S27	225	1.167
S12, S28	247.5	1.186
S13, S29	270	7.236
S14, S30	292.5	1.186
S15, S31	315	2.335
S16, S32	337.5	7.46

Table 4.8
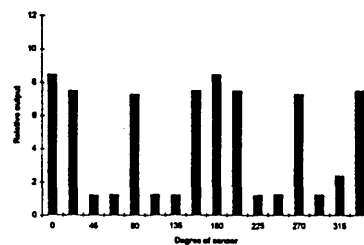
Figure 4.34. Predicted output relative voltage for channel (2) flow

4.7.9 Annular flow

The calculation outlined in section 4.7.1 are repeated for annular flow with the baffle position shown in 4.35. The result is shown in table 4.9 and graphically in figure 4.36.
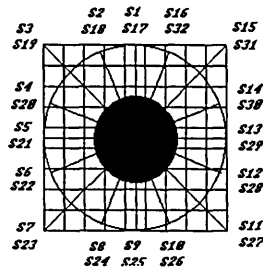
Figure 4.35. Position of the core baffle for annular flow

Sensor number	Angle of sensor to datum	Relative voltage
S1, S17	0	10.51
S2, S18	22.5	10.47
S3, S19	45	10.48
S4, S20	67.5	10.47
S5, S21	90	10.51
S6, S22	112.5	10.47
S7, S23	135	10.48
S8, S24	157.5	10.48
S9, S25	180	10.51
S10, S26	202.5	10.47
S11, S27	225	10.48
S12, S28	247.5	10.47
S13, S29	270	10.51
S14, S30	292.5	10.47
S15, S31	315	10.48
S16, S32	337.5	10.47

Table 4.9
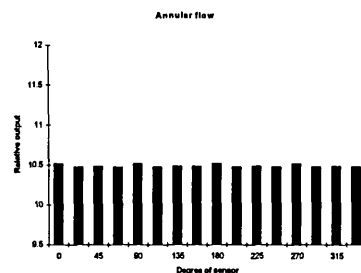
Figure 4.36. Predicted output relative voltage for annular flow

4.7.10 Core flow

The calculation outlined in section 4.7.1 are repeated for core flow with the baffle position shown in figure 4.37. The result is shown in table 4.10 and graphically in figure 4.38.
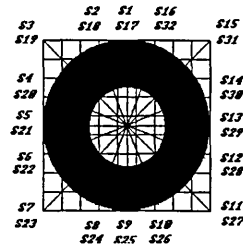

Figure 4.37. Position of ring baffle for core flow

Sensor number	Angle of sensor to datum	Relative voltage
S1, S17	0	1.225
S2, S18	22.5	1.229
S3, S19	45	1.226
S4, S20	67.5	1.229
S5, S21	90	1.225
S6, S22	112.5	1.229
S7, S23	135	1.226
S8, S24	157.5	1.229
S9, S25	180	1.225
S10, S26	202.5	1.229
S11, S27	225	1.226
S12, S28	247.5	1.229
S13, S29	270	1.225
S14, S30	292.5	1.229
S15, S31	315	1.226
S16, S32	337.5	1.229

Table 4.10
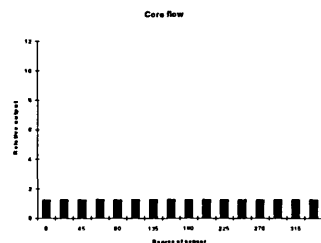
Figure 4.38. Predicted output relative voltage for core flow

69

CHAPTER 5

Transducer characterisation

Chapter summary

The linearity and frequency bandwidth of the sensor electronics is measured. The effect of sensor size on sensitivity and spatial filtering are investigated for circular and rectangular electrodes.

5.1 Introduction

This chapter describes the experiments to determine the sensitivity and spatial filtering effect of the sensor. For qualitative measurements it is important to characterise the system. This requires the gains, linearity, sensitivity and frequency bandwidths to be determined. Results from several sensors are presented in order to determine the potential variability between them.

5.2 Linearity test of the electrodynamic sensor

Linearity tests have been performed on the electronic section of the electrodynamic sensor. An ac voltage has been injected into the input of the sensor at point P2 (figure 4.3) and varied in amplitude from 0 mV up to 50 mV at a frequency of 100 Hz with a step size of 5 mV. The outputs of the sensor are averaged voltage (o/p3, figure 4.3) and rectified voltage (o/p2, figure 4.3) and were measured with a digital voltmeter. The system arrangement for the linearity test is shown in figure 5.1.
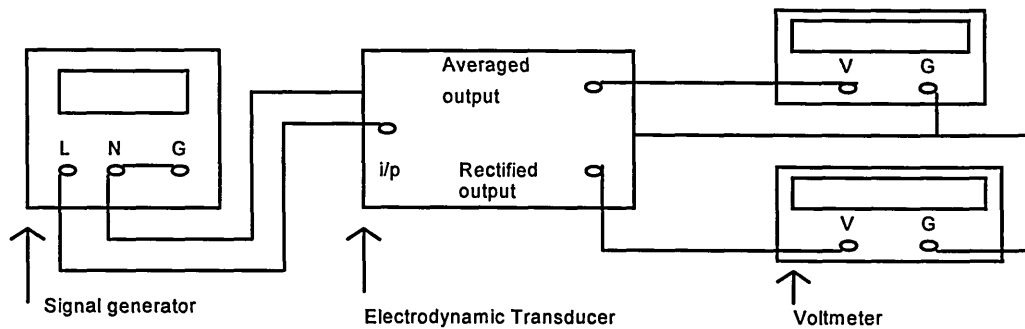
Figure 5.1. Block diagram of linearity test for electrodynamic sensor electronics

Voltage values from the output of the sensor are plotted against the input values. Linear regression analysis is applied to the results from each sensor and the best straight line equation relating input voltage, Vi, to the output voltage, Vo is determined i.e. $V_0 = mV_i + c$. Ideally the value of c=0, however due to amplifier offset and noise, non-zero values were obtained. A typical result of the linearity test for the electrodynamic sensor electronic circuit is shown in figure 5.2.
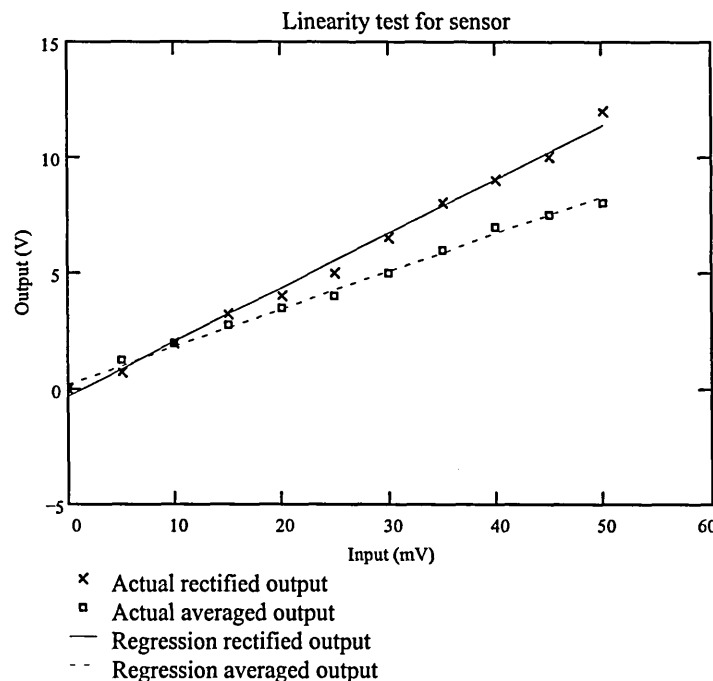
Figure 5.2. Linearity test for an electrodynamic sensor

From figure 5.2 the equation of the regression lines are

V rectified = 0.238Vi - 0.43

71

V averaged = 0.156Vi + 0.24

The correlation coefficient between the straight lines and the measured results is 0.99 in both cases. The results of all the linearity tests are summarised in table 5.1.

Sensor number	Slope, v/v		Constant		Correlation coef.	
	rectified	averaged	rectified	averaged	rectified	averaged
1	0.257	0.174	-0.75	-0.01	0.99	0.99
2	0.213	0.145	-0.22	0.07	0.97	0.98
3	0.241	0.156	-0.69	0.02	0.99	0.99
4	0.236	0.159	-0.70	-0.04	0.99	0.99
5	0.238	0.156	-0.43	0.24	0.99	0.99
6	0.232	0.154	-0.41	0.20	0.99	0.99
7	0.236	0.160	-0.41	0.27	0.99	0.99
8	0.239	0.162	0.02	0.17	0.99	0.99
9	0.225	0.145	0.16	0.77	0.99	0.98
Mean	0.235	0.157	-0.38	0.19	0.99	0.99
Std. Dev.	0.012	0.009	0.32	0.24	0.007	0.004

Table 5.1. Summary for linearity test

From table 5.1 above, the mean of the rectified output gains is 0.235 with a standard deviation of 0.012. The averaged output gains have a mean of 0.157 and a standard deviation of 0.009. The correlation coefficients indicate how closely the best straight lines fitted the individual sets of data. All the correlation coefficients exceed 0.96 which indicates that the steady state transfer characteristics of the electronics are linear.

5.3 Frequency Response test of the electrodynamic sensor

Frequency responses were determined for the sensor electronics to characterise the high frequency dynamic response of the system. The block diagram for the frequency response test is shown in figure 5.3.
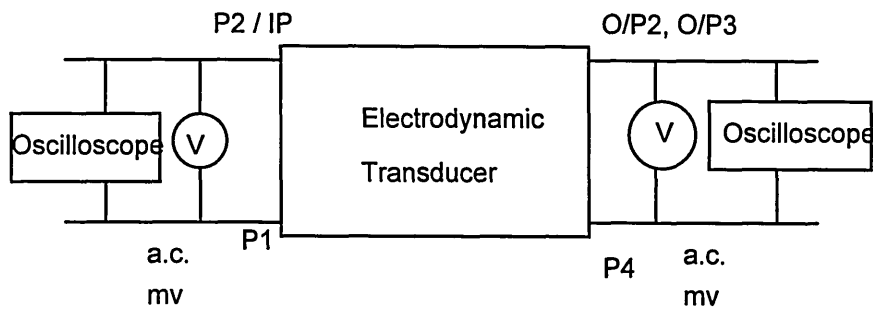
Figure 5.3. Block diagram of frequency response test for electrodynamic sensor

The output from the ac amplifier is a sinusoidal voltage. The rectified gain is

defined as $20\log[\dfrac{V_{out}peaktopeak}{V_{in}peaktopeak}]$ and the averaged gain as

$20\log[\dfrac{V_{out}dc}{V_{in}peaktopeak}]$.

The input level was set at 50 mV peak to peak and both outputs (rectified and

averaged) were monitored on the oscilloscope as the frequency was varied from

10 Hz to 70 kHz. The gain (ratio of output voltage to input voltage) was

expressed in dB. A typical relationship between gain (dB) and frequency (Hz) is

shown in figure 5.4.

— Rectified output
- - Averaged output
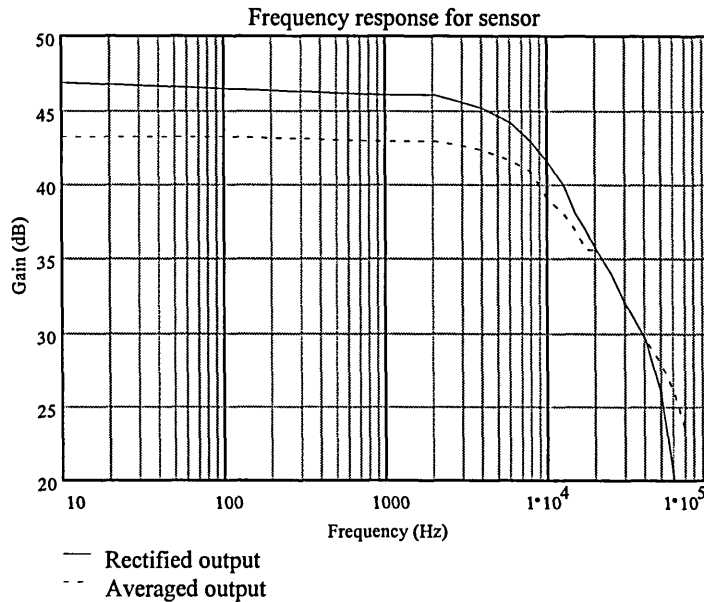
Figure 5.4. Frequency response from electrodynamic sensor 6

The results of all the frequency response tests are summarised in table 5.2.

Sensor	Bandwidth at -3 dB point, Hz		Gain at low freq. (100 Hz), dB	
number	rectified	averaged	rectified	averaged
1	8000	10 000	46.85	43.23
2	9000	9000	46.85	43.52
3	8000	10 000	46.85	42.92
4	8000	9000	47.23	43.52
5	8500	10 000	45.58	42.28
6	7000	9000	46.44	43.23
7	8000	9000	46.44	43.23
8	7000	9000	47.23	43.81
9	7000	8000	47.96	43.52
Mean	7833	9222	46.83	43.25
Std. Dev.	707	667	0.66	0.44

Table 5.2. Summary for frequency response test

5.4 Sensitivity measurements

Several sizes of electrode have been tested in order to investigate the proposed mathematical model of the sensor (section 3.2.1.1) and to choose the most suitable electrode size for use during the remainder this project. Eight electrode diameters i.e. 1.5 mm, 2.5 mm, 3 mm, 3.5 mm, 4 mm, 5 mm, 6 mm, and 10 mm have been tested. Each sensor is identified in the tests by a number (table 5.3). The sensors were arranged in a vertical section of the flow pipe with sensor 1 at the top, all the other sensors in a vertical line below it and with sensor 9 at the bottom as shown in figure 5.10. The sand flows pass each of the sensors in turn. Sensors 1 and 9 are the same diameter to check that no significant variation has occurred in the flow in passing through the test section.

diameter (mm)	Sensor number
1.5	1
10	2
6	3
5	4
4	5
3.5	6
3	7
2.5	8
1.5	9

Table 5.3. Diameter configuration

During the tests, eight flow rates were used. With the flow rate set to zero, 500 samples were recorded for each channel. This information provides a reference level e.g. noise level and offset, for the subsequent measurements. The flow indicator was set at 33 g/s (1 unit) and data gathered from all nine sensors. This was repeated for flow rates up to 412 g/s (7 unit) with indicator step size 1 unit.
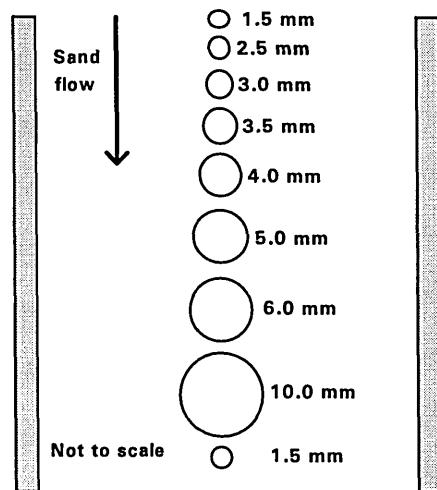
Figure 5.10. Arrangement of flat ended, circular electrodes for sensitivity measurements

5.5.1 Sensitivity results for the rectified output

Sensitivity may be defined as the increase in output voltage due to a change in the mass flow rate, with units of Volts per gram per second (V/g/s). Figure 5.11

shows a typical rectified voltage response to variations in sand flow rate for flows ranging from 0 to 433 g/s.
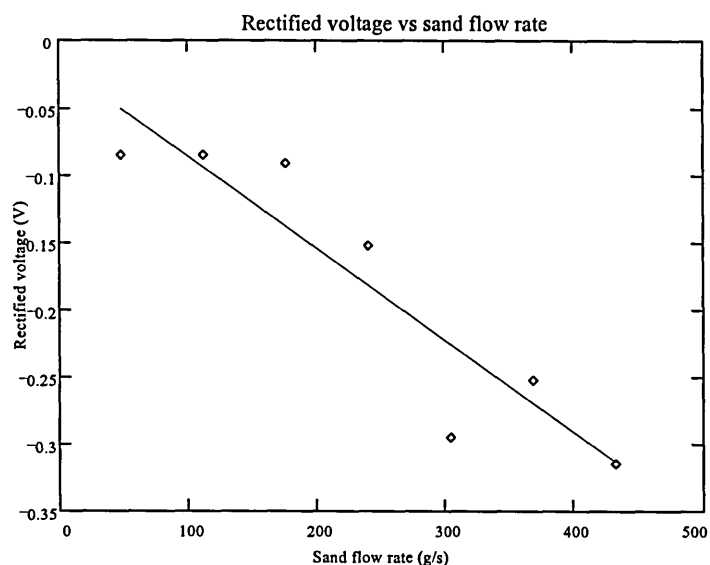
Figure 5.11. Rectified voltage versus sand flow rate

A linear regression has been used to obtain the nominal gradient (sensitivity, 0.45 mV/g/s) for the sensor under these flow conditions. This analysis was used for each of the data sets obtained for the different sensors. The results are tabulated in table 4.6.

Sensor number	Diameter (mm)	Slope rectified (mV/g/s)	Correlation coefficient
1	1.5	-0.452593	0.93
2	10	-0.808202	0.92
3	6	-0.436429	0.95
4	5	-0.484921	0.92
5	4	-0.323281	0.93
6	3.5	-0.323281	0.95
7	3	-0.323281	0.94
8	2.5	-0.242461	0.93
9	1.5	-0.436429	0.90

Table 5.3. Summary of rectified output

Results for rectified sensitivity are shown plotted against sensor diameter in figure 5.12. A linear regression line has been fitted to the results shown in table 5.3, though the sensitivity values for sensors 1 and 9 have been omitted for the analysis.
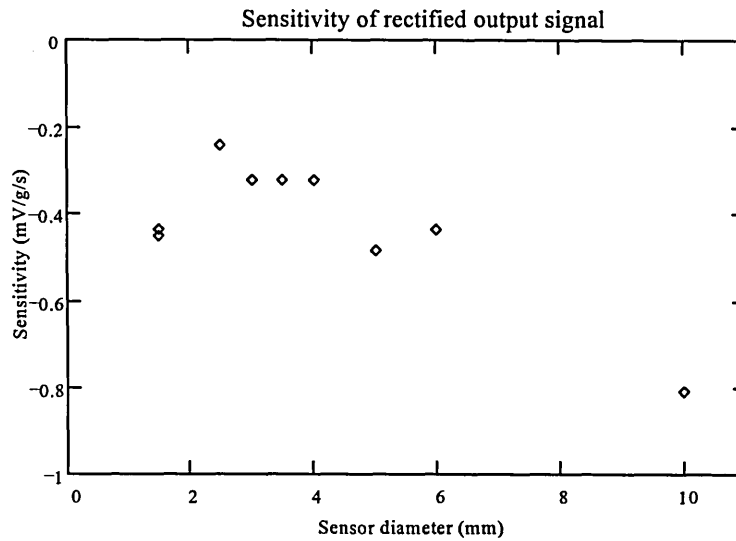
Figure 5.12. Sensitivity of rectified output signal

The two anomalous results occur when the sensor diameter is 1.5 mm probably because the shape of the 1.5 mm sensors is radically different from the other sensors, figure 5.15. The pointed end appears to have some effect on the level of induced charge (Irwin and Kerns 1995) and the shape of the sensor requires further investigation (section 9.3).

5.5.2 Sensitivity results for the averaged output

Figure 5.13 shows a typical averaged voltage response to variations in sand flow rate for flows ranging from 0 to 433 g/s. A linear regression line has been used to obtain the gradient (sensitivity, 0.42 mV/g/s) for the sensor under these flow conditions. This analysis was used for each of the data sets obtained for the different sensors.
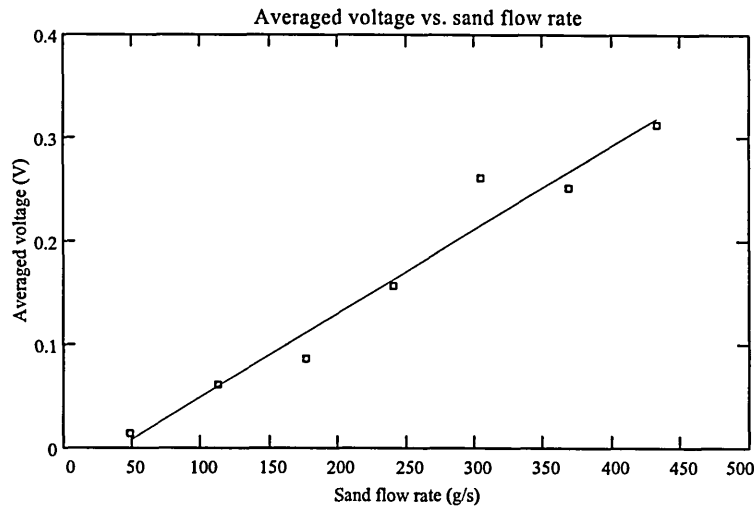
Figure 5.13. Averaged voltage versus sand flow rate (3 mm)

The results are tabulated in table 5.4 below.

Sensor number	Diameter (mm)	Slope averaged (mV/g/s)	Correlation coefficient
1	1.5	0.420265	0.96
2	10	0.775874	0.96
3	6	0.436421	0.96
4	5	0.452593	0.96
5	4	0.339445	0.97
6	3.5	0.323281	0.97
7	3	0.323281	0.96
8	2.5	0.242461	0.96
9	1.5	0.452593	0.93

Table 5.4. Summary of averaged output

Results for averaged output sensitivity are shown plotted against sensor diameter in figure 5.14. Again there are two anomalous results when the sensor diameter is 1.5 mm. These points are also omitted from the following analysis because the shape of the 1.5 mm sensors is radically different from the other sensors, figure 5.15.

78
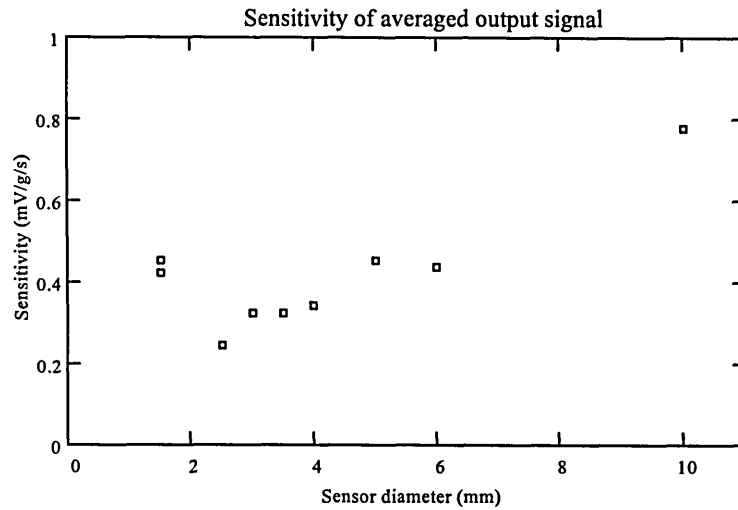
Figure 5.14. Sensitivity of averaged output signal

5.5.3 Analysis of results of sensitivity investigation

In this experiment, we have ignored the results from sensors 1 and 9 for an electrode size 1.5 mm diameter because the shape of this electrode is different from other electrodes and the sensitivity gradients for sensors 1 and 9 are comparable, showing that the flow has not changed as it passes through the measurement section. Figure 5.15 below shows the different shapes of the electrodes:-

electrode shape for 1.5 mm   electrode shape for other than 1.5 mm
(pointed end shape)   (flat ended, circular electrode shape)
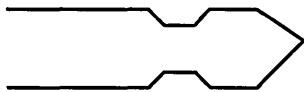
Figure 5.15. Electrode shape

The results shown in tables 5.3 and 5.4 include the effect of the sensor and the electronic amplifier. However, different sensor systems have slightly different amplifier gains. To minimise the effect of the electronics, the values presented in

79

tables 5.3 and 5.4 have been modified using the measured gains listed in table 5.1 using the formulas

Modified averaged slope = Averaged slope experiment / Averaged slope electronic circuit

Modified rectified slope = Rectified slope experiment / Rectified slope electronic circuit

The resulting values are shown in table 5.5 and 5.6. Note the values for sensor diameter 1.5 mm have been omitted for the reasons stated above.

diameter (mm)	diameter^2 (mm^2)	Averaged o/p slope experiment (mV/g/s)	Averaged o/p slope electronic circuit	Modified averaged o/p slope (μV/g/s)	Sensor number
2.5	6.25	0.2450	162	1.512	8
3	9	0.3208	160	2.005	7
3.5	12.25	0.3196	154	2.075	6
4	16	0.3284	156	2.105	5
5	25	0.4513	159	2.838	4
6	36	0.4301	156	2.757	3
10	100	0.7668	145	5.288	2

Table 5.5. Modified averaged output slope

diameter (mm)	diameter^2 (mm^2)	Rectified o/p slope experiment (mV/g/s)	Rectified o/p slope electronic circuit	Modified rectified o/p slope (mV/g/s)	Sensor number
2.5	6.25	-0.242461	239	-0.001014	8
3	9	-0.323281	236	-0.001370	7
3.5	12.25	-0.323281	232	-0.001393	6
4	16	-0.323281	238	-0.001358	5
5	25	-0.484921	233	-0.000208	4
6	36	-0.436429	241	-0.001811	3
10	100	-0.808202	213	-0.003794	2

Table 5.6. Modified rectified output slope

There are some problems in determining the rectified voltages because of their rapid fluctuations (one of the reasons for rectification and averaging). The

averaged output has smoothing which provides signal averaging. This is emphasised by the correlation coefficients shown in table 5.3 and 5.4. The averaged signal, which has been derived from the rectified signal by the measurement system has numerically higher values than the rectified signal (one of the reasons for having the averaging circuit in the system in the first place).

The regression line fitted to the measured points shown in figure 5.16 supports the suggestion that the induced voltage is proportional to the square of the sensor diameter (equation 1.7). It should pass through zero but the intercept of 1.56×10^{-6} V/g/s may be due to a permanent offset in the rectification stages. The equation of the regression line is,

electrode sensitivity = (0.038*(diameter squared) + 1.56) micro volts/g/s

for sand flow on the test rig.
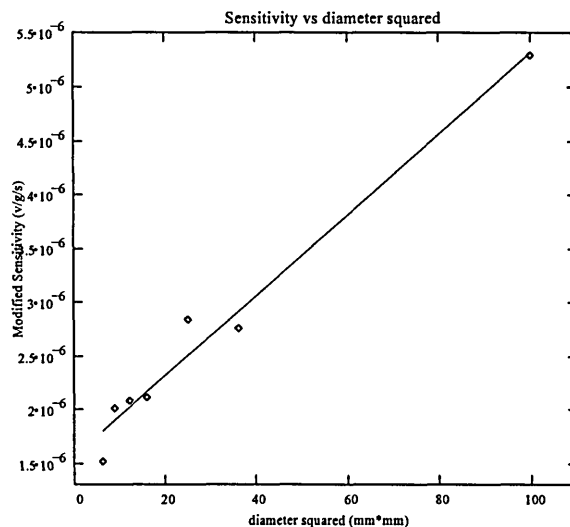
Figure 5.16. Plot showing sensitivity versus electrode diameter squared (flat ended, circular electrode).

The tests were repeated using rectangular electrodes 10 mm wide, but with lengths ranging from 20 to 300 mm. Similar analyses were carried out on the results and these are summarised in figure 5.17.
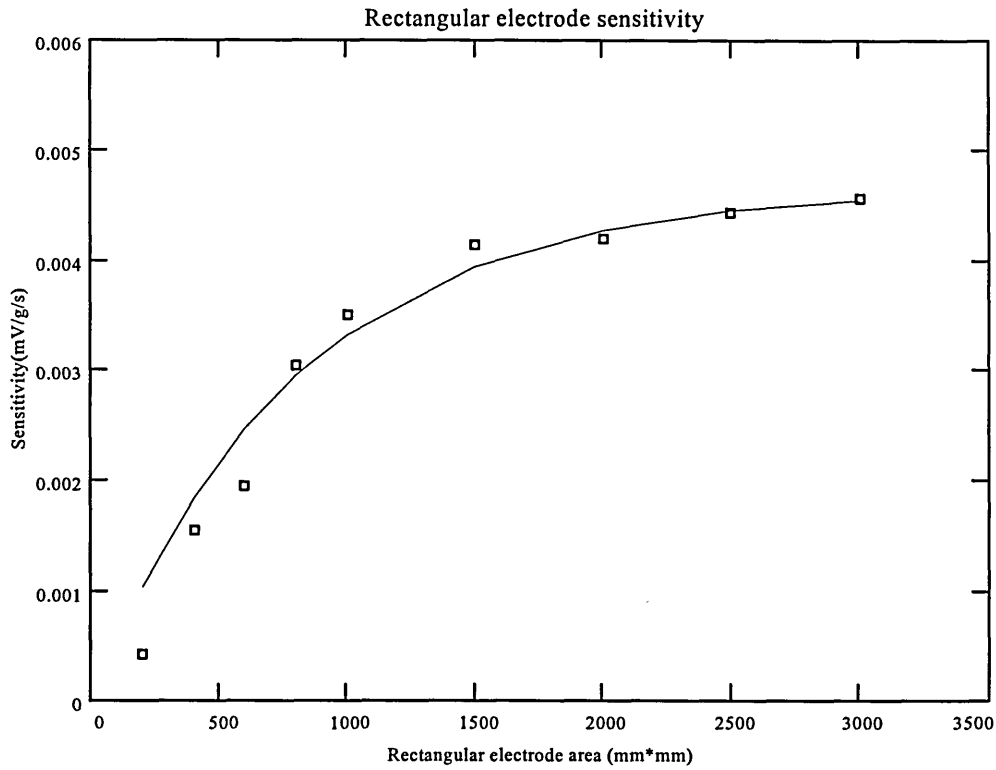
Figure 5.17. Plot showing sensitivity versus electrode area (rectangular sensors)

From figure 5.17, the equation of the regression line is,

Sensitivity = 0.00465*[1- exp (- rectangular electrode area / 800)] mV/g/s

for the sand flow on the test rig.

5.6 Spatial filtering effect experiment

This section presents the results relating to the spatial filtering experiment which is based on the apparatus shown figure 5.18. A plastic ball is mounted on the wooden rod, which is rotated by a dc motor. The plastic ball obtains charge from an electrostatic ioniser. A pulse of charge is created every time the ball passes the electrode sensor. The electrodynamic transducer senses the charge carried by the plastic ball and converts it to a voltage signal. The speed of the charged ball is varied by varying the voltage supply to the dc motor. The speed of the charged ball is calculated by measuring the circumference of the path traversed by the ball

82

when it rotates and dividing this distance by the time between adjacent pulses.

The Hewlett Packard Dynamic Signal Analyser, model 35665 A, is used to

measure the time between adjacent pulses and to derive the frequency spectrum

from the measured pulse response from the sensor (figure 5.18 and 5.20).
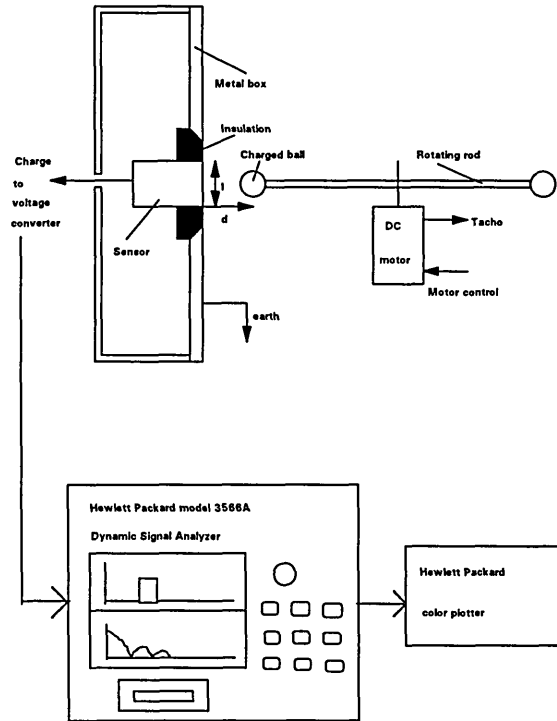
Figure 5.18. Spatial filtering effect experiment.

5.6.1 Spatial filtering results

Two types of electrode were investigated in this experiment i.e. circular flat

ended and rectangular. The electrode diameters of the circular sensor and the

front view of the apparatus in figure 5.18 are shown in figure 5.19.
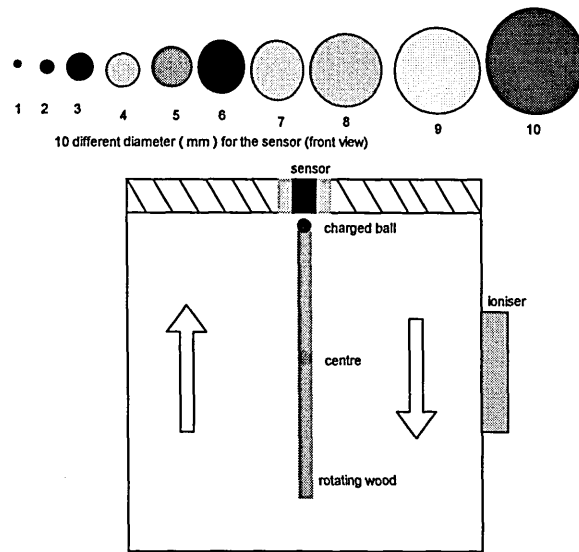
Figure 5.19. Flat ended, circular electrode diameters (mm) for the spatial filtering experiment

A typical signal from the sensor in both the time and frequency domains for the 3

mm diameter electrode is shown in figure 5.20.
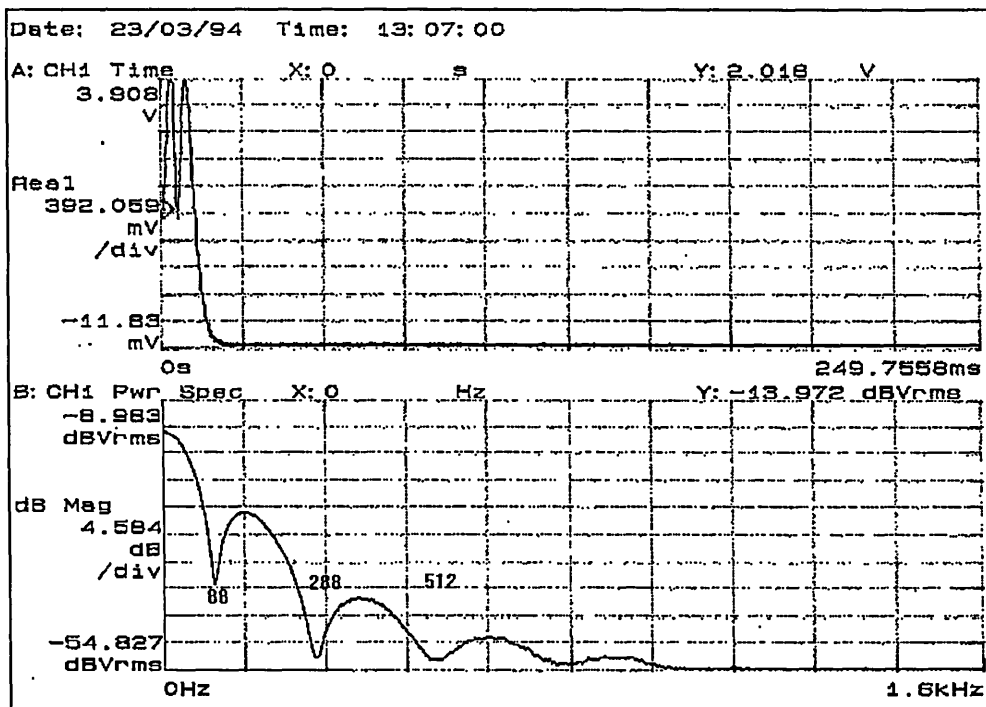
Figure 5.20. Pulse from electrodynamic sensor

From figure 5.20, the pulse width is 12.5 ms. The first frequency minimum, f_0,

read from the signal analyser is 88 Hz. To confirm the above result is valid, an

ideal pulse with pulse width of 12.5 ms from a pulse generator was injected into the signal analyser resulting in the same cut-off frequency i.e. 88 Hz as shown in figure 5.21. The pulse shown in figure 5.21 is rectangular, however the pulse shown in figure 5.20 is more complex, showing two peaks. The two peaks arise due to the rectification provided by the signal conditioning (section 4.2). The dip in the pulse complicates the frequency spectrum (figure 5.20) when compared to the rectangular pulse (figure 5.21).
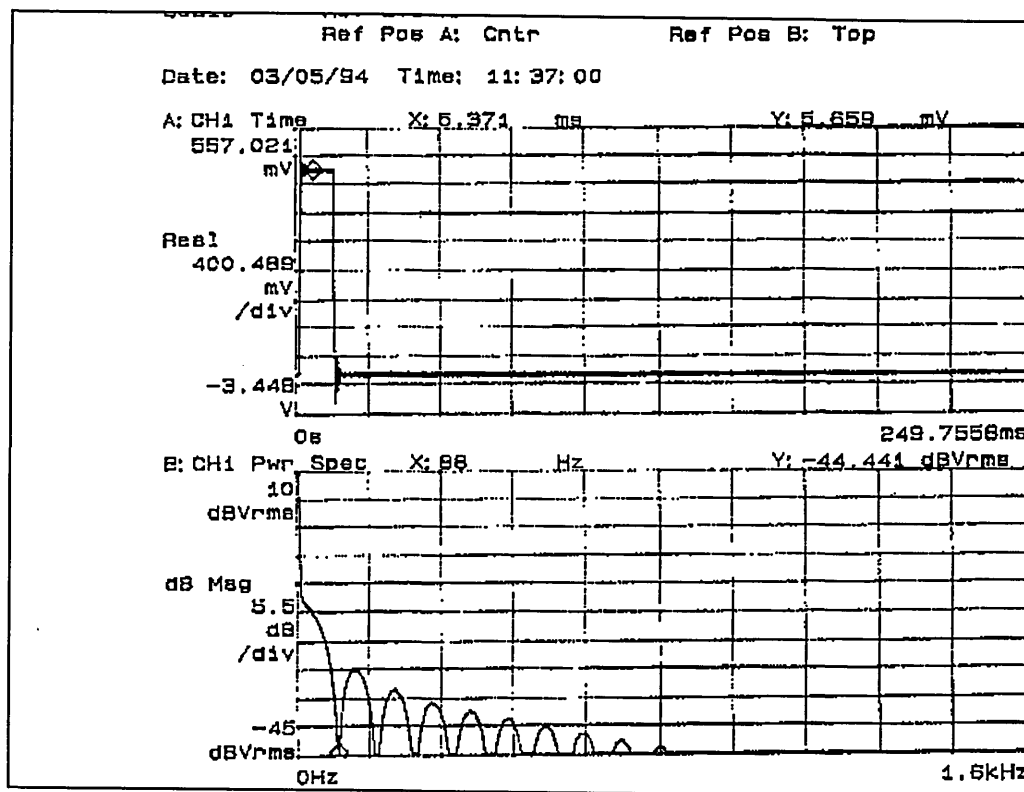
Figure 5.21. Pulse from pulse generator

Measurements were made for velocities ranging from 2.46 to 39.76 m/s using 3 mm diameter electrode. Results are shown in table 5.7.

	Electrode diameter, d (mm)	Velocity, υ (m/s)	Measured cut-off frequency, f_0m Hz	Calculated cut-off frequency, $f_0c = \upsilon/d$ Hz	Equivalent electrode diameter, b $= \upsilon/f_0m$ mm	Electrode diameter coefficient, b/d
1	3	2.46	88	820	28	9.3
2	3	8.68	256	2893	34	11.3
3	3	15.19	336	5063	45	15.1
4	3	22.74	416	7580	55	18.2
5	3	26.19	640	8730	41	13.6
6	3	32.28	480	10760	67	22.4
7	3	36.64	608	12213	60	20.1
8	3	39.76	704	13253	56	18.8
					Mean	16.1
					Std. Dev.	4.5

Table 5.7. 3 mm electrode diameter analysis

The purpose of table 5.7 is to obtain an average effective electrode diameter coefficient and the standard deviation of the 3 mm electrode. The same procedure applied to other electrode diameter. Figure 5.22 shows the relationship between the average effective electrode diameter coefficient and the actual electrode diameter for electrodes ranging in diameter from 1 mm to 10 mm.

Electrode diameter (mm)	Mean	Standard deviation
1	43.58	6.44
2	22.56	4.23
3	16.11	4.53
4	12.51	3.46
5	9.27	1.73
6	8.42	2.08
7	6.35	1.80
8	6.62	1.16
9	5.85	0.98
10	5.06	0.85

Table 5.8. Electrode diameter coefficient
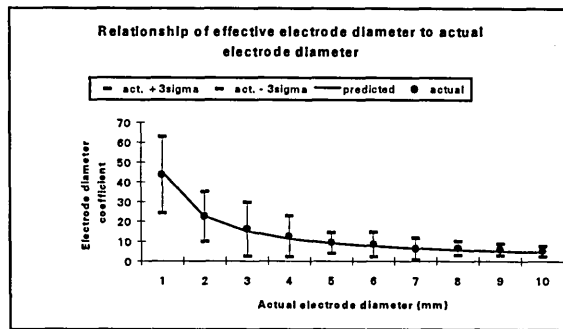
Figure 5.22. Relationship between effective electrode diameter and actual electrode

From figure 5.22, the effective length of the electrode does not depend on the diameter of the sensor. The effective length is 45 mm and the electronic circuit of the transducer is ac coupled. As the electrode length does not appear to effect the spatial filtering, 3 mm electrode being readily available were used for the remainder of the tests presented in this thesis.

A typical response in time and frequency domain for a 100 mm length rectangular sensor is shown in figure 5.24.
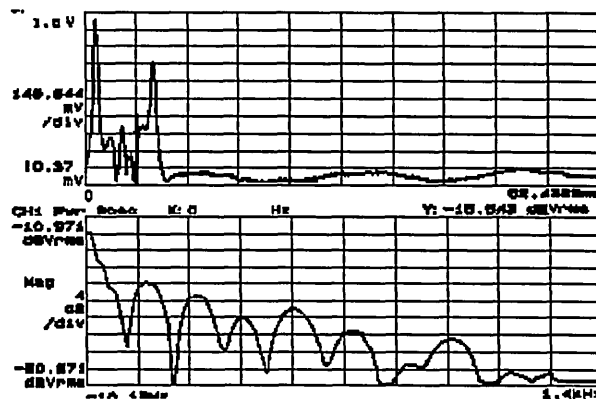
Figure 5.24. Typical result from rectangular sensor

The spatial frequency of the rectangular electrode is more difficult to determine from the frequency domain result than for the circular electrode, because a small change in bead speed causes the overall shape of the spectrum to alter for the rectangular electrode. This is not so for the circular electrode, where the position of the first minimum is a function of bead velocity.

87

CHAPTER 6

Concentration and velocity measurements

Chapter summary

Estimates of the solid concentration of flowing particles are made using individual sensors. Concentration profiles are generated and compared with predicted values. Peripheral velocities of the flowing material are determined from transit times calculated by cross correlation of upstream and downstream sensor signals.

6.1 Introduction

The aim of this section is to investigate the use of the electrodynamic sensor array for concentration and velocity measurements around the periphery of the pipe. For all measurements presented in this chapter the position of the sensors, relative to the screw feeder and baffle, are as shown in figure 4.5 section 4.4.

6.2 Concentration measurements with thirty-two sensors

Measurements were made by energising all thirty two electrodynamic sensors and monitoring the output at several solids flow rates using the data acquisition system to obtain 312 samples, with a sampling frequency of 5 Hz per channel for 60 seconds, for each flow measurement. The flow rig feeds silica sand and plastic beads vertically downwards through the measurement section at a controlled rate (section 4.4). The mean particle size for the sand is 600 micron and the electrodynamic sensor output voltage was measured at flow rates ranging from 85 g/s to 336 g/s. The mean particle size for plastic beads is 3 mm and the electrodynamic sensor output voltage was measured at flow rates ranging from 52 to 107 g/s. The tests were repeated for a range of artificially created flow regimes (section 4.6).

6.3 Results with sand flow

In this section measurements are made on six types of flow regimes as defined in section 4.6. These are full, three quarter, half, quarter, stratified (1) and stratified (2). The remaining flow regimes will not be presented and will be discussed in chapter 9.

6.3.1 Full flow

No obstruction is used in the pipe so that, under ideal conditions, the solids would be uniformly distributed within the flow section. Figure 6.1 shows the averaged output of each upstream and downstream sensor at different feed rates for full flow. The predicted values (section 4.7.1) have been scaled to provide the same mean flow rate and are shown along side the measured values for comparison. The predicted values are approximately achieved. The results show an increase in sensor output with solids flow rate. The calculation of scaling factor is shown below.

(a). Find the total sensitivity of sensors, S_T.

$$S_T = \sum_{i=1}^{16} S_i = 188 \qquad (6.1)$$

(b). Find the total voltage reading from upstream sensors, U_T.

$$U_T = \sum_{i=1}^{16} U_i \qquad (6.2)$$

(c). Find the total voltage reading from downstream sensors, D_T.

$$D_T = \sum_{i=1}^{16} D_i \qquad (6.3)$$

(d). Find the upstream scaling factor, K_U.

$$K_U = \frac{U_T}{S_T} \qquad (6.4)$$

(e). Find the downstream scaling factor, K_D.

$$K_D = \frac{D_T}{S_T} \tag{6.5}$$

(f). Find the overall scaling factor, K.

$$K = \frac{K_U + K_D}{2} \tag{6.6}$$

(g). Predicted voltage = Sensitivity*K

$$P_i = S_i \times K \tag{6.7}$$
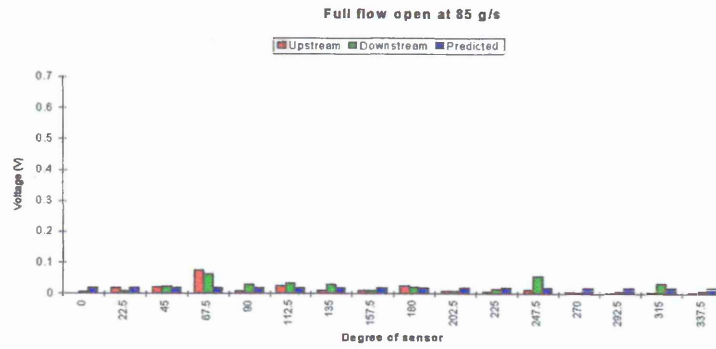
Figure 6.1a. Full flow for sand at 85 g/s
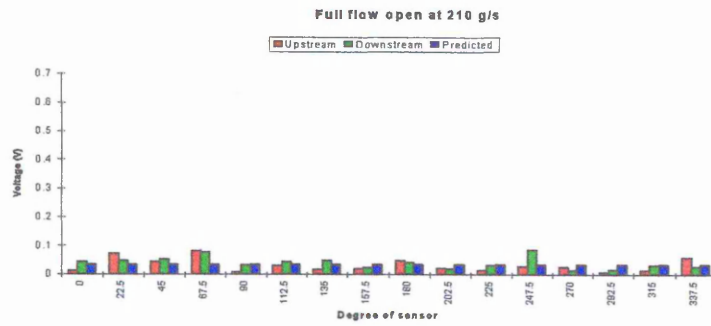
Figure 6.1b. Full flow for sand at 210 g/s
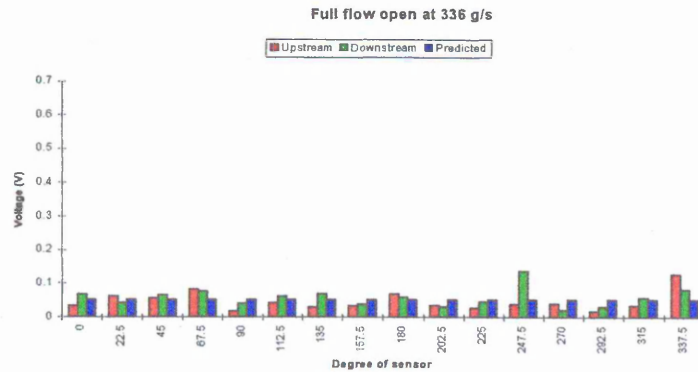
Figure 6.1c. Full flow for sand at 336 g/s

The sixteen sensor outputs have been summed to obtain an overall output. This is repeated for the upstream and downstream sensors at all the flow rates. The summary of the results for full sand flow is shown in table 6.1 and graphically in figure 6.2.

Mass flow rate,	Summed concentration, volts	
g/s	V_u	V_d
85	0.222	0.343
210	0.488	0.626
336	0.735	0.916

Table 6.1. Summary for full sand flow

For figure 6.2, the legends are defined as :-

solid line = summation of the upstream sensor voltages, dotted line = summation of the downstream sensor voltages with bars to represent the $\pm 3\sigma$. The summations described in section 6.3.1 have been repeated for the next sections.
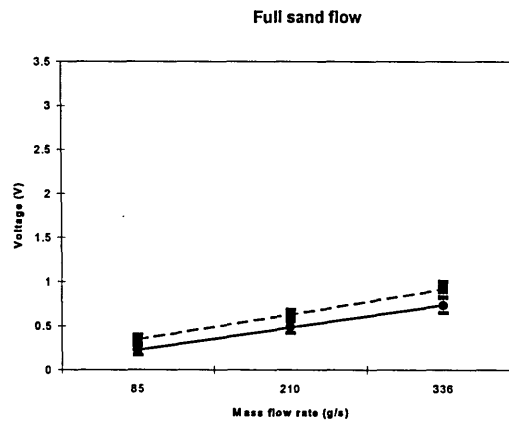
Figure 6.2. Summed sensor outputs versus mass flow rate for full sand flow (solid line for upstream and dotted line for downstream)

6.3.2 Three quarter flow

This is created by the baffle blocking a quarter of the pipe diameter leaving three quarters clear for the sand flow (figure 4.11). Results for different flow rates are shown in figure 6.3, which includes values predicted using the model of section 4.7.2.
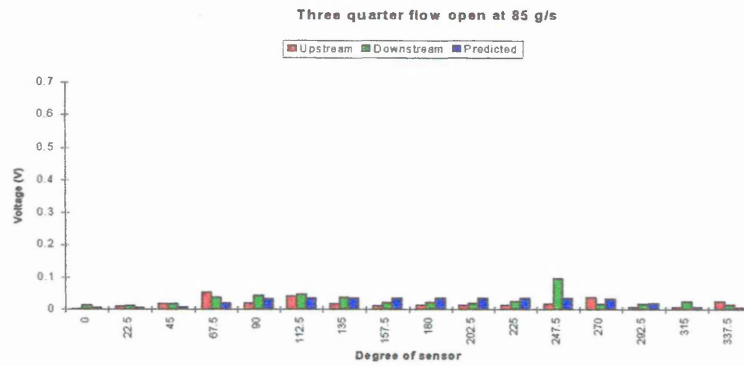
Figure 6.3a. Three quarter flow for sand at 85 g/s
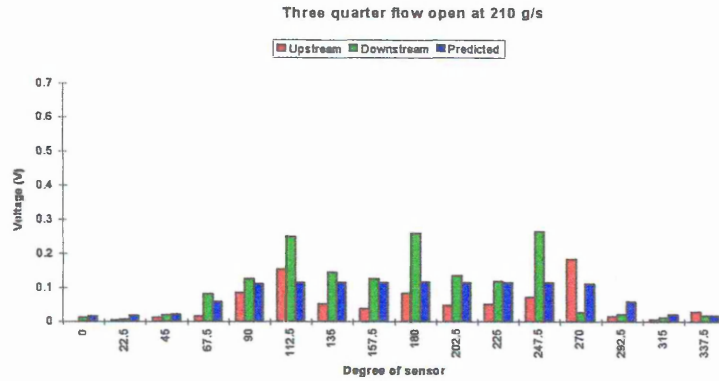
Figure 6.3b. Three quarter flow for sand at 210 g/s
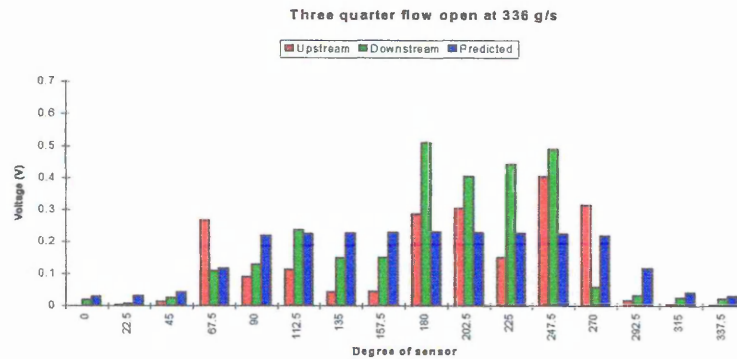
Figure 6.3c. Three quarter flow for sand at 336 g/s

The summary of results for three quarter sand flow is shown in table 6.2 and graphically in figure 6.4.

Mass flow rate,	Total concentration, V	
g/s	Upstream	Downstream
85	0.292	0.451
210	0.839	1.611
336	2.050	2.806

Table 6.2. Summary for three quarter sand flow

Three quarter sand flow
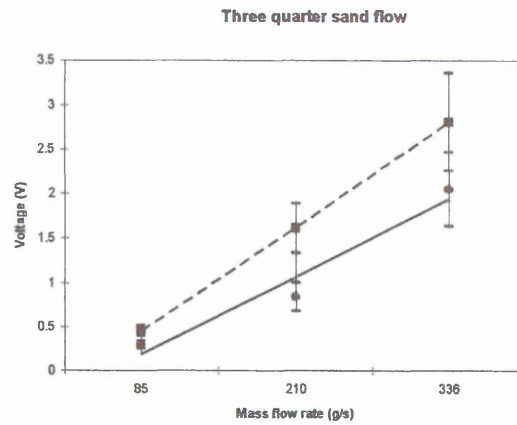
Figure 6.4. Summed sensor outputs versus mass flow rate for three quarter sand flow (solid line for upstream and dotted line for downstream)

6.3.3 Half flow

This is created by the baffle blocking half the pipe diameter so that the other half will be clear for sand flow. Results for different flow rates are shown in figure 6.5, which includes values predicted using the model of section 4.7.3.

Half flow open at 85 g/s
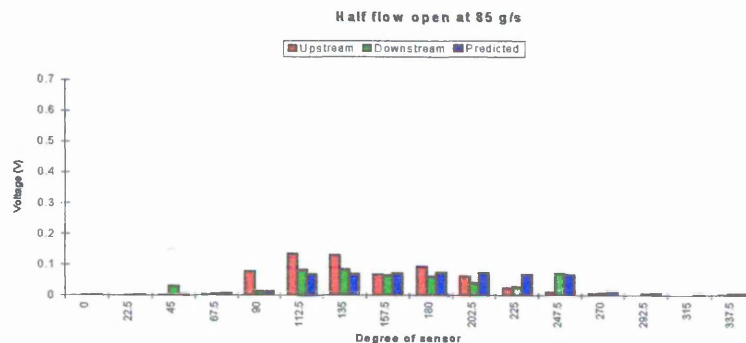
Figure 6.5a. Half flow for sand at 85 g/s

Half flow open at 210 g/s
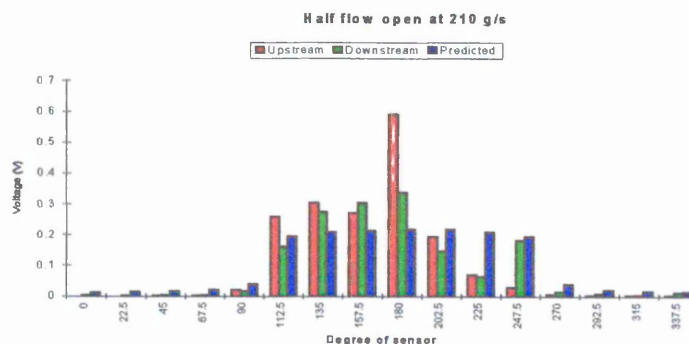
Figure 6.5b. Half flow for sand at 210 g/s
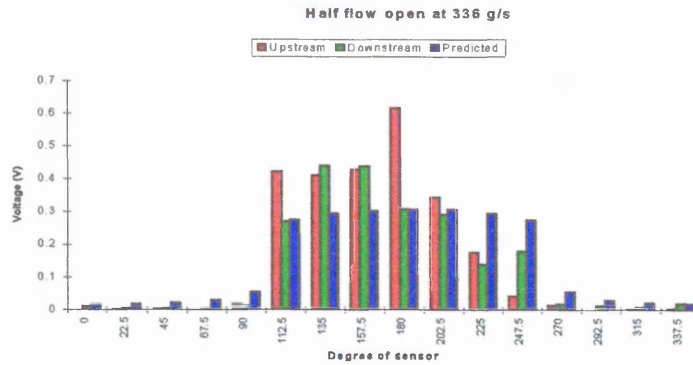
Figure 6.5c. Half flow for sand at 336 g/s

The summary of results for half sand flow is shown in table 6.3 and graphically in figure 6.6.

Mass flow rate,	Total concentration, V	
g/s	Upstream	Downstream
85	0.608	0.495
210	1.745	1.530
336	2.474	2.155

Table 6.3. Summary for half sand flow
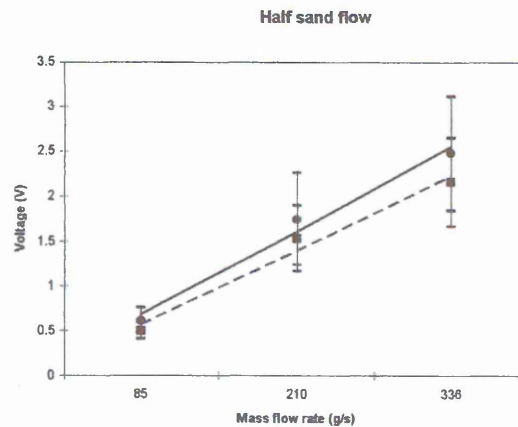
Figure 6.6. Summed sensor outputs versus mass flow rate for half sand flow (solid line for upstream and dotted line for downstream)

6.3.4 Quarter flow

This is created by the baffle blocking three quarters of the pipe diameter so that only a quarter is clear for sand flow. Results for different flow rates are shown in figure 6.7, which includes values predicted using the model of section 4.7.4.
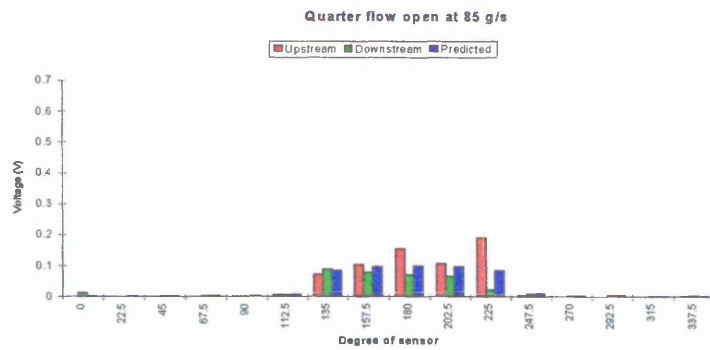
Figure 6.7a. Quarter flow for sand at 85 g/s
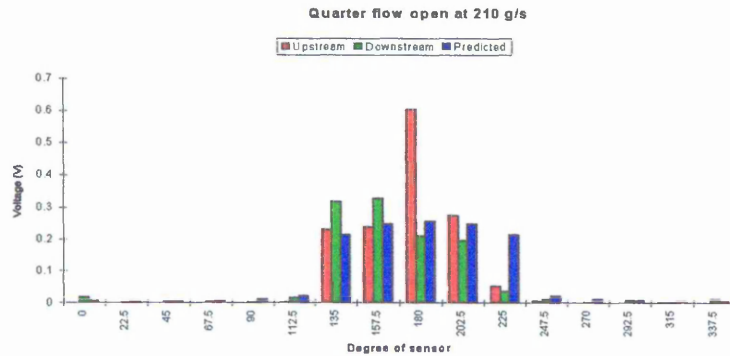
Figure 6.7b. Quarter flow for sand at 210 g/s
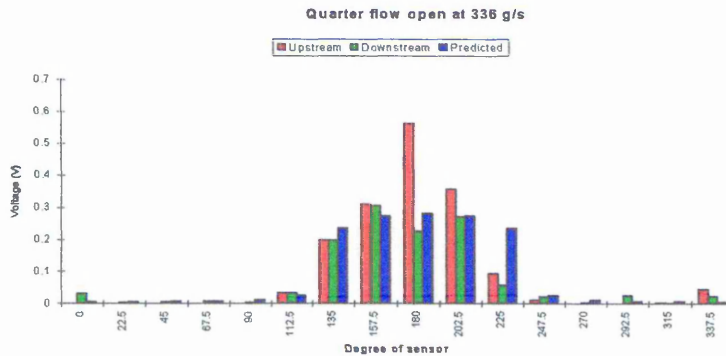
Figure 6.7c. Quarter flow for sand at 336 g/s

The summary of results for quarter sand flow is shown in table 6.4 and graphically in figure 6.8.

Mass flow rate,	Total concentration, V	
g/s	Upstream	Downstream
85	0.634	0.357
210	1.402	1.147
336	1.612	1.205

Table 6.4. Summary for quarter sand flow

95

Figure 6.8. Summed sensor outputs versus mass flow rate for quarter sand flow
(solid line for upstream and dotted line for downstream)

6.3.5 Stratified (1) flow

This is created by the baffle blocking the middle of the pipe so that only the left and right

section of the pipe is clear for sand flow. Results for different flow rates are shown in

figure 6.9, which includes values predicted using the model of section 4.7.5.
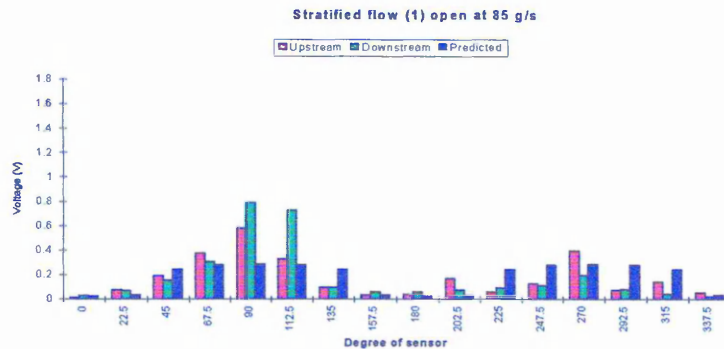
Figure 6.9a. Stratified (1) flow for sand at 85 g/s
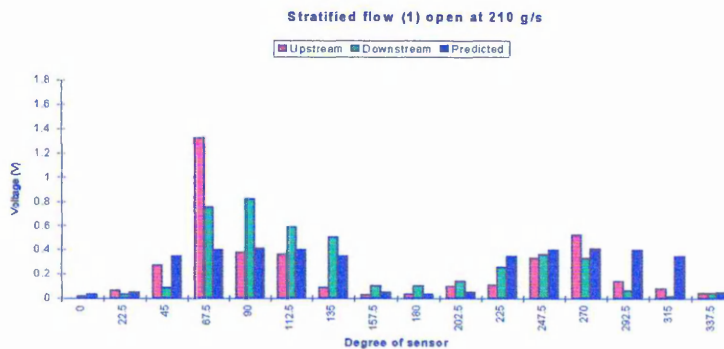
Figure 6.9b. Stratified (1) flow for sand at 210 g/s

96
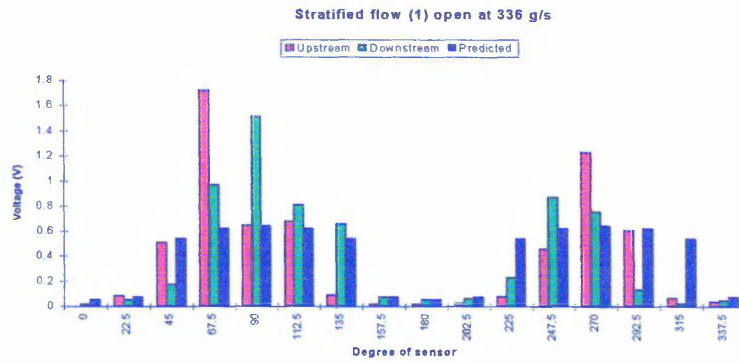
Figure 6.9 c. Stratified (1) flow for sand at 336 g/s

The summary of results for sand stratified (1) flow is shown in table 6.5 and graphically

in figure 6.10.

Mass flow rate,	Total concentration, V	
g/s	Upstream	Downstream
85	2.722	2.882
210	3.828	4.165
336	6.240	6.408

Table 6.5. Summary for stratified (1) flow

**Figure 6.10. Summed sensor outputs versus mass flow rate for stratified (1) flow
(solid line for upstream and dotted line for downstream)**

6.3.6 Stratified (2) flow

This is created by the baffle blocking the middle of the pipe so that only the front and

rear section of the pipe is clear for sand flow. Results for different flow rates are shown

in figure 6.11, which includes values predicted using the model of section 4.7.6.

97
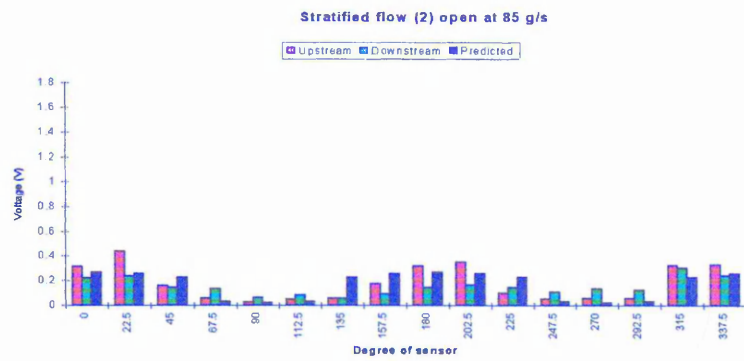
Figure 6.11a. Stratified (2) flow for sand at 85 g/s

Figure 6.11b. Stratified (2) flow for sand at 210 g/s

Figure 6.11c. Stratified (2) flow for sand at 336 g/s

The summary of results for stratified (2) flow is shown in table 6.6 and graphically in figure 6.12.

Mass flow rate,	Total concentration, V	
g/s	Upstream	Downstream
85	2.871	2.397
210	3.063	2.384
336	5.591	4.672

Table 6.6. Summary for stratified (2) flow

Figure 6.12. **Summed sensor outputs versus mass flow rate for stratified (2) flow (solid line for upstream and dotted line for downstream)**

6.3.7 Discussion on sand flow results

The repeatability of the measurements at specific mass flow rates is worse than that obtained using plastic beads (section 6.4). This is demonstrated by the greater spacing of the $\pm$ 3σ points shown on figures 6.2, 6.4, 6.6, 6.8, 6.10 and 6.12 compared with figures 6.14, 6.16, 6.18, 6.20, 6.22 and 6.24. This may be due to sand being more affected by humidity than plastic, however further work is required (section 9.3). The gradients of the graph shown in section 6.3 are summarised in table 6.7. The maximum error occurs for quarter flow and has a value of 14.3 % of the mean gradient.

Flow profile	Upstream gradient	Downstream gradient	Mean gradient	% difference
Full	0.002	0.002	0.002	0
Three quarter	0.007	0.009	0.008	12.5
Half	0.007	0.007	0.007	0
Quarter	0.004	0.003	0.0035	14.3
Stratified (1)	0.014	0.014	0.014	0
Stratified (2)	0.011	0.009	0.010	10

Table 6.7. Gradient for six flow regimes (sand)

6.4 Results with plastic beads flow

In this section measurements are made on six types of flow regimes as defined in section 4.6. These are full, three quarter, half, quarter, stratified (1) and stratified (2). The remaining flow regimes will not be presented and will be discuss in chapter 9.

6.4.1 Full flow

No obstruction is used in the pipe so that, under ideal conditions, the solids would be uniformly distributed within the flow section. Figure 6.13 shows the averaged output of each sensor at different feed rates for full flow. The predicted values (section 4.7.1) have been scaled to provide the same mean flow rate and are shown along side the measured values for comparison. The predicted values are approximately achieved.
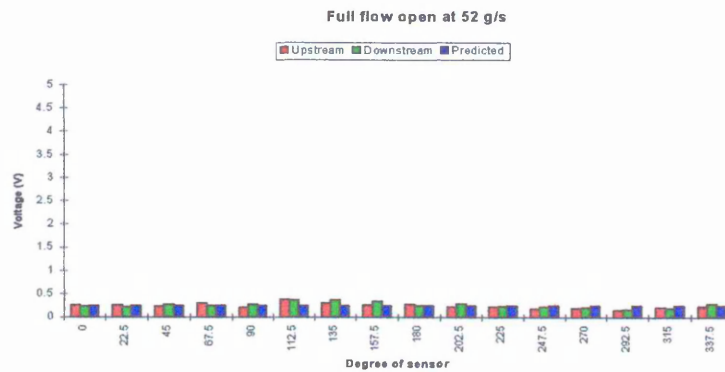
Figure 6.13a. Full flow for plastic beads at 52 g/s
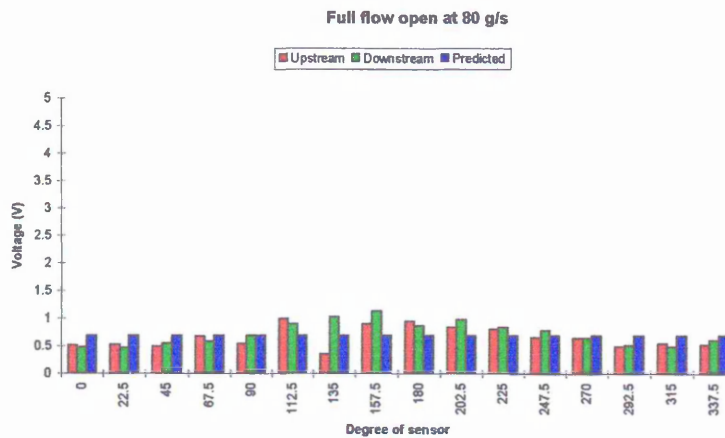
Figure 6.13 b. Full flow for plastic beads at 80 g/s
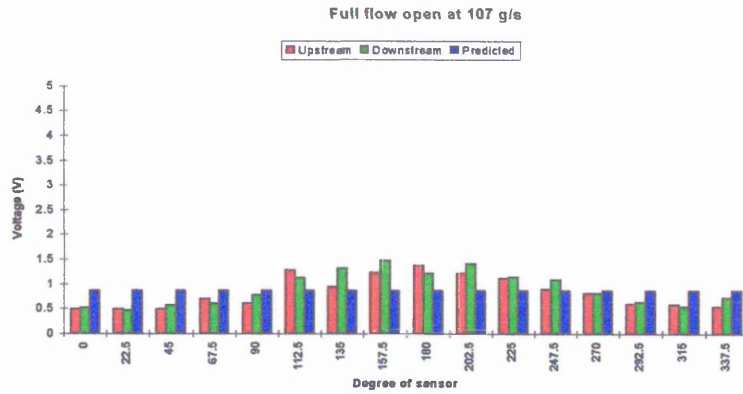
Figure 6.13c. Full flow for plastic beads at 107 g/s

The summary of results for full plastic beads flow is shown in table 6.8 and graphically in figure 6.14.

Mass flow rate,	Total concentration, V	
g/s	Upstream	Downstream
52	3.869	4.093
80	10.374	11.484
107	13.352	14.390

Table 6.8. Summary for full plastic beads flow
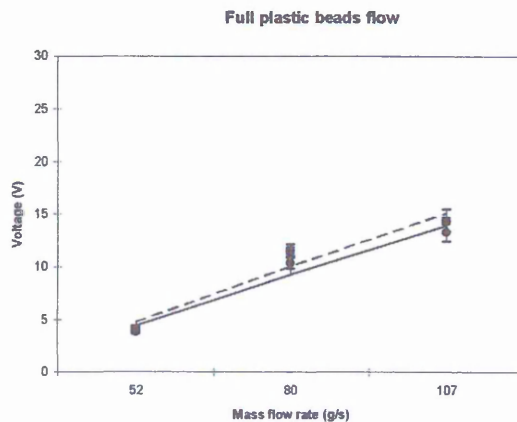
Figure 6.14. Summed sensor outputs versus mass flow rate for full plastic beads flow (solid line for upstream and dotted line for downstream)

6.4.2 Three quarter flow

This is created by the baffle blocking a quarter of the pipe diameter leaving three quarters clear for the plastic bead flow. Results for different flow rates are shown in figure 6.15, which includes values predicted using the model of section 4.7.2.
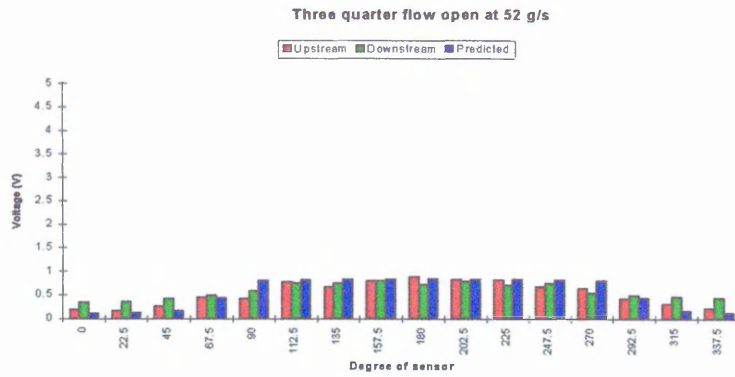
Figure 6.15a. Three quarter flow for plastic beads at 52 g/s
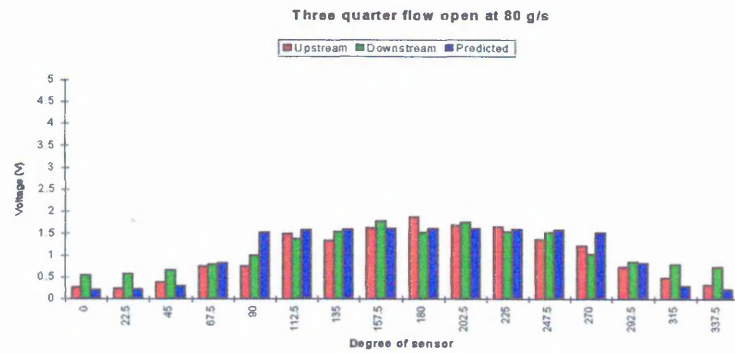

Figure 6.15b. Three quarter flow for plastic beads at 80 g/s
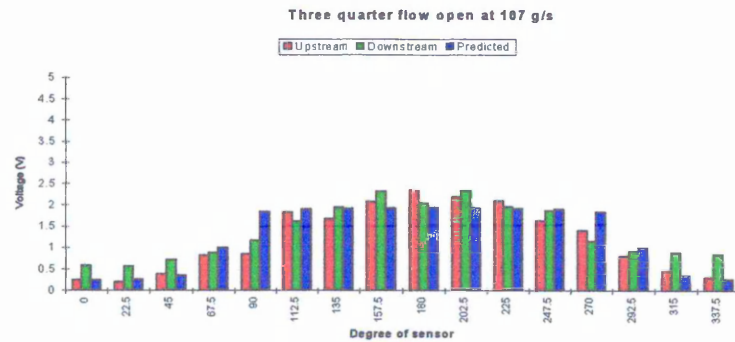
Figure 6.15c. Three quarter flow for plastic beads at 107 g/s

The summary of results for three quarter plastic beads flow is shown in table 6.9 and graphically in figure 6.16.

Mass flow rate,	Total concentration, V	
g/s	Upstream	Downstream
52	8.444	9.288
80	16.113	17.953
107	19.348	21.832

Table 6.9. Summary for three quarter plastic beads flow

Three quarter plastic beads flow
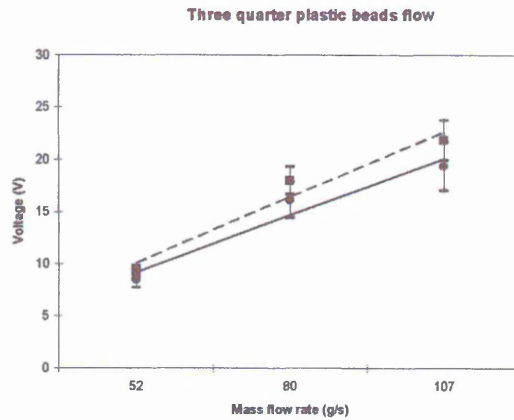
Figure 6.16. Summed sensor outputs versus mass flow rate for three quarter plastic beads flow (solid line for upstream and dotted line for downstream)

6.4.3 Half flow

This is created by the baffle blocking half the pipe diameter so that the other half will be clear for plastic bead flow. Results for different flow rates are shown in figure 6.17, which includes values predicted using the model of section 4.7.3.

Half flow open at 52 g/s
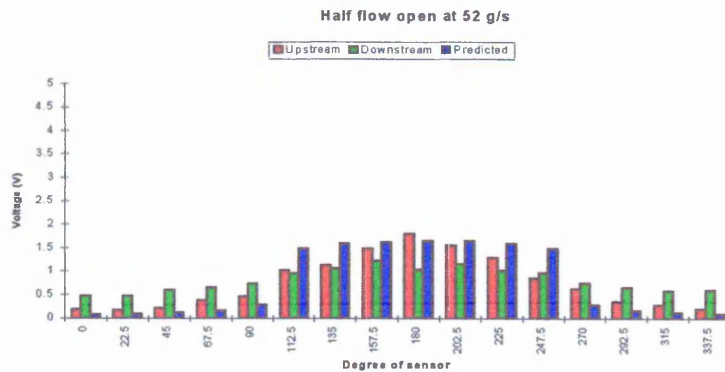
Figure 6.17a. Half flow for plastic beads at 52 g/s

Half flow open at 80 g/s
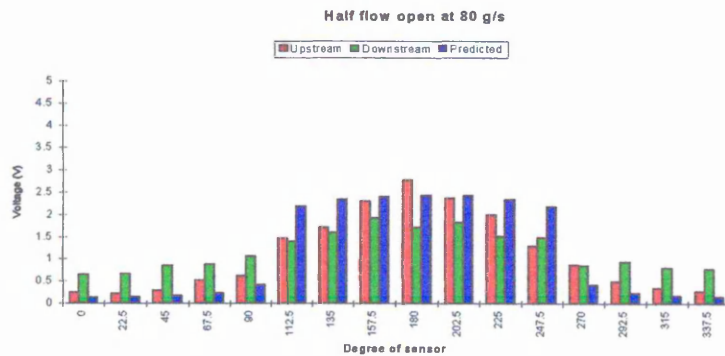
Figure 6.17b. Half flow for plastic beads at 80 g/s
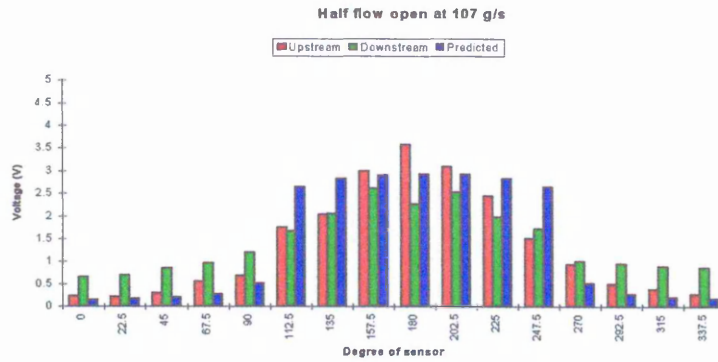
Figure 6.17c. Half flow for plastic beads at 107 g/s

The summary of results for half plastic beads flow is shown in table 6.10 and graphically

in figure 6.18.

Mass flow rate, g/s	Total concentration, V	
	Upstream	Downstream
52	12.016	12.907
80	17.762	18.879
107	21.463	22.919

Table 6.10. Summary for half plastic beads flow
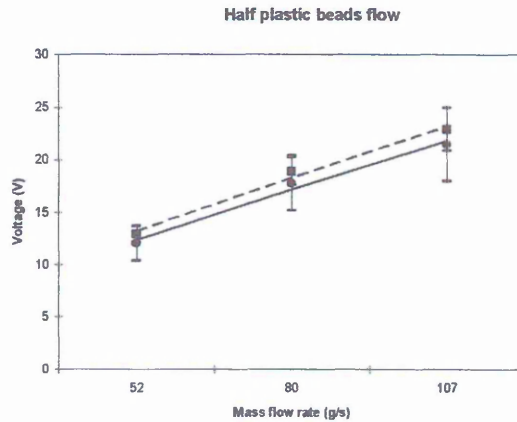
Figure 6.18. Summed sensor outputs versus mass flow rate for half plastic beads flow (solid line for upstream and dotted line for downstream)

6.4.4 Quarter flow

This is created by the baffle blocking three quarters of the pipe diameter so that only a

quarter is clear for plastic bead flow. Results for different flow rates are shown in figure

6.19, which includes values predicted using the model in section 4.7.4.
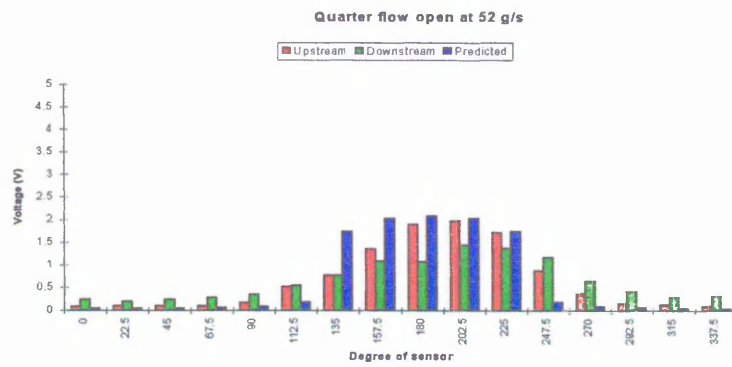
Figure 6.19a. Quarter flow for plastic beads at 52 g/s
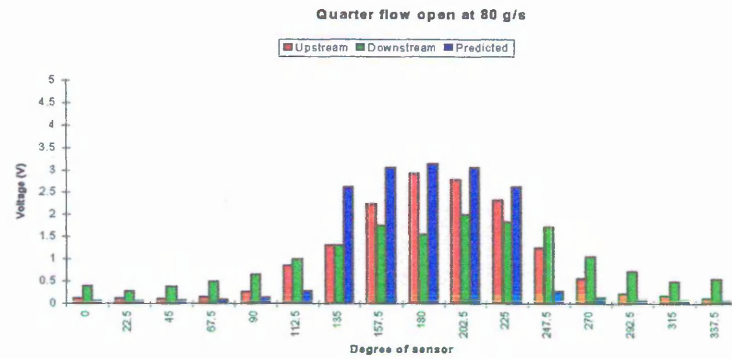

Figure 6.19b. Quarter flow for plastic beads at 80 g/s
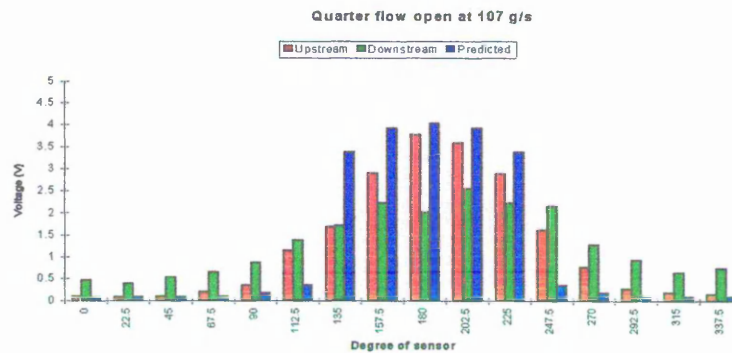
Figure 6.19c. Quarter flow for plastic beads at 107 g/s

The summary of results for quarter plastic beads flow is shown in table 6.11 and graphically in figure 6.20.

Mass flow rate,	Total concentration, V	
g/s	Upstream	Downstream
52	10.395	10.492
80	15.430	16.084
107	19.756	20.745

Table 6.11. Summary for quarter plastic beads flow
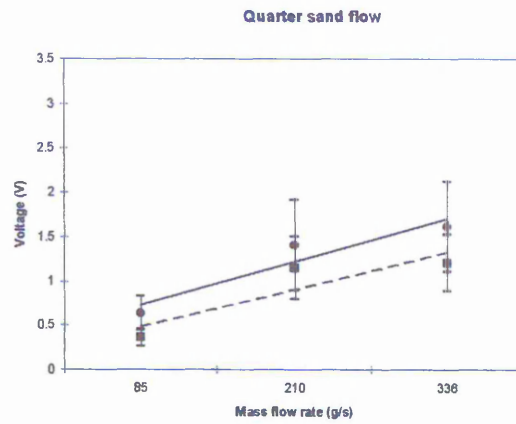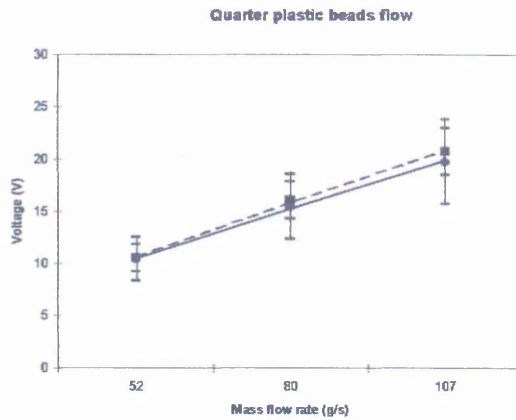
Figure 6.20. Summed sensor outputs versus mass flow rate for quarter plastic beads flow (solid line for upstream and dotted line for downstream)

6.4.5 Stratified (1) flow

This is created by the baffle blocking the middle of the pipe so that only the left and the right section of the pipe is clear for plastic beads flow. Results for different flow rates are shown in figure 6.21, which includes values predicted using the model of section 4.7.5.
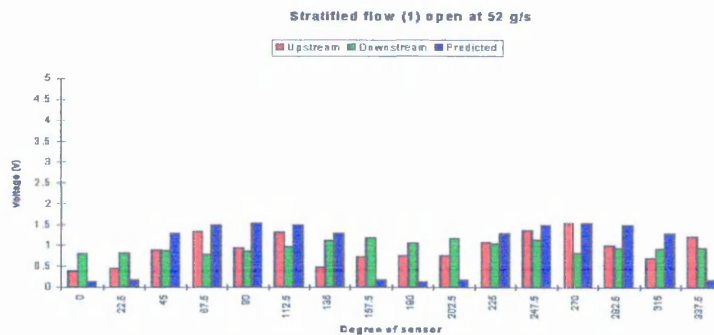

Figure 6.21a. Stratified (1) flow for plastic beads at 52 g/s
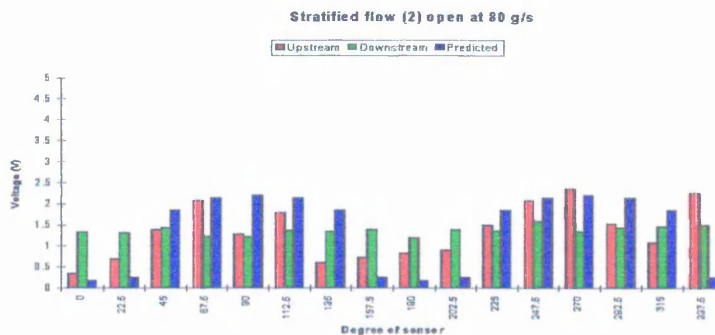


Figure 6.21b. Stratified (1) flow for plastic beads at 80 g/s

106

Stratified flow (1) open at 107 g/s
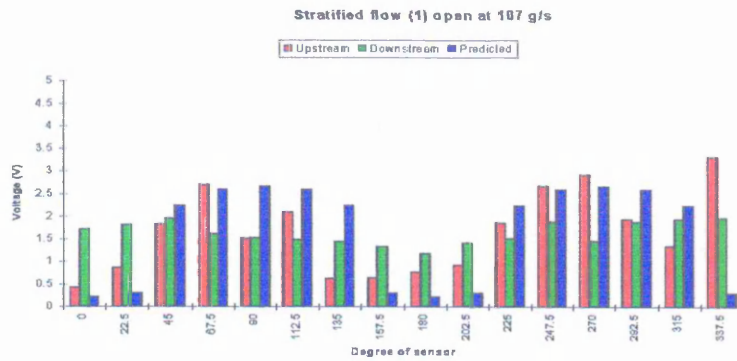
Figure 6.21c. Stratified (1) flow for plastic beads at 107 g/s

The summary of results for stratified (1) flow is shown in table 6.12 and graphically in

figure 6.22.

Mass flow rate,	Total concentration, V	
g/s	Upstream	Downstream
52	14.768	15.272
80	21.322	21.849
107	26.368	26.106

Table 6.12. Summary for stratified (1) flow

Stratified flow (1) for plastic beads
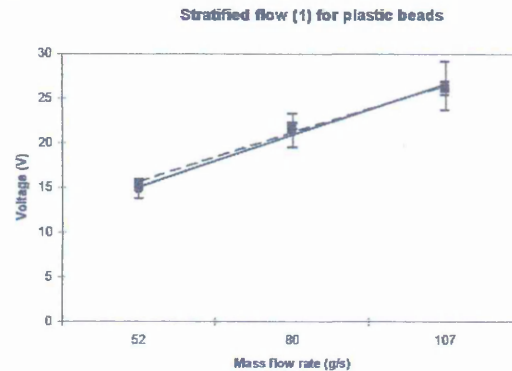
Figure 6.22. Summed sensor outputs versus mass flow rate for stratified (1) flow
(solid line for upstream and dotted line for downstream)

6.4.6 Stratified (2) flow

This is created by the baffle blocking the middle of the pipe so that only the front and the

rear section of the pipe is clear for plastic beads flow. Results for different flow rates are

shown in figure 6.23, which includes values predicted using the model of section 4.7.6.
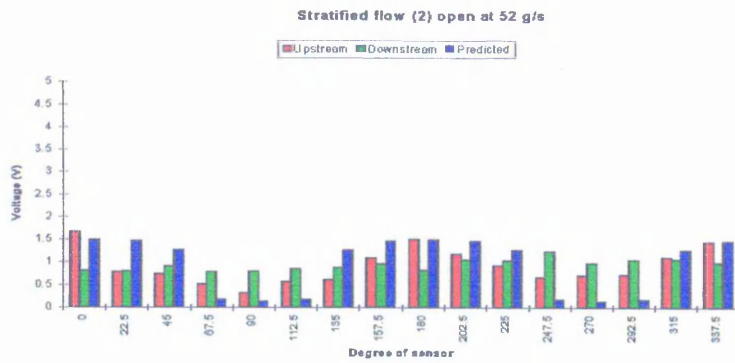
Figure 6.23a. Stratified (2) flow for plastic beads at 52 g/s
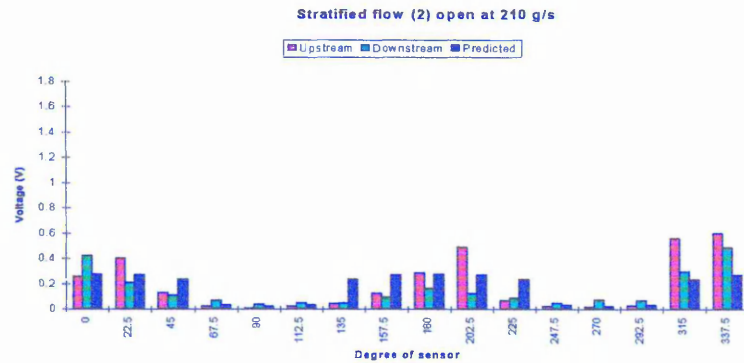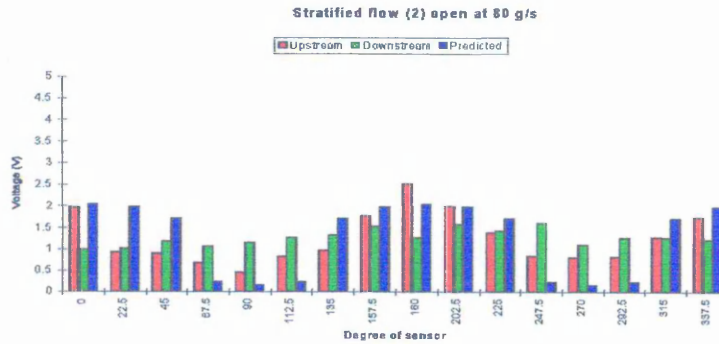

Figure 6.23b. Stratified (2) flow for plastic beads at 80 g/s
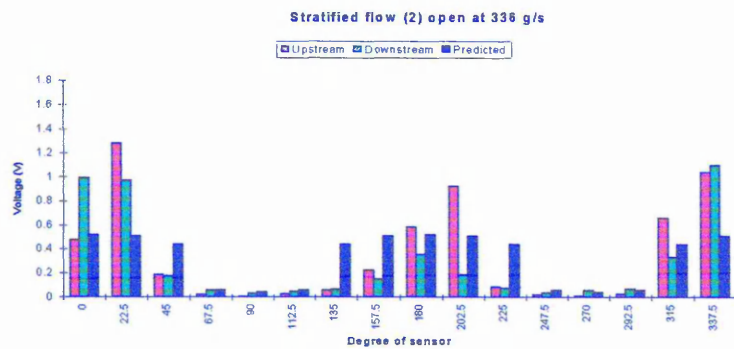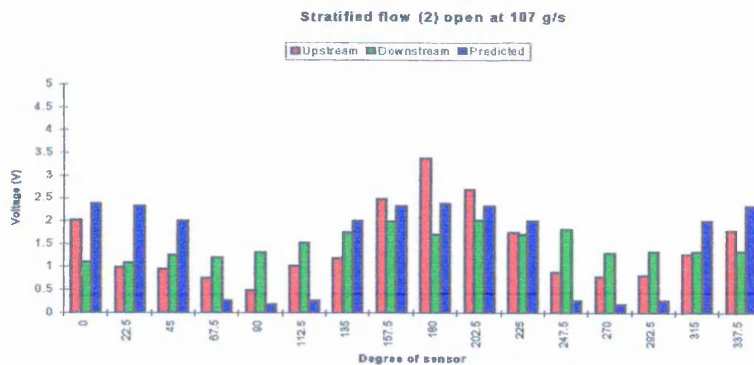

Figure 6.23c. Stratified (2) flow for plastic beads at 107 g/s

The summary of results for stratified (2) flow is shown in table 6.13 and graphically in figure 6.24.

Mass flow rate,	Total concentration, V	
g/s	Upstream	Downstream
52	14.469	14.950
80	19.796	20.184
107	23.247	23.746

Table 6.13. Summary for stratified (2) flow
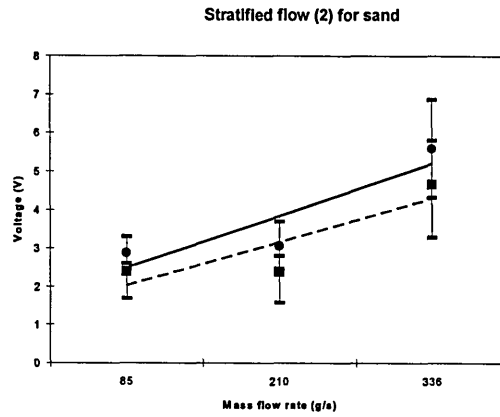
108

Stratified flow (2) for plastic beads
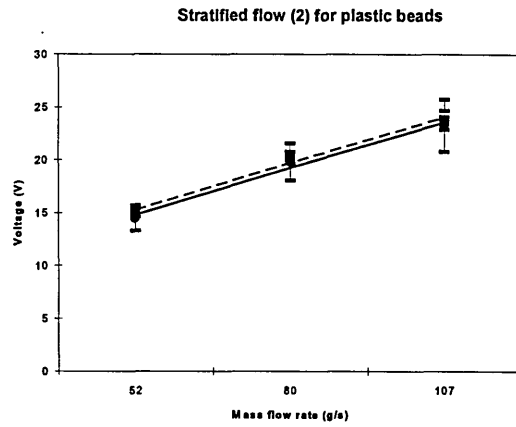
**Figure 6.24. Summed sensor outputs versus mass flow rate for stratified (2) flow
(solid line for upstream and dotted line for downstream)**

6.4.7 Discussion on plastic beads results

The gradients of the graph shown in section 6.3 are summarised in table 6.14. The graphs shown in this section show very good agreement between upstream and downstream sensing arrays. The maximum error occurs for three quarter flow and has a value of 7.01 % of the mean gradient.

Flow profile	Upstream gradient	Downstream gradient	Mean gradient	% difference
Full	0.173	0.188	0.180	4.44
Three quarter	0.199	0.229	0.214	7.01
Half	0.172	0.182	0.177	2.82
Quarter	0.170	0.186	0.178	4.49
Stratified (1)	0.211	0.197	0.204	3.43
Stratified (2)	0.160	0.160	0.160	0

Table 6.14. Gradient for six flow regimes (plastic beads)

6.5 Velocity measurement

The aim of this section is to investigate the use of the electrodynamic sensor array for velocity measurements around the circumference of the pipe and hence the peripheral velocity profile. Measurements were made by cross correlating the dynamic outputs of on upstream and a downstream sensor at several solids flow rates using the data

109

acquisition system to obtain 312 samples, with a sampling frequency varied from 1 kHz to 5 kHz per channel for 3 seconds, for each flow measurement. For sand, the dynamic sensor output voltage was measured at flow rates ranging from 85 g/s to 336 g/s. For plastic beads, the dynamic sensor output voltage was measured at flow rates ranging from 52 g/s to 107 g/s. In this section cross correlation of axially displaced sensor outputs is used to determine the peripheral velocity profile. Attempts to produce and measure non-uniform velocities are made by injecting air at a pressure of 7 Bar approximately inside the pipe.

6.4.1 Peripheral velocity

Velocity can be measured on line using the Hewlett Packard dynamic signal analyser to cross correlate two selected signals. One output signal from an upstream sensor and one output signal from a downstream sensor can be cross correlated to find the transit time of particles travelling from the upstream sensor to the downstream sensor. For all the tests reported in this dissertation, the separation between upstream and downstream sensors is 5 cm. Test were carried out using sand and plastic beads as the conveyed medium.

6.4.1.1 Sand flow

Typical signals for both upstream and downstream sensors for flowing sand are shown in figure 6.13. Correlograms are shown for three different mass flow rates (figure 6.14 to 6.16).
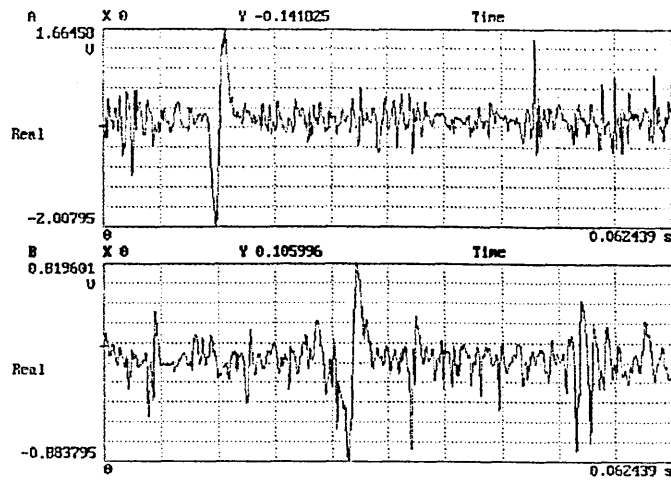
Figure 6.13. Typical dynamic output sensor signal from sensor 5 (upstream) and sensor 21 (downstream) for sand flow at 103 g/s

The Hewlett Packard dynamic signal analyser is used to cross correlate the output signals from the electrodynamic transducers as shown in figure 6.13. The result is shown in figure 6.14.
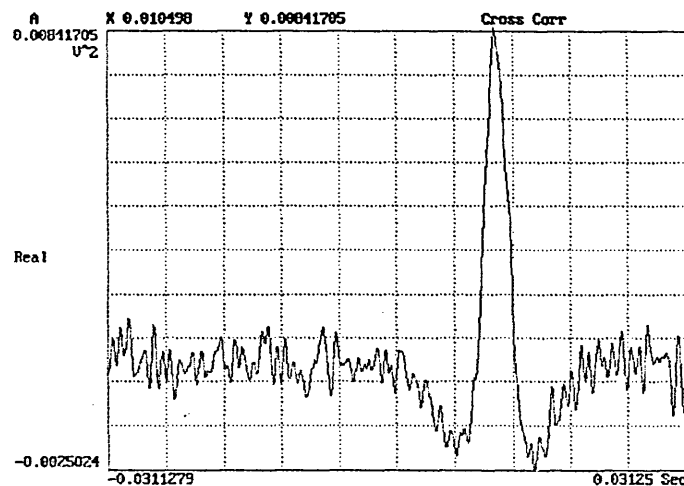
Figure 6.14. Cross correlation from HP signal analyser for sand flow at 103 g/s

From figure 6.14, the correlogram peak occurred at 10.5 ms. The corresponding velocity can be calculated as υ=0.05/0.0105 = 4.76 m/s. The correlations were repeated with flow rates of 193 g/s and 254 g/s. The results are shown in figures 6.15 and 6.16.

111
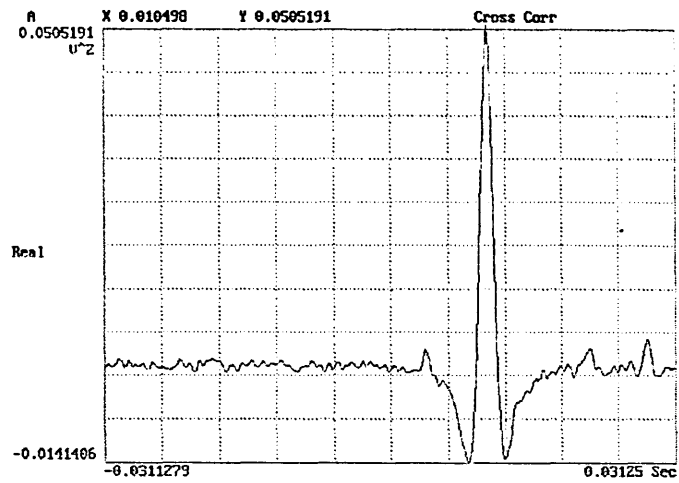
Figure 6.15. Cross correlation from HP signal analyser for sand flow at 193 g/s

From figure 6.15, the peak correlogram occurred at 10.5 ms and the corresponding

velocity is 4.76 m/s.
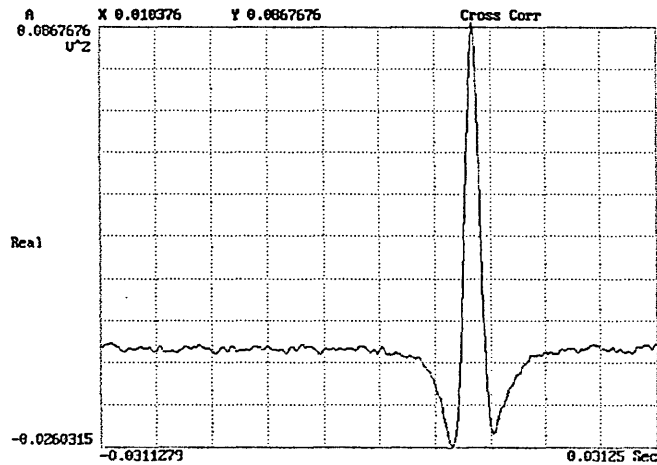
Figure 6.16. Cross correlation from HP signal analyser for sand flow at 254 g/s

From figure 6.16, the peak correlogram occurred at 10.4 ms and again the resulting

velocity is 4.81 m/s.

112

6.4.1.2 Plastic beads flow

The output signals from the electrodynamic transducers produced by the plastic bead particles are higher compared to the sand particles. This is shown in figure 6.17 compared to figure 6.13. This increase in signal level improves the signal to noise ratio of the signals (section 4.2).
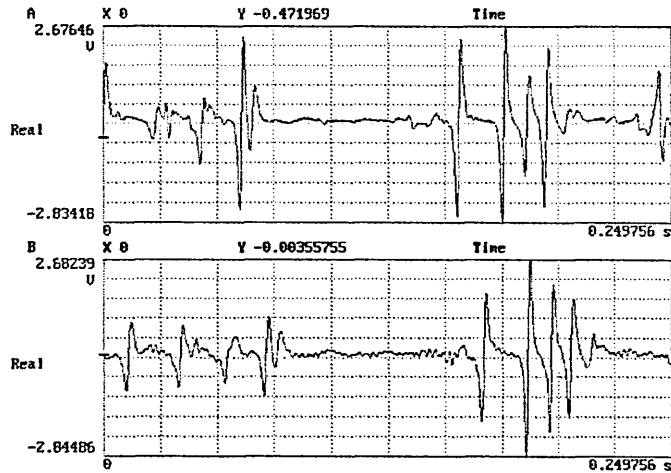
Figure 6.17. A typical dynamic output signal from sensor 3 (upstream) and sensor 19 (downstream) for plastic beads flow at 14 g/s

As a result the cross correlation coefficients shown in the correlograms in figures 6.18 and 6.19 are larger compared to figures 6.14 to figure 6.16 for sand.
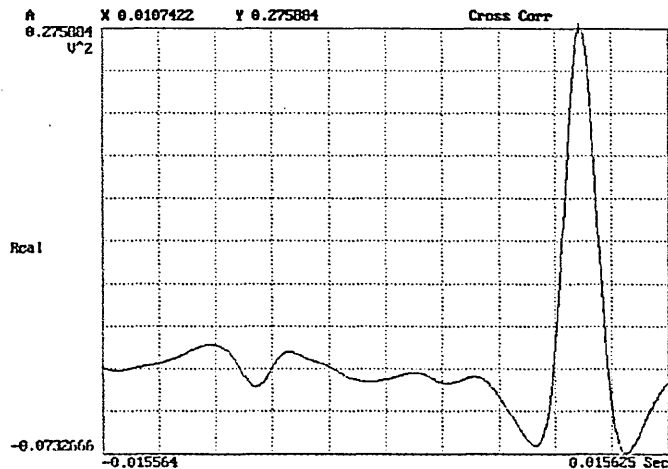
Figure 6.18. Cross correlation from HP signal analyser for plastic beads flow at 14 g/s

113

From figures 6.18 and 6.19, the correlogram peaks occurred at 10.74 ms with a corresponding velocity of 4.66 m/s.
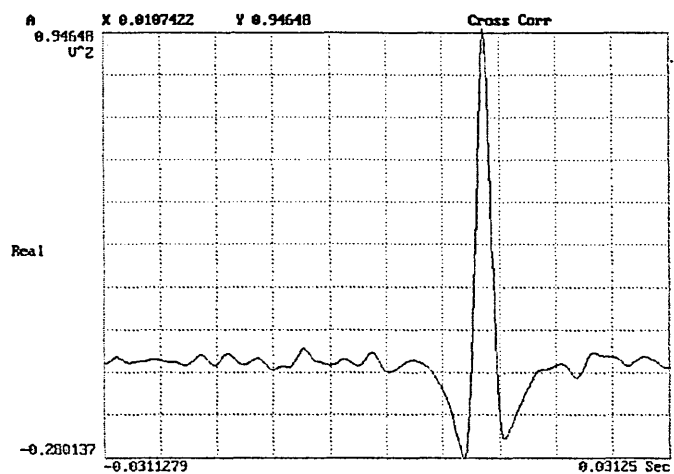
Figure 6.19. **Cross correlation from HP signal analyser for plastic beads flow at 52 g/s**

CHAPTER 7

Concentration and velocity profiles

Chapter summary

Concentration profiles are calculated using linear back projection and filtered back projection algorithms from data measured by the sensor arrays. Velocity profiles are obtained by cross correlation of upstream and downstream pixel concentration values.

7.1 Introduction

In this chapter, linear back projection (section 3.4.2.1) and filtered back projection (section 3.4.2.2) are used to generate a tomographic image of the measurement cross-section using the data described in chapter 6. All the tomograms have the same sensor orientations with respect to the baffle, which is positioned relative to the top side of the image except for stratified flow. As the flow profile is changed from full to quarter, the baffle is moved progressively to the bottom side of the image. The screw feeder is positioned on the bottom side with respect to the tomographic images (section 4.4, figure 4.5).

7.2 Concentration profiles

For the concentration measurements the data are collected from the averaged sensor output. Tomographic images of the concentration distributions over both the upstream and downstream measurement sections are calculated using the linear back projection algorithm and the filtered back projection algorithm. Results from the measurements are compared with the known flow rates in order to determine the accuracy of the

reconstruction. For brevity tomograms of the upstream sensor are shown. The total concentration measurement of the profile is obtained by summing the values of all the pixel concentrations. A full list of results is shown in table 7.1, 7.2, 7.3 and 7.4 for upstream and downstream.

7.2.1 Sand

A steady flow of sand was established down the conveyor at a known flow rate. For the purpose of concentration profiles, only tomograms at 210 g/s will be shown. The averaged outputs from sensors 1 to 16 were sampled at a rate of 5 Hz per channel for 60 seconds. The 16 measurements provide a data set for calculating an upstream concentration profile. Readings are obtained for sensors 17 to 32 to provide data for the downstream concentration profile.

7.2.1.1 Full flow

The data set for the upstream sensor for full flow is used with the linear back projection algorithm (section 3.4.2.1). The results are shown for a sand flow rate of 210 g/s in numerical format in figure 7.1 (a) and as a colour tomogram in figure 7.1 (b). Visual inspection of the conveyor shows that the sand is relatively uniformly distributed over the measurement cross-section. The error between this and figure 7.1 (a) arises due to the non-linear sensing of the electrodynamic sensor (section 4.2). However, the centre pixels show much lower concentration values than peripheral pixels. The filtered linear back projection algorithm is used on the data. The effect of the filter on the tomographic reconstruction are shown in figures 7.2 (a) and (b). These show a more even distribution of solid material within the measurement section, which is closer agreement with optical fibre measurements (Abdul Rahim, 1996).

0	0	0.06	0.16	0.13	0.13	0.28	0	0
0	0.30	0.10	0.07	0.05	0.06	0.07	0.11	0
0.40	0.11	0.06	0.04	0.03	0.03	0.03	0.04	0.06
0.17	0.07	0.04	0.03	0.03	0.03	0.03	0.03	0.05
0.10	0.04	0.03	0.03	0.02	0.02	0.02	0.03	0.18
0.08	0.04	0.03	0.02	0.02	0.02	0.03	0.04	0.08
0.15	0.06	0.03	0.03	0.03	0.03	0.03	0.06	0.14
0	0.12	0.05	0.04	0.04	0.04	0.05	0.11	0
0	0	0.10	0.08	0.31	0.09	0.11	0	0
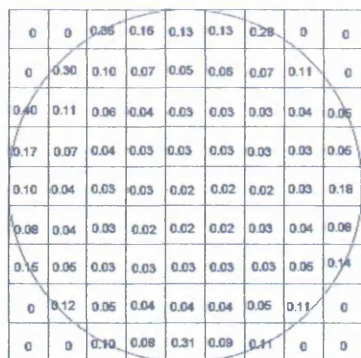
Figure 7.1 (a). Numerical concentration profile for sand at 210 g/s (linear back projection)
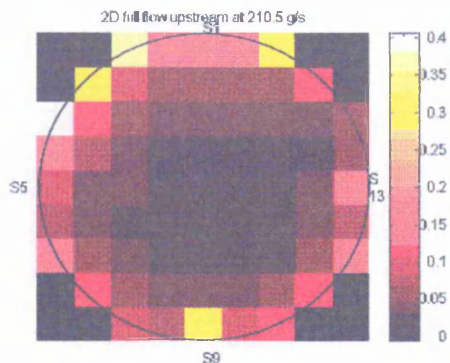
Figure 7.1 (b). 2D image concentration profile for sand at 210 g/s (linear back projection)

0	0	0.49	0.37	0.13	0.30	0.38	0	0
0	0.32	0.36	0.33	0.26	0.26	0.24	0.12	0
0.54	0.38	0.32	0.28	0.26	0.23	1.93	1.35	0.07
0.39	0.33	0.29	0.26	0.24	0.22	0.18	0.15	0.11
0.10	0.23	0.24	0.24	0.22	0.21	0.19	0.17	0.18
0.18	0.20	0.21	0.22	0.21	0.20	0.18	0.18	0.19
0.20	0.18	0.19	0.20	0.20	0.19	0.17	0.16	0.20
0	0.13	0.16	0.19	0.22	0.20	0.16	0.12	0
0	0	0.14	0.19	0.32	0.20	0.15	0	0
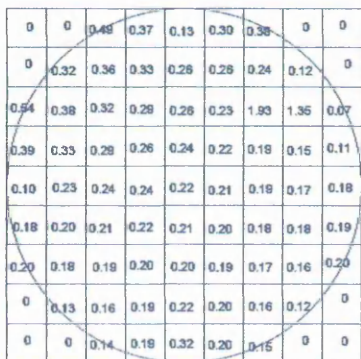
Figure 7.2 (a). Numerical concentration profile for sand at 210 g/s (filtered back projection)
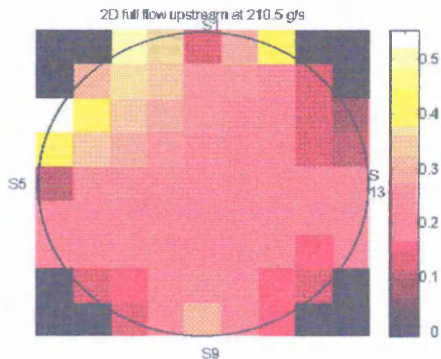
Figure 7.2 (b). 2D image concentration profile for sand at 210 g/s (filtered back projection)

117

7.2.1.2 Three quarter flow

A data set is collected for three quarter flow (figure 4.10) in a similar manner to that described in section 7.2.1. The data are treated in a similar manner to determine the concentration profile using the linear back projection algorithm. Figures 7.3 (a) and (b) show the concentration profile at 210 g/s. The filtered back projection algorithm is used to produce the result shown in figures 7.4 (a) and (b) at 210 g/s.

0	0	0.03	0.03	0.03	0.07	0.14	0	0
0	0.09	0.04	0.03	0.03	0.04	0.05	0.07	0
0.09	0.05	0.04	0.03	0.03	0.04	0.04	0.06	0.10
0.12	0.07	0.04	0.04	0.04	0.04	0.05	0.08	0.19
0.59	0.10	0.06	0.04	0.04	0.04	0.06	0.12	1.18
0.36	0.14	0.07	0.05	0.05	0.05	0.07	0.12	0.29
0.76	0.18	0.09	0.06	0.06	0.06	0.08	0.14	0.37
0	0.38	0.12	0.09	0.09	0.09	0.12	0.36	0
0	0	0.22	0.17	0.57	0.18	0.26	0	0

Figure 7.3 (a). Numerical concentration profile for three quarter sand flow at 210 g/s (linear back projection)
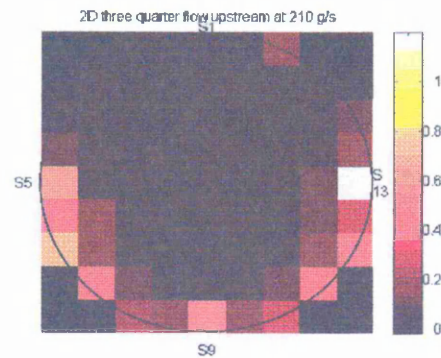
Figure 7.3 (b). 2D image concentration profile for three quarter sand flow at 210 g/s (linear back projection)

0	0	0	0	0	0	0	0	0
0	0	0	0	0	0	0	0	0
0.12	0.18	0.21	0.23	0.24	0.26	0.25	0.22	0.14
0.28	0.31	0.32	0.32	0.32	0.34	0.37	0.42	0.44
0.58	0.49	0.42	0.39	0.38	0.40	0.46	0.62	1.18
0.85	0.64	0.50	0.44	0.42	0.44	0.48	0.58	0.68
1.04	0.63	0.49	0.45	0.44	0.44	0.45	0.48	0.53
0	0.40	0.41	0.42	0.46	0.43	0.41	0.39	0
0	0	0.30	0.39	0.57	0.42	0.36	0	0

Figure 7.4 (a). Numerical concentration profile for three quarter sand flow at 210 g/s (filtered back projection)
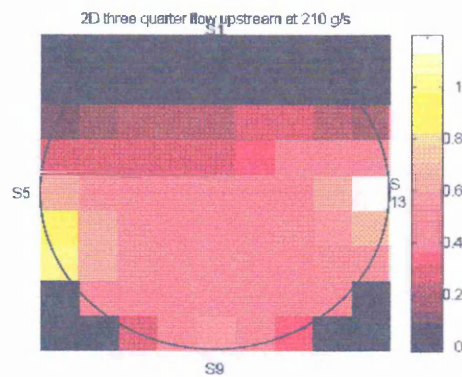
Figure 7.4 (b). 2D image concentration profile for three quarter sand flow at 210 g/s (filtered back projection)

7.2.1.3 Half flow

A data set is collected for half flow (figure 4.11) in a similar manner to that described in section 7.2.1. The data are treated in a similar manner to determine the concentration profile using the linear back projection algorithm. Figures 7.5 (a) and (b) show the concentration profile at 210 g/s. The filtered back projection algorithm is used to produce the result shown in figures 7.6 (a) and (b) at 210 g/s.

0	0	0.02	0.03	0.03	0.02	0.02	0	0
0	0.04	0.04	0.04	0.04	0.03	0.03	0.03	0
0.03	0.06	0.05	0.05	0.04	0.04	0.04	0.04	0.02
0.06	0.08	0.07	0.07	0.06	0.06	0.05	0.05	0.04
0.27	0.14	0.11	0.10	0.08	0.08	0.07	0.06	0.08
0.57	0.27	0.17	0.14	0.12	0.11	0.10	0.10	0.11
1.35	0.50	0.29	0.23	0.20	0.18	0.16	0.18	0.17
0	2.03	0.67	0.44	0.42	0.36	0.33	0.54	0
0	0	1.48	1.04	3.87	0.88	1.04	0	0

Figure 7.5 (a). Numerical concentration profile for half sand flow at 210 g/s (linear back projection)
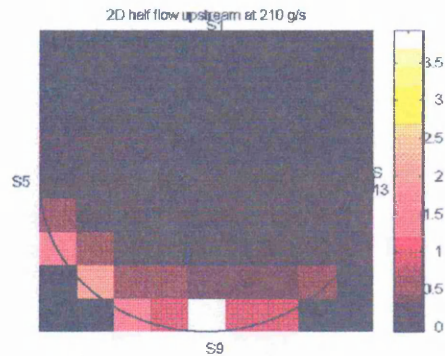
Figure 7.5 (b). 2D image concentration profile for half sand flow at 210 g/s (linear back projection)

0	0	0	0	0	0	0	0	0
0	0	0	0	0	0	0	0	0
0	0	0	0	0	0	0	0	0
0	0	0	0	0	0	0	0	0
0	0	0	0	0	0	0	0	0
1.33	1.26	1.23	1.20	1.11	0.94	0.71	0.44	0.25
1.84	1.73	1.65	1.61	1.52	1.27	0.91	0.56	0.2
0	2.16	1.97	2.07	2.18	1.88	1.13	0.57	0
0	0	2.01	2.42	3.87	2.04	1.41	0	0

Figure 7.6 (a). Numerical concentration profile for half sand flow at 210 g/s (filtered back projection)
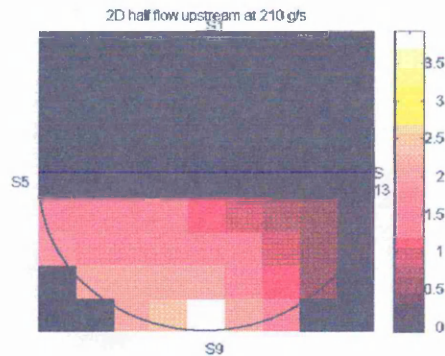
Figure 7.6 (b). 2D image concentration profile for half sand flow at 210 g/s (filtered back projection)

7.2.1.4 Quarter flow

A data set is collected for quarter flow (figure 4.12) in a similar manner to that described

in section 7.2.1. The data are treated in a similar manner to determine the concentration

profile using the linear back projection algorithm. Figures 7.7 (a) and (b) show the

concentration profile at 210 g/s. The filtered back projection algorithm is used to

produce the result shown in figures 7.8 (a) and (b) at 210 g/s.

Figure 7.7 (a). Numerical concentration profile for quarter sand flow at 210 g/s (linear back projection)
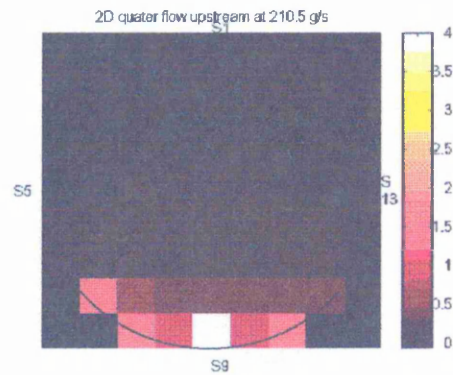
Figure 7.7 (b). 2D image concentration profile for quarter sand flow at 210 g/s (linear back projection)

Figure 7.8 (a). Numerical concentration profile for quarter sand flow at 210 g/s (filtered back projection)
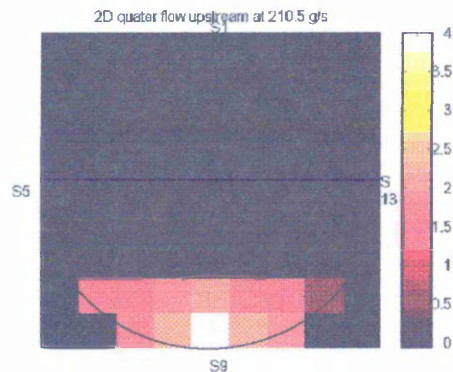
Figure 7.8 (b). 2D image concentration profile for quarter sand flow at 210 g/s (filtered back projection)

120

7.2.1.5 Stratified (1) flow

A data set is collected for stratified (1) flow (figure 4.13) in a similar manner to that described in section 7.2.1. The data are treated in a similar manner to determine the concentration profile using the linear back projection algorithm. Figures 7.9 (a) and (b) show the concentration profile at 210 g/s. The filtered back projection algorithm is used to produce the result shown in figures 7.10 (a) and (b) at 210 g/s.
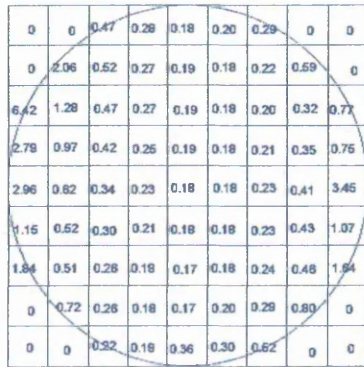
Figure 7.9 (a). Numerical concentration profile for stratified (1) sand flow at 210 g/s (linear back projection)
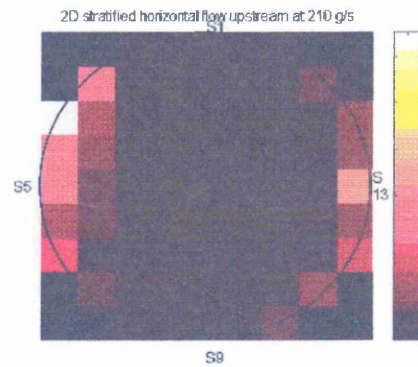
Figure 7.9 (b). 2D image concentration profile for stratified (1) sand flow at 210 g/s (linear back projection)
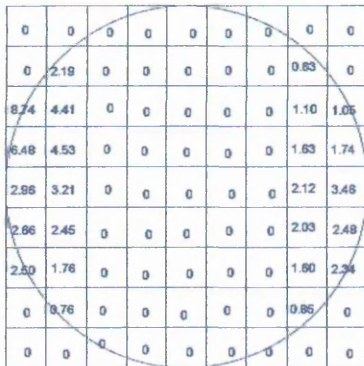
Figure 7.10(a). Numerical concentration profile for stratified (1) sand flow at 210 g/s (filtered back projection)
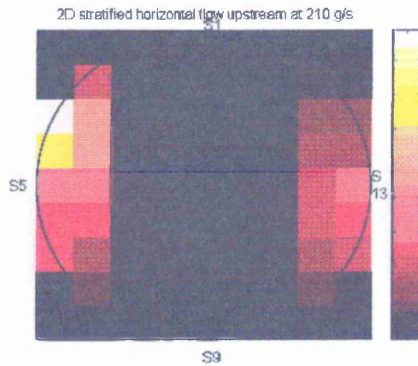
Figure 7.10 (b). 2D image concentration profile for stratified (1) sand flow at 210 g/s (filtered back projection)

7.2.1.6 Stratified (2) flow

A data set is collected for stratified (2) flow (figure 4.14) in a similar manner to that described in section 7.2.1. The data are treated in a similar manner to determine the concentration profile using the linear back projection algorithm. Figures 7.11 (a) and (b) show the concentration profile at 210 g/s. The filtered back projection algorithm is used to produce the result shown in figures 7.12 (a) and (b) at 210 g/s.

Figure 7.11(a). Numerical concentration profile for stratified (2) sand flow at 210 g/s (linear back projection)
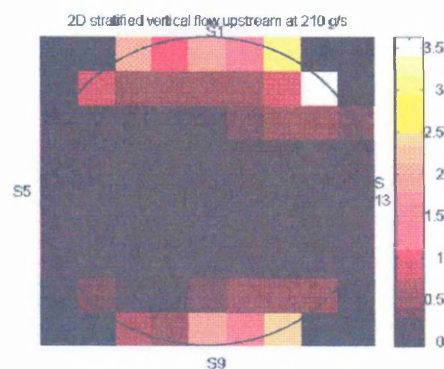
Figure 7.11 (b). 2D image concentration profile for stratified (2) sand flow at 210 g/s (linear back projection)

Figure 7.12(a). Numerical concentration profile for stratified (2) sand flow at 210 g/s (filtered back projection)
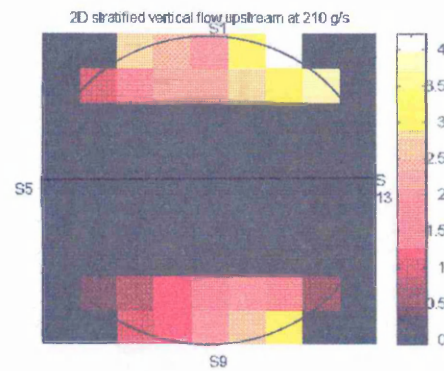
Figure 7.12 (b). 2D image concentration profile for stratified (2) sand flow at 210 g/s (filtered back projection)

7.2.1.7 Discussion of results

The numerical values from each concentration tomogram have been summed at the different flow conditions for linear back projection. The results are shown numerically in table 7.1 and graphically in figure 7.13 and 7.14.

Sand, g/s	Linear back projection					
Upstream	Full	3 Quarter	Half	Quarter	Strat. (1)	Strat. (2)
85	2.56	4.1	7.03	7.28	31.56	33.18
210	5.63	9.73	20.21	16.26	44.22	35.34
336	8.49	23.71	28.58	18.66	72.22	64.54
Downstream						
85	3.96	5.2	5.71	4.13	33.38	27.68
210	7.23	18.61	17.68	13.25	48.17	27.58
336	10.58	32.34	24.84	13.92	74.23	54.08

Table 7.1. Summary of concentration profile for linear back projection
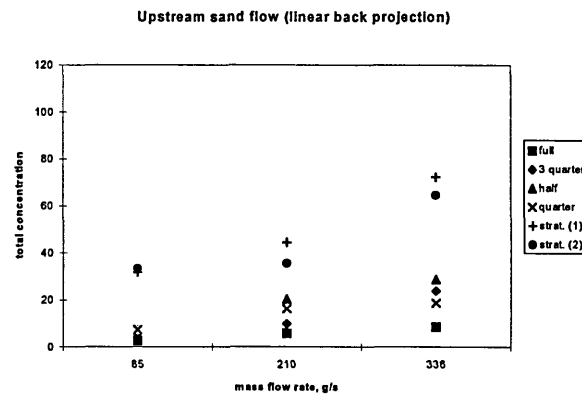
Figure 7.13. Upstream sand flow(linear back projection)
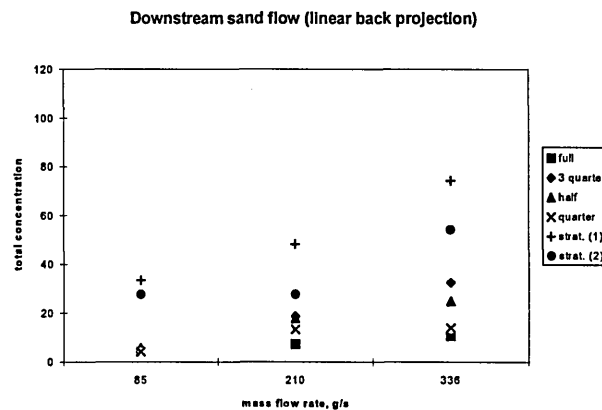
Figure 7.14. Downstream sand flow (linear back projection)

The numerical values from each concentration tomogram have been summed at the different flow conditions for filtered back projection. The results are shown numerically in table 7.2 and graphically in figure 7.15 and 7.16.

Sand, g/s	Filtered back projection					
Upstream	Full	3 Quarter	Half	Quarter	Strat. (1)	Strat. (2)
85	7.1	10.11	13.74	9.53	40.74	44.36
210	15.59	24.88	43.35	22.84	63.64	50.14
336	23.4	62.93	61.66	25.29	107.89	96.58
Downstream						
85	10.89	12.88	11.03	5.14	45.61	29.99
210	19.86	49.04	37.38	17.38	64.76	35.13
336	29.08	85.37	52.67	17.6	106.2	77.58

Table 7.2. Summary of concentration profile for filtered back projection
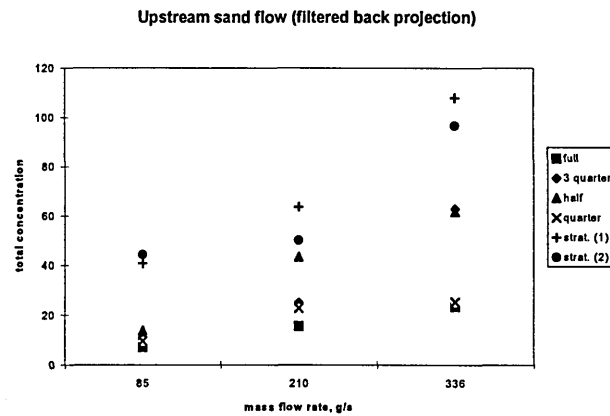
Figure 7.15. Upstream sand flow (filtered back projection)
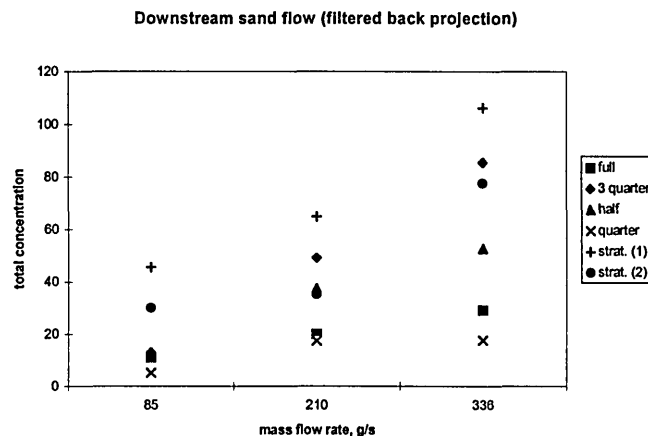
Figure 7.16. Downstream sand flow (filtered back projection)

Results in figure 7.13, 7.14, 7.15 and 7.16 tend to show an increased concentration at a specified mass flow rate as the flow section is reduced from full flow. This may be due to the baffle modifying the amount of charge carried by the sand when interaction occurs (section 9.3). Anomalies in the increased concentration with mass flow rate may be due to day to day variations in physical conditions such as temperature and humidity in the laboratory.

7.2.2 Plastic beads

A steady flow of plastic beads was established down the conveyor at a known flow rate. The averaged outputs from sensors 1 to 32 were sampled at a rate of 5 Hz per channel for 60 seconds.

7.2.2.1 Full flow

The data set for the upstream sensor for full flow is used with the linear back projection algorithm (section 3.4.2.1). The results are shown for a plastic beads flow rate of 107 g/s in numerical format in figure 7.17 (a) and as a colour tomogram in figure 7.17 (b). The filtered linear back projection algorithm is used on the data. The results are shown in figures 7.18 (a) and (b).

0	0	2.70	1.65	3.70	1.75	3.00	0	0
0	1.54	1.19	0.91	0.84	0.94	1.29	4.11	0
3.72	1.36	0.83	0.68	0.65	0.69	0.86	1.37	3.28
2.20	1.12	0.76	0.64	0.61	0.64	0.76	1.12	2.15
4.77	1.13	0.80	0.68	0.64	0.68	0.80	1.14	5.97
3.25	1.50	0.96	0.80	0.76	0.79	0.94	1.39	2.75
6.37	2.20	1.30	1.05	0.99	1.05	1.30	2.07	4.55
0	5.83	2.29	1.76	1.61	1.76	2.34	7.55	0
0	0	6.59	3.84	9.71	3.81	6.45	0	0

Figure 7.17(a). Numerical concentration profile for full plastic beads flow at 107 g/s (linear back projection)
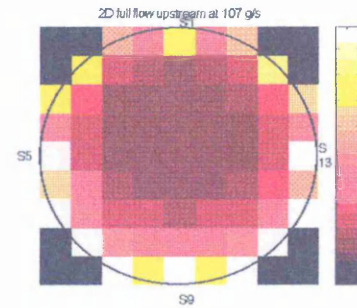
Figure 7.17 (b). 2D image concentration profile for full plastic beads flow at 107 g/s (linear back projection)

0	0	3.87	3.82	3.70	4.07	4.08	0	0
0	3.76	4.11	4.25	4.35	4.42	4.44	4.36	0
5.87	4.67	4.71	4.83	4.90	4.92	4.86	4.72	4.48
5.11	5.25	5.37	5.45	5.48	5.47	5.40	5.24	5.00
4.78	5.87	6.05	6.10	6.11	6.08	6.01	5.92	5.98
7.54	7.03	6.79	6.78	6.77	6.74	6.65	6.50	6.39
8.34	7.58	7.37	7.45	7.48	7.45	7.35	7.15	6.50
0	7.03	7.85	8.22	8.34	8.23	8.06	8.01	0
0	0	8.86	8.91	9.71	8.85	8.75	0	0

Figure 7.18(a). Numerical concentration profile for full plastic beads flow at 107 g/s (filtered back projection)
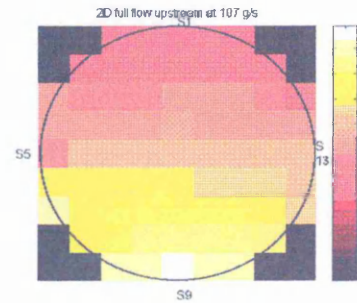
Figure 7.18 (b). 2D image concentration profile for full plastic beads flow at 107 g/s (filtered back projection)

7.2.2.2 Three quarter flow

A data set is collected for three quarter flow (figure 4.10) in a similar manner to that described in section 7.2.2. The data are treated in a similar manner to determine the concentration profile using the linear back projection algorithm. Figures 7.19 (a) and (b) show the concentration profile at 107 g/s. The filtered back projection algorithm is used to produce the result shown in figures 7.20 (a) and (b) at 107 g/s.
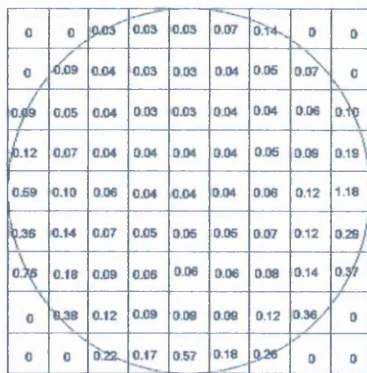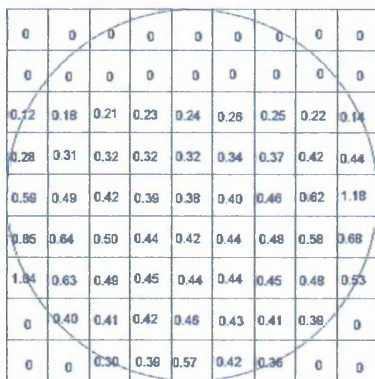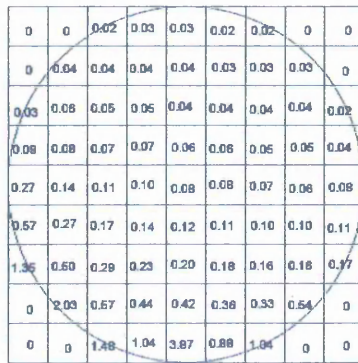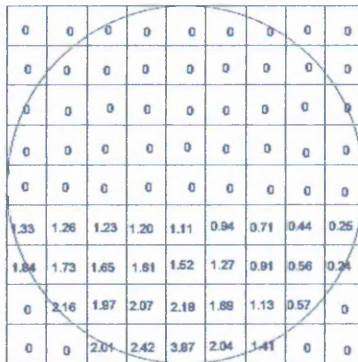

Figure 7.19(a). Numerical concentration profile for three quarter plastic beads flow at 107 g/s (linear back projection)
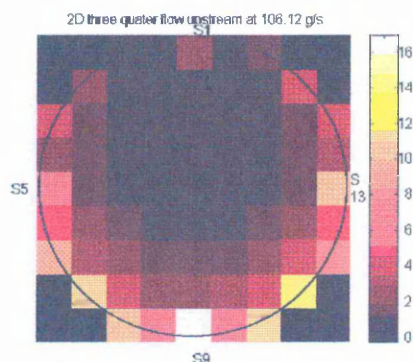
Figure 7.19 (b). 2D image concentration profile for three quarter plastic beads flow at 107 g/s (linear back projection)

Figure 7.20(a). Numerical concentration profile for three quarter plastic beads flow at 107 g/s (filtered back projection)
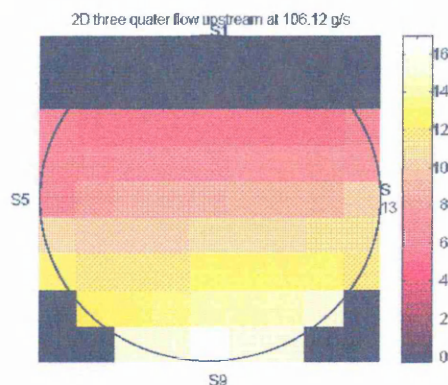
Figure 7.20 (b). 2D image concentration profile for three quarter plastic beads flow at 107 g/s (filtered back projection)

127

7.2.2.3 Half flow

A data set of plastic beads is collected for half flow (figure 4.11) in a similar manner to that described in section 7.2.2. The data are treated in a similar manner to determine the concentration profile using the linear back projection algorithm. Figures 7.21 (a) and (b) show the concentration profile at 107 g/s. The filtered back projection algorithm is used to produce the result shown in figures 7.22 (a) and (b) at 107 g/s.
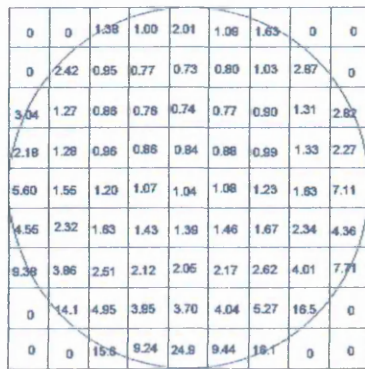
Figure 7.21(a). Numerical concentration profile for half plastic beads flow at 107 g/s (linear back projection)
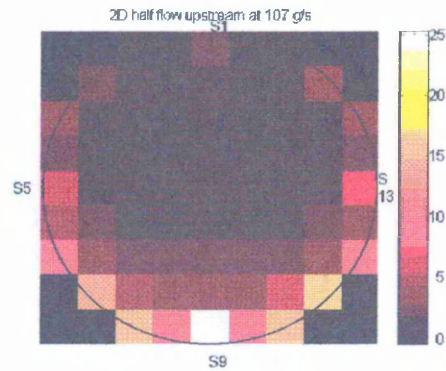
Figure 7.21 (b). 2D image concentration profile for half plastic beads flow at 107 g/s (linear back projection)
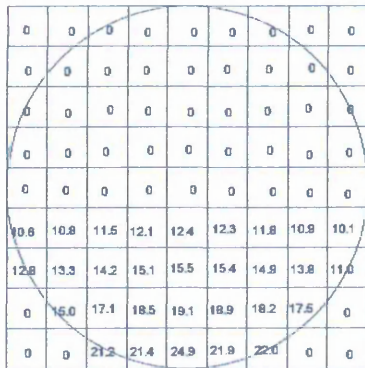
Figure 7.22(a). Numerical concentration profile for half plastic beads flow at 107 g/s (filtered back projection)
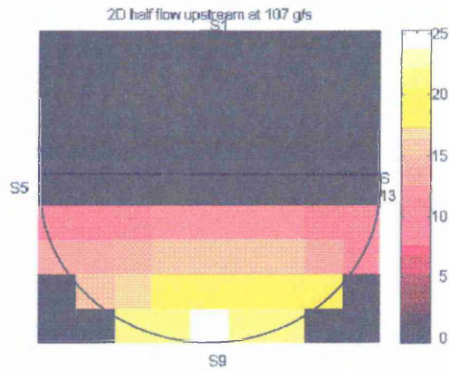
Figure 7.22 (b). 2D image concentration profile for half plastic beads flow at 107 g/s (filtered back projection)

128

7.2.2.4 Quarter flow

A data set of plastic beads is collected for quarter flow (figure 4.12) in a similar manner to that described in section 7.2.2. The data are treated in a similar manner to determine the concentration profile using the linear back projection algorithm. Figures 7.23 (a) and (b) show the concentration profile at 107 g/s. The filtered back projection algorithm is used to produce the result shown in figures 7.24 (a) and (b) at 107 g/s.

0	0	0.64	0.56	1.05	0.67	0.92	0	0
0	0.98	0.57	0.53	0.53	0.59	0.72	1.60	0
1.26	0.73	0.60	0.58	0.60	0.64	0.72	0.96	1.7
1.16	0.84	0.73	0.72	0.73	0.78	0.88	1.12	1.72
3.12	1.12	0.97	0.94	0.95	1.03	1.18	1.53	6.00
3.07	1.76	1.38	1.31	1.34	1.45	1.71	2.40	4.46
6.30	3.09	2.22	2.02	2.05	2.28	2.83	4.40	8.20
0	11.8	4.56	3.88	3.81	4.37	5.91	19.2	0
0	0	15.8	9.16	26.1	10.5	18.6	0	0
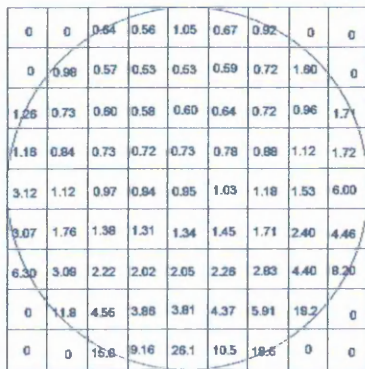
Figure 7.23(a). Numerical concentration profile for quarter plastic beads flow at 107 g/s (linear back projection)
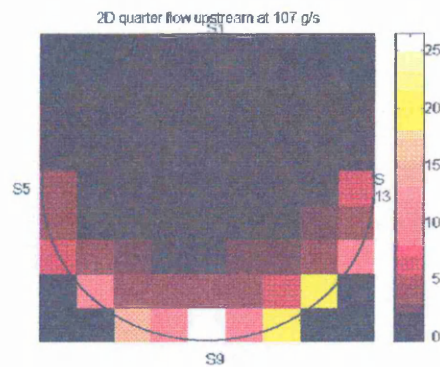
Figure 7.23 (b). 2D image concentration profile for quarter plastic beads flow at 107 g/s (linear back projection)

0	0	0	0	0	0	0	0	0
0	0	0	0	0	0	0	0	0
0	0	0	0	0	0	0	0	0
0	0	0	0	0	0	0	0	0
0	0	0	0	0	0	0	0	0
0	0	0	0	0	0	0	0	0
0	0	0	0	0	0	0	0	0
0	12.5	15.7	18.1	19.7	20.5	20.4	20.4	0
0	0	20.4	21.3	26.1	24.3	25.8	0	0
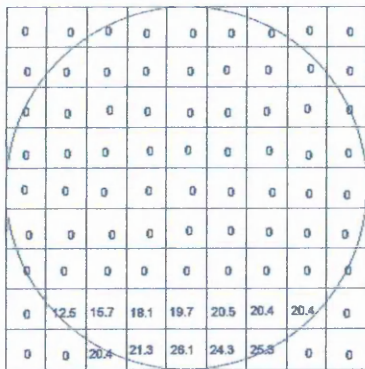
Figure 7.24(a). Numerical concentration profile for quarter plastic beads flow at 107 g/s (filtered back projection)
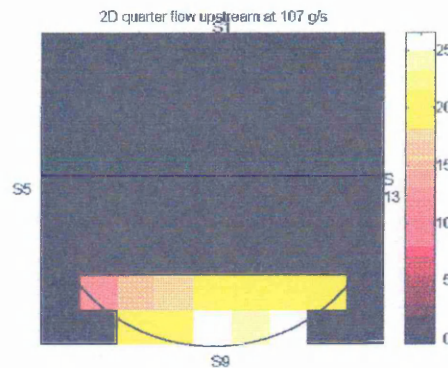
Figure 7.24 (b). 2D image concentration profile for quarter plastic beads flow at 107 g/s (filtered back projection)

7.2.2.5 Stratified (1) flow

A data set of plastic beads is collected for stratified (1) flow (figure 4.13) in a similar manner to that described in section 7.2.2. The data are treated in a similar manner to determine the concentration profile using the linear back projection algorithm. Figures 7.25 (a) and (b) show the concentration profile at 107 g/s. The filtered back projection algorithm is used to produce the result shown in figures 7.26 (a) and (b) at 107 g/s.

0	0	5.12	3.09	4.78	7.17	16.5	0	0
0	12.4	3.10	2.07	2.08	3.08	4.40	10.1	0
13.8	4.20	2.18	1.63	1.59	1.86	2.42	3.89	10.4
8.94	3.03	1.78	1.43	1.37	1.54	1.97	3.19	6.79
11.5	2.43	1.60	1.32	1.27	1.44	1.88	3.12	20.3
5.76	2.56	1.55	1.28	1.26	1.44	1.95	3.46	8.00
10.6	2.92	1.62	1.32	1.33	1.56	2.25	4.40	13.3
0	5.02	1.99	1.80	1.60	1.96	3.15	12.7	0
0	0	3.70	2.53	6.03	3.17	5.38	0	0
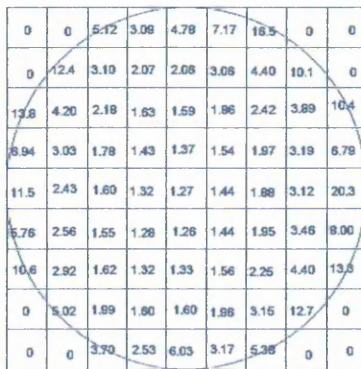
Figure 7.25(a). Numerical concentration profile for stratified (1) plastic beads flow at 107 g/s (linear back projection)
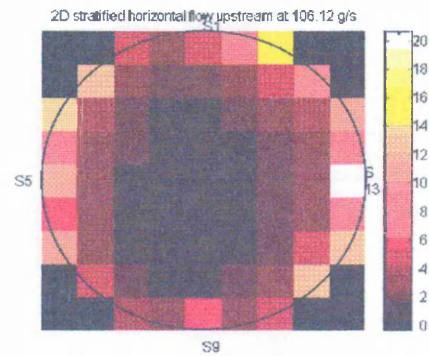
Figure 7.25 (b). 2D image concentration profile for stratified (1) plastic beads flow at 107 g/s (linear back projection)

0	0	0	0	0	0	0	0	0
0	13.2	0	0	0	0	0	10.7	0
18.8	14.5	0	0	0	0	0	13.4	14.1
16.1	14.2	0	0	0	0	0	14.9	15.8
11.8	12.6	0	0	0	0	0	16.2	20.4
13.4	12.0	0	0	0	0	0	16.2	18.6
14.4	10.1	0	0	0	0	0	16.2	19.1
0	5.33	0	0	0	0	0	13.5	0
0	0	0	0	0	0	0	0	0
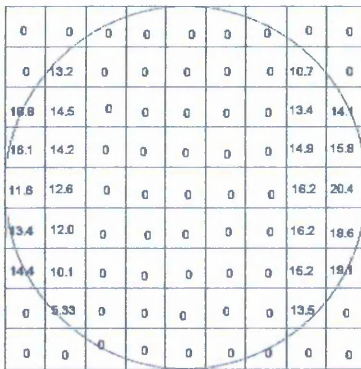
Figure 7.26(a). Numerical concentration profile for stratified (1) plastic beads flow at 107 g/s (filtered back projection)
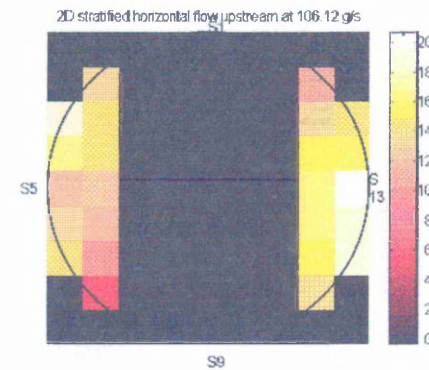
Figure 7.26 (b). 2D image concentration profile for stratified (1) plastic beads flow at 107 g/s (filtered back projection)

130

7.2.2.6 Stratified (2) flow

A data set of plastic beads is collected for stratified (2) flow (figure 4.14) in a similar manner to that described in section 7.2.2. The data are treated in a similar manner to determine the concentration profile using the linear back projection algorithm. Figures 7.27 (a) and (b) show the concentration profile at 107 g/s. The filtered back projection algorithm is used to produce the result shown in figures 7.28 (a) and (b) at 107 g/s.
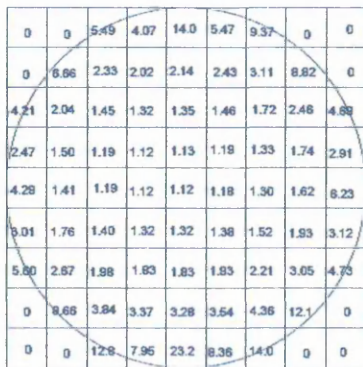
Figure 7.27(a). Numerical concentration profile for stratified (2) plastic beads flow at 107 g/s (linear back projection)
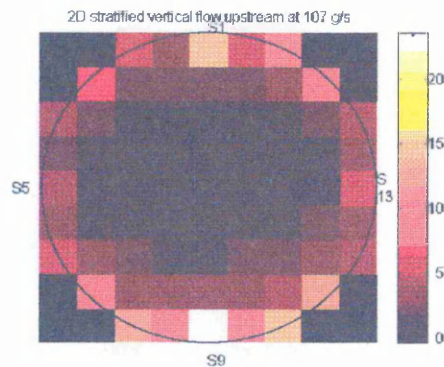
Figure 7.27 (b). 2D image concentration profile for stratified (2) plastic beads flow at 107 g/s (linear back projection)
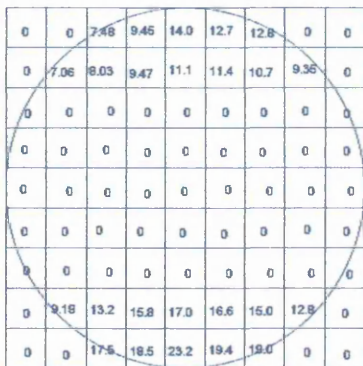
Figure 7.28(a). Numerical concentration profile for stratified (2) plastic beads flow at 107 g/s (filtered back projection)
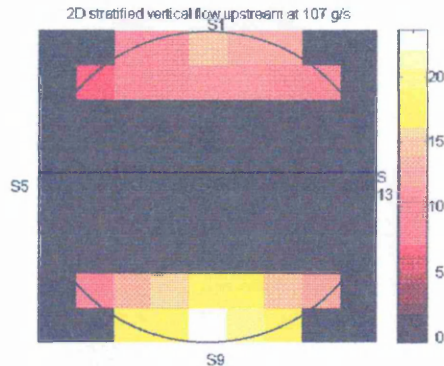
Figure 7.28 (b). 2D image concentration profile for stratified (2) plastic beads flow at 107 g/s (filtered back projection)

7.2.2.7 Discussion of results

The numerical values from each concentration tomogram have been summed at the different flow conditions for linear back projection. The results are shown numerically in table 7.3 and graphically in figure 7.29 and 7.30.

Plastic, g/s	Linear back projection					
Upstream	Full	3 Quarter	Half	Quarter	Strat. (1)	Strat. (2)
52	44.67	97.12	138.66	119.78	170.47	167.24
80	119.76	185.96	204.95	177.84	246.08	228.8
107	154.1	223.24	247.61	227.76	304.26	268.65
Downstream						
52	47.26	107.22	148.96	120.92	176.28	175.56
80	132.56	207.16	217.87	185.44	252.25	232.96
107	166.06	251.89	264.44	239.19	301.39	274.07

Table 7.3. Summary of concentration profile for linear back projection
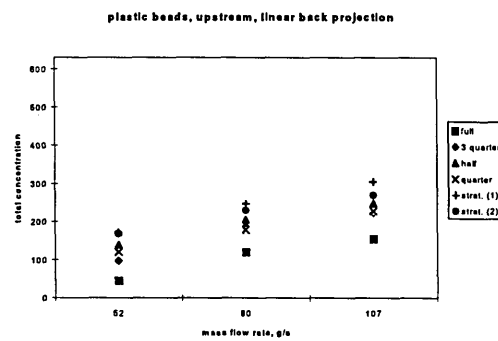
Figure 7.29. Upstream plastic beads flow (linear back projection)
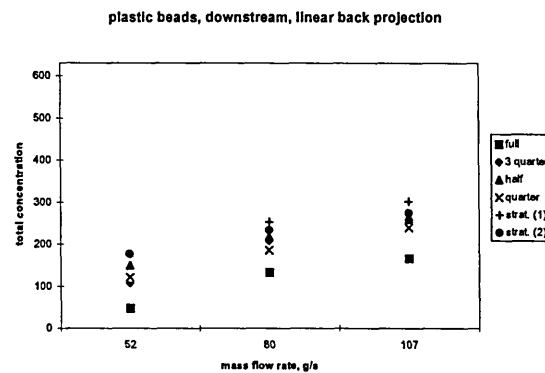
Figure 7.30. Downstream plastic beads flow (linear back projection)

132

The numerical values from each concentration tomogram have been summed at the different flow conditions for filtered back projection. The results are shown numerically in table 7.4 and graphically in figure 7.31 and 7.32.

Plastic, g/s	Filter back projection					
Upstream	Full	3 Quarter	Half	Quarter	Strat. (1)	Strat. (2)
52	122.23	243.29	247.34	120.92	186.94	190.51
80	328.43	472.54	373.76	185.44	276.13	266.24
107	422.07	573.44	464.35	239.19	344.11	320.59
Downstream						
52	129.32	257.15	215.21	95.93	164.54	162.72
80	363.09	505.82	326.29	141.89	241.31	223.88
107	455.11	621.48	417.22	180.9	291.44	267.54

Table 7.4. Summary of concentration profile for filtered back projection
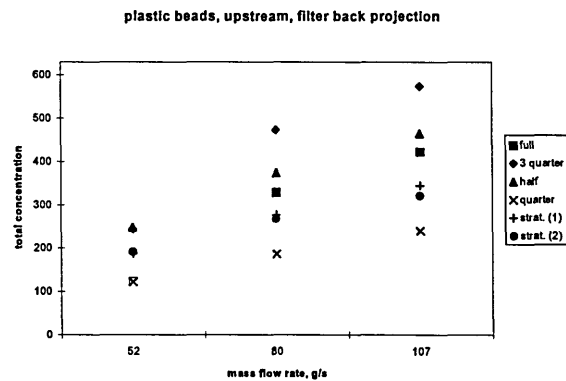
Figure 7.31. Upstream plastic beads flow (filtered back projection)
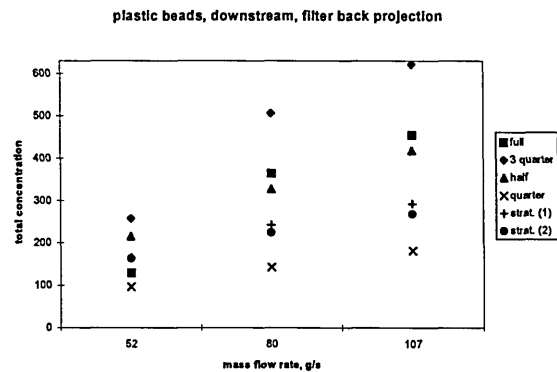
Figure 7.32. Downstream plastic beads flow (filtered back projection)

133

Results in figure 7.29, 7.30, 7.31 and 7.32 tend to show an increased concentration at a specified mass flow rate as the flow section is reduced from full flow. This may be due to the baffle modifying the amount of charge carried by the plastic bead when interaction occurs (section 9.3). Anomalies in the increased concentration with mass flow rate may be due to day to day variations in physical conditions such as temperature and humidity in the laboratory.

7.3 Three dimension concentration profile

An alternative way of presenting the results shown in sections 7.2 and 7.3 is as a three dimensional diagram by presenting the voltage as a vertical scale superimposed on a plan of the pipe cross section. Section 7.3.1 shows the isometric representation for sand flow for each flow regime with different flow rates. Section 7.3.2 shows the isometric representation for plastic bead flow for each flow regime with different flow rates. Both sections are presented using linear and filtered back projection.

7.3.1 Sand flow

Figures 7.33 (a) and (b) show the isometric representation for full sand flow at 210 g/s. Figures 7.34 (a) and (b) show the isometric representation when a quarter baffle was inserted inside the pipe to create a three quarter sand flow. There is little effect from the baffle at three quarter flow (figure 7.34 (a) and (b)) and the picture is similar to full flow (figure 7.33 (a) and (b)). At half and quarter flow the baffle becomes more effective (figures 7.35 (a) and (b), figures 7.36 (a) and (b)). At stratified flow the baffle effect the sand flow by dividing it into two section flow (figures 7.37(a) and (b), figures 7.38(a) and (b)).
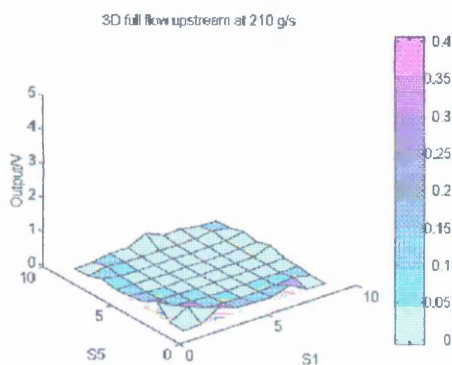
Figure 7.33(a). Full sand flow at 210 g/s (linear back projection)   **Figure 7.33(b). Full sand flow at 210 g/s (filtered back projection)**
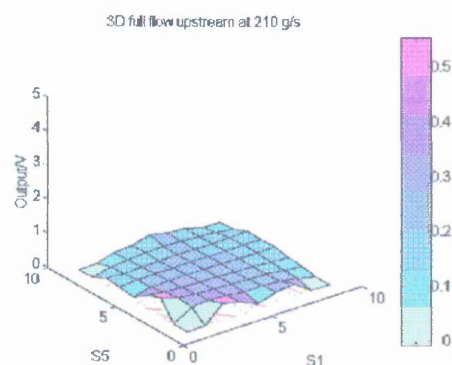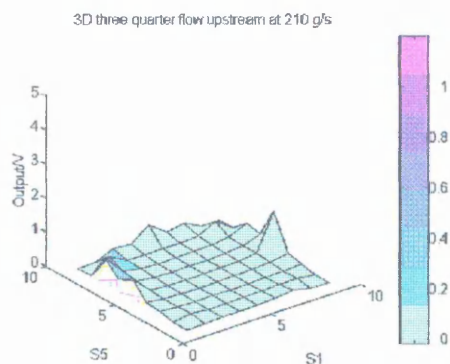
Figure 7.34(a). Three quarter sand flow at 210 g/s (linear back projection)
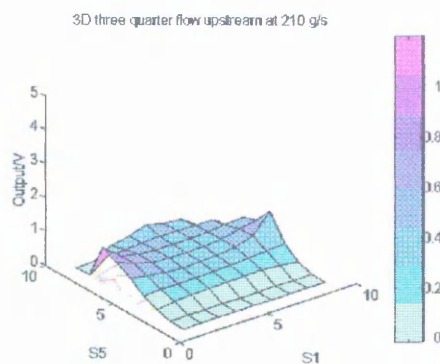
Figure 7.34(b). Three quarter sand flow at 210 g/s (filtered back projection)
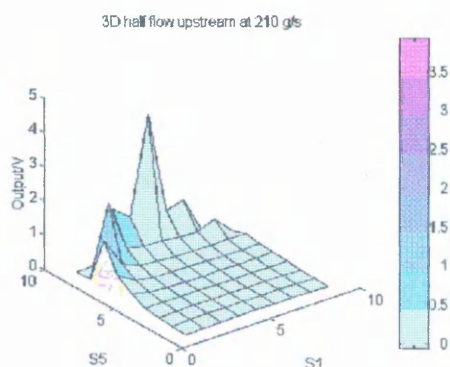
Figure 7.35(a). Half sand flow at 210 g/s (linear back projection)
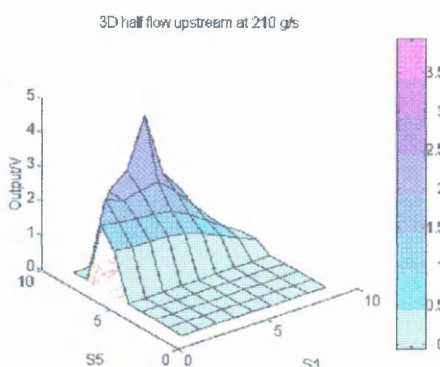
Figure 7.35(b). Half sand flow at 210 g/s (filtered back projection)
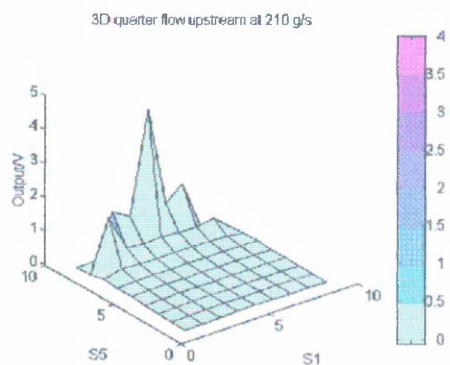
Figure 7.36(a). Quarter sand flow at 210 g/s (linear back projection)
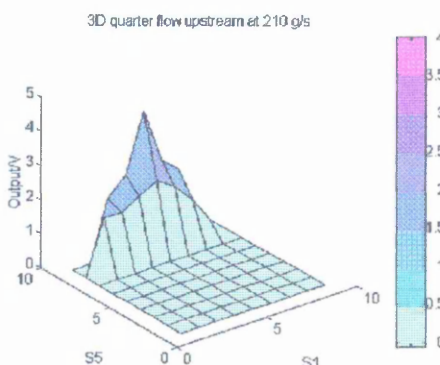
Figure 7.36(b). Quarter sand flow at 210 g/s (filtered back projection)
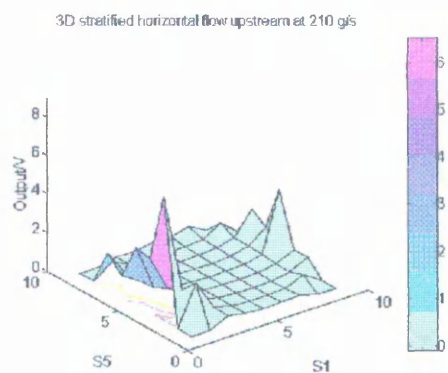
Figure 7.37(a). Stratified (1) sand flow at 210 g/s (linear back projection)
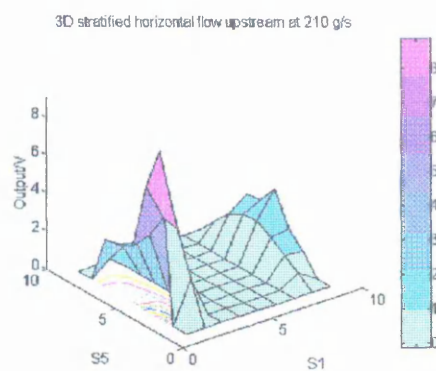
Figure 7.37(b). Stratified (1) sand flow 210 g/s (filtered back projection)
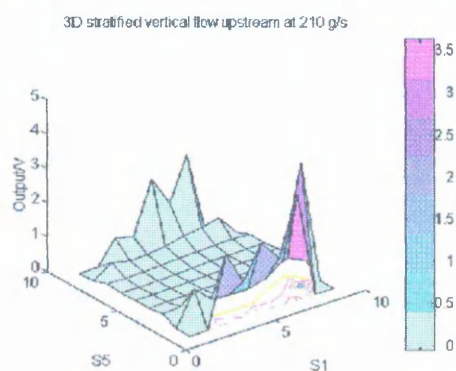
Figure 7.38(a). Stratified (2) sand flow at 210 g/s (linear back projection)
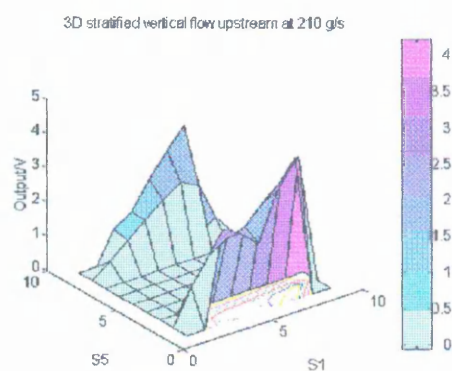
Figure 7.38(b). Stratified (2) sand flow at 210 g/s (filtered back projection)

137

7.3.2 Plastic beads flow

Figures 7.39 (a) and (b) show the isometric representation for full plastic beads flow at 107 g/s. Figures 7.40 (a) and (b) show the isometric representation when a quarter baffle was inserted inside the pipe to create a three quarter plastic bead flow. At half and quarter flow the baffle becomes more effective (figures 7.41 (a) and (b), figures 7.42 (a) and (b)). At stratified flow the baffle divide the flow into two section (figures 7.43 (a) and (b), figures 7.44 (a) and (b)).
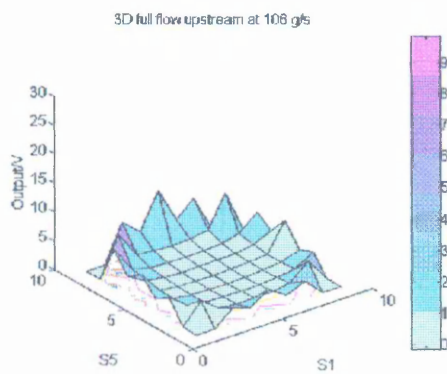
Figure 7.39(a). Full flow at 107 g/s (linear back projection)
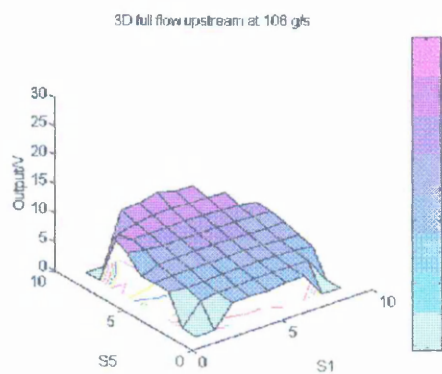
Figure 7.39(b). Full flow at 107 g/s (filtered back projection)
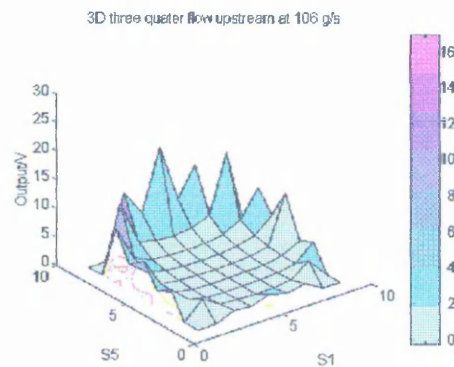
Figure 7.40(a). Three quarter flow at 107 g/s (linear back projection)
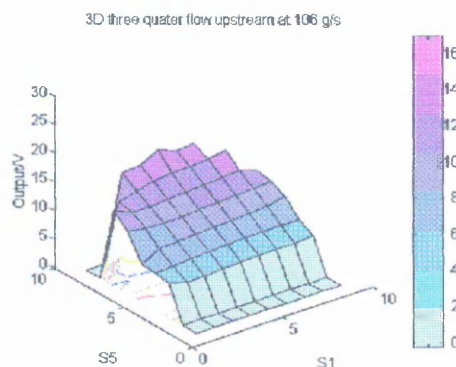
Figure 7.40(b). Three quarter flow at 107 g/s (filtered back projection)
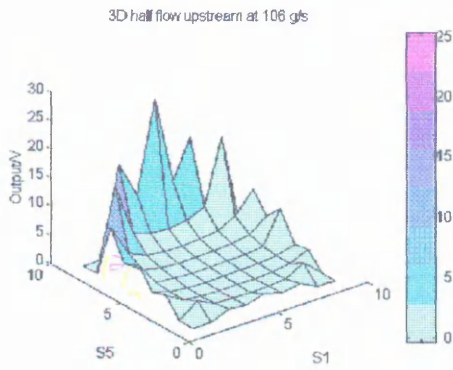
Figure 7.41(a). Half flow at 107 g/s (linear back projection)
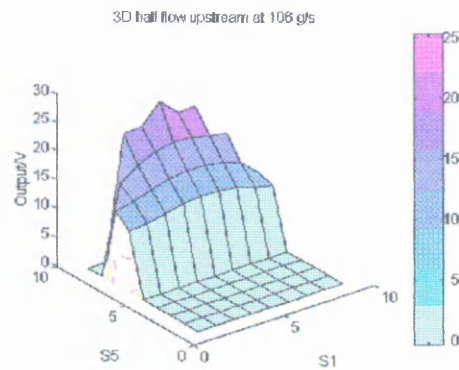
Figure 7.41(b). Half flow at 107 g/s (filtered back projection)
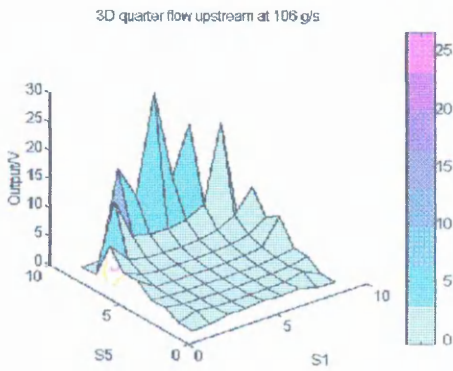
Figure 7.42(a). Quarter flow at 107 g/s (linear back projection)
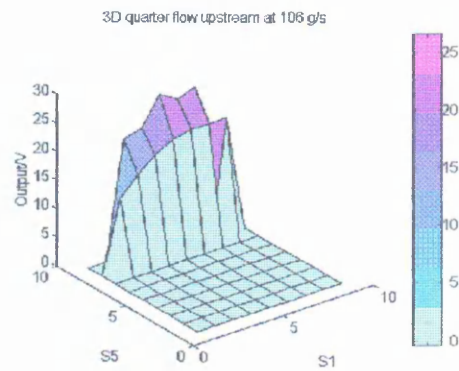
Figure 7.42(b). Quarter flow at 107 g/s (filtered back projection)
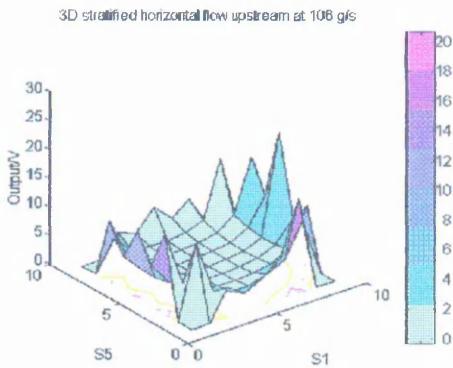
Figure 7.43(a). Stratified (1) flow at 107 g/s (linear back projection)
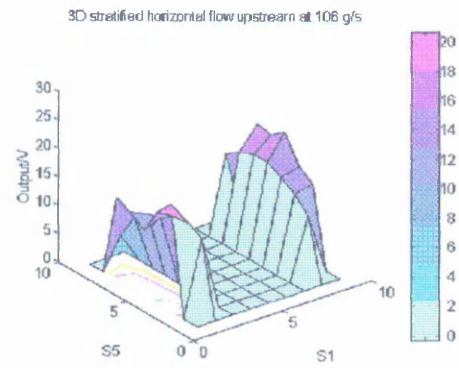
Figure 7.43(b). Stratified (1) flow at 107 g/s (filtered back projection)
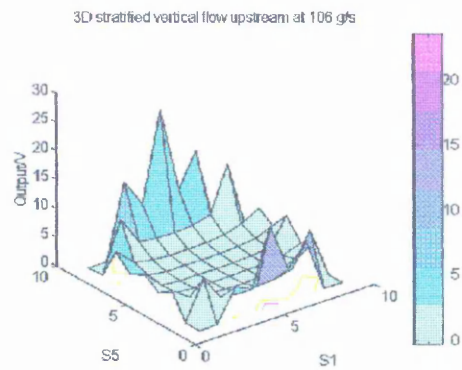
Figure 7.44(a). Stratified (2) flow at 107 g/s (linear back projection)
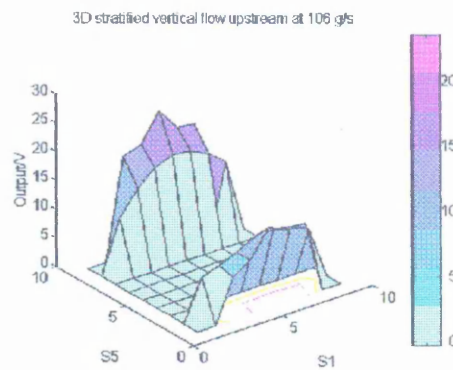
Figure 7.44(b). Stratified (2) flow at 107 g/s (filtered back projection)

7.3.3 Discussion on three dimensional tomograms

Three dimensional tomograms for sand in section 7.3.1 and plastic beads in section 7.3.2 are useful aids to visualising the distribution of the flowing solids within the measurement cross section. The filter appears to smooth the diagrams and produce the types of result which are expected.

140

7.4 Velocity profiles

In this section, grey level cross correlation, uniform and non uniform velocity will be discussed.

7.4.1 Grey level(pixel) cross correlation

The dynamic outputs from the sensors may be sampled sequentially as described for the averaged sensor outputs described in section 6. The dynamic sensor outputs are sampled at a nominal 1 kHz per channel, with a corresponding data capture rate of 32 kHz. Each thirty two readings (obtained in 1 ms) are used to calculate a concentration tomogram as described in section 7.1 using the unfiltered back projection algorithm. This results in 312 tomograms for each test, which are identified as Tu_i and Td_i where Tu and Td are the upstream and downstream tomograms respectively and i refers to the number of the tomogram in the series ($1 \leq i \leq 312$). For any specified tomogram the individual pixels are described by P_{ij} (section 3.4.1) where i is the column and j is the row number respectively. Consider a specific pixel P_{ij}, in all the tomograms in the measurement set. Then P_{ij} has 312 numerical values associated with it, and consecuting values occur every 1 ms. Thus P_{ij} can be represented as a time series of 312 values. This process is repeated for the upstream and downstream tomograms resulting in sixty nine upstream and sixty nine downstream time series. Each value in these series can be represented as a grey level, but the time series can also be used for cross correlation. By cross correlating (section 3.3.3.2) the upstream P_{ij} time series with the downstream P_{ij} time series the peak position of the correlation provides the time taken for the upstream solids concentration to arrive at the downstream measurement cross section. This has been termed grey level or pixel cross correlation in this thesis. Figure 7.45 show the position of pixel relative to the sensors.

141
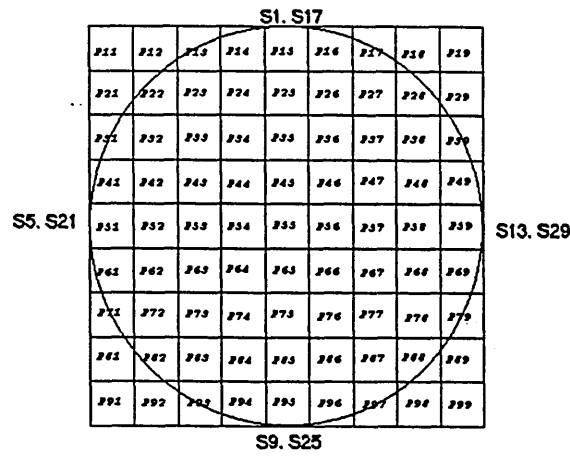
Figure 7.45. The position of pixels in profile relative to sensors

Before generating velocity profiles from all the measured results a short study is presented of how the correlation coefficient varies with pixel position in the cross section.

7.4.1.1 Sand flow

Data for sand are sampled at 3 kHz per sensor (sampling time = 0.33 ms). Pixels 51, 53 and 55 are considered for grey level cross correlation. Figure 7.46 shows the grey level time series for both upstream and downstream of pixel 51. Figure 7.47 shows the results obtained by cross correlating the time series shown in figure 7.46. The peak value of the correlogram is 27.5 and occurs at a parametric time shift of 32 units (each unit represents 0.33 ms) corresponding to a transit time of 10.56 ms and velocity of 4.74 m/s.
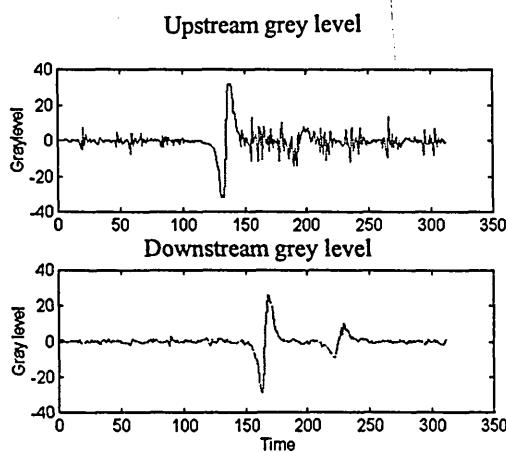
Figure 7.46. Grey level for pixel 51
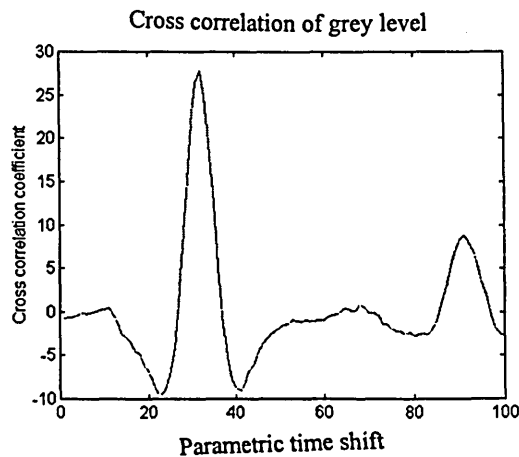
Figure 7.47. Grey level cross correlation for pixel 51

142

Figure 7.48 shows the grey level time series for both upstream and downstream pixel 53. The variation in amplitude of the grey level is smaller compared with the results shown in figure 7.46. From figure 7.49, the peak amplitude of the correlogram is 0.031 and occurs at a parametric time shift of 32 units corresponding to a transit time of 10.56 ms and a velocity of 4.74 m/s.
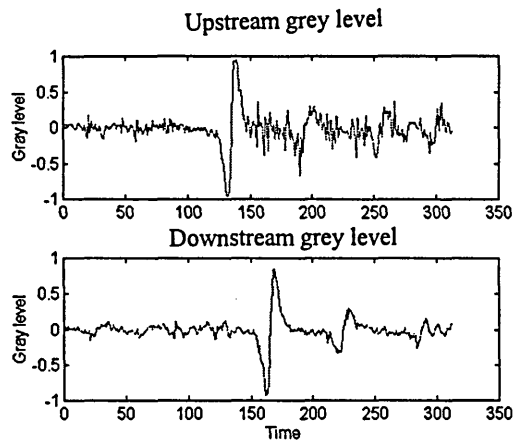
Figure 7.48. Grey level for pixel 53
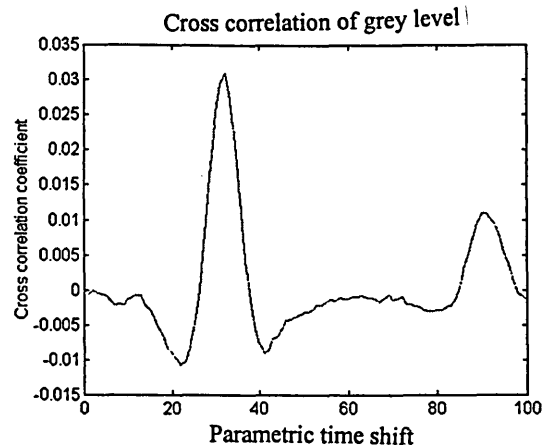
Figure 7.49. Grey level cross correlation for pixel 53

The grey level time series for pixel 55 is shown in figure 7.50. From figure 7.51, the peak amplitude of the correlogram is 0.0058 and occurs at a parametric time shift of 32 units corresponding to a transit time is 10.56 ms and a velocity of 4.74 m/s.
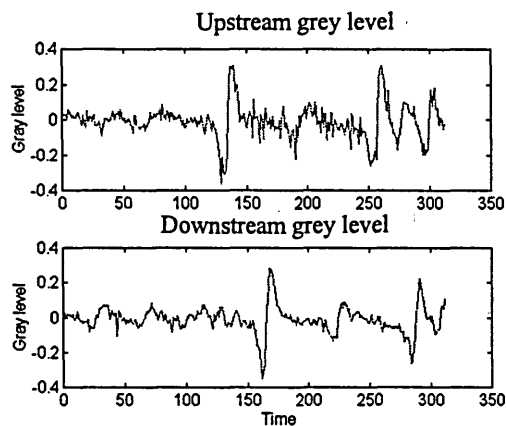
Figure 7.50. Grey level for pixel 55
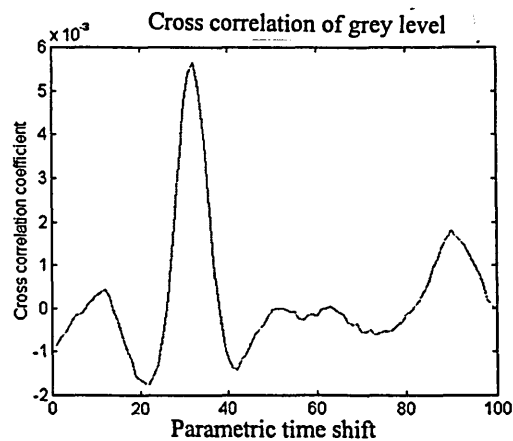
Figure 7.51. Grey level cross correlation for pixel 55

These three measurements using sand show the peak amplitude of the correlogram reduces as the pixels being correlated move towards the centre pixel (i.e. the pipe central axis). However, in all the cases considered, the correlogram peak is well defined.

7.4.1.2 Plastic beads flow

A similar investigation to that presented in section 7.5.2 was carried out using the plastic beads. In this test the data for plastic beads is sampled at 2 kHz and the sampling time is 0.5 ms. Pixels 51, 53 and 55 are considered for grey level cross correlation in this test using plastic beads as a conveyed material. Figure 7.52 shows the upstream and downstream grey level time histories for pixel 51. From figure 7.53, the maximum cross correlation coefficient is 38.44 and occurs at a parametric time shift value of 23 corresponding to a transit time of 11.5 ms and a velocity of 4.35 m/s.
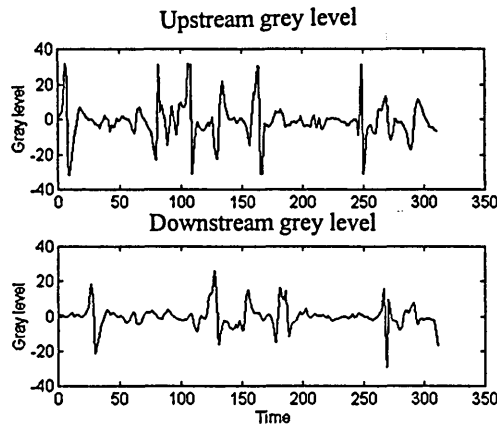
Figure 7.52. Grey level for pixel 51
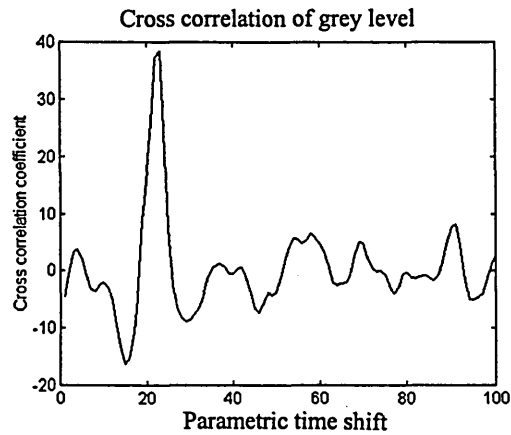
Figure 7.53. Grey level cross correlation for pixel 51

The grey level time series for both upstream and downstream pixel 53 is shown in figure 7.54. From figure 7.55, the maximum cross correlation coefficient is 1.52 and occurs at a parametric time shift of 23 units corresponding to a transit time of 11.5 ms and a velocity of 4.35 m/s.
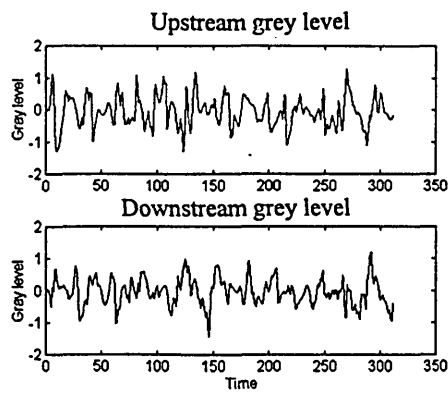
Figure 7.54. Grey level for pixel 53
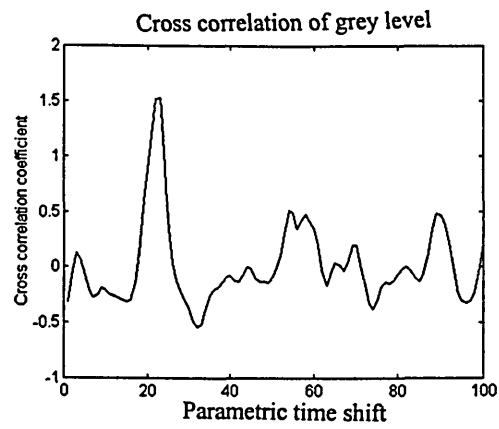
Figure 7.55. Grey level cross correlation for pixel 53

The grey level time history for upstream and downstream pixel 55 is shown in figure 7.56. From figure 7.57, the maximum cross correlation coefficient is 0.65 and occurs at a parametric time shift of 23 units corresponding to a transit time is 11.5 ms and a velocity of 4.35 m/s.
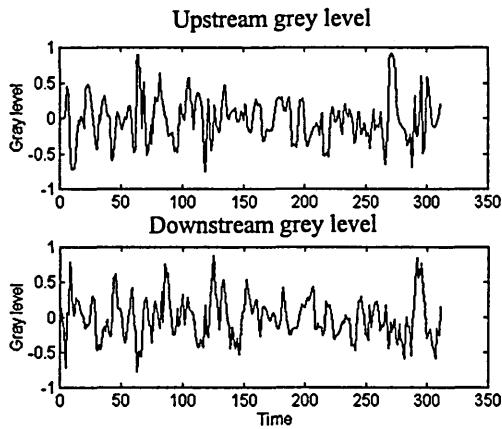
Figure 7.56. Grey level for pixel 55
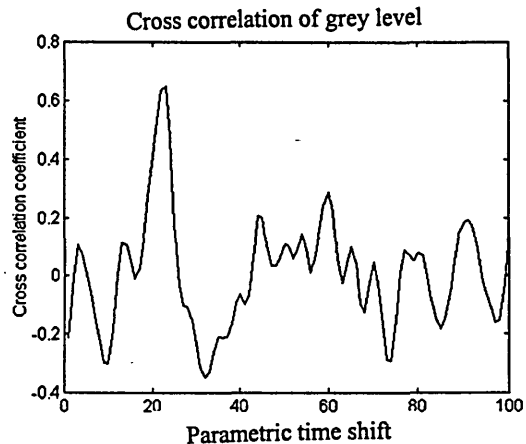
Figure 7.57. Grey level cross correlation for pixel 55

These three measurements using plastic beads show the peak amplitude of the correlogram reduces as the pixels being correlated more towards the centre pixel (i.e. the pipe central axis). However, in all the cases considered, the correlogram peak is well defined.

145

7.4.2 Uniform velocity

Uniform velocity profiles are derived from experimental data. Different sampling times are investigated. Figures 7.58 (a) and (b) show the velocity profile for sand flowing at 324 g/s expressed as a matrix of numerical values and as a three dimensional display. These results were obtained using data sampled at 3 kHz (sampling time = 0.33 ms).

0	0	5.22	5.05	4.89	4.74	4.74	0	0
0	4.89	5.05	4.89	4.89	4.74	4.74	4.74	0
4.89	4.89	4.89	4.89	4.74	4.74	4.74	4.74	4.59
4.74	4.74	4.74	4.74	4.74	4.74	4.74	4.74	4.58
4.74	4.74	4.74	4.74	4.74	4.74	4.74	4.74	4.21
4.74	4.74	4.74	4.74	4.74	4.74	4.74	4.21	4.21
4.74	4.74	4.74	4.74	4.74	4.74	4.46	4.21	4.21
0	4.89	4.89	4.89	4.89	4.89	4.89	4.89	0
0	0	4.89	4.89	4.89	4.89	4.89	0	0

Figure 7.58(a). Numerical velocity profile for sand flow at 324 g/s.
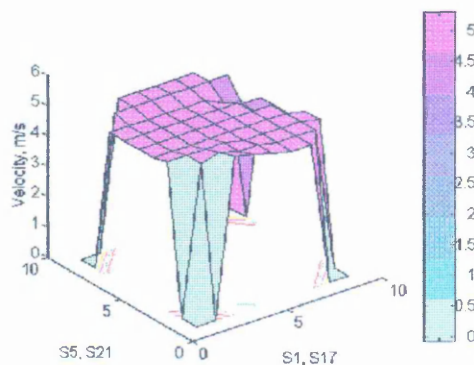
Figure 7.58(b). 3D velocity profile for sand flow at 324 g/s.

Figures 7.59 (a) and (b) show the velocity profile for plastic beads flowing at a rate of 52 g/s. The results were calculated from data sampled at 2 kHz (sampling time = 0.5 ms).

0	0	4.35	4.35	4.35	4.55	4.55	0	0
0	4.35	4.35	4.35	4.55	4.55	4.35	4.35	0
4.35	4.35	4.35	4.35	4.55	4.35	4.35	4.35	4.35
4.35	4.35	4.55	4.55	4.35	4.35	4.35	4.35	4.36
4.35	4.35	4.55	4.55	4.35	4.35	4.35	4.17	4.17
4.35	4.35	4.55	4.55	4.35	4.35	4.35	4.35	4.35
4.35	4.55	4.55	4.55	4.35	4.35	4.35	4.35	4.35
0	4.76	4.55	4.35	4.35	4.35	4.35	4.35	0
0	0	4.35	4.35	4.35	4.35	4.35	0	0

Figure 7.59(a). Numerical velocity profile for plastic beads at 52 g/s.
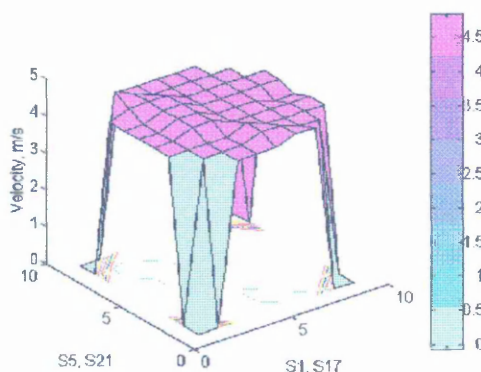
Figure 7.59(b). 3D velocity profile for plastic beads at 52 g/s.

146

Figures 7.60 (a) and (b) show the velocity profile for plastic beads flowing at a rate of 52 g/s with data sampled at 3 kHz (sampling time = 0.33 ms).

0	0	4.89	4.73	4.59	4.59	4.59	0	0
0	4.89	4.89	4.73	4.59	4.59	4.59	4.59	0
4.73	4.89	4.73	4.73	4.59	4.59	4.59	4.59	4.59
4.59	4.59	4.59	4.59	4.59	4.59	4.59	4.59	4.59
4.59	4.59	4.59	4.59	4.46	4.59	4.59	4.46	4.46
4.46	4.46	4.46	4.46	4.46	4.46	4.46	4.46	4.46
4.46	4.46	4.46	4.33	4.46	4.46	4.46	4.46	4.46
0	4.46	4.33	4.33	4.33	4.46	4.46	4.33	0
0	0	4.33	4.33	4.33	4.46	4.46	0	0
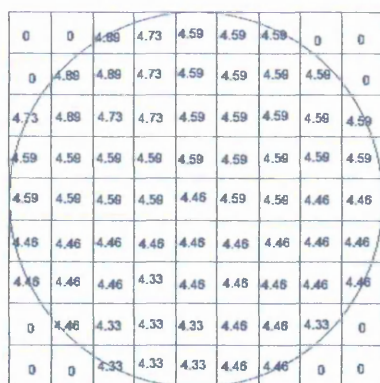
Figure 7.60(a). Numerical velocity profile for plastic beads at 52 g/s
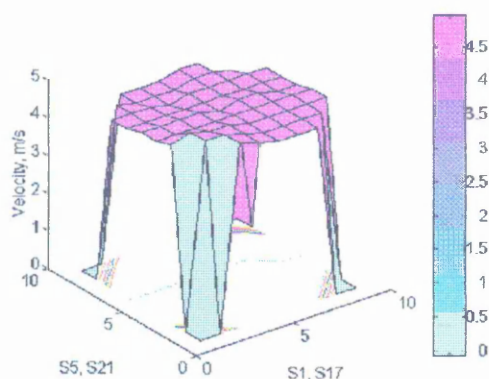
Figure 7.60(b). 3D velocity profile for plastic beads at 52 g/s.

Figures 7.61 (a) and (b) show the velocity profile for plastic beads flowing at rate of 52 g/s. The measured data was sampled at 5 kHz (sampling time is 0.2 ms).

0	0	4.55	4.55	4.31	4.24	4.24	0	0
0	4.55	4.56	4.46	4.39	4.24	4.10	4.03	0
3.97	4.39	4.46	4.46	4.39	4.39	4.17	4.46	4.46
4.10	4.31	4.39	4.46	4.46	4.46	4.46	4.39	4.46
4.39	4.39	4.46	4.55	4.55	4.55	4.46	4.39	4.31
4.39	4.46	4.55	4.55	4.63	4.72	4.63	4.39	4.31
4.46	4.56	4.55	4.63	4.72	4.72	4.72	4.64	4.31
0	4.55	4.55	4.63	4.63	4.55	4.63	4.63	0
0	0	4.31	4.31	4.39	4.46	4.39	0	0
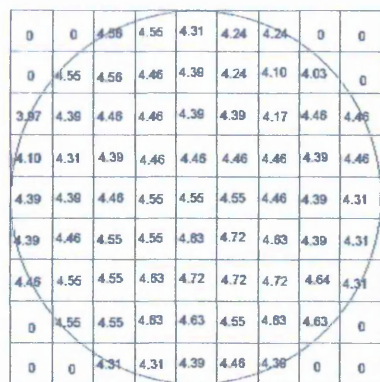
Figure 7.61(a). Numerical velocity profile for plastic beads at 52 g/s
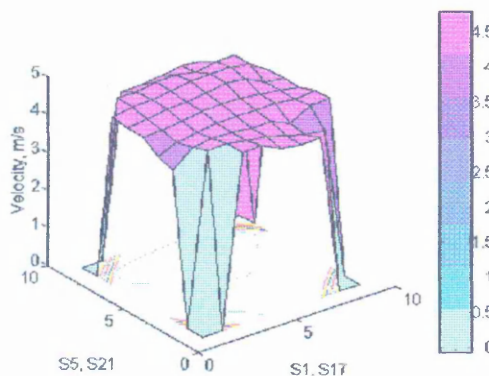
Figure 7.61(b). 3D velocity profile for plastic beads at 52 g/s.

This result of figure 7.58, 7.59, 7.60 and 7.61 are very similar, showing that there is no noticeable improvement in the image by using sampling frequencies in excess of 2 kHz for the velocities which arise with this gravity flow system.

7.4.3 Non-uniform velocity

The results presented in section 7.4.2 present a reasonably uniform velocity profile over the measurement cross section. This result is expected with this type of conveying where all the particles are being accelerated by gravity and, neglecting particle/particle and particle/wall collisions, have a similar acceleration distance (1.4 m). This section presents results where the uniform flow is disturbed by injection a flow of air from a source at approximately 7 Bar. The aim is investigate if the reconstruction and cross correlation algorithms generate tomograms for non uniform flows. Air at a pressure of 7 Bar was injected inside the pipe and the position of the air nozzle varied from 10 to 50 cm above the upstream sensor plane. The screw feeder was set to provide a flow rate of 52 g/s of plastic beads. All data are sampled at 3 kHz (sampling time = 0.33 ms). Figures 7.62 (a) and (b) show the velocity profile when the air nozzle is 10 cm above the upstream sensors.

		1.54	1.35	0.57	4.33	1.28			
	1.25	4.33	4.46	4.46	4.33	0.9	2.91		
5	4.46	4.46	4.46	4.46	4.33	0.9	1.11	1.11	
4.89	4.89	1.92	4.46	4.46	4.46	1.13	1.11	1.11	
4.89	4.89	4.73	4.59	4.46	1.14	1.14	1.47	1.46	
1.89	1.89	4.59	4.46	4.46	4.46	0.68	0.68	0.68	
1.89	4.33	4.33	4.46	4.46	4.46	1.23	1.23	1.23	
	4.46	4.33	4.33	4.33	4.46	4.33	4.33		
		4.21	4.33	4.33	4.46	1.29			
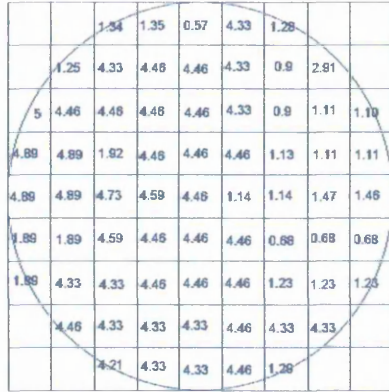
Figure 7.62(a). Numerical velocity profile for plastic beads(10 cm).
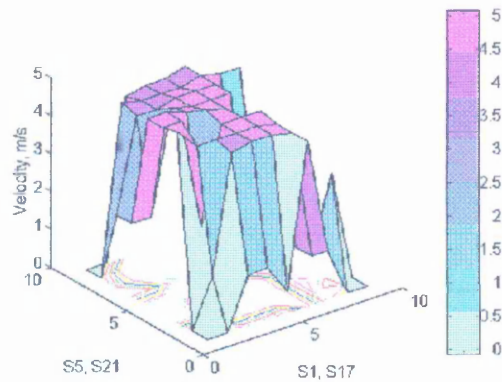
Figure 7.62(b). 3D velocity profile for plastic beads(10 cm).

Figures 7.63 (a) and (b) show the velocity profile when the air nozzle is 40 cm above the

upstream sensors.

0	0	0.65	37.88	4.33	0.53	0.53	0	0
0	4.33	4.33	0.86	0.96	4.73	4.89	4.89	0
4.48	4.33	4.33	1.5	1.5	4.73	4.89	4.89	4.89
4.46	4.33	4.33	4.33	4.46	4.59	4.73	4.73	4.73
1.89	4.09	4.21	4.33	4.46	4.46	4.59	4.59	4.73
4.21	4.21	4.21	4.33	4.46	4.46	4.46	4.46	4.46
4.21	4.21	0.94	0.66	0.66	4.46	4.33	4.46	4.46
0	1.58	1.17	0.66	4.46	0.66	0.66	4.46	0
0	0	1.17	1.17	1.31	0.66	0.66	0	0

Figure 7.63(a). Numerical velocity profile for plastic beads(40 cm).
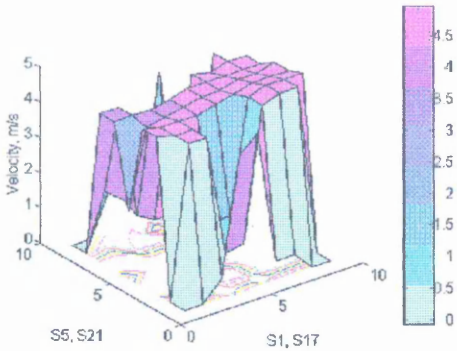
Figure 7.63(b). 3D velocity profile for plastic beads(40 cm).

Figures 7.64 (a) and (b) show the velocity profile when the air nozzle is 50 cm above the

upstream sensors.

0	0	4.89	4.73	0.84	4.73	4.73	0	0
0	1.24	4.89	4.73	4.73	4.73	4.89	4.73	0
3.37	0.51	1.48	4.73	4.73	4.89	4.89	4.73	4.21
3.37	1.53	1.52	4.73	4.73	4.73	4.73	0.73	4.21
4.33	4.46	4.46	4.59	4.59	4.73	4.59	4.59	4.73
4.46	4.46	4.59	4.59	4.59	4.59	4.46	4.21	4.33
4.46	4.59	4.59	0.52	0.52	4.46	4.46	3.99	0.88
0	4.73	4.59	0.52	4.59	4.46	4.46	2.81	0
0	0	3.09	3.03	2.97	4.46	4.46	0	0

Figure 7.64(a). Numerical velocity profile for plastic beads(50 cm).
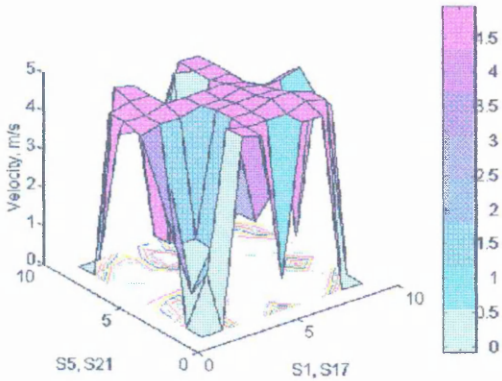
Figure 7.64(b). 3D velocity profile for plastic beads(50 cm).

The result shown in figures 7.62 to 7.64 strongly suggest that non uniform velocity

profile are being generated by injecting air. The cross correlation of upstream and

downstream pixel time histories appears to work satisfactorily, though the effects of

swirl have not been investigated.

CHAPTER 8

Mass flow rate

Chapter summary

Estimates of the mass flow rate are obtained by combining concentration and velocity profiles.

8.1 Introduction

The concentration and velocity profiles are determined in chapter 7. This chapter investigates the possibility of combining these two parameters to provide a measure of the mass flow rate of the solid material. The electrodynamic sensor detects charges on particles. Since the level of charge depends upon many factors (section 4.2) the sensor must be calibrated for specific materials if it to be used to estimate concentration or mass flow rate. In comparison, an optical system measures areas being obscured (Abdul Rahim, 1996) so when combined with velocity it provides a signal which is proportional to mass flow rate. The mass flow rate, MFR, through any pixel, P_{ij}, in the measurement cross section depends on the instantaneous concentration associated with the pixel, C_{ij}, multiplied by the velocity associated with the pixel, V_{ij}. Then the mass flow rate through the measurement section is given by equation 8.1.

$$MFR = k \sum_{i=1, j=1}^{i=n, j=n} C_{ij}.V_{ij}$$ (8.1)

where, MFR is the mass flow rate in g/s, C is the concentration expressed in Volt, V is velocity in m/s, n is the number of pixels in the measurement cross section and k is a

calibration constant in g/V/m. The following sections present results of estimates of mass flow rates through the upstream and downstream measurement sections for a range of mass flow rates of plastic beads for full flow and quarter flow.

8.2 Full flow

The flow of plastic beads was established and the dynamic output signals from all 32 sensors sampled at 1 kHz sampling frequency. This data was then processed to obtain the concentration velocity profiles. The concentration profile was processed using both linear and filtered back projection to investigate the effect of the type of algorithm on measurement accuracy.

8.2.1 Linear back projection

In this section, the mass flow rate of plastic beads is calculated for full flow. As an example the steps in the process are shown for a flow rate of 130 g/s. Figures 8.1 (a) and (b) show the numerical concentration profile for both the upstream and the downstream measurement sections based on the linear back projection algorithm at this flow rate.

0	0	2.65	1.49	2.23	1.52	2.83	0	0
0	5.98	1.55	1.02	0.88	0.99	1.41	4.79	0
4.56	1.96	1.16	0.88	0.81	0.85	1.06	1.69	3.71
3.38	1.70	1.10	0.89	0.83	0.87	1.04	1.54	2.92
10.4	1.81	1.19	0.98	0.91	0.96	1.16	1.77	9.88
1.82	2.23	1.41	1.16	1.09	1.16	1.40	2.32	5.29
8.13	3.15	1.90	1.54	1.44	1.49	1.86	3.28	9.59
0	1.71	3.32	2.60	2.38	2.40	3.02	9.50	0
0	0	9.37	5.76	16.1	4.95	7.12	0	0

Figure 8.1(a). Upstream numerical concentration profile for full plastic beads flow at 130 g/s

0	0	3.34	2.27	6.31	2.51	4.05	0	0
0	6.58	1.72	1.28	1.20	1.27	1.50	3.38	0
5.79	2.10	1.24	0.98	0.89	0.90	1.00	1.43	3.29
3.68	1.79	1.14	0.92	0.84	0.84	0.93	1.27	2.30
9.97	1.83	1.20	0.97	0.88	0.88	1.00	1.37	6.47
1.75	2.26	1.43	1.14	1.03	1.03	1.19	1.78	3.73
8.64	3.36	1.97	1.50	1.33	1.34	1.60	2.60	6.59
0	12.0	3.55	2.49	2.09	2.19	2.78	8.05	0
0	0	9.94	5.42	11.4	4.64	7.81	0	0
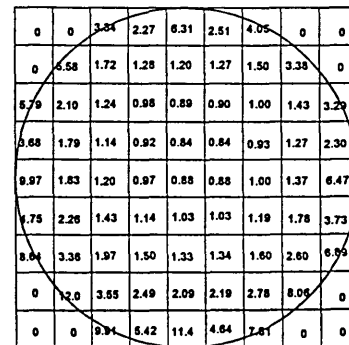
Figure 8.1(b). Downstream numerical concentration profile for full plastic beads flow at 130 g/s

In order to obtain the mass flow rate, the above numerical concentration profiles are

multiplied, pixel by pixel, by the numerical velocity profile at 130 g/s as shown in

figure 8.2.
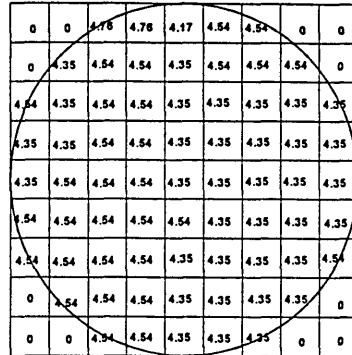
Figure 8.2. Numerical velocity profile for plastic beads at 130 g/s

The results of the multiplication, shown in figures 8.3 (a) and (b), provide a numerical

estimate of the relative mass flow rate through each pixel before the final scaling factor

(based on k in equation 8.1) is applied.
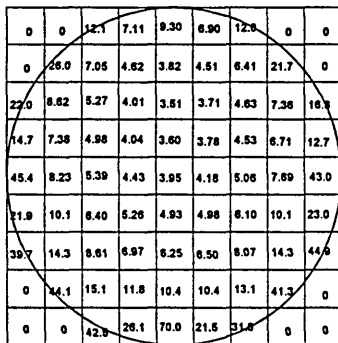
**Figure 8.3(a). Upstream numerical
mass flow rate profile for full plastic
beads flow at 130 g/s before scaling**

**Figure 8.3(b). Downstream numerical
mass flow rate profile for full plastic
beads flow at 130 g/s before scaling**

Two separate estimates of the overall mass flow rate are obtained by summing all the

pixel values in figures 8.3 (a) and (b) to provide unscaled estimates of the mass flow

rate values. The estimate of the upstream unscaled mass flow rate for plastic beads with

uniform flow at a solids loading of 130 g/s is 966 units and the downstream unscaled

mass flow rate for plastic beads 934 units. This calculation of mass flow rate is repeated

for several values of solid flow rate and the results plotted in figure 8.4. Regression

lines have been fitted to both the upstream and downstream estimates of mass flow rate

data.

Figure 8.4. Summation of pixel values in mass flow rate profile versus flow rate for plastic beads full flow (linear back projection)

The gradient of both the upstream and the downstream equations are 5.8 g/V/m. This

gradient represents an estimate of the constant k in equation (8.1) based on the linear

back projection algorithm. The correlation coefficient value for the upstream regression

line is 0.94 and the corresponding downstream value is 0.96.

The results shown in figure 8.4 should be stated as gram per second rather than pixel

values. The conversion is based on equation 8.1, where the value of k is estimated at

5.8 g/V/m (the gradient of figure 8.4). Ideally, the regression lines shown in figure 8.4

should pass through the origin for zero mass flow rate. However, noise and offset in the

measurement system produce non zero values (upstream = 291, downstream 163,

average = 227) of tomographic estimates of the mass flow rate (TEMFR) values at zero

mass flow rate. The experimentally determined values of TEMFR have been scaled using :-

(TEMFR - zero reading offset value) / gradient

The upstream points are shown as squares, the downstream as diamonds in figure 8.5.

Figure 8.5. Tomographic estimation of mass flow rate versus indicated mass flow rate

8.2.2 Filtered back projection

The calculation of mass flow rate presented in section 8.2.1 is repeated using the filtered back projection algorithm (section 3.5.2) to determine the concentration profiles. Figures 8.6 (a) and (b) show the numerical concentration profile for the upstream and downstream measurement cross sections based on filtered back projection (section 3.5.2).

0	0	3.47	3.47	2.23	3.53	3.53	0	0
0	5.34	5.35	4.77	4.55	4.65	4.87	5.05	0
6.51	6.83	6.58	6.25	6.08	6.04	6.03	5.83	6.12
7.85	7.94	7.77	7.55	7.41	7.37	7.37	7.22	6.77
10.4	9.38	8.96	8.73	8.62	8.62	8.77	9.15	9.89
11.2	10.4	9.99	9.82	9.73	9.71	9.94	10.9	12.3
11.3	10.8	10.7	10.9	10.8	10.6	10.5	11.3	14.2
0	10.3	11.5	12.2	12.3	11.2	10.4	10.1	0
0	0	12.9	13.4	16.1	11.5	9.70	0	0

Figure 8.6(a). Upstream numerical concentration profile for full plastic beads flow at 130 g/s

0	0	4.55	5.27	6.32	5.82	5.53	0	0
0	5.92	5.92	6.01	6.22	5.93	5.16	3.59	0
7.19	7.25	7.02	6.91	6.74	6.37	5.69	4.92	4.47
8.55	8.37	8.08	7.80	7.49	7.08	6.57	5.95	5.34
9.98	9.48	9.09	8.71	8.32	7.92	7.51	7.11	6.47
11.0	10.6	10.1	9.65	9.19	8.76	8.41	8.35	8.67
11.8	11.6	11.2	10.6	10.0	9.52	9.06	8.94	9.97
0	12.7	12.2	11.6	10.8	10.2	9.59	8.54	0
0	0	13.4	12.6	11.4	10.8	10.4	0	0

Figure 8.6(b). Downstream numerical concentration profile for full plastic beads flow at 130 g/s

The mass flow rates are obtained by multiplying the numerical concentration profiles in figures 8.6 (a) and (b) by the numerical velocity profile (figure 8.2) pixel by pixel. Two numerical estimates of the relative mass flow rate through each pixel, before the final scaling factor (k in equation 8.1) is applied, are shown in figure 8.7.

0	0	14.5	16.5	9.31	16.0	16.7	0	0
0	27.6	24.3	21.6	19.8	21.1	22.1	23.1	0
30.1	29.7	29.9	28.4	26.5	26.3	26.2	25.4	22.5
34.1	34.5	35.3	34.3	32.2	32.1	32.1	31.4	29.4
45.4	42.6	40.7	39.7	37.5	37.5	38.2	39.8	43.0
50.8	47.4	45.3	44.6	44.2	42.3	43.3	47.2	53.4
54.0	49.2	48.8	49.4	47.2	46.0	45.7	49.1	64.5
0	48.7	52.0	55.2	53.7	48.8	45.3	43.6	0
0	0	57.9	60.7	70.1	50.0	42.2	0	0

Figure 8.7 (a). Upstream numerical mass flow rate for full plastic beads flow at 130 g/s before scaling

0	0	21.7	25.1	26.3	26.4	25.1	0	0
0	25.7	26.9	27.3	27.1	26.9	23.4	16.3	0
35.8	31.5	31.9	31.4	29.3	27.7	24.8	21.4	19.5
37.2	36.4	36.7	35.4	32.6	30.8	28.6	25.9	23.2
43.4	43.0	41.3	39.6	36.2	34.4	32.7	30.9	28.1
50.0	48.0	45.9	43.8	41.7	38.1	36.6	36.3	37.7
53.4	52.6	50.6	48.2	43.6	41.4	39.4	38.9	44.8
0	57.7	55.5	52.9	47.1	44.6	41.7	37.7	0
0	0	61.4	57.1	49.8	46.9	45.3	0	0

Figure 8.7(b). Downstream numerical mass flow rate for full plastic beads flow at 130 g/s before scaling

The separate estimates of the overall mass flow rates are achieved by summing all the pixel values in figures 8.7 (a) and (b) to provide unscaled estimates of the mass flow rate values. The estimate of the upstream unscaled mass flow rate for plastic beads with uniform flow at a solids loading of 130 g/s is 2637 units and the corresponding downstream estimate is 2557 units. This calculation of unscaled mass flow rate is repeated for several values of solid flow rate and the results are plotted in figure 8.8.

155

Plastic beads (filtered back projection)

Figure 8.8. Summation of pixel values in mass flow rate profile versus flow rate for plastic beads full flow (filtered back projection)

Linear regression lines have been fitted to both sets of data. The gradient of both regression lines is 15.9 g/V/m. The gradient represents an estimate of the constant k in equation (8.1) when using the filtered back projection algorithm. The correlation coefficient values for the upstream regression line is 0.94 and for the downstream is 0.96. The results shown in figure 8.8 should be stated as gram per second rather than pixel values. The conversion is based on equation 8.1, where the value of k is estimated at 15.9 g/V/m (the gradient of figure 8.8). Ideally, the regression lines shown in figure 8.8 should pass through the origin for zero mass flow rate. However, noise and offset in the measurement system produce non zero values (upstream = 797, downstream = 446, average = 621) of TEMFR values at zero mass flow rate. The experimentally determined values of TEMFR have been scaled using :-

(TEMFR - zero reading offset value) / gradient

The result is shown in figure 8.9.

Plastic beads (filtered back projection)

□ upstream
◇ downstream
— ideal
- - ideal+25%
- - ideal-25%
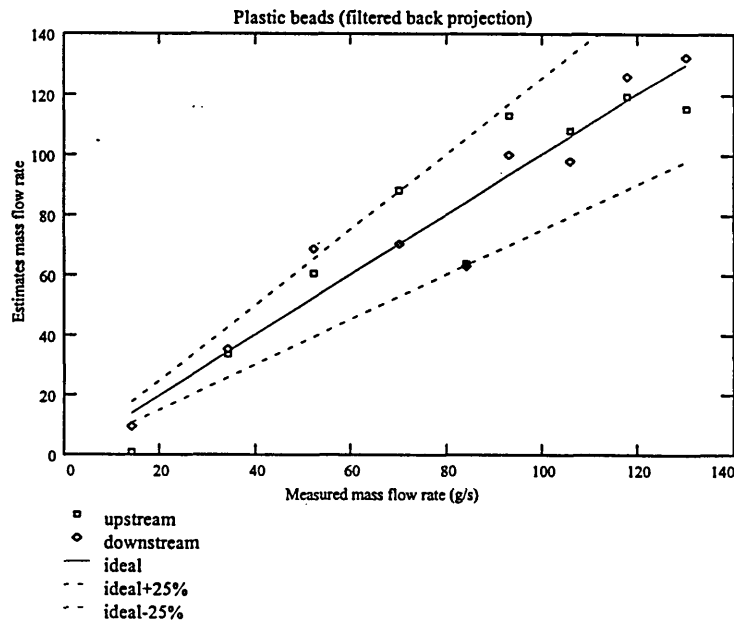
Figure 8.9. Tomographic estimation of mass flow rate versus indicated mass flow rate

8.3 Quarter flow

The experiment described in section 8.2 was repeated with the baffle positioned so that three quarters of the conveyor cross section was blocked off. The purpose of this experiment is to compare the values of estimates of the constant k in equation 8.1 for two types of flow regime i.e. full and quarter. Ideally many different flow regimes should be compared (section 9.3).

8.3.1 Linear back projection

In this section, the mass flow rate of plastic beads is estimated using the linear back projection algorithm for the concentration profiles. Figures 8.10 (a) and (b) show the numerical concentration profiles for both upstream and downstream measurement cross sections based on the linear back projection algorithm.

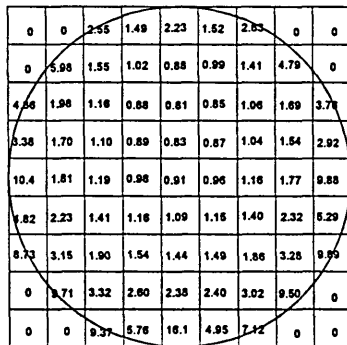| 0	0	0.64	0.78	2.87	1.30	2.10	0	0
0	1.12	0.63	0.60	0.66	0.73	0.84	1.41	0
3.79	1.01	0.65	0.60	0.60	0.62	0.67	0.82	1.31
1.87	1.00	0.74	0.68	0.67	0.69	0.74	0.91	1.34
2.81	1.07	0.90	0.84	0.83	0.86	0.95	1.18	4.68
2.48	1.54	1.24	1.16	1.14	1.19	1.33	1.74	2.93
4.62	2.72	2.01	1.79	1.73	1.82	2.19	3.24	4.86
0	10.9	4.30	3.52	3.23	3.45	4.51	15.0	0
0	0	15.2	8.68	22.1	8.04	13.4	0	0
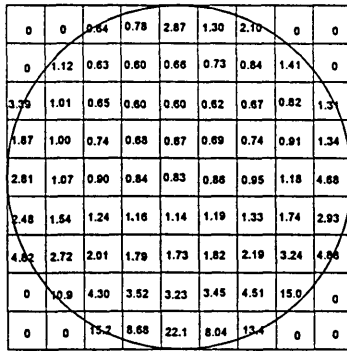
Figure 8.11(a). Upstream numerical concentration profile for quarter plastic beads flow at 107 g/s

0	0	2.21	1.57	4.11	2.15	3.80	0	0
0	3.80	1.22	0.97	0.98	1.16	1.58	4.49	0
3.81	1.36	0.92	0.80	0.80	0.89	1.11	1.79	4.67
2.11	1.19	0.88	0.79	0.80	0.87	1.06	1.58	3.07
6.81	1.28	0.97	0.88	0.88	0.97	1.18	1.73	8.37
3.11	1.66	1.20	1.08	1.08	1.19	1.47	2.32	4.95
6.65	2.57	1.74	1.60	1.48	1.64	2.10	3.56	8.75
0	8.29	3.31	2.64	2.49	2.85	3.87	12.1	0
0	0	10.3	5.99	14.9	6.42	11.4	0	0
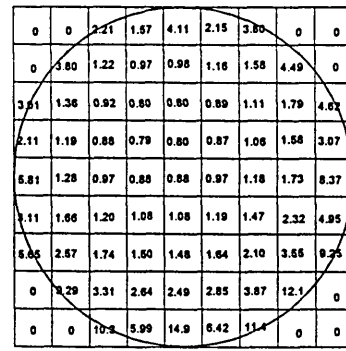
Figure 8.11(b). Downstream numerical concentration profile for quarter plastic beads flow at 107 g/s

The mass flow rates, are estimated by multiplying them by the numerical velocity profile (figure 8.12).

0	0	1.04	4.76	4.35	0.32	0.34	0	0
0	0.35	1.56	7.69	4.35	0.47	0.47	0.50	0
1.69	1.56	1.56	0.64	2.08	2.08	0.42	4.76	0.36
1.59	1.59	1.59	2.08	2.08	2.08	0.42	4.55	0.91
4.35	1.61	0.37	2.04	2.04	2.08	2.08	4.55	0.43
0.71	0.72	0.37	2.04	2.04	2.04	2.08	1.75	4.17
0.71	0.72	2.00	2.04	2.04	2.04	2.04	2.00	0.42
0	0.37	0.60	1.89	2.04	2.08	2.04	1.09	0
0	0	0.80	1.89	1.96	2.13	0.41	0	0
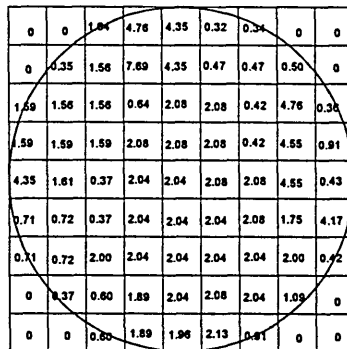
Figure 8.12. Numerical velocity profile for quarter flow plastic beads at 107 g/s

This provides two numerical estimates of the relative mass flow rate, one through the upstream and the other through the downstream measurement section (figures 8.13(a) and (b)) before the final scaling factor (k in equation 8.1) is applied.

Figure 8.13(a)

0	0	1.96	3.69	12.5	41.5	0.71	0	0
0	0.39	0.99	4.65	2.87	0.34	0.39	0.71	0
5.79	1.58	1.02	0.38	1.24	1.29	0.28	3.91	0.47
2.97	1.59	1.17	1.41	1.39	1.43	0.31	4.12	1.22
12.2	1.72	0.33	1.72	1.69	1.79	1.97	5.37	2.01
1.76	1.11	0.46	2.36	2.33	2.43	2.77	3.05	12.2
3.42	1.96	4.01	3.64	3.54	3.72	4.46	6.48	2.05
0	1.05	2.58	6.66	6.58	7.18	9.20	16.3	0
0	0	9.74	16.4	43.4	17.1	122	0	0

Figure 8.13(b)

|								
0	0	1.62	7.45	17.9	0.69	1.29	0	0
0	1.33	1.91	7.49	4.27	0.55	0.74	2.24	0
4.79	2.13	1.43	0.51	1.67	1.85	0.47	8.51	1.65
3.35	1.89	1.39	1.85	1.66	1.82	0.45	7.21	2.79
25.3	2.07	0.36	1.80	1.80	2.02	2.45	7.86	3.60
2.21	1.19	0.44	2.21	2.21	2.43	3.05	4.05	20.7
4.04	1.85	3.47	3.06	3.03	3.34	4.27	7.09	3.96
0	3.44	1.99	5.00	5.07	5.93	7.90	13.2	0
0	0	6.16	11.3	29.2	13.7	10.4	0	0

Figure 8.13(a). Upstream numerical mass flow rate profile for quarter plastic beads flow at 107 g/s before scaling
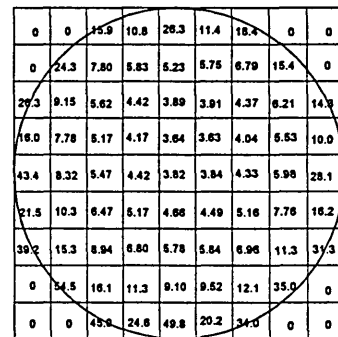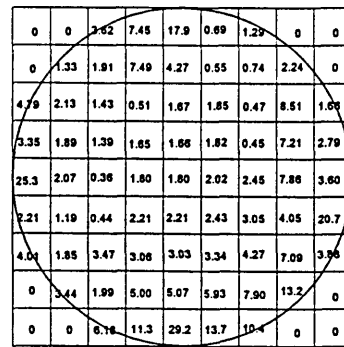
Figure 8.13(b). Downstream numerical mass flow rate profile for quarter plastic beads flow at 107 g/s before scaling

Two separate estimates of the overall mass flow rates are achieved by summing all the pixel values in figures 8.13 (a) and (b) to provide unscaled estimates of the mass flow rate values. The estimate of the upstream unscaled mass flow rate for plastic beads using quarter flow at 107 g/s is 301 units and the corresponding downstream unscaled mass flow rate is 328 units. This calculation of unscaled mass flow rate is repeated for several values of solid flow rate and the results are plotted in figure 8.14.

Plastic beads (linear back projection)

□ actual upstream
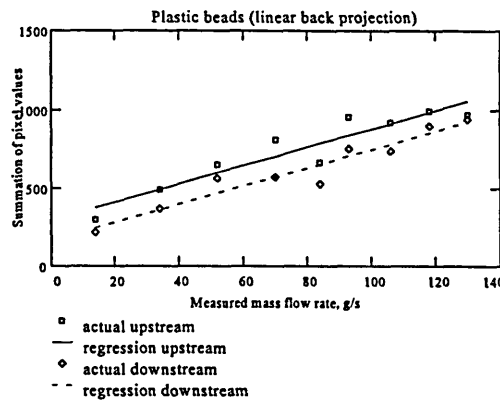— regression upstream
◇ actual downstream
-- regression downstream
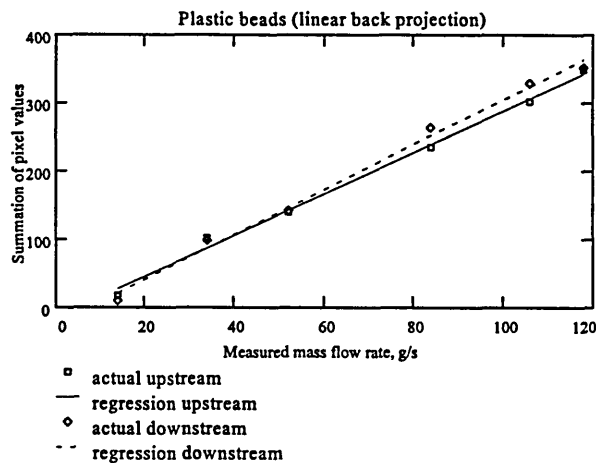
Figure 8.14. Summation of pixel values in mass flow rate profile versus flow rate for plastic beads quarter flow (linear back projection)

Linear regression lines were fitted to both sets of results. The two lines are very similar in gradient and intercept. The gradient for the upstream is 3 g/V/m and the downstream

is 3.3 g/V/m. These slopes represent estimates of the constant k in equation (8.1) for quarter flow. The correlation coefficient value for both the upstream and downstream regressions is 0.99. The results shown in figure 8.14 should be stated as gram per second rather than pixel values. The conversion is based on equation 8.1, where the value of k is estimated using 3.2 g/V/m (the average gradient of figure 8.14). Ideally, the regression lines shown in figure 8.14 should pass through the origin for zero mass flow rate. However, noise and offset in the measurement system produce non zero values of TEMFR values (upstream = -16.5, downstream = -25.5, average = -21) at zero mass flow rate. The experimentally determined values of TEMFR have been scaled using :-

(TEMFR - zero reading offset value) / gradient
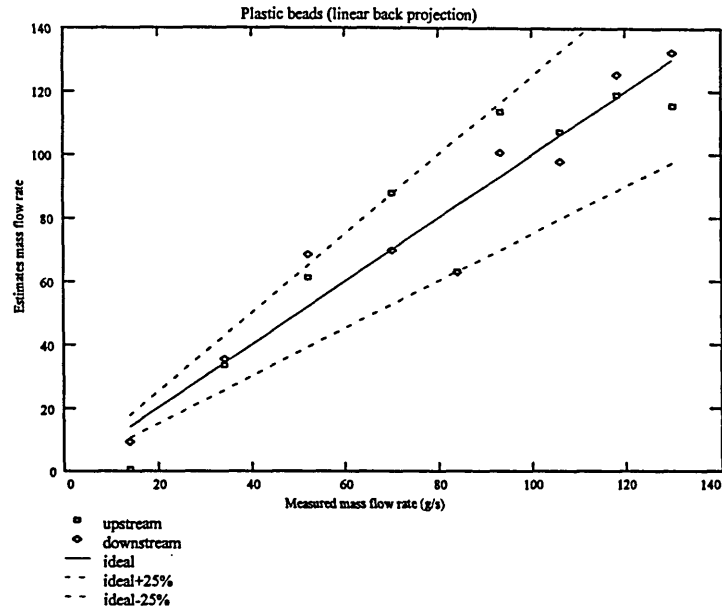
The result is shown figure 8.15.
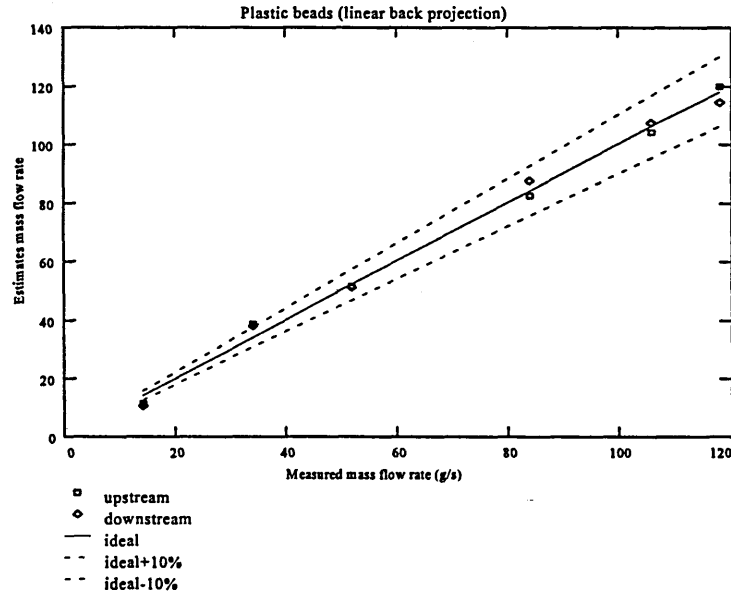
Figure 8.15. Tomographic estimation of mass flow rate versus indicated mass flow rate

160

8.3.2 Filtered back projection

The calculation of mass flow rate presented in section 8.3.1 is repeated using the filtered back projection algorithm to determine the concentration profiles. Figures 8.16 (a) and (b) show the numerical concentration profile for the upstream and downstream measurement cross sections based on the filtered back projection algorithm.
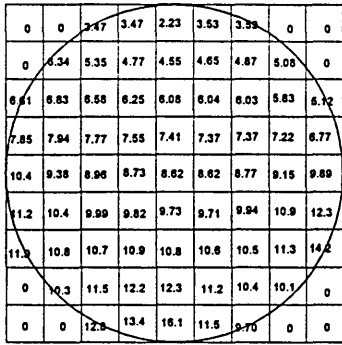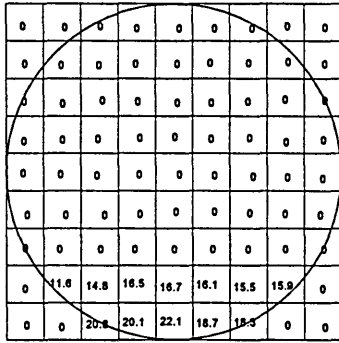

Figure 8.16(a). Upstream numerical concentration profile for quarter plastic beads flow at 107 g/s
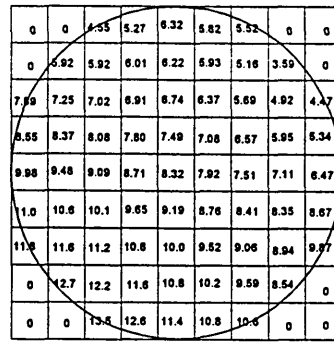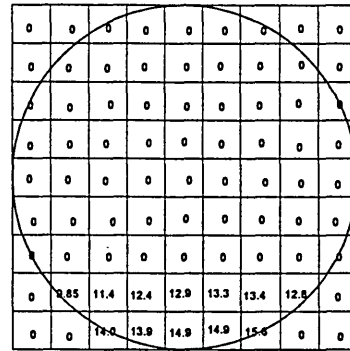

Figure 8.16(b). Downstream numerical concentration profile for quarter plastic beads flow at 107 g/s

The mass flow rates are estimated by multiplying the numerical concentration profiles in figures 8.16 (a) and (b) by the numerical velocity profile (figure 8.12), pixel by pixel. Numerical estimates of relative mass flow rates through the upstream and downstream sensing mass are shown in figures 8.17 (a) and (b) respectively.
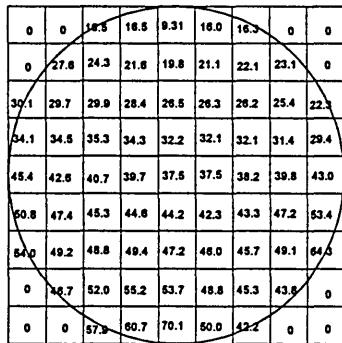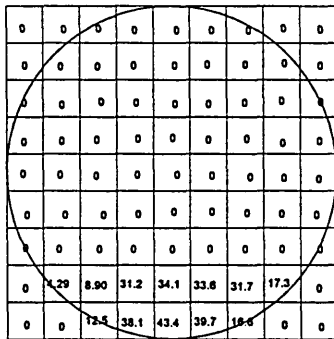

Figure 8.17(a). Upstream numerical mass flow rate for quarter plastic beads flow at 107 g/s before scaling
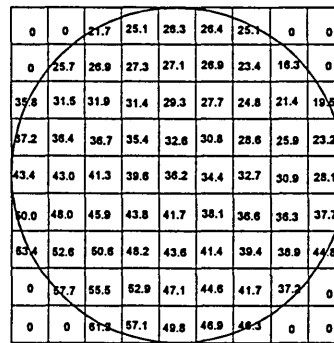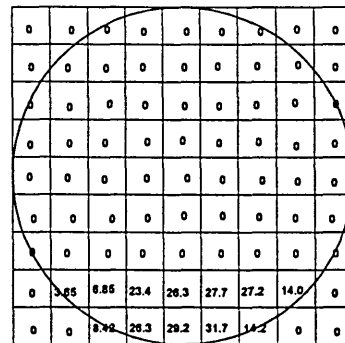

Figure 8.17(b). Downstream numerical mass flow rate for quarter plastic beads flow at 107 g/s before scaling

161

Two separate estimates of overall unscaled mass flow rates are achieved, by summing all the pixel values in figures 8.17 (a) and (b) to provide unscaled estimates of the mass flow rate values. The estimates of the upstream unscaled mass flow rate for plastic beads using a quarter flow at a solids loading of 107 g/s is 311 units and the corresponding downstream unscaled mass flow rate is 239 units. This calculation of mass flow rate is repeated for several values of solid flow rate and the results are plotted in figure 8.18.
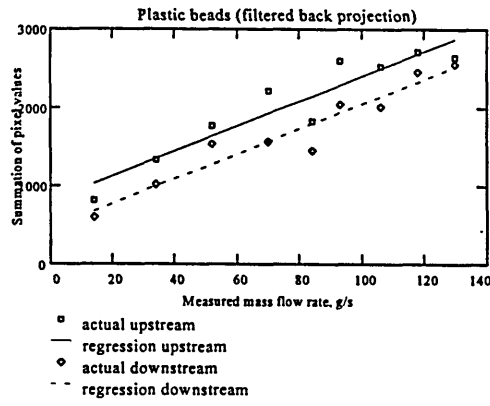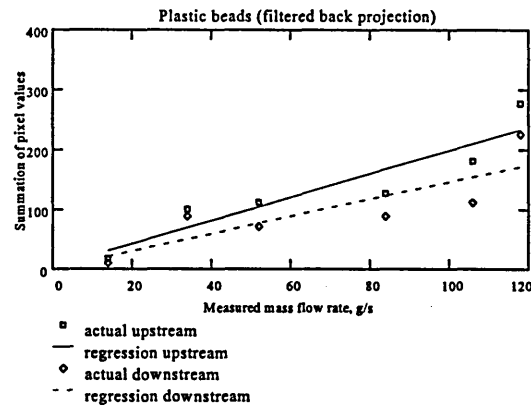

Figure 8.18. Summation of pixel values in mass flow rate profile versus flow rate for plastic beads quarter flow (filtered back projection)

Linear regression lines were fitted to both sets of data. The gradient for the upstream is 1.9 g/V/m and the downstream is 1.4 g/V/m. This gradient represents an estimate of the constant k in equation (8.1) for quarter flow using the filtered back projection algorithm. The correlation coefficient value for the upstream regression line is 0.98 and for the downstream is 0.94. The results shown in figure 8.18 should be stated as gram per second rather than pixel values. The conversion is based on equation 8.1, where the value of k is estimated at 1.7 g/V/m (the gradient of figure 8.18). Ideally, the regression lines shown in figure 8.18 should pass through the origin for zero mass flow rate. However, noise and offset in the measurement system produce non zero values

(upstream = 3.1, downstream = 2.1, average = 2.6) of TEMFR values at zero mass flow

rate. The experimentally determined values of TEMFR have been scaled using :-

(TEMFR - averaged zero reading offset value) / gradient

This is shown figure 8.19.
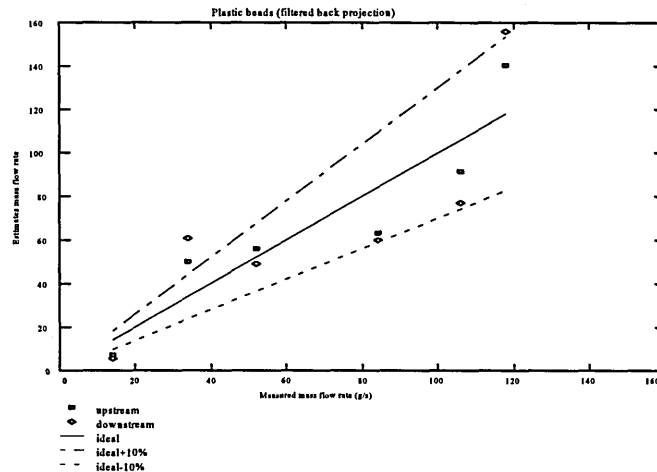
Figure 8.19. Tomographic estimation of mass flow rate versus indicated mass flow rate

8.4 Discussion

The results shown in figures 8.5, 8.9, 8.15 and 8.19 show that estimates of mass flow

rate may be obtained tomographically using the system described in this thesis. For

uniform flow the measured values are within ± 25 % of actual flow rate for both linear

back projection and filtered back projection methods of reconstruction. However for

quarter flow, the measured values are within ± 5 % using the linear back projection

method and ± 10 % using the filtered back projection algorithm. This suggests further

work is required to evaluate the effectiveness of the filter. Further work is needed to

investigate the response of the measurement system to a wide range of flow regimes and

different velocities (section 9.3).

CHAPTER 9

Conclusion and suggestions for future work

9.1 Conclusion

The specific objectives of the thesis have been met as follows

- The review of sensor types suitable for use with pneumatically conveyed solid materials is presented in chapter two (first objective).

- Chapter three presents a model of an electrical charge concentration measurement system (objective two) and introduces the back projection reconstruction algorithm which is tested in chapter seven (objective six).

- An electrodynamic sensor has been designed (chapter four, objective three). An array of electrodynamic sensors (dual 16 channel) has been used for concentration measurement and to measure particle velocity (chapter four, objective four).

- A data capture system to provide data from electrodynamic sensors has been designed (chapter four, objective five).

- Arrays of electrodynamic sensors have been used for concentration measurements (chapter six) to determine concentration profiles (chapter seven, objective six) and for velocity measurements (chapter six) and to determine velocity profiles (chapter seven, objective six).

- Tomographic images of concentration and velocity are presented in chapter seven (objective six). All the concentration and velocity testing made use of the gravity drop conveyor (objective seven).

- Calculation of mass flow rates based on concentration and velocity measurement are presented in chapter eight (objective eight).

- Suggestions for further work are presented in chapter eight (objective nine).

9.2 Contribution to the field of process tomography

The 16 electrodynamic sensor array is capable of making concentration measurements using sand of nominal size range of 600 μm and plastic beads of nominal diameter 3 mm and mass flow rates ranging from 40 g/s to 320 g/s on a gravity drop conveyor. Two arrays, each of 16 electrodynamic sensors, are capable of making velocity measurements using the same material by using cross correlation. Tomograms of the concentration and velocity profile have been determined and mass flow rates of particles have been achieved using concentration and velocity information.

9.3 Suggestions for future work

- If further work is to be carried out using the gravity drop system to artificially produce flow profiles, the baffles must be positioned very near to the screw feeder and their shape should be investigated to maximise the required profile with the least effect of the measured velocity profile.

- The measurement system should be tested on an industrial pneumatic flow rig to determine the concentration and velocity measurement limitations and accuracies. Different sizes and types of particle should be used with the measurement system on

the pneumatic conveyor to investigate the range of materials which is suitable for. There measurements should also be used for an assessment of the effects of particle size.

- Further investigations should be carried out to determine the optimum shape of the electrode which will provide a compromise between concentration (sensitivity, section 3.2.1) and velocity measurement (spatial filtering, section 3.2.2).

- The electronics circuit should be redesigned to optimise the gain, bandwidth and signal to noise ratio using the new, improved operational amplifier integrated circuits (eg. MAX 410 and 412) which have higher bandwidth, lower noise and drift. The circuit layout should be reduced in size and built robustly so that it can be incorporated into the sensing head. A decision on whether to rectify and average in hardware or software should be made. For the mass flow measurements presented in section 8.2 velocity was determined by cross correlation of concentration pixels determined from the rectified outputs, so only a single output from each sensor may be required.

- The present mixture of on line measurement and off line calculation should be replaced by an on line measurement system. The concentration and cross correlation algorithms should be optimised for speed. If necessary some of the calculations should be carried out in parallel. Potential industrial users should be asked whether they require on line images of concentration profile (heavy on computation and display time), concentration matrices or a single mass flow rate reading.

- The possibility of using this system for slurries or mixture where the conveying fluid is a non conducting liquid should be investigated.

- The electrodynamic sensor is susceptible to variations in humidity etc. (section 4.2) when used for concentration measurement. Tests should be made on the effect of moisture content in the particles on the sensitivity of the measurement system by using test materials of known moisture content. The use of a dual modality system based on capacitance or some other mode (section 2.2) for concentration profile and electrodynamic for velocity profile should be investigated.

- The effect of pixel size on factors such as mass flow rate repaetability and accuracy when determined from the reconstructed tomographic results should be investigated. At present there is a compromise between processing time and accuracy of the measurement.

References

Abdul Rahim R, Green RG, Horbury N, Dickin FJ, Naylor BD and Pridmore TP, Further development of a tomographic imaging system using optical fibres for pneumatic conveyors, Meas. Sci. Technol., vol 7, p 419-422, 1996a.

Abdul Rahim R, A tomographic imaging system for pneumatic conveyors using optical fibres, PhD Thesis, Sheffield Hallam University, 1996b.

Abdullah MZ, Application of resistive electrical impedance tomography to observe hydrocyclone separator dynamics, PhD Thesis, UMIST, 1993.

Asher RC, Ultrasonic sensors in the chemical and process industries, J. Phys. E : Sci. Instrum. , vol 16, pg 959-63, 1983.

Barber DC and Brown BH, Applied potential tomography, J Phys.E: Sci Instrum, vol 17 p 723-733, 1984.

Beck CM, Instrumentation and control for minimum energy consumption in pneumatic conveying, Ph.D thesis, University of Bradford, 1986.

Beck MS and Plaskowski A, Cross correlation flow meters : their design and application, Adam Hilger, 1987.

Beck MS and Williams RA, Process tomography : a European innovation and its applications, Meas. Sci. Technol., vol 7, 1996, p 215-224.

Bidin AR, Electrodynamics sensors and neural networks for electrical charge tomography, PhD Thesis, Sheffield Hallam University, 1993.

Brown GJ, Reilly D and Mills D, Ultrasonic transmission-mode tomography applied to gas/solids flow, Proc. 4th ECAPT Conf. at Bergen, pg 176-86, 1995.

Brown GJ, Reilly D and Mills D, Development of an ultrasonic tomography system for application in pneumatic conveying, Meas. Sci. Technol., Vol. 7, 1996, p396-405.

Browne MA, Deloughry RJ, Green RG and Thorn R, State-sequenced polarity crosscorrelator, Electronics Letters, 10 th June 1982, Vol 18, No. 12, p 528-530.

Cottam AJ, Application of neural networks for flow regime identification, ESCEIV project report, Sheffield Hallam University, 1994.

Dickin FJ, Zhao XJ, Abdullah MZ and Waterfall RC, Tomographic imaging of industrial process equipment using electrical impedance sensors, Proc. V Conf. Sensors and their applications, Edinburgh, Scotland, September 1991a, pp. 215-220

Dickin FJ, Tomography for improving the design and control of particulate processing systems, KONA - Powder and Particle, 1992b, 10, pp 4-14.

Duckworth HE, Electricity and magnetism, Holt, Rinehart and Winston, 1960.

ECAPT92 proceeding, first meeting of the European Concerted Action on Process Tomography, Manchester UK 1992.

ECAPT93 proceeding, second meeting of the European Concerted Action on Process Tomography, Karlshure Germany 1993.

ECAPT94, third meeting of the European Concerted Action on Process Tomography, Porto Portugal 1994.

ECAPT95, fourth meeting of the European Concerted Action on Process Tomography, Bergen Norway 1995.

Ghassemlooy Z, Fibre optic a revolution in communication, Page 2, EIT Publication for ESCE IV, Sheffield Hallam University, 1992.

Green RG, Horbury NM, Abdul Rahim R, Dickin FJ, Naylor BD, Pridmore TP, Optical fibre sensors for process tomography, Meas.Sci. Technol., Vol. 6, 1995, p1699-1704.

Gregory IA, Shot velocity measurement using electrodynamic transducers, PhD Thesis, UMIST, May 1987.

Helicon encyclopaedia, Helicon publishers 1991

Hammer EA and Green RG, The spatial filtering effect of capacitance transducer electrodes, J. Phys. E: Sci. Instrum. , Vol. 16. 1983, pg. 438-443.

Huang SM, Stott AL, Green RG and Beck MS, Electronic transducers for industrial measurement of low value capacitance, J Phys E: Sci Instrum vol 21 1988.

Huang SM, Xie CG, Thorn R, Snowden D, Beck MS, Tomographic Imaging of industrial process equipment - design of capacitance sensing electronics for oil and gas based processes, in Gratan, KTV (ed); Sensors - Technology, Systems and applications, 1991.

Ifeachor EC and Jervis BW, Digital Signal Processing : A Practical Approach, Addison Wesley, 1993.

Irwin JD and Kerns DV, Introduction to electrical engineering, Prentice Hall, 1995.

Isaksen O and Nordtvedt JE, Capacitance tomography: Reconstruction based on optimisation theory, ECAPT 1992, page 178-189.

KEITHLEY data acquisition, DAS-1800 Series Function Call Driver user's guide, Nov. 1993.

KEITHLEY data acquisition, DAS-1800HC Series user's guide, Dec. 1993.

Nordin MJ, An image reconstruction algorithm for a dual modality tomographic system, PhD Thesis 1995, Sheffield Hallam University.

Reilly D, Mills D and Brown GJ, Ultrasonics for measurement in bulk solids handling, Proc. 19th Powder and bulk solids Conf. at Chicago, pg 11-20, 1994

Scott DM, Introduction to Process Tomography, Engineering Foundation Conferences on Frontiers in Industrial Process Tomography, Shell Beach, California, 1995.

Shackleton ME, Electrodynamic transducer for gas/solids flow measurement, MPhil thesis, 1982, University of Bradford.

Williams, R.A., Xie, C.G., Dickin, F.J., Simons, S.J.R. and Beck, M.S., Multi-phase flow measurements in powder processing, Powder Technology, 66 (1991) 203-224.

Xie CG, Electrical Capacitance Tomography, ECAPT 1993, page 225-228.

Yan Y, Byrne B, Woodhead S, Coulthard J, (1995a), Velocity measurement of pneumatically conveyed solids using electrodynamic sensors, Meas. Sci. Technol., 6, 515-537.

Bibliography

Abdullah MZ, Dyakowski T, Dickin FJ and Williams RA, Observation of hydrocyclone separator dynamics using resistive electrical impedance tomography, ECAPT93 Conference, Germany 1993.

Beck MS, Drane J, Plaskowski A and Wainwright N, Particle velocity and mass flow measurement in pneumatic conveyors, Powder Technology, Vol. 2, 1968/69, pg 269-277.

Beck MS and Wainwright N, Current industrial methods of solids flow detection and measurement, Powder Technology, Vol. 2, 1968/69, pg. 189-197.

Beck MS, Coulthard J, Hewitt PJ and Sykes D, Flow velocity and mass flow measurement using natural turbulence signals, International Conference On Modern Development In Flow measurement, AERE Harwell, 1971, pg 292-304.

Beck MS, Jordan JR and Kelly RG, Cross-Correlation Flow measurement using a microelectronic hard-wired programmed digital computer, IEE Conference Publications, 1973, No. 103, pp 104-108.

Beck MS, Cross Correlation Flow meters, NRDC Bull., 52, 1981b

Beck MS, Green RG, Hammer EA and Thorn R, On-line measurement of oil/gas/water mixtures, using a capacitance sensor, Measurement, Vol. 3, No. 1, Jan-Mar 1985, pg. 7-14.

Beck MS, Green RG and Thorn R, Non-intrusive measurement of solids mass flow in pneumatic conveying, J. Phys. E : Sci. Instrum., Vol. 20, page 835-840, 1987.

Beck MS, Green RG, Plaskowski A and Stott AL, Capacitance measurement applied to a pneumatic conveyor with very low solids loading, Meas. Sci. Technol., vol. 1, 1990, pg. 561 - 564.

Beck MS, Hoyle BS and Lenn C, Process tomography in pipelines, SERC Bulletin, Volume 4 No 10 Summer 1992.

Beck MS, Powder and Fluid flow measurement using correlation techniques, PhD Thesis, University of Bradford, January 1969.

Bidin AR, Green RG, Shackleton ME, Taylor RW, Neural networks for flow regime identification with dry particulate flows, Part. Syst. Charact., 10, (1993b), pages 234-238.

Chen Q, Hoyle BS and Strangeways HJ, Electric field interaction and enhanced reconstruction algorithm in capacitance process tomography, ECAPT 1992, page 170-177

Dickin FJ, Hoyle BS, Hunt SM, Illyas O, Lenn C, Waterfall RC, Williams RA, Xie CG and Beck MS, Tomographic Imaging of industrial equipment - reviews of needs and methods in Grattan, KTV (ed); Sensors - Technology, Systems and applications, 1991b.

Dugdale P, Green RG, Hartley AJ, Jackson RJ, Landauro J, Tomographic imaging in industrial process equipment using optical sensor arrays, Sensor technology systems and application 5th conference paper edited by K. T. V. Grattan, 1993.

Dugdale P, Green RG, Hartley AJ . Jackson RJ, Landauro J, Optical sensors for process tomography, ECAPT 1992, Process Tomography: A Strategy for Industrial Exploitation, European Concerted Action on Process Tomography 26 - 29 March 1992, Manchester, United Kingdom.

Dugdale P, Green RG, Hartley AJ, Jackson A, Laundro, Using optical sensor arrays in Grattan, KTV (ed); Sensors - Technology, Systems and Applications, 1991.

Dyakowski T, Process tomography applied to multi-phase flow measurement, Meas. Sci. Technol., vol 7, 1996, p 343-353.

Featherstone AM, Green RG, Shackleton ME, Yarn velocity measurement, J. Phys. E: Sci. Instrum., Vol. 16, 1983, p 462-464.

Gabor H., Image reconstruction from projections : the fundamental of computerized tomography, Academic press, 1980.

Gajewski JB, Continuous Non-contact measurement of electric charges of solid particles in pipes of pneumatic transport Part I & II, Conference Record of the 1989 IEEE/IAS annual meeting, San Diego, USA.

Henry RM and Zhang L, Short delay measurement by polarity cross correlation, Electronic Letters, vol. 26, no. 3, Feb. 90, page 202-203.

Henry RM and Beck MS, Incipient fault detection in pipeline transporting solid material, On-line surveillance and monitoring of process plant, Society of chemical industry, 1977.

Horowitz P, The art of electronics, Cambridge university press, 1993

Hoyle BS and Xu LA Ultrasonic sensors, Process Tomography: Principles, techniques and applications, edited by R.A williams and M.S Beck , chapter 8 page 118 published by Butterworth-Heinemann Ltd Oxford 1995.

Huang SM, Xie CG, Salkeld JA, Plaskowski A, Thorn R, Williams RA, Hunt A and Beck MS, Process tomography for identification, design and measurement in industrial systems, Powder Technology, 69(1992) 85-92

Kelly EG and Spottiswood DJ 1989, The theory of electrostatic separations: A review Part 3: Particle Charging, Minerals Eng., vol. 2 No 2 , page 193-205.

King PW, Mass flow measurement of conveyed solids, by monitoring of intrinsic electrostatic noise levels, 2nd. Int. Conf. on the Pneumatic Transport of Solids in Pipes, Cranfield, 1973.

Li W and Hoyle BS, Sensor optimisation for ultrasonic process tomography, ECAPT 93 Conference, Germany 1993.

Li W and Hoyle BS, Multiple active sensors in ultrasonic process tomography systems, Frontiers on process tomography conference in California 1995, pp 289.

McKee S L, Williams RA, Dyakowski T, Bell T, Allen T, Solids flow imaging and attrition studies in a pneumatic conveyor, Powder Technology, Vol. 82, p 105-113, 1995.

Plaskowski A, Bukalski P, Habdas T, Skolimaski, Tomographic imaging of process equipment - application to pneumatic transport of solid material, Grattan, KTV (ed); Sensors - Technology, Systems and Applications, 1991.

Plaskowski A, Beck MS, Thorn R, Dyakowski T, Imaging industrial flows: Application of electrical process tomography, Institute of Physics Publishing Bristol and Philadelphia, 1995.

Proakis JG and Manolakis DG, Digital Signal Processing : Principle, Algorithms and Application, 2 nd Edition

Rhodes MJ, Pneumatic conveying, chapter 7 in Principles of powder technology, ed M Rjodes, John Wiley & Sons 1990.

Saeed N,. Browne MA, Green RG and Martin P, Two component flow regime identification and imaging with optical sensors, IMEKO XI Houston, Texas, 16 - 21 October 1988.

Xie CG, Huang SM, Hoyle BS, Beck MS, Tomographic Imaging of industrial process equipment - development of system model & image reconstruction algorithm for capacitive tomography, in Grattan, KTV (ed); Sensors - Technology, Systems and applications, 1991.

Xie CG, Plaskowski A, Beck MS, 8 electrode capacitance for two component flow 3 identification, IEE proc vol 136 ptA no 4 July 1989.

Xu LA, Green RG, Plaskowski A and Beck MS, 1988. The pulsed ultrasonic cross-correlation flowmeter for two-phase flow measurement, Journal of Physics, E: Sci. Instrum, Vol. 21, pp 406-414.

Yan Y, Woodhead S, Byrne B, Coulthard J, 1992, Measurement of pneumatically conveyed pulverised fuel using non-restrictive techniques, International Conference On Electronic Measurement & Instrumentation (ICEMI) 1992, China, pp 153-156.

Yan Y, Byrne B, and Coulthard J, Radiometric determination of dilute in homogeneous solids loading in pneumatic conveying systems, Meas. Sci. Technol., Vol. 5, 1994, p110-119.

Yan Y, Byrne B, Coulthard J, Sensing homogeneity in mass flow rate measurement of pneumatically conveyed solids, Flow Measurement and Instrumentation, Vol. 6, No 2, p 115-119, 1995.

Appendices

Appendix A. Data sheet for data acquisition system

Appendix B. Program for concentration, velocity and mass flow rate calculations

Appendix C. Publications

1. An electrodynamic sensor for process tomography. Presented at International Conference on Advances in Strategic Technologies (Electronics and Information Technology) ICAST'95, 12 - 15 June 1995, Faculty of Engineering, Universiti Kebangsaan Malaysia, Bangi, Malaysia.

2. Electrodynamic sensors for process tomography. Presented at Engineering Foundation Conference on Frontiers in Industrial Process Tomography, October 29 to November 3 1995, The Cliffs Shell Beach, San Luis Obispo, California, USA.

3. Concentration profiles of dry powders in a gravity conveyor using an electrodynamic tomography system. Accepted for publication in the Journal of Measurement, Science and Technology IOP publisher in October 1996.

4. Velocity and mass flow rate profiles of dry powders in a gravity conveyor using an electrodynamic tomography system. Offered to the Journal of Measurement, Science and Technology IOP publisher in October 1996.

Tables A-1 to A-4 list specifications for the DAS-1800HC Series boards.

Table A-1. Analog Input Specifications

Attribute	DAS-1801HC Boards	DAS-1802HC Boards
Number of channels	Software-selectable as 32 differential or 64 single-ended	
Input mode	Software-selectable as unipolar or bipolar	
Resolution	12-bit (1 part in 4096)	
Data format	16-bit twos complement, right-justified	
FIFO size	1024 word	
Channel-gain QRAM size	64 locations	
Gain (range)	1 (0.0 to +5.0 V for unipolar 1 (±5.0 V for bipolar)	1 (0.0 to +10 V for unipolar) 1 (±10 V for bipolar)
	5 (0.0 to +1.0 V for unipolar) 5 (±1.0 V for bipolar)	2 (0.0 to +5.0 V for unipolar) 2 (±5.0 V for bipolar)
	50 (0 to 100 mV for unipolar) 50 (±100 mV for bipolar)	4 (0.0 to +2.5 V for unipolar) 4 (±2.5 V for bipolar)
	250 (0 to +20 mV for unipolar) 250 (±20 mV for bipolar)	8 (0.0 to 1.25 V for unipolar) 8 (±1.25 V for bipolar)
Absolute accuracy	Typical: 0.01% of reading ±1 LSB for all ranges	
	Maximum error: • 0.02% of reading ±1 LSB max @ 25° C for gain < 250 • 0.03% of reading ±1 LSB max @ 25° C for gain = 250	

Table A-1. Analog Input Specifications (cont.)

Attribute	DAS-1801HC Boards	DAS-1802HC Boards
Temperature coefficient of accuracy (includes ADC)	Offset: • Bipolar: ±20 µV/ °C ±(12 µV/° C ÷ gain) max • Unipolar: ±20 µV/ °C ±(14 µV/° C ÷ gain) max	
	Gain: • ±20 ppm/ °C for gain of < 50 • 30 ppm/° C for gain = 50 • 35 ppm/° C for gain = 250	
Linearity[1]	Integral: ±½ LSB typical, ±1 LSB max.	
	Differential: ±1 LSB	
Throughput	Refer to "Maximum Achievable Throughput Rates" on page 2-4	
Dynamic parameters	Acquisition time: 0.3 µs	
	Aperture delay: 13.0 ns	
	Aperture uncertainty: 150 ps rms	
	Conversion time: 3.0 µs max. (includes acquisition time)	
Input bias current	±40 nA max. @ 25° C	
	±60 nA max. over operating range	
Common mode rejection ratio	74 dB for gain = 1	74 dB for gain = 1
	80 dB for gain = 5	80 dB for gain = 2
	100 dB for gain = 50	80 dB for gain = 4
	100 dB for gain = 250	86 dB for gain = 8
Input overvoltage	±15 V continuous powered	
	±15 V continuous unpowered	

Table A-1. Analog Input Specifications (cont.)

Attribute	DAS-1801HC Boards	DAS-1802HC Boards
Noise:[2]	Bipolar electrical noise (in counts) • Gain = 1: p-p = 1; rms = 0.1 • Gain = 5: p-p = 1; rms = 0.1 • Gain = 50: p-p = 4; rms = 0.5 • Gain = 250: p-p = 8; rms = 1.0	Bipolar electrical noise (in counts) • Gain = 1: p-p = 1; rms = 0.1 • Gain = 2: p-p = 1; rms = 0.1 • Gain = 4: p-p = 1; rms = 0.1 • Gain = 8: p-p = 1; rms = 0.1
	Unipolar electrical noise (in counts): • Gain = 1: p-p = 1; rms = 0.1 • Gain = 5: p-p = 1; rms = 0.1 • Gain = 50: p-p = 6; rms = 0.9 • Gain = 250: p-p = 9; rms = 1.4	Unipolar electrical noise (in counts): • Gain = 1: p-p = 1; rms = 0.1 • Gain = 2: p-p = 1; rms = 0.1 • Gain = 4: p-p = 1; rms = 0.1 • Gain = 8: p-p = 1; rms = 0.1
DMA levels	5, 6, and 7	
Interrupt levels	3, 5, 7, 10, 11, and 15	
Minimum external pacer clock pulse width	10 ns	
Maximum external pacer clock rate	333 kHz	
Minimum hardware trigger pulse width	10 ns	

Notes

[1] Monotonicity is guaranteed over the operating range.

[2] The figures in the table show the electrical noise introduced by the analog front end *but do not include the uncertainty inherent in the quantization process*. The inherent quantization noise introduced by any ADC is due to uncertainty at code boundaries and adds a peak-to-peak value of 1 LSB to the electrical noise; it also makes the rms level 0.5 LSBs.

Table A-2. Analog Output Specifications

Attribute	DAS-1801HC Specifications	DAS-1802HC Specifications
Resolution	12-bit (one part in 4096 or 224 ppm)	
Data format	Right justified, offset binary	
Range	±10.00 V	
Linearity[1]	Integral: ±¼ LSB typical; ±½ LSB max.	
	Differential: ±1 LSB	
Output current drive	±5 mA max.	
Capacitive load drive	100 μF	
Gain accuracy	Adjustable to 0	
Offset accuracy	Adjustable to 0	
Glitch energy	300 nV * seconds	
Power up	DACs power up to 0.0 V at reset	

Notes
[1] Monotonicity is guaranteed over the operating range.

Table A-3. Digital I/O Specifications

Attributes	DAS-1801HC Specifications	DAS-1802HC Specifications
Digital output (including SSHO, DOSTB, and TGOUT)	V_{OH} (min.) = 2.7 V @ I_{OH} = −400 μA	
	V_{OL} (max.) = 0.5 V @ I_{OL} = 8 mA	
Digital input	V_{IH} (min.) = 2.0 V; I_{IH} (max.) = 20 μA	
	V_{IL} (max.) = 0.8 V; I_{IL} (max.) = −0.2 mA	
Digital output strobe pulse width	300 ns typical; data is latched on the rising edge of DOSTB	

Table A-4. Power Supply Requirements

Attribute	DAS-1801HC and DAS-1802HC Specifications
+5 VDC input	430 mA typical; 870 mA maximum
+12 VDC input	400 mA typical; 550 mA maximum
Maximum current available at the ±15 V outputs	30 mA
Maximum current available at the +5 V output	1.0 A

Appendix B
% Program written in MATLAB to generate
% concentration, velocity and mass flow rate profile
% Tomographic measurement system configuration.
% Sensor 1 till sensor 16 represent upstream sensors
% Sensor 17 till sensor 32 represent downstream sensors

% Sensor 1 and 17 sensitivity map
```
s1=[0 0 0.127 0.781 6.199 0.781 0.127 0 0;
    0 0.072 0.16 0.308 0.442 0.308 0.16 0.072 0;
    0.025 0.065 0.096 0.136 0.157 0.136 0.096 0.065 0.025;
    0.031 0.046 0.061 0.074 0.08 0.074 0.061 0.046 0.031;
    0.027 0.034 0.041 0.046 0.048 0.046 0.041 0.034 0.027;
    0.019 0.025 0.029 0.032 0.033 0.032 0.029 0.025 0.019;
    0.009 0.019 0.021 0.023 0.023 0.023 0.021 0.019 0.009;
    0 0.012 0.016 0.017 0.018 0.017 0.016 0.012 0;
    0 0 0.007 0.012 0.014 0.012 0.007 0 0 ];
```

% Sensor 2 and 18 sensitivity map
```
s2=[0 0 4.733 1.803 0.338 0.12 0.039 0 0;
    0 0.282 0.729 0.544 0.231 0.113 0.065 0.034 0
    0.056 0.159 0.209 0.189 0.129 0.082 0.053 0.037 0.014
    0.058 0.085 0.098 0.094 0.076 0.057 0.041 0.031 0.02
    0.044 0.052 0.057 0.055 0.048 0.04 0.032 0.025 0.02
    0.028 0.035 0.037 0.036 0.033 0.029 0.024 0.02 0.015
    0.012 0.025 0.026 0.026 0.024 0.022 0.019 0.016 0.008
    0 0.015 0.019 0.019 0.018 0.017 0.015 0.011 0
    0 0 0.008 0.013 0.014 0.012 0.007 0 0 ];
```

% Sensor 3 and 19 sensitivity map
```
s3=[0 0 0.294 0.164 0.092 0.049 0.019 0 0;
    0 6 0.722 0.207 0.097 0.056 0.037 0.021 0;
    0.294 0.722 0.356 0.16 0.085 0.052 0.035 0.025 0.01;
    0.164 0.207 0.16 0.103 0.066 0.044 0.031 0.023 0.016;
    0.092 0.097 0.085 0.066 0.049 0.036 0.027 0.02 0.016;
    0.049 0.056 0.052 0.044 0.036 0.028 0.022 0.018 0.012;
    0.019 0.037 0.035 0.031 0.027 0.022 0.018 0.015 0.007;
    0 0.021 0.025 0.023 0.02 0.018 0.015 0.01 0;
    0 0 0.01 0.016 0.016 0.013 0.007 0 0 ];
```

% Sensor 4 and 20 sensitivity map
```
s4=[0 0 0.056 0.058 0.044 0.028 0.012 0 0;
    0 0.282 0.159 0.085 0.052 0.035 0.025 0.015 0;
    4.733 0.729 0.209 0.098 0.057 0.037 0.026 0.019 0.008;
    1.803 0.544 0.189 0.094 0.055 0.036 0.026 0.019 0.013;
    0.338 0.231 0.129 0.076 0.048 0.033 0.024 0.018 0.014;
    0.12 0.113 0.082 0.057 0.04 0.029 0.022 0.017 0.012;
    0.039 0.065 0.053 0.041 0.032 0.024 0.019 0.015 0.007;
    0 0.034 0.037 0.031 0.025 0.02 0.016 0.011 0;
    0 0 0.014 0.02 0.02 0.015 0.008 0 0 ];
```

```
% Sensor 5 and 21 sensitivity map
s5=[0 0 0.025 0.031 0.027 0.019 0.009 0 0;
    0 0.072 0.065 0.046 0.034 0.025 0.019 0.012 0;
    0.127 0.16 0.096 0.061 0.041 0.029 0.021 0.016 0.007;
    0.781 0.308 0.136 0.074 0.046 0.032 0.023 0.017 0.012;
    6.199 0.442 0.157 0.08 0.048 0.033 0.023 0.018 0.014;
    0.781 0.308 0.136 0.074 0.046 0.032 0.023 0.017 0.012;
    0.127 0.16 0.096 0.061 0.041 0.029 0.021 0.016 0.007;
    0 0.072 0.065 0.046 0.034 0.025 0.019 0.012 0;
    0 0 0.025 0.031 0.027 0.019 0.009 0 0 ];

% Sensor 6 and 22 sensitivity map
s6=[0 0 0.014 0.02 0.02 0.015 0.008 0 0;
    0 0.034 0.037 0.031 0.025 0.02 0.016 0.011 0;
    0.039 0.065 0.053 0.041 0.032 0.024 0.019 0.015 0.007;
    0.12 0.113 0.082 0.057 0.04 0.029 0.022 0.017 0.012;
    0.338 0.231 0.129 0.076 0.048 0.033 0.024 0.018 0.014;
    1.803 0.544 0.189 0.094 0.055 0.036 0.026 0.019 0.013;
    4.733 0.729 0.209 0.098 0.057 0.037 0.026 0.019 0.008;
    0 0.282 0.159 0.085 0.052 0.035 0.025 0.015 0;
    0 0 0.056 0.058 0.044 0.028 0.012 0 0];

% Sensor 7 and 23 sensitivity map
s7=[0 0 0.01 0.016 0.016 0.013 0.007 0 0;
    0 0.021 0.025 0.023 0.02 0.018 0.015 0.01 0;
    0.019 0.037 0.035 0.031 0.027 0.022 0.018 0.015 0.007;
    0.049 0.056 0.052 0.044 0.036 0.028 0.022 0.018 0.012;
    0.092 0.097 0.085 0.066 0.049 0.036 0.027 0.02 0.016;
    0.164 0.207 0.16 0.103 0.066 0.044 0.031 0.023 0.016;
    0.294 0.722 0.356 0.16 0.085 0.052 0.035 0.025 0.01;
    0 6 0.722 0.207 0.097 0.056 0.037 0.021 0;
    0 0 0.294 0.164 0.092 0.049 0.019 0 0 ];

% Sensor 8 and 24 sensitivity map
s8=[0 0 0.008 0.013 0.014 0.012 0.007 0 0;
    0 0.015 0.019 0.019 0.018 0.017 0.015 0.011 0;
    0.012 0.025 0.026 0.026 0.024 0.022 0.019 0.016 0.008;
    0.028 0.035 0.037 0.036 0.033 0.029 0.024 0.02 0.015;
    0.044 0.052 0.057 0.055 0.048 0.04 0.032 0.025 0.02;
    0.058 0.085 0.098 0.094 0.076 0.057 0.041 0.031 0.02;
    0.056 0.159 0.209 0.189 0.129 0.082 0.053 0.037 0.014;
    0 0.282 0.729 0.544 0.231 0.113 0.065 0.034 0;
    0 0 4.733 1.803 0.338 0.12 0.039 0 0 ];
```

% Sensor 9 and 25 sensitivity map
s9=[0 0 0.007 0.012 0.014 0.012 0.007 0 0;
    0 0.012 0.016 0.017 0.018 0.017 0.016 0.012 0;
    0.009 0.019 0.021 0.023 0.023 0.023 0.021 0.019 0.009;
    0.019 0.025 0.029 0.032 0.033 0.032 0.029 0.025 0.019;
    0.027 0.034 0.041 0.046 0.048 0.046 0.041 0.034 0.027;
    0.031 0.046 0.061 0.074 0.08 0.074 0.061 0.046 0.031;
    0.025 0.065 0.096 0.136 0.157 0.136 0.096 0.065 0.025;
    0 0.072 0.16 0.308 0.442 0.308 0.16 0.072 0;
    0 0 0.127 0.781 6.199 0.781 0.127 0 0];

% Sensor 10 and 26 sensitivity map
s10=[0 0 0.007 0.012 0.014 0.013 0.008 0 0;
    0 0.011 0.015 0.017 0.018 0.019 0.019 0.015 0;
    0.008 0.016 0.019 0.022 0.024 0.026 0.026 0.025 0.012;
    0.015 0.02 0.024 0.029 0.033 0.036 0.037 0.035 0.028;
    0.02 0.025 0.032 0.04 0.048 0.055 0.057 0.052 0.044;
    0.02 0.031 0.041 0.057 0.076 0.094 0.098 0.085 0.058;
    0.014 0.037 0.053 0.082 0.129 0.189 0.209 0.159 0.056;
    0 0.034 0.065 0.113 0.231 0.544 0.729 0.282 0;
    0 0 0.039 0.12 0.338 1.803 4.733 0 0];

% Sensor 11 and 27 sensitivity map
s11=[0 0 0.007 0.012 0.016 0.016 0.01 0 0;
    0 0.01 0.015 0.018 0.02 0.023 0.025 0.021 0;
    0.007 0.015 0.018 0.022 0.027 0.031 0.035 0.037 0.019;
    0.013 0.018 0.022 0.028 0.036 0.044 0.052 0.056 0.049;
    0.016 0.02 0.027 0.036 0.049 0.066 0.085 0.097 0.092;
    0.016 0.023 0.031 0.044 0.066 0.103 0.16 0.207 0.164;
    0.01 0.025 0.035 0.052 0.085 0.16 0.356 0.722 0.0294;
    0 0.021 0.037 0.056 0.097 0.207 0.722 6 0;
    0 0 0.019 0.049 0.092 0.164 0.294 0 0];

% Sensor 12 and 28 sensitivity map
s12=[0 0 0.008 0.015 0.02 0.02 0.014 0 0;
    0 0.011 0.016 0.02 0.025 0.031 0.037 0.034 0;
    0.007 0.015 0.019 0.024 0.032 0.041 0.053 0.065 0.039;
    0.012 0.017 0.022 0.029 0.04 0.057 0.082 0.113 0.12;
    0.014 0.018 0.024 0.033 0.048 0.076 0.129 0.231 0.338;
    0.013 0.019 0.026 0.036 0.055 0.094 0.189 0.544 1.803;
    0.008 0.019 0.026 0.037 0.057 0.098 0.209 0.729 4.733;
    0 0.015 0.025 0.035 0.052 0.085 0.159 0.282 0;
    0 0 0.012 0.028 0.044 0.058 0.056 0 0];

```
% Sensor 13 and 29 sensitivity map
s13=[0 0 0.009 0.019 0.027 0.031 0.025 0 0;
    0 0.012 0.019 0.025 0.034 0.046 0.065 0.072 0;
    0.007 0.016 0.021 0.029 0.041 0.061 0.096 0.16 0.127;
    0.012 0.017 0.023 0.032 0.046 0.074 0.136 0.308 0.781;
    0.014 0.018 0.023 0.033 0.048 0.08 0.157 0.442 6.199;
    0.012 0.017 0.023 0.032 0.046 0.074 0.136 0.308 0.781;
    0.007 0.016 0.021 0.029 0.041 0.061 0.096 0.16 0.127;
    0 0.012 0.019 0.025 0.034 0.046 0.065 0.072 0;
    0 0 0.009 0.019 0.027 0.031 0.025 0 0 ];

% Sensor 14 and 30 sensitivity map
s14=[0 0 0.012 0.028 0.044 0.058 0.056 0 0;
    0 0.015 0.025 0.035 0.052 0.085 0.159 0.282 0;
    0.008 0.019 0.026 0.037 0.057 0.098 0.209 0.729 4.733;
    0.013 0.019 0.026 0.036 0.055 0.094 0.189 0.544 1.803;
    0.014 0.018 0.024 0.033 0.048 0.076 0.129 0.231 0.338;
    0.012 0.017 0.022 0.029 0.04 0.057 0.082 0.113 0.12;
    0.007 0.015 0.019 0.024 0.032 0.041 0.053 0.065 0.039;
    0 0.011 0.016 0.02 0.025 0.031 0.037 0.034 0;
    0 0 0.008 0.015 0.02 0.02 0.014 0 0];

% Sensor 15 and 31 sensitivity map
s15=[0 0 0.019 0.049 0.092 0.164 0.294 0 0;
    0 0.021 0.037 0.056 0.097 0.207 0.722 6 0;
    0.01 0.025 0.035 0.052 0.085 0.16 0.356 0.722 0.294;
    0.016 0.023 0.031 0.044 0.066 0.103 0.16 0.207 0.164;
    0.016 0.02 0.027 0.036 0.049 0.066 0.085 0.097 0.092;
    0.012 0.018 0.022 0.028 0.036 0.044 0.052 0.056 0.049;
    0.007 0.015 0.018 0.022 0.027 0.031 0.035 0.037 0.019;
    0 0.01 0.015 0.018 0.02 0.023 0.025 0.021 0;
    0 0 0.007 0.013 0.016 0.016 0.01 0 0];

% Sensor 16 and 32 sensitivity map
s16=[0 0 0.039 0.12 0.338 1.803 4.733 0 0;
    0 0.034 0.065 0.113 0.231 0.544 0.729 0.282 0;
    0.014 0.037 0.053 0.082 0.129 0.189 0.209 0.159 0.056;
    0.02 0.031 0.041 0.057 0.076 0.094 0.098 0.085 0.058;
    0.02 0.025 0.032 0.04 0.048 0.055 0.057 0.052 0.044;
    0.015 0.02 0.024 0.029 0.033 0.036 0.037 0.035 0.028;
    0.008 0.016 0.019 0.022 0.024 0.026 0.026 0.025 0.012;
    0 0.011 0.015 0.017 0.018 0.019 0.019 0.015 0;
    0 0 0.007 0.012 0.014 0.013 0.008 0 0 ];
```

% Full flow filter mask
ffm=[0 0 1.36186 2.321598 1.000684 2.320862 1.36186 0 0;
0 1.060255 3.446328 4.680307 5.176803 4.680307 3.446328 1.060255 0;
1.36186 3.446328 5.665635 7.086157 7.546392 7.086157 5.665635 3.446328
1.36186;
2.320862 4.680307 7.086157 8.482039 8.959608 8.482039 7.086157 4.680307
2.321598;
1.000684 5.176803 7.546392 8.959608 9.481865 8.959608 7.546392 5.176803
1.000684;
2.321598 4.680307 7.086157 8.482039 8.959608 8.482039 7.086157 4.680307
2.321598;
1.36186 3.446328 5.665635 7.086157 7.546392 7.086157 5.665635 3.446328
1.432373;
0 1.060255 3.446328 4.680307 5.176803 4.680307 3.446328 1.060255 0;
0 0 1.36186 2.320862 1.000684 2.320862 1.36186 0 0];

% quater flow filter mask
qfm=[0 0 0 0 0 0 0 0;
0 0 0 0 0 0 0 0;
0 0 0 0 0 0 0 0;
0 0 0 0 0 0 0 0;
0 0 0 0 0 0 0 0;
0 0 0 0 0 0 0 0;
0 0 0 0 0 0 0 0;
0 1.060255 3.446328 4.680307 5.176803 4.680307 3.446328 1.060255 0;
0 0 1.36186 2.320862 1.000684 2.320862 1.36186 0 0];

% half flow filter mask
hfm=[0 0 0 0 0 0 0 0;
0 0 0 0 0 0 0 0;
0 0 0 0 0 0 0 0;
0 0 0 0 0 0 0 0;
0 0 0 0 0 0 0 0;
2.321598 4.680307 7.086157 8.482039 8.959608 8.482039 7.086157 4.680307
2.321598;
1.36186 3.446328 5.665635 7.086157 7.546392 7.086157 5.665635 3.446328
1.432373;
0 1.060255 3.446328 4.680307 5.176803 4.680307 3.446328 1.060255 0;
0 0 1.36186 2.320862 1.000684 2.320862 1.36186 0 0];

% three quater filter mask

tqfm=[0 0 0 0 0 0 0 0;

0 0 0 0 0 0 0 0 0;

1.36186 3.446328 5.665635 7.086157 7.546392 7.086157 5.665635 3.446328 1.36186;

2.320862 4.680307 7.086157 8.482039 8.959608 8.482039 7.086157 4.680307 2.321598;

1.000684 5.176803 7.546392 8.959608 9.481865 8.959608 7.546392 5.176803 1.000684;

2.321598 4.680307 7.086157 8.482039 8.959608 8.482039 7.086157 4.680307 2.321598;

1.36186 3.446328 5.665635 7.086157 7.546392 7.086157 5.665635 3.446328 1.432373;

0 1.060255 3.446328 4.680307 5.176803 4.680307 3.446328 1.060255 0;

0 0 1.36186 2.320862 1.000684 2.320862 1.36186 0 0];

% stratified vertical filter mask

svfm=[0 0 1.36186 2.321598 1.000684 2.320862 1.36186 0 0;

0 1.060255 3.446328 4.680307 5.176803 4.680307 3.446328 1.060255 0;

0 0 0 0 0 0 0 0 0;

0 0 0 0 0 0 0 0 0;

0 0 0 0 0 0 0 0 0;

0 0 0 0 0 0 0 0 0;

0 0 0 0 0 0 0 0 0;

0 1.060255 3.446328 4.680307 5.176803 4.680307 3.446328 1.060255 0;

0 0 1.36186 2.320862 1.000684 2.320862 1.36186 0 0];

% stratified horizontal filter mask

shfm=[0 0 0 0 0 0 0 0;

0 1.060255 0 0 0 0 1.060255 0;

1.36186 3.446328 0 0 0 0 3.446328 1.36186;

2.320862 4.680307 0 0 0 0 4.680307 2.321598;

1.000684 5.176803 0 0 0 0 5.176803 1.000684;

2.321598 4.680307 0 0 0 0 4.680307 2.321598;

1.36186 3.446328 0 0 0 0 3.446328 1.432373;

0 1.060255 0 0 0 0 1.060255 0;

0 0 0 0 0 0 0 0];

```
% Voltage reading from upstream sensors multiply
% by sensitivity map
% v1 till v32 are the average value of each sensor
vs1=v1*s1;
vs2=v2*s2;
vs3=v3*s3;
vs4=v4*s4;
vs5=v5*s5;
vs6=v6*s6;
vs7=v7*s7;
vs8=v8*s8;
vs9=v9*s9;
vs10=v10*s10;
vs11=v11*s11;
vs12=v12*s12;
vs13=v13*s13;
vs14=v14*s14;
vs15=v15*s15;
vs16=v16*s16;

% Voltage reading from downstream sensors multiply
% by sensitivity map
vs17=v17*s1;
vs18=v18*s2;
vs19=v19*s3;
vs20=v20*s4;
vs21=v21*s5;
vs22=v22*s6;
vs23=v23*s7;
vs24=v24*s8;
vs25=v25*s9;
vs26=v26*s10;
vs27=v27*s11;
vs28=v28*s12;
vs29=v29*s13;
vs30=v30*s14;
vs31=v31*s15;
vs32=v32*s16;

% Total concentration for upstream sensors base on linear back projection
x=vs1+vs2+vs3+vs4+vs5+vs6+vs7+vs8+vs9+vs10+vs11+vs12+vs13+vs14+vs15+vs16;

% Total concentration for downstream sensors base on linear back projection
y=vs17+vs18+vs19+vs20+vs21+vs22+vs23+vs24+vs25+vs26+vs27+vs28+vs29+vs30+vs31+vs32;
```

```
% Concentration base on filtered back projection
for i=1:9
for j=1:9
% Upstream
cux(i,j)=x(i,j)*ffm(i,j);
% Downstream
cdy(i,j)=y(i,j)*ffm(i,j);
end
end

% 2D colour image for upstream concentration
% base on linear back projection
imagesc(cu)
colormap(hot(32))
axis off
colorbar
title('2D full flow upstream at ? g/s')
text(5,0.35,'S1')
text(-0.25,5,'S5')
text(5,10,'S9')
text(9.5,4.75,'S')
text(9.5,5.25,'13')

% 3D colour image for upstream concentration
% base on linear back projection
surfc(cu)
colormap(cool(32))
colorbar
title('3D full flow upstream at ? g/s')
xlabel('        S1')
ylabel('S5')
zlabel('Output/V')

% 2D colour image for downstream concentration
% base on filtered back projection
imagesc(cdy)
colormap(hot(32))
axis off
colorbar
title('2D full flow downstream at ? g/s')
text(4.75,0.35,'S17')
text(-0.25,5,'S21')
text(4.75,10,'S25')
text(9.5,4.75,'S')
text(9.5,5.25,'29')
```

```matlab
% 3D colour image for downstream concentration
% base on filtered back projection
surfc(cdy)
colormap(cool(32))
colorbar
title('3D full flow downstream at ? g/s')
xlabel('        S17')
ylabel('S21')
zlabel('Output/V')


% Upstream sensor matrices 16x312
% 16 means 16 readings from 16 sensors
% 312 means each sensor have 312 data length
um=[...............;
.
.
.
...............];


% Downstream sensor matrices 16x312
dm=[...............;
.
.
.
...............];

for j=1:9
for k=1:9
for i=1:312
% Upstream sensors
    a1=um(i,1)*s1;
    a2=um(i,2)*s2;
    a3=um(i,3)*s3;
    a4=um(i,4)*s4;
    a5=um(i,5)*s5;
    a6=um(i,6)*s6;
    a7=um(i,7)*s7;
    a8=um(i,8)*s8;
    a9=um(i,9)*s9;
    a10=um(i,10)*s10;
    a11=um(i,11)*s11;
    a12=um(i,12)*s12;
    a13=um(i,13)*s13;
    a14=um(i,14)*s14;
    a15=um(i,15)*s15;
    a16=um(i,16)*s16;
```

```
% Downstream sensors
    a17=dm(i,1)*s1;
    a18=dm(i,2)*s2;
    a19=dm(i,3)*s3;
    a20=dm(i,4)*s4;
    a21=dm(i,5)*s5;
    a22=dm(i,6)*s6;
    a23=dm(i,7)*s7;
    a24=dm(i,8)*s8;
    a25=dm(i,9)*s9;
    a26=dm(i,10)*s10;
    a27=dm(i,11)*s11;
    a28=dm(i,12)*s12;
    a29=dm(i,13)*s13;
    a30=dm(i,14)*s14;
    a31=dm(i,15)*s15;
    a32=dm(i,16)*s16;

% Upstream gray level
    A=a1+a2+a3+a4+a5+a6+a7+a8+a9+a10+a11+a12+a13+a14+a15+a16;
% Downstream gray level
    B=a17+a18+a19+a20+a21+a22+a23+a24+a25+a26+a27+a28+a29+a30+a31+a32;
% Pixel jk means pixel at row number j and column number k
% Upstream gray level at index time i pixel jk
    u(i)=A(j,k);
% Downstream gray level at index time i pixel jk
    d(i)=B(j,k);
end
u;
y=d';
% Cross correlation function
x=kxcorr(u,y);
x=x';
% Separation distance between upstream and downstream sensors is 0.05 m
% Peak cross correlation function and index transit time it
[z,it]=max(x)
% Velocity
% Time sampling Ts
v=0.05/(it*Ts)
end
end
```

```matlab
% Velocity matrices
v=[0 0 . . . . . 0 0;
   0 . . . . . . . 0;
   . . . . . . . . .;
   . . . . . . . . .;
   . . . . . . . . .;
   . . . . . . . . .;
   . . . . . . . . .;
   0 . . . . . . . 0;
   0 0 . . . . . 0 0];

for i=1:9
for j=1:9
% Mass flow rate = Concentration*Velocity
% Mass flow rate calculation for pixel ij
% Mass flow rate for upstream base on linear back projection
mfru(i,j)=u(i,j)*v(i,j);
% Mass flow rate for downstream base on linear back projection
mfrd(i,j)=d(i,j)*v(i,j);
% Mass flow rate for upstream base on filtered back projection
mfruf(i,j)=cu(i,j)*v(i,j);
% Mass flow rate for downstream base on filtered back projection
mfrdf(i,j)=cd(i,j)*v(i,j);
end
end

% Total mass flow rate for upstream base on linear back projection
tmfru=sum(sum(mfru))
% Total mass flow rate for downstream base on linear back projection
tmfrd=sum(sum(mfrd))
% Total mass flow rate for upstream base on filtered back projection
tmfruf=sum(sum(mfruf))
% Total mass flow rate for downstream base on filtered back projection
tmfrdf=sum(sum(mfrdf))
```

AN ELECTRODYNAMIC SENSOR FOR PROCESS TOMOGRAPHY

M F RAHMAT[1,2], R G GREEN[2], A GOUDE[2], R M HENRY[3].

1. Department of Control Engineering, Faculty of Electrical Engineering, Universiti Teknologi Malaysia, Jalan Semarak, 54100 Kuala Lumpur, Malaysia.
2. School of Engineering Information Technology, City Campus, Sheffield Hallam University, Pond Street, S1 1WB, UK.
3. Department of Chemical Engineering, University of Bradford, Bradford BD7 1DP UK.

ABSTRACT

Electrodynamic sensors are low cost and robust. They are frequently used in the process industry for measurement but very little fundamental work on their design has been reported. This paper describes an investigation into two characteristics of the sensor. The effect of sensor electrode diameter on the sensitivity of the sensor and the spatial filtering effect of the sensor due to its finite size are investigated. Models are proposed and results obtained using them compared with experimental values.

Tomography comes from the Greek words tomo (slice) and graph (picture) (Bidin, 1993). Helicon encyclopaedia define tomography as the obtaining of plane section images which show a slice through an object. In this project at Sheffield Hallam University electrodynamic sensors and image reconstruction algorithms are being used to produce images of velocity and concentration profiles at a cross-section of a pipe conveying dry particulates. When solids particles flow in pipe line and pass the sensor, they induce a charge. Electrodynamic transducers sense the charge and convert this physical signal to a voltage signal. A basic system for process tomography is shown in figure 1. Three basic components in a process tomography system are :-
(a) The sensors
(b) The data acquisition system
(c) The image reconstruction system and display
This paper investigates the relationships between sensor size, sensor sensitivity and the frequency bandwidth, termed the spatial filtering effect (Hammer and Green, 1983) of the transduced signal.

ELECTRODE SENSITIVITY

Sensitivity is important because it shows the changing in output of the transducer due to a change in the mass flow rate with different size of sensor and the unit of the sensitivity is volts/gram/second.

The electrode sensitivity is modelled by considering the effect of a single charged particle, q, as it moves vertically downwards at a constant velocity, υ.

The assumptions for the model are:

The charge is travelling in an axial direction parallel to the axis of the pipe, the particle has a constant, finite amount of charge which is not dissipated during the time it travels through the sensing volume, the surface area of the electrode is small compared to the radius of the pipe, the charge acts as a point source and the pipe is of non conducting material.

Then for a single charged particle, assumed to be a point charge of value q, the field is uniformly radial

$$E = \frac{q}{4\pi r_i^2 \varepsilon_0} \qquad (1)$$

This point charge induces a potential onto the surface of the small, flat electrode used to sense the change in potential at a point on the wall of a non-conducting or dielectric pipe. It is assumed that there are no other interacting fields on the electrode since there is no surface charge on the pipe wall.

For a given sensor, the surface area is πr_e^2 which is considered normal to the flux (figure 2). So the proportion of flux passing through the sensor due to the charged particle at a distance i from it is

$$\frac{\pi r_e^2}{4\pi r_i^2} \qquad (2)$$

The charge induced in the sensor is proportional to q. Hence,

$$Q_e = \frac{kqr_e^2}{r_i^2} \qquad (3)$$

Equation 3 suggests the amount of charge induced onto an electrode depends upon the radius of the sensor (electrode) squared.

This charge is stored on a capacitor (figure 5) and provides a voltage V_e given by

$$Q_e = CV_e \qquad (4)$$

This voltage is amplified, rectified smoothed and averaged.

The sensitivity of the sensor is defined as $\dfrac{Q_e}{q_i}$. This value is difficult to determine and in this paper a series of sensor diameters are compared simultaneously so that the same q_i is detected by them all. Also it is the amplified, rectified and averaged voltage which is measured.

SPATIAL FILTERING

Spatial filtering effect is important in this paper because it investigate the relationship between sensor size and frequency bandwidths of the transducer base upon the frequency response from the pulse which correspond to a detecttable particle.

Assume that a change in the form of a pulse $\rho(t)$ of the conveyed component (termed a concentration pulse) passes the electrode, of length d with velocity υ as shown in figure 3. If the electrostatic field between the sensor and screen are homogeneous and non fringing, the charge pulse will create a change in the charge induced in the sensor which can be described by a rectangular pulse of duration $\dfrac{d}{\upsilon}$ (figure 3). The amplitude of the charge pulse can be determined from

$$\Delta Q_p = k \frac{\upsilon}{d} \int_0^\infty \rho_p(t) dt \qquad (5)$$

where k is a constant of proportionality with appropriate dimensions. If the pulse of concentration is short compared to $\dfrac{d}{\upsilon}$ it can be regarded as a Dirac pulse :

$$\rho_p(t) = \rho_0 \delta(t) \qquad (6)$$

where $\int_0^\infty \delta(t) dt = 1$ and ρ_0 is the amplitude of the concentration pulse.

The corresponding amplitude of the change in charge is

$$\Delta Q_p = \frac{k\rho_0\upsilon}{d} \qquad (7)$$

and the charge response may be described by the following equation

$$\Delta Q_p(s) = (\frac{k\rho_0\upsilon}{ds}).(1 - \exp(-\frac{ds}{\upsilon})) \qquad (8)$$

where s is the Laplace variable = $\sigma + j\omega$. Hence the electrode transfer function is

196

$$h(s) = (\frac{1}{\rho_0}).\Delta Q_p(s) = (\frac{k\upsilon}{ds}).(1-\exp(-\frac{ds}{\upsilon})) \qquad (9)$$

and, in the frequency domain,

$$h(j\omega) = (\frac{k\upsilon}{dj\omega}).(1-\exp(-\frac{dj\omega}{\upsilon})) \qquad (10)$$

Equation (10) may be rewritten :

$$h(j\omega) = \frac{k\upsilon}{d}[\sin(\frac{\omega d}{\upsilon}) - j(1-\cos(\frac{\omega d}{\upsilon}))] \qquad (11)$$

and the amplitude frequency response for the transfer function between ρ_0 and ΔQ_p is

$$|h(j\omega)| = \left|\frac{\Delta Q_p}{\rho_0}\right| = k\left|\frac{\sin(\frac{\omega d}{2\upsilon})}{\frac{\omega d}{2\upsilon}}\right| \qquad (12)$$

This transfer function is plotted in figure 4. Equation (12) enables the transfer function between the conveyed component concentration and the electrode sensor to be measured by recording the response generated by a travelling pulse of concentration passing between the electrodes, provided that the pulse length is short compared to the electrode length.

The transfer function minima occur when $sin(\frac{\omega d}{2\upsilon}) = 0$. Therefore $\frac{\omega d}{2\upsilon}$ =π, 2π, 3π,........

and minima occur when $\frac{\upsilon}{d} = \frac{\omega}{2\pi}, \frac{\omega}{4\pi}, \frac{\omega}{6\pi}$........

ELECTRODYNAMIC SENSOR

The circuit diagram of the electrodynamic transducer is shown in figure 5. The sensor consists of a plain metal rod, termed the electrode, which is isolated from the walls of the metal conveying pipe by an insulator, e.g. glass or plastic. This electrode has a capacitance to earth, which is very small (fraction of a pico Farad) but variable due to manufacturing tolerances. To minimise the effect of this capacitance a low value capacitor (several pico Farad) is connected in parallel with it. A resistor is connected in parallel with the capacitors to provide a charge/discharge path.

The charged particles in the pipe flow past the electrode and induce charge into the electrode. The flow of current through the resistor due to this induced charge results in a varying voltage. This voltage is buffered by a unity gain non inverting amplifier whose output provides a driven guard for the input circuitry and is amplified and conditioned by further circuitry.

MEASUREMENTS

Two experiments are presented. The first is used to determine the sensitivity of the sensing electrode using an axial array of sensors and flowing sand. The second investigates the spatial filtering effect by using a charge moving past the electrode at a known velocity.

Sensor sensitivity

The sensitivity is determined by arranging a number of differently sized sensors so that sand flows past each of them in turn as shown in figure 6. The level of charge on the flowing sand is very difficult to quantify, however since the sensors are evaluated at the same time, their outputs may be compared directly with one another. The small electrode at each end of the section checks that the flowing sand does not change its characteristics as it traverses the section.

The gain and linearity of each electronic amplifier is measured and the electrode sensitivities obtained by dividing the channel's voltage output by the channel's electronic gain as shown in table 1 below. A series of different sand flow rates are made to pass the electrodes and the resulting outputs determined. Typical results for several diameters of electrode are shown in figure 7.

diameter (mm)	(diameter)^2 (mm^2)	DC slope experiment (mV/g/s)	DC slope electronic circuit	Modified DC slope (μV/g/s)
2.5	6.25	0.242461	162	1.512
3	9	0.323281	160	2.005
3.5	12.25	0.323281	154	2.075
4	16	0.339445	156	2.105
5	25	0.452593	159	2.838
6	36	0.436421	156	2.757
10	100	0.775874	145	5.288

Table 1 : Modified DC slope

Spatial filtering

The spatial filtering experiment is based on the apparatus shown figure 8. A plastic ball is mounted on the wooden rod. This rod is rotated by a dc motor. The plastic ball obtains charge from an electrostatic ioniser. A charge pulse is created every time the ball passes the electrode sensor. The electrodynamic transducer senses the charge carried by the plastic ball and converts it to a physical voltage signal. The speed of the charged ball is varied by varying the voltage supply to the dc motor. The speed of the charged ball is calculated by measuring the circumference of the path traversed by the ball when it rotates and dividing this distance by the time between adjacent pulses.

RESULTS

Figure 7 shows the result of sensitivity versus the square of the sensor diameter. The diamond points show the actual data from the experiment. Linear regression analysis was used to achieve the best straight line for all the points. The value of the correlation coefficient is 0.94. The graph in figure 7 supports the suggestion that induced voltage is proportional to the

square of the sensor diameter (equation 3). The vertical axis intercept should pass through zero but the value of 1.23 may due to electrical noise and permanent offsets in the rectification stages. The equation of the line is :

electrode sensitivity = [0.038*(diameter squared) + 1.56] micro volts/g/s

for sand flowing in the test rig.

Figure 9 shows the spatial filtering effect for an electrodynamic sensor with a 3 mm diameter sensing electrode. The speed of the charged ball is 2.46 m/s. The power spectrum in figure 9 is an approximation of the sinc function. The first cut-off frequency is 88 Hz, the second is 288 Hz, the third is 512 Hz, the fourth is 732 Hz and the fifth cut-off frequency is 996 Hz.

CONCLUSION

This study shows the relationships between electrode diameter and sensitivity and spatial filtering. These results provide the information required to design optimum electrodynamic tomographic measurement systems.

ACKNOWLEDGEMENT

REFERENCES

Beck, M.S. and Plaskowski, A. 1987, *Cross correlation flow meters : their design and application*, Adam Hilger.

Bidin, A.R. 1993, *Electrodynamic sensors and neural networks for electrical charge tomography*, PhD Thesis, Sheffield Hallam University.

Gajewski, J.B. 1989, Continuous Non-contact measurement of electric charges of solid particles in pipes of pneumatic transport Part I & II, *Conference Record of the 1989 IEEE/IAS annual meeting*, San Diego, USA.

Hammer, E.A. and Green, R.G. 1983, The spatial filtering effect of capacitance transducer electrodes, *J. Phys. E : Sci. Instrum.*, Vol. 16, pg. 438-443.

Kelly, E.G. and Spottiswood, D.J. 1989, The theory of electrostatic separations: A review Part 3: Particle Charging, *Minerals Eng.*, vol. 2 No 2, page 193-205.

King, P.W. 1973, Mass flow measurement of conveyed solids, by monitoring of intrinsic electrostatic noise levels, *Pneumotransport 2 : Second international conference on the pneumatic transport of solids in pipes*, page D2-9 - D2-17.

Shackleton M.E. 1981, *Electrodynamic sensors for process measurement*, MPhil Thesis, University of Bradford.
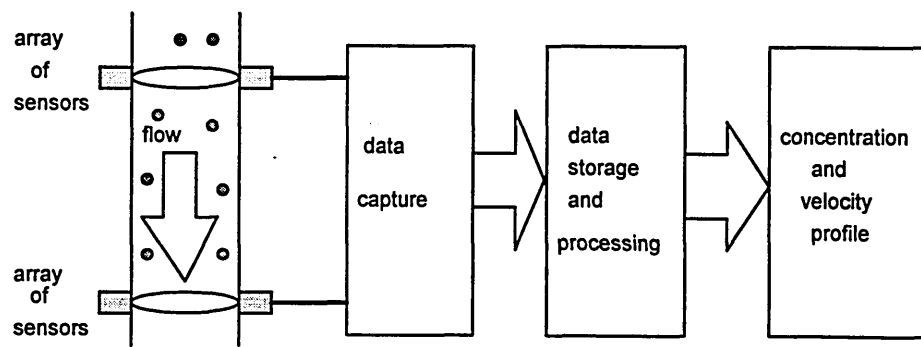
Figure 1 : A basic system for process tomography

Sensor (Cross section area $= \pi R_e^2$)

R_e = Radius of the electrode sensor

R_i = Radius of sphere
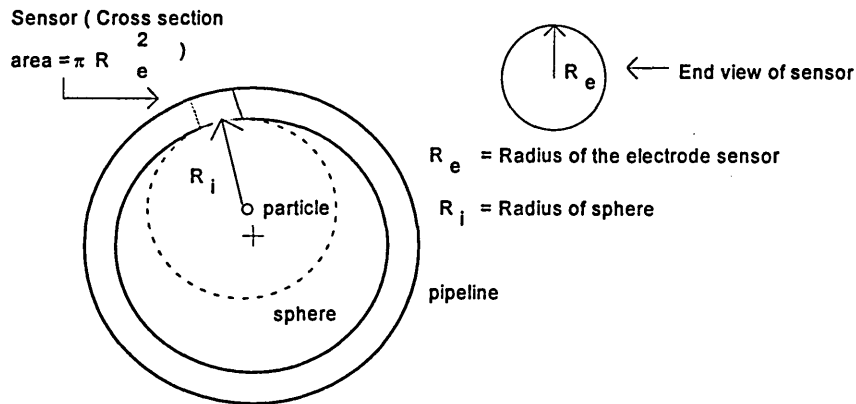
Figure 2 : Model of a charged particle in a sensing volume

(a) : A pulse $\rho(t)$ passes the electrode

(b) : A rectangular pulse of duration d/υ
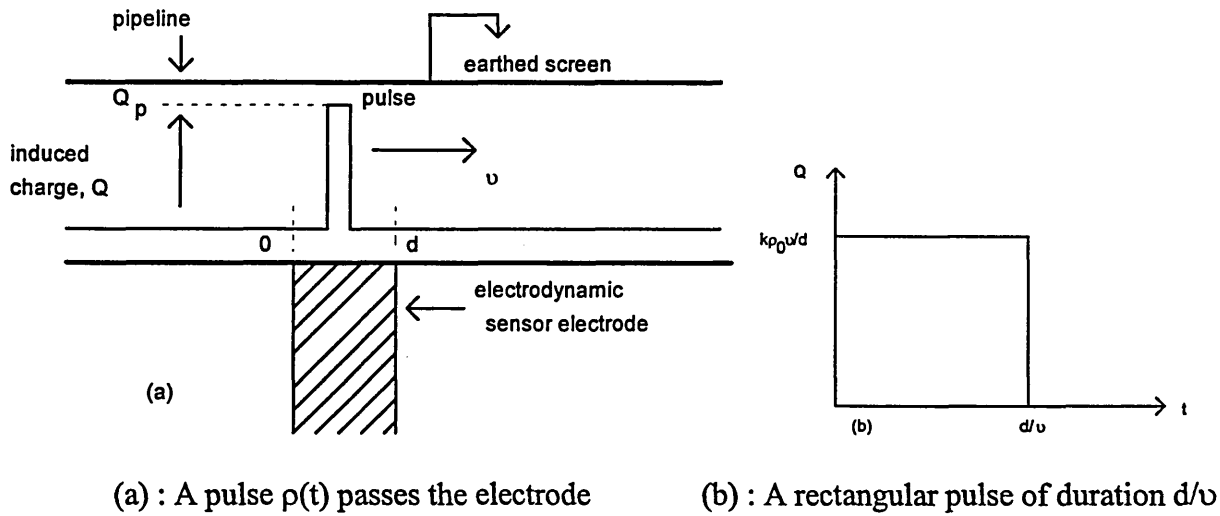
Figure 3 : Time history of concentration pulse

200
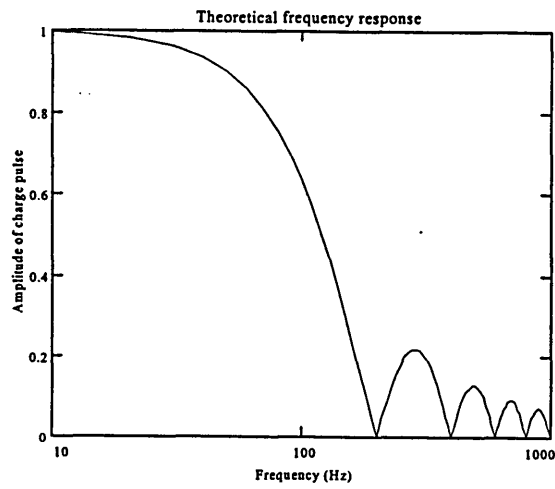
Figure 4 : Theoretical transfer function, $\upsilon = 2$ m/s, d = 0.01 m and $f_o = 200$ Hz
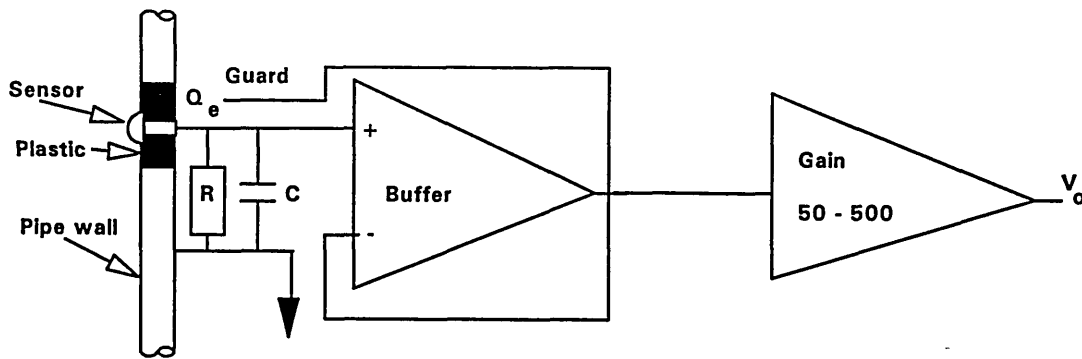
Figure 5 :The transducer circuit
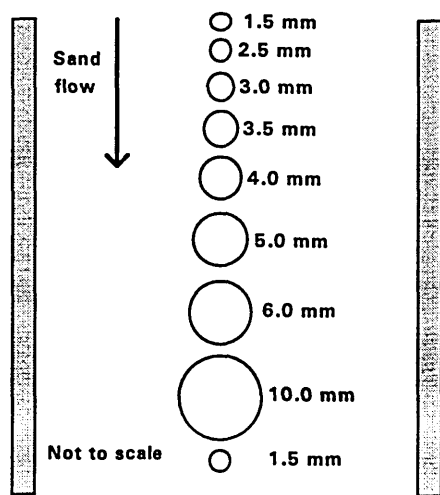
Figure 6. Arrangement of sensors for sensitivity measurements
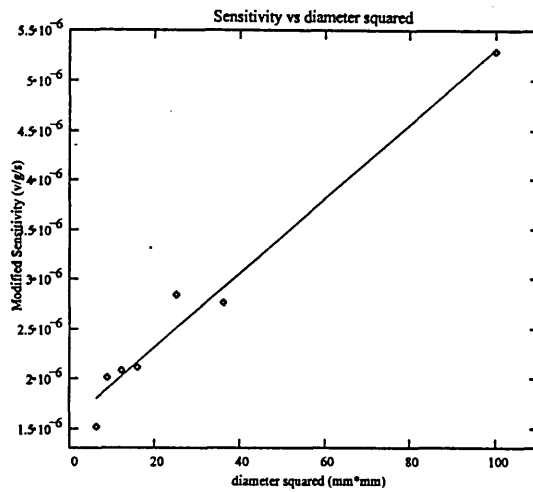
Figure 7 : Sensitivity versus diameter squared
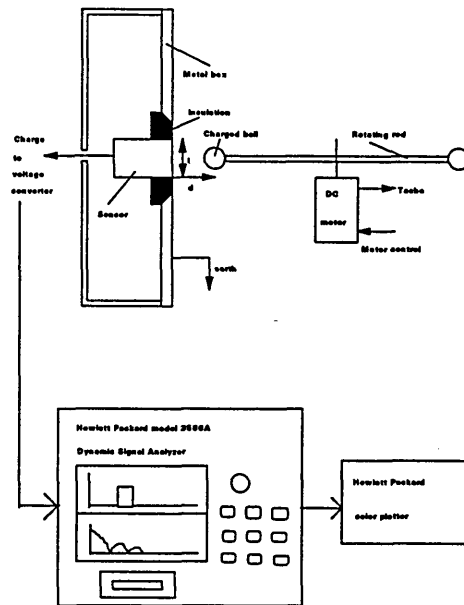
Figure 8 : Experiment setup for spatial filtering
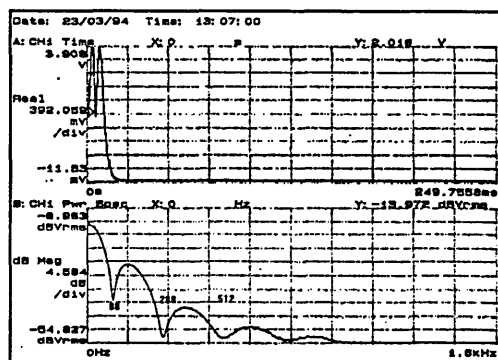
Figure 9 : Spatial filtering result for time and frequency domain

202

Electrodynamic Sensors for Process Tomography

R G Green[1], J Cottam[1], K Evans[1], A Goude[1], M Henry[3], C S Johnson[1], A Meehan[1], B Naylor[1], M F Rahmat[1,2].

1.   School of Engineering Information Technology, Sheffield Hallam University, Sheffield, S1 1WB, UK.
2.   Department of Control Engineering, Faculty of Electrical Engineering, Universiti Teknologi Malaysia, Jalan Semarak, 54100 Kuala Lumpur, Malaysia.
3.   Department of Chemical Engineering, University of Bradford, Bradford BD7 1DP UK.

1. Introduction

Transducers which sense the electrostatic charge carried by dry solids have applications in determining flow parameters e.g. the velocity of conveyed materials, the solids volume flow rate in pneumatic conveyors [1]. The measurement is based on charge being induced into the sensor as the charged particles flow past. The transducer is robust, low cost and has potential for applications in process tomography. In process tomography several identical transducers provide measurements from a section of the process being monitored which are then used to reconstruct dynamic images of the movement of the material within the section being monitored.

For applications where the process is varying rapidly, e.g. pneumatically conveyed solids, the measurement system characteristics should be known and the first part of this paper investigates the relationships between sensor size, sensor sensitivity and the frequency bandwidth, termed the spatial filtering effect, of the transducer signals. The second part discusses the application of electrodynamic sensors to tomographic imaging.

2. Sensor theory.

The theoretical relationships between the size of the electrode, the sensor sensitivity and the frequency bandwidth of the induced signal due to an impulsive input are derived. These models are tested using a rotating machine where the velocity and size of the moving charged particle can be controlled and using flowing, dry sand.

2.1. *Electrode sensitivity*

The electrode sensitivity is modelled by considering the effect of a single charged particle, q, as it moves vertically downwards at a constant velocity, v. Then for the single charged particle, assumed to be a point charge of value q, the field is uniformly radial

$$E = \frac{q}{4\pi r_i^2 \varepsilon_0} \qquad (1)$$

This point charge induces a potential onto the surface of the small, flat electrode used to sense the change in potential at a point on the wall of a non-conducting or dielectric pipe. It is assumed that there are no other interacting fields on the electrode since there is no surface charge on the pipe wall. For a given sensor, the cross-sectional area is πr_e^2 which is considered normal to the flux (figure 1). So the proportion of flux passing through the sensor due to the charged particle at a distance r_i from it is

$$\frac{\pi r_e^2}{4\pi r_i^2} \qquad (2)$$

Sensor (Cross sectional area = πR_e^2)

End view of sensor

R_e = Radius of the electrode sensor

R_i = Radius of sphere

pipeline

sphere

particle

Figure 1 : Model of a charged particle in a sensing volume

The charge, Q_e, induced in the sensor is proportional to q. Hence,

$$Q_e = \frac{kqr_e^2}{r_i^2} \qquad (3)$$

This charge is stored on a capacitor (figure 4) and provides a voltage V_e given by

$$Q_e = CV_e \qquad (4)$$

This voltage is amplified, rectified and some smoothing applied. Equation 3 suggests the amount of charge induced onto an electrode depends upon the radius of the electrode squared. The sensitivity of the sensor is defined as $\frac{Q_e}{q_i}$. This value is

difficult to determine because q_i is difficult to control or measure directly and in this paper a series of sensor diameters are compared simultaneously so that the same q_i is detected by them all.

2.2. The spatial filtering effect

The spatial filtering effect arising from capacitance electrodes is described in a paper by Hammer and Green [2], which relates the velocity of flowing discontinuous material to the frequency bandwidth of the sensed signal. This paper extends the concept to electrodynamic sensors. Assume that a single charged particle moving past the sensor at a distance d, with a velocity v, can be considered as a pulse of charge q(t). This moving charge results in a charge being induced into the sensor. If the sensor is shielded by the surrounding earthed screen so charge is only induced into the sensor as the particle passes along its length and assuming the inverse square law applies, the induced charge can be described by a rectangular pulse of duration a/v (figure 2). The amplitude of the charge induced into the sensor is described by:

$$\delta q_i(t) = k\frac{v}{a}\int_0^\infty \frac{q(t)}{d^2}dt \tag{5}$$

where q(t) represents the charge pulse provided by the moving particle and k is a constant of proportionality with appropriate dimensions. If the pulse duration is short compared with a/v it may be regarded as a Dirac pulse:

$$q(t) = q_o\delta(t) \tag{6}$$

and

$$\int_0^\infty \delta(t)dt = 1 \tag{7}$$

and q_o is the amplitude of the charge pulse.

The amplitude of the induced charge is:

$$\delta q_i = k\frac{vq_0}{ad^2} \tag{8}$$

The transfer function of the charge response may be written

$$\delta q_i(s) = (\frac{kvq_0}{ad^2 s})(1-\exp(-\frac{as}{v})) \tag{9}$$

where s is the Laplace operator. Hence the electrode transfer function is

$$g(s) = (\frac{kv}{ad^2 s})(1-\exp(-\frac{as}{v})) \tag{10}$$

which may be written in the frequency domain as

$$g(j\omega) = (\frac{kv}{ad^2 jw})(1-\exp(-\frac{aj\omega}{v})) \tag{11}$$

The effect of a and v on the modulus of equation 11 is a sync function, shown graphically in figure 3
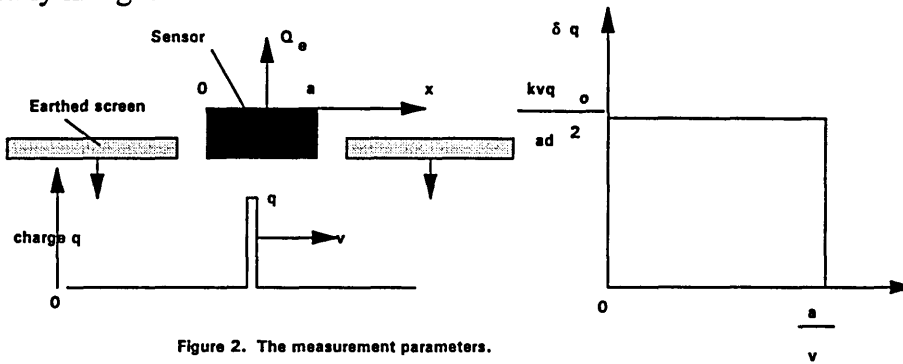
Figure 2. The measurement parameters.
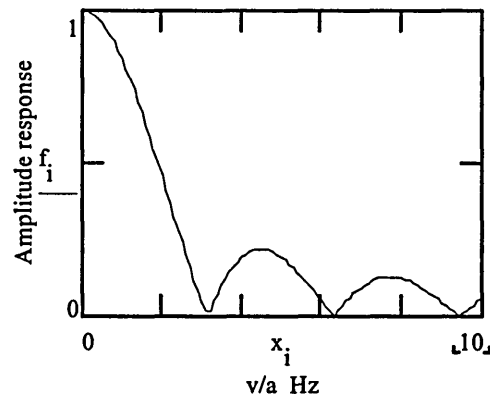
Figure 3. The predicted spatial filtering effect response.

The transfer function minima occur when $sin(\frac{\omega d}{2\upsilon}) = 0$. Therefore $\frac{\omega d}{2\upsilon} = \pi, 2\pi, 3\pi,...$

and minima occur when $\frac{\upsilon}{d} = \frac{\omega}{2\pi}, \frac{\omega}{4\pi}, \frac{\omega}{6\pi}$......... (12)

3. Electrodynamic transducer

A schematic circuit diagram of the electrodynamic transducer used in the tests is shown in figure 4.
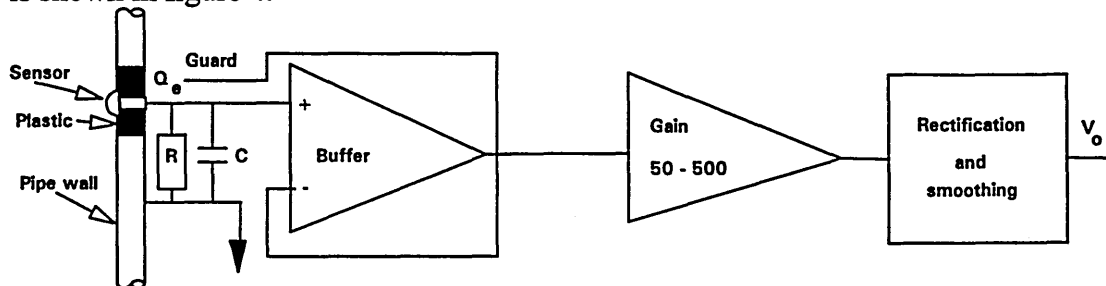
Figure 4. The transducer circuit.

The sensor consists of a metal rod, termed the electrode, which is isolated from the walls of the metal conveying pipe by an insulator, e.g. glass or plastic. This electrode

has a small but variable capacitance to earth (fraction of a pico Farad), due to manufacturing tolerances. To minimise the effect of this capacitance a low value capacitor (several pico Farad) is connected in parallel with it. A resistor is connected in parallel with the capacitors to provide a charge/discharge path. The charged particles in the conveyor flow past the electrode and induce charge into it. The flow of current through the resistor due to this induced charge results in a varying voltage. This voltage is buffered by a unity gain, non inverting amplifier whose output provides a driven guard for the input circuitry and is amplified and conditioned by further circuitry.

Two experiments are presented. The first is used to determine the sensitivity of the electrode using an array of sensors and flowing sand. The second investigates the spatial filtering effect by using a charge moving past the electrode at a known velocity.

3.1. *Electrode sensitivity*

The sensitivity is determined by arranging a number of differently sized sensors so that sand flows past each of them in turn (figure 5). The level of charge on the flowing sand is very difficult to quantify, however since the sensors are evaluated at the same time their outputs may be compared directly with one another. The small electrode at each end of the section checks that the flowing sand does not change its characteristics as it traverses the section.
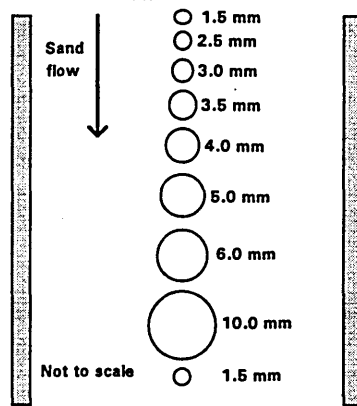
Figure 5. Arrangement of sensors for sensitivity measurements

A series of different sand flow rates are made to pass the electrodes and the resulting outputs determined. The results for each sensor are plotted graphically and a straight line regression fitted to the points; figure 6 shows a typical result for the 10 mm

207

diameter electrode. The transducer sensitivity, consisting of the electrode sensitivity and the amplifier gain, is defined as the gradient of the graph (mV/g s^{-1})

The gain and linearity of each electronic amplifier is measured and the electrode sensitivity, defined as the transducer sensitivity divided by the electronic voltage gain, is shown in table 1 and figure 7. Figure 7 shows the result of sensitivity versus the square of the sensor diameter. The diamond points show the actual data from the experiment. Linear regression analysis was used to achieve the best straight line for all the points. The value of the correlation coefficient is 0.94. This graph supports the suggestion that the induced voltage is proportional to the square of the sensor diameter (equation 3).
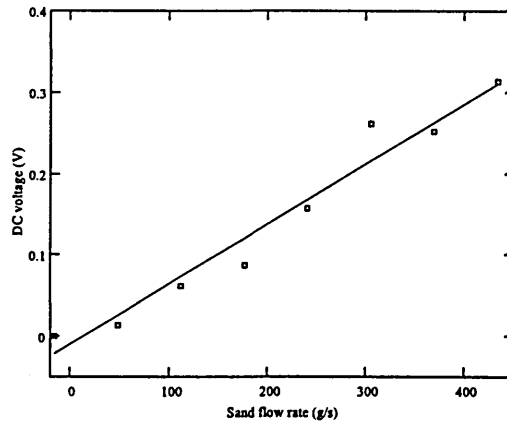
Figure 6. A typical graph for determining transducer sensitivity.

Electrode diameter (mm)	(Electrode diameter)^2 (mm^2)	Transducer sensitivity (mV/g/s)	Electronic gain	Electrode sensitivity (mV/g/s)
2.5	6.25	0.242461	162	0.00150
3	9	0.323281	160	0.00202
3.5	12.25	0.323281	154	0.00210
4	16	0.339445	156	0.00218
5	25	0.452593	159	0.00285
6	36	0.436421	156	0.00280
10	100	0.775874	145	0.00535

Table 1. Electrode sensitivity.

3.2. Spatial filtering

The spatial filtering experiment is based on the apparatus shown figure 8. A plastic ball is mounted on the wooden rod. This rod is rotated by a dc motor. The plastic ball obtains charge from an electrostatic ioniser. A charge pulse is created every time the ball passes the electrode sensor. The electrodynamic transducer senses the charge carried by the plastic ball and converts it to a voltage signal. The speed of the charged ball is varied by varying the voltage supply to the dc motor. The speed of the charged ball is calculated by measuring the circumference of the path traversed by the ball when it rotates and dividing this distance by the time between adjacent pulses.

Figure 7. Electrode sensitivity versus electrode diameter squared.
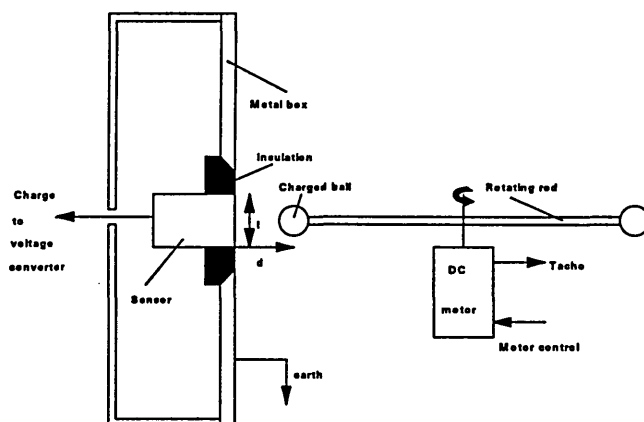
Figure 8 : Experimental set-up for spatial filtering

Figure 9 shows the spatial filtering effect for an electrodynamic sensor with a 3 mm diameter sensing electrode. The speed of the charged ball is 2.46 m/s. The power spectrum is an approximation of the sinc function, with the first cut-off frequency at 88 Hz. The spatial filtering effect is repeated for the range of electrode

sizes. For a range of velocities the corresponding frequency of the first peak is determined. Equation 12 is used to calculate the predicted length of sensor corresponding to the measured frequency and velocity; this length is termed the effective length of the electrode. The mean and standard deviation of the effective length is calculated for each electrode and the bars shown in figure 10 show the mean ±3 standard deviations. This shows the unexpected effect that the effective electrode is approximately 50 mm for the range of conditions in this experiment. Tests investigating the input network of the circuit shown in figure 4 show that the time constant of the input RC is an important factor in defining the effective electrode length. Shortening the time constant, by reducing the value of R, decreases the effective electrode length, but reduces the electronic gain of the system, e.g.

Time constant seconds	Effective electrode length mm
1.55×10^{-5}	42
3.60×10^{-6}	28
1.42×10^{-6}	26

Table 2 : Relationship between time constant and effective electrode length
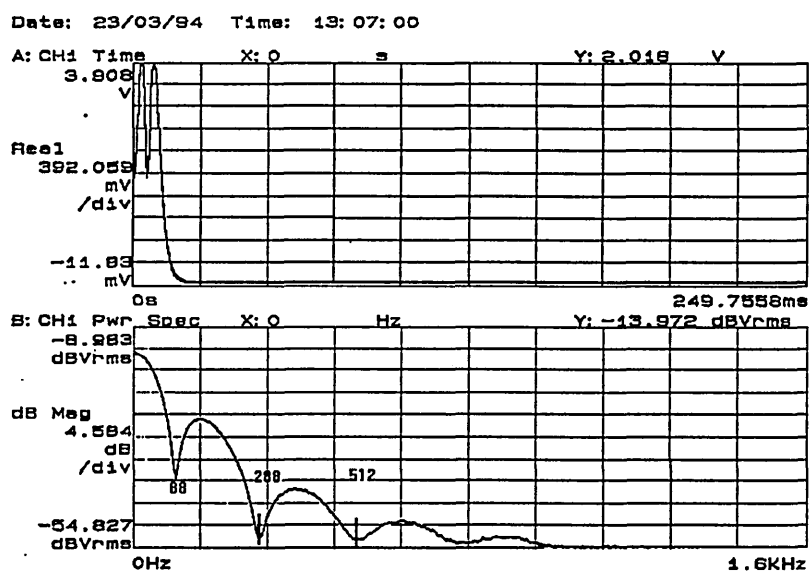
Figure 9. Spatial filtering for a 3 mm diameter sensor with v= 2.46 m s^{-1}

An improved circuit by Shackleton [1], designed to have a wide bandwidth, is being investigated with the specific aim of minimising the effective electrode length.
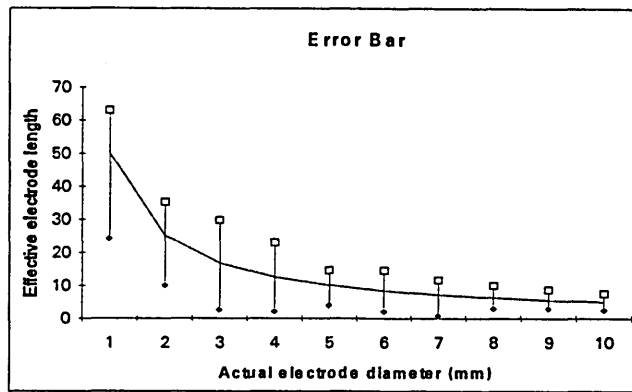
Figure 10. Effective electrode length versus actual electrode length.

3.3. *Discussion on electrode tests*

The tests investigating the relationship between electrode diameter and electrode sensitivity suggest a square law as predicted by equation 3. The effective electrode length appears to be independent of the physical length of the sensor at 50 mm, but is dependent upon the design of the electronic circuit attached to the sensor. This is currently being investigated.

4. Process tomography using electrodynamic sensors.

4.1. *Introduction*

In this part of the project electrodynamic sensors and image reconstruction algorithms are being developed to produce images of velocity and concentration profiles within a cross-section of a pipe conveying the dry particulates. The basic system for process tomography is shown in figure 11. The three basic components in a process tomography system are :-(a) the sensors, (b) the data acquisition system and (c) the image reconstruction system and display. A difficulty with producing concentration images using electrodynamic sensors is that the reconstruction algorithms, which process the measured data to convert the information into a concentration profile, are dependent on the initial distribution of the solids in the sensing volume, i.e. the flow regime. If the flow regime is known, the reconstruction may be simplified and accelerated. Some flow regimes may be recognised by a suitably organised and trained neural network.

This section describes a neural network designed to classify the flow regime and select the appropriate reconstruction algorithm.

211
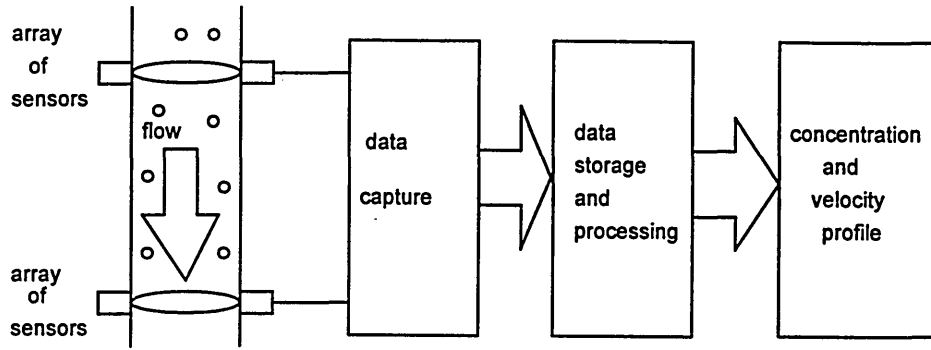
Figure 11. A process tomography system

4.2. *The measurement system*

A block diagram of the measurement system is shown in figure 12. Thirty-two sensors and transducers are positioned at equal intervals around the circumference of the pipe to provide a sensing array. This array is surrounded by an earthed metal screen, which is also connected to the pipe wall. The flowing charged particles induce charges into the sensors. These signals are conditioned, rectified and low pass filtered. These thirty-two signals are sampled and converted to eight bit format. They are then sent to both the neural network and the reconstruction algorithm.
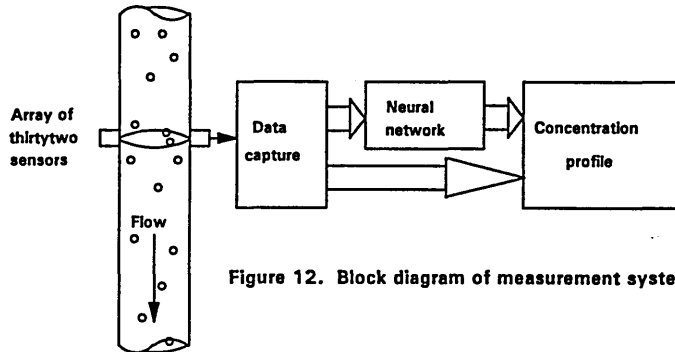
Figure 12. Block diagram of measurement system

4.3. *Neural networks*

The neural network consists of a three layer perceptron consisting of thirty-two input neurons, a reference neuron, eight hidden neurons and eight output neurons (figure 13). All input neurons are connected to all the hidden layer neurons. Each neuron in the hidden layer is connected to each output neuron. Both the hidden and output layer neurons use a thresholding function in the shape of a sigmoid function. The sigmoid function is represented by equation 13:

$$f(net) = \frac{1}{(1 + e^{-k(net)})} \tag{13}$$

212

and has the range $0 < f(net) < 1$, where k is a positive constant that controls the spread of the function and f(net) is the Heaviside function. The system is trained using the Back Propagation Rule. This is applied by feeding appropriately processed and stored signals from the transducers for the known flow regimes to be identified into the network. The network generates a solution, which is compared with the known solution to provide an error. This error is fed back and used to modify the weightings between individual neurons. The process is repeated until the error reaches a predetermined level.

A typical data set is shown in figure 14. The input data consists of thirty-two values representing the voltages on the sensors. These voltage points are represented graphically and have been joined up to produce a voltage profile around the circumference of the pipe. A column of numbers representing the output neuron values is also included. The flow regime shown in figure 14 represents stratified flow.
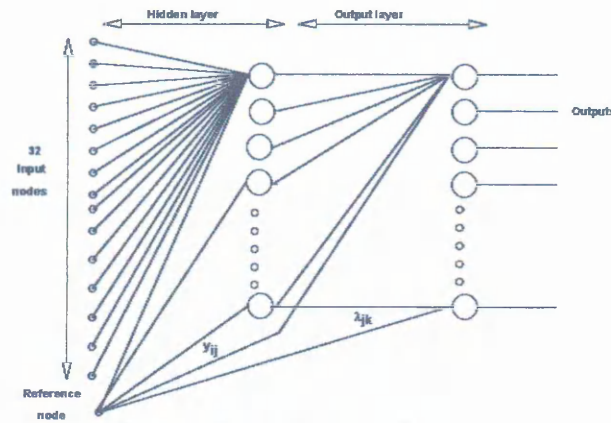
Figure 13. The multilayer perceptron
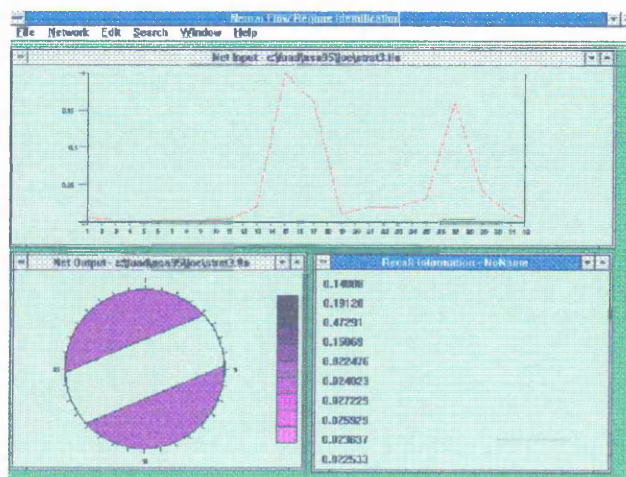
Figure 14. Example of input and output data for the neural network.

213

4.4. *The reconstruction algorithm*

This reconstruction algorithm is based on sensitivity distributions reported by Bidin [3] and ratio back projection. Each block of thirty-two sensor voltage values are normalised to the maximum value of the set to simplify the computation. The maximum value is stored to scale the calculated values. The pipe is considered as being divided into five radial sections and thirty-two arcs (figure 15). The algorithm calculates the quantity of charge in each sector corresponding to the value on the appropriate sensor taking into account the flow profile, which is used as a weighting filter with values stored in a look up table. These calculated values are mapped onto a rectangular grid representing the cross-section of the conveyor. The loading of all the pixels are summed to provide an estimate of the total concentration in the cross-section.
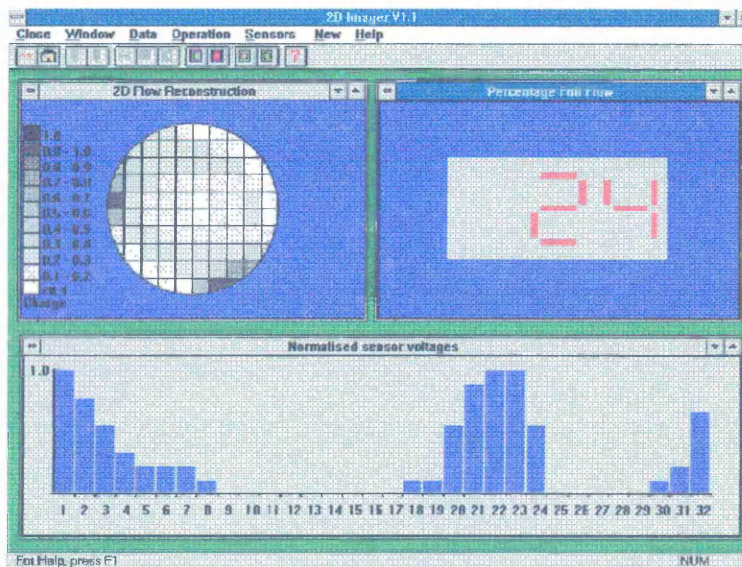
Figure 15 : Image of the cross section pipe

5. Discussion

Electrical charge tomography is a relatively new technique for imaging in lightly loaded pneumatic conveyors. The successful application of the method requires careful design of the transducers (electrodes and electronics) to ensure maximum sensitivity commensurate with a bandwidth adequate with the expected range of flow velocities. Neural networks can identify several flow regimes and, after further development, may be capable of direct flow imaging [4]. However, the present work uses a purpose built reconstruction algorithm to provide tomographic images and an averaged concentration for the cross-section. Plant tests are required to verify the accuracy of the algorithms.

6. References

[1] Shackleton M.E. 1982, *Electrodynamic sensors for process measurement*, MPhil Thesis, University of Bradford.

[2] Hammer, E.A. and Green, R.G. 1983, The spatial filtering effect of capacitance transducer electrodes, *J. Phys. E : Sci. Instrum.* , Vol. 16, pg. 438-443.

[3] Bidin, A.R. 1993, *Electrodynamic sensors and neural networks for electrical charge tomography*, PhD Thesis, Sheffield Hallam University.

[4] Nooralahiyan, A. Y., Hoyle, B. S. and Bailey, N. J., *Performance on neural network with noise and parameter variation in electrical capacitance tomography*, Process Tomography 1995 - Industrial for Industrial Processes, Ed M. S. Beck et al, UMIST.

Concentration profiles of dry powders in a gravity conveyor using an electrodynamic tomography system.

R G Green[1], M F Rahmat[2], K Evans[1], A Goude[1], M Henry[3], J A R Stone[1].

1. School of Engineering, Sheffield Hallam University, Sheffield
2. Control Dept., Faculty of Electrical Engineering, Universiti Teknologi Malaysia
3. Chemical Engineering Department, University of Bradford, Bradford

Abstract

This paper presents results for a tomographic system using an array of electrodynamic sensors. Sensitivity maps are derived for the individual sensors and then used by a back projection algorithm to calculate concentration profiles from measured sensor values. Limitations in linearity over the sensing area are reduced by applying a filter to the images. The filtered back projection algorithm is tested on both uniformly and artificially produced non-uniformly distributed solids flows.

1. Introduction

Measurement of concentration profiles of dry powders flowing in pneumatic and gravity conveyors is a problem which has to be solved in order to progress to determination of volume flow rates. Present methods of concentration measurement include capacitance [McKee et al 1995], optical [Green et al 1996], gamma densitometer [Yan et al 1995] and electrodynamic sensors, each with specific advantages and limitations.

Capacitance sensors are robust, low cost and are very useful for measurement with dense phase conveying of dry powders. However they pose problems where the conveying density is below 10 % vol./vol., they have a soft field mode of sensing where the shape of the electrical field depends upon the distribution of the dielectric within it and they have a large sensing volume due to the axial length of the electrodes [Hammer and Green 1983].

In comparison, optical sensors have a relatively high spatial resolution [Green et al 1995], but there are problems associated with keeping the optics clear of dust.

Gamma densitometers are potentially very linear in their response to solids' concentration and have the advantage of use without damaging the integrity of the conveyor. However, in order to provide high count rates the activity of the source may cause safety problems [Yan et al 1995].

216

Electrodynamic sensors are robust, low cost and sensitive to low flow rates of dry solid material. This paper explains their use in the determination of concentration profiles within the measurement cross-section of a gravity drop conveyor.

2. The measurement system

Transducers which can be used to sense the electrostatic charge carried by dry solids have applications in determining flow parameters in pneumatic conveyors, e.g. the velocity of conveyed materials [Featherstone et al 1983, Yan et al 1995b] and the solids mass flow rate [King 1973]. Dry solids, moving through a conveyor, generate static electric charge by friction with the conveyor wall. The amplitude of this charge depends on many factors including type, shape and size of materials, humidity, etc. [Shackleton 1982], however, in many manufacturing systems the process control provides repeatable conditions, resulting in repeatable levels of charge on the particles. Measurements are based on charge being induced in the sensors as they are passed by the flowing charged particles. These induced charges are converted to voltages, amplified to a level suitable for the data acquisition system and processed off-line.

Sensors generally consist of metal structures insulated from the walls of the conveyor. In process measurements ring electrodes are widely used and have been thoroughly investigated [Shackleton 1982, Yan et al 1995b]. However, they are limited in their application as they provide averaged signals relating to the concentration of the conveyed material and do not allow the determination of the concentration profile.

Discrete electrodynamic transducers are robust, low cost and have the potential to be used for process tomography [Williams and Beck 1995] where several identical transducers (typically 8, 16 or 32) are positioned around the vessel being interrogated. These provide the data which is used to reconstruct dynamic images of the movement of the material being monitored.

In the work presented in this paper, an array of sixteen, equi-spaced, circular sensors is mounted around the circumference of the vertical flow pipe (figure 1).
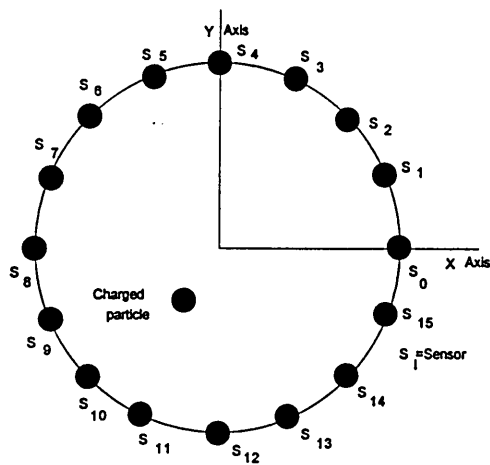
Figure 1. Cross-section through pipe at measurement section

The solids are fed into the pipe from a hopper at a controlled rate via a rotary feeder (figure 2). Information from the sensors is collected by a proprietary data acquisition system and processed off-line to produce tomographic images of the solids concentration within the cross-section.
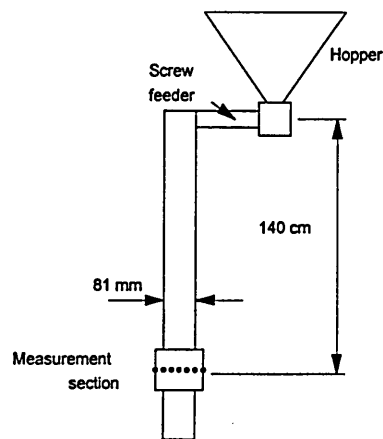
Figure 2. The gravity flow rig

A typical sensor calibration graph for the flow of dry sand is shown in figure 3.
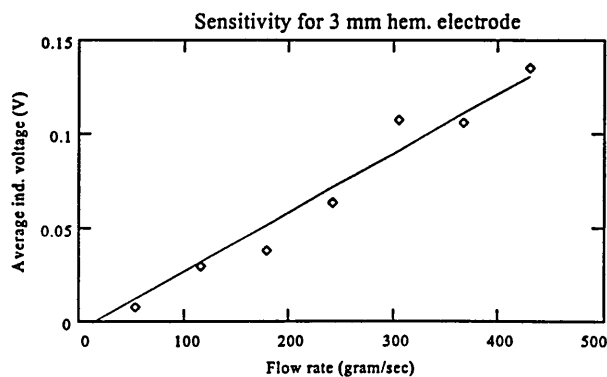
Figure 3. Averaged induced voltage versus mass flow rate for 3 mm hemispherical electrode.

The tomographic image is calculated from the measurements using a filtered back projection algorithm, which is derived from the forward problem.

2. The forward problem

The forward problem determines the theoretical output of each of the sensors when the sensing area is considered to be two dimensional and contains a uniformly distributed charge of σ coulombs per square metre. The cross-section of the pipe is mapped onto a nine by nine rectangular array consisting of 81 pixels as shown in figure 3 below.
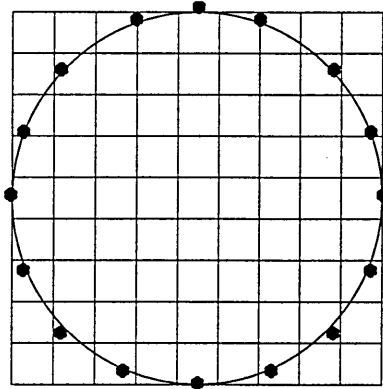
Figure 3 : 9x9 rectangular array consists of 81 pixels

Each sensor is considered separately and the effect on it due to the uniform surface charge, σ Coulombs m^{-2}, on each pixel determined. To minimise boundary problems the sensor is placed 0.5 mm outside the pipe wall. Each pixel is considered in turn. The sensitivity map is generated by calculating the charge which a chosen pixel would induce into the sensor.

Calculation of the sensitivity map for sensor one is outlined below.
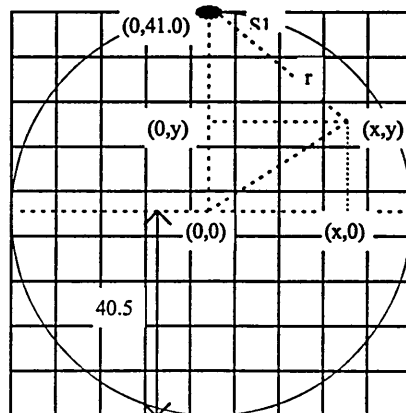
Figure 4: Sensitivity model for sensor 1

The centre of the pipe has rectangular co-ordinates (0,0). The pipe diameter is 81 mm and each pixel is 9x9 mm. The general sensitivity equation corresponding to sensor 1 is,

$$I_1 = \iint \frac{\sigma}{r^2} dA = \int_x dx \int_y \frac{\sigma}{x^2 + (41-y)^2} dy$$

where (x,y) are the co-ordinates of the part of the pixel contributing to the sensor output, r is the distance of the charge to the sensor and the inverse square law is obeyed. The total induced charge for sensor 1 when σ is assumed to be $1\ C\ m^{-2}$ is,

$$I_1 = \int_{-40.5}^{40.5} dx. \int_{-\sqrt{40.5^2-x^2}}^{\sqrt{40.5^2-x^2}} \frac{1}{x^2 + (41-y)^2} dy \approx 11.75 \text{ Coulombs}$$

However the sensitivity map requires the contribution from each pixel to be evaluated. Each pixel is identified numerically, the first number is the column number, the second is the row number starting with 11 for the top left hand pixel. Two examples of the sensitivity calculation are shown below.

$$Pixel51 = \int_{-4.5}^{4.5} dx. \int_{31.5}^{40.5} \frac{1}{x^2 + (41-y)^2} dy \approx 6.20$$

$$Pixel59 = \int_{-4.5}^{4.5} dx. \int_{-40.5}^{-31.5} \frac{1}{x^2 + (41-y)^2} dy \approx 0.01$$

This is repeated for all pixels. Complete pixels and parts of pixels outside the pipe contribute zero induced charge to the sensor and so have a sensitivity value of zero i.e. pixel 11, 12, 21, 81, 91, 92, 18, 19, 29, 89, 98 and 99. However, pixels intersected by the pipe boundary have a contribution to the induced charge from the fraction of the pixel within the conveyor.

The resulting sensitivity map for sensor 1 is shown in figure 5.

0	0	0.13	0.78	6.20	0.78	0.13	0	0
0	0.07	0.16	0.31	0.44	0.31	0.16	0.07	0
0.02	0.06	0.10	0.14	0.16	0.14	0.10	0.06	0.02
0.03	0.05	0.06	0.07	0.08	0.07	0.06	0.05	0.03
0.03	0.03	0.04	0.05	0.05	0.05	0.04	0.03	0.03
0.02	0.02	0.03	0.03	0.03	0.03	0.03	0.02	0.02
0.01	0.02	0.02	0.02	0.02	0.02	0.02	0.02	0.01
0	0.01	0.02	0.02	0.02	0.02	0.02	0.01	0
0	0	0.01	0.01	0.01	0.01	0.01	0	0

Sensitivity mapping in 3D
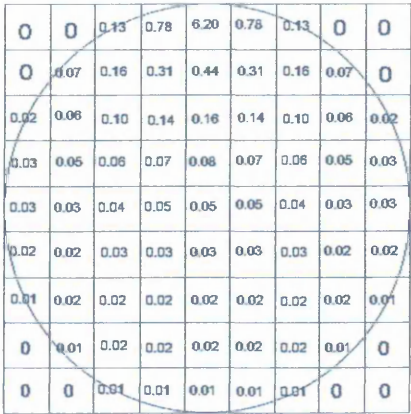
Figure 5. Sensitivity map for sensor 1   Figure 6. Sensitivity map in 3D for sensor 1
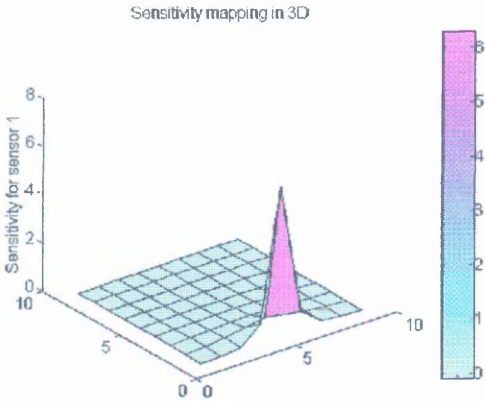
The sensitivity map for sensor 1 may be plotted in three dimensions (figure 6), where (x,y) represent the pipe cross-section and the z-axis the sensitivity. This shows the significant localised sensitivity of the sensor. These calculations are repeated for each of the sixteen sensors, resulting in sixteen separate sensitivity maps. These maps are then used to solve the inverse problem.

3. The Inverse Problem

Solution of the inverse problem aims to provide an image of the charge concentration distribution within the conveyor, which would result in the measured sensor outputs.

3.1 Basic back projection

A linearized back projection algorithm is used [Abdullah 1993]. The back projection algorithm combines each sensor reading with its sensitivity map to generate the charge concentration map within the pipe which would provide these readings (assuming all particles carry the same charge). The procedure is to multiply each sensor voltage reading by its sensitivity map to produce sixteen 9x9 matrices. The corresponding individual elements from the 16 matrices are summed to produce a single matrix i.e. the concentration matrix.

The theoretical concentration profile has been calculated assuming all the sensors are reading 1 Volt. The concentration matrix is shown in figure 7 with the relative position of the pipe mapped onto it. Figure 8 displays the result as a coloured tomogram, where colour relates to solids concentration.

0	0	5.38	3.15	7.32	3.15	5.38	0	0
0	6.9	2.12	1.56	1.41	1.56	2.12	6.9	0
5.38	2.12	1.29	1.03	0.97	1.03	1.29	2.12	5.38
3.15	1.56	1.03	0.86	0.82	0.86	1.03	1.56	3.15
7.32	1.41	0.97	0.82	0.77	0.82	0.97	1.41	7.32
3.15	1.56	1.03	0.86	0.82	0.86	1.03	1.56	3.15
5.38	2.12	1.29	1.03	0.97	1.03	1.29	2.12	5.38
0	6.9	2.12	1.56	1.41	1.56	2.12	6.9	0
0	0	5.38	3.15	7.32	3.15	5.38	0	0
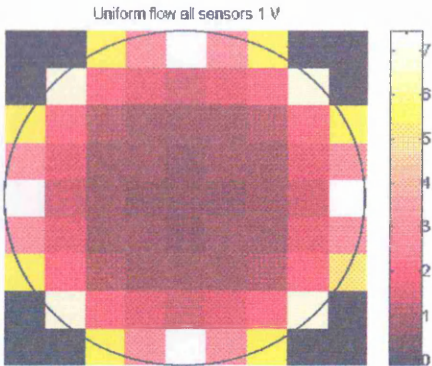
Figure 7. Theoretical numerical concentration distribution obtained using the linear back projection algorithm: all sensors set to 1 volt

Figure 8. Theoretical image of concentration distribution obtained using the linear back projection algorithm when all sensors is 1 volt

Figures 7 and 8 identify the limitation of the simple linear back projection algorithm; the low estimation of solids at the centre of the conveyor. This problem may be reduced by using a filtered back projection algorithm.

3.2 Filtered back projection

The major limitation of the linear back projection algorithm arises due to the non-linear sensing mechanism of the electrical charge transducer. When the conveyor has a uniformly distributed solids flow the resulting concentration matrix, calculated using the linear back projection algorithm, is not uniform at 7.32 units per pixel, but shows lower values as the centre of the pipe is approached, reaching 0.77 units at the centre. However a filter can be determined, which, combined with the back projection algorithm, provides a filtered linear back projection algorithm [Barber and Brown 1984]. This filter provides weighting to individual pixels to provide a uniform concentration profile.

The coefficients of the filter are obtained by assuming all the sensors have an output of 1 volt. and using these values to calculate the concentration matrix described in section 3.1. The expected result is a uniform concentration matrix with each values of 7.32 units per pixel.

The filter matrix is obtained by taking the maximum value of 7.32 units per pixel which is then divided by each value of pixel within the pipe mapping. The resulting filter is shown in figure 9.
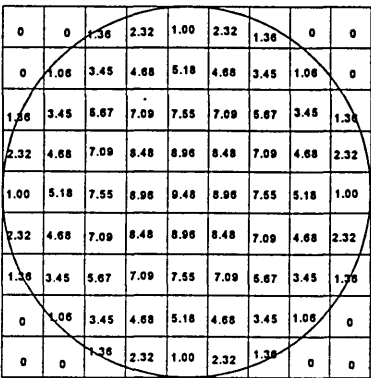
Figure 9. Full flow filter mask

Mathematically, this filter is only applicable to full flow. Similar filters should be calculated for different flow patterns. However to be useful, this requires the flow regime or flow pattern with the conveyor to be known. Flow regimes have been identified using an array of electrodynamic sensors placed around the circumference of a conveyor [Bidin et al 1993] as shown in figure 1.

A filter mask for the specific non-uniform flow of separated flow is shown in figure 10.
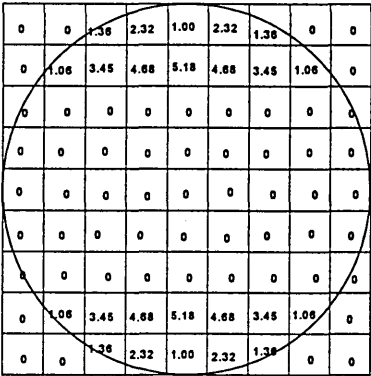
Figure 10: Separated flow filter mask

4 Results

Tests were made using both plastic particles approximately 3 mm in diameter and sand with a mean diameter of 600 μm over a range of solid flow rates. Non-linear concentration profiles were created by blocking sections of the conveyor upstream of the sensors with obstructions of know shape. A range of solid feed rates were used and the measurements were logged using a proprietary data acquisition system. The results were processed off-line using a PC with a 486

processor. The concentration profiles were determined using both linear back projection and filtered back projection algorithms.

0	0	1.17	0.71	1.69	0.81	1.45	0	0
0	1.83	0.52	0.37	0.34	0.38	0.49	1.32	0
1.34	0.56	0.33	0.26	0.24	0.24	0.28	0.42	0.90
0.82	0.41	0.27	0.22	0.20	0.20	0.23	0.32	0.58
1.99	0.40	0.27	0.22	0.20	0.20	0.22	0.31	1.51
1.02	0.48	0.30	0.24	0.22	0.22	0.24	0.35	0.68
1.91	0.71	0.40	0.30	0.26	0.27	0.32	0.49	1.10
0	2.50	0.69	0.47	0.39	0.41	0.54	1.61	0
0	0	1.77	0.96	0.19	0.84	1.46	0	0

Figure 11: Concentration profile obtained using the linear back projection algorithm: plastic

beads, full flow at a flow rate of 52 g/s

0	0	1.59	1.65	1.69	1.87	1.98	0	0
0	1.94	1.79	1.74	1.75	1.78	1.68	1.40	0
1.82	1.89	1.86	1.82	1.78	1.72	1.61	1.44	1.23
1.89	1.93	1.93	1.88	1.82	1.74	1.63	1.49	1.36
2.00	2.06	2.02	1.96	1.87	1.78	1.68	1.58	1.51
2.38	2.27	2.15	2.04	1.93	1.83	1.73	1.64	1.58
2.60	2.45	2.29	2.12	1.99	1.88	1.78	1.69	1.58
0	2.65	2.39	2.19	2.01	1.93	1.85	1.71	0
0	0	2.41	2.23	1.88	1.96	1.99	0	0

Figure 12. Measured image of concentration distribution obtained using the filtered linear back projection algorithm: plastic beads full flow at a flow rate of 52 g/s
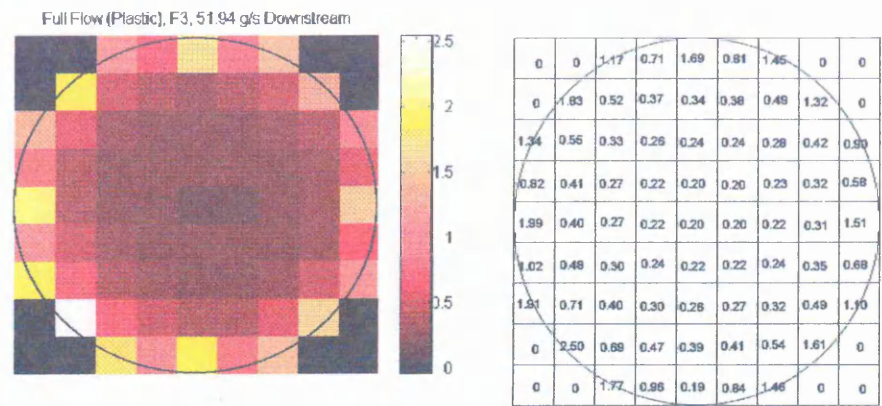

0	0	4.31	3.21	11.3	4.38	7.55	0	0
0	5.07	1.75	1.54	1.65	1.90	2.50	7.51	0
2.86	1.44	1.03	0.95	0.98	1.09	1.33	2.00	4.07
1.63	0.98	0.78	0.75	0.76	0.83	0.97	1.34	2.42
2.65	0.86	0.72	0.69	0.70	0.75	0.87	1.17	5.30
1.70	1.00	0.78	0.74	0.75	0.80	0.92	1.27	2.29
3.08	1.42	1.03	0.85	0.95	1.02	1.21	1.80	3.46
0	4.44	1.86	1.61	1.67	1.71	2.16	6.33	0
0	0	5.71	3.60	10.4	3.79	8.22	0	0

Figure 13. Measured image of concentration distribution obtained using the linear back projection algorithm: plastic beads separated flow at a flow rate of 52 g/s
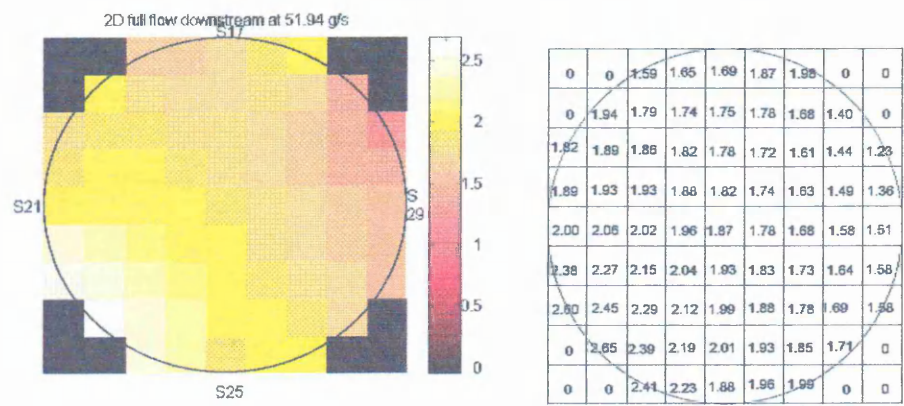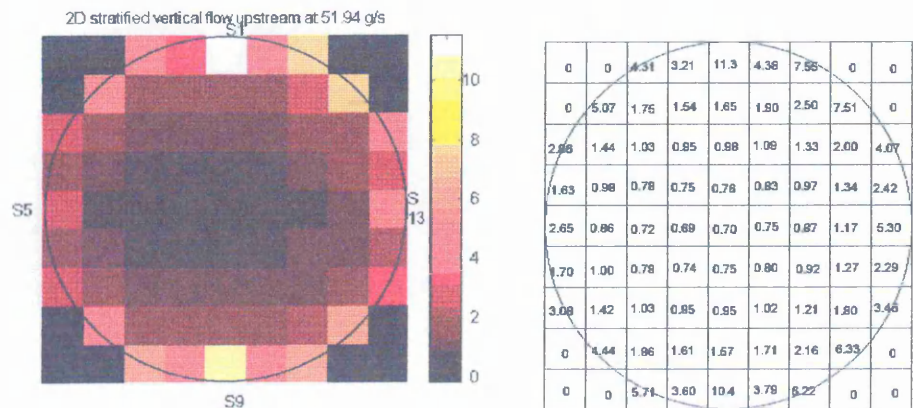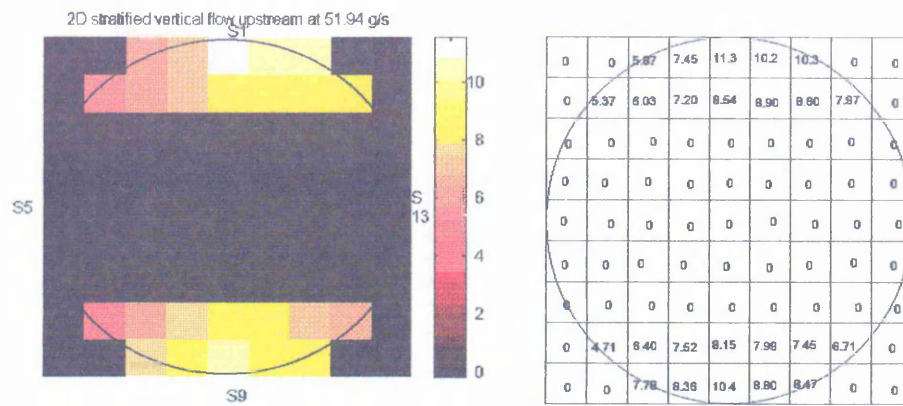
Figure 14. Measured image of concentration distribution obtained using the linear back projection algorithm: plastic beads separated flow at a flow rate of 52 g/s

5 Discussion of results

The measured results obtained for uniformly distributed solids flow, using the linearized back projection algorithm (figure 11), show concentration values are lower towards the centre of the conveyor as predicted. These measurements are improved by using the filtered back projection algorithm (figure 12).

The measured concentration profiles determined for non-uniformly distributed flow show that the solids are not uniformly distributed. However by visual inspection of the solid flow, the result obtained using the simple linear back projection algorithm (figure 13) seems less representative of the shape of the flow profile being produced than that obtained using the filtered back projection algorithm (figure 14).

In the tests, the error between the calculated concentrations and the measured flow rates had a standard deviation of 20% of calculated concentration when using the plastic beads. It is thought that the accuracy will be significantly improved by using a pneumatic conveyor rather than the gravity drop system and baffles, as the baffles may interact with the particles and modify the charge being carried by them.

6 Conclusions

Tomographic images of solids concentration may be obtained using electrodynamic sensors. The non-linear field of the sensor requires that the concentration profile be calculated using a filtered back projection algorithm. As with all electrodynamic sensors, quantitative values will only be reliable and repeatable if the process being monitored is well controlled in terms of

moisture content and particle size range. However, the system described in this paper provides a very low cost method for producing tomographic images of solids concentration profiles.

The system could be made to work on-line, but would require a dedicated data acquisition system and modifications to the algorithm. A processor capable of 25 Mflop should be capable of providing approximately 500 to 1000 concentration matrices per second. This paper describes a feasibility study into obtaining concentration profiles of flowing dry powders using electrodynamic sensors. Further testing with a wide range of materials and flow rates is required to determine the limitations of the measurement system.

7 References

Abdullah, M Z, "Application of resistive electrical impedance tomography to observe hydrocyclone separator dynamics." PhD Thesis, UMIST, 1993.

Barber, D C and Brown, B H, "Applied potential tomography" J. Phys. E: Sci. Instrum., Vol. 17, 1984, p 723-733.

Bidin, A R., Green, R G, Shackleton, M E, Taylor, R W, "Neural networks for flow regime identification with dry particulate flows." Part. Part. Syst. Charact. 10, (1993), pages 234-238.

Featherstone, A M, Green, R G, Shackleton, M E, "Yarn velocity measurement." J. Phys. E: Sci. Instrum., Vol. 16, 1983, p 462-464.

Green, R G, Horbury, N M, Abdul Rahim, R, Dickin, F J, Naylor, B D, Pridmore, T P, "Optical fibre sensors for process tomography.", Meas. Sci. Technol., Vol. 6, 1995, p1699-1704.

Green, R G, Abdul Rahim, R, Evans, K, Dickin, F J, Naylor, B D, Pridmore, T P, "Concentration profiles in a pneumatic conveyor by optical tomography measurement." Meas. Sci. Technol., Vol. 7, 1996, p419-422.

Hammer, E A and Green, R G, "The spatial filtering effect of capacitance transducer electrodes." J. Phys. E: Sci. Instrum., Vol. 16, 1983, p 438-443.

King, P.W, "Mass flow measurement of conveyed solids, by monitoring of intrinsic electrostatic noise levels." 2nd. Int. Con. on the Pneumatic Transport of Solids in Pipes, Cranfield, 1973.

McKee, S L, Williams, R A, Dyakowski, T, Bell, T, Allen, T, "Solids flow imaging and attrition studies in a pneumatic conveyor." Powder Technology, Vol. 82, p 105-113, 1995.

Shackleton ME, "Electrodynamic sensors for process measurement." MPhil Thesis, University of Bradford, 1982.

Yan, Y, Byrne, B, Coulthard, J, "Sensing homogeneity in mass flow rate measurement of pneumatically conveyed solids." Flow Measurement and Instrumentation, Vol. 6, No 2, p 115-119, 1995.

Yan, Y, Byrne, B, Woodhead, S, Coulthard, J, "Velocity measurement of pneumatically conveyed solids using electrodynamic sensors." Meas. Sci. Technol., Vol. 6, p 515-537, 1995b.

Williams, R A and Beck, M S, Ed "Process Tomography: Principles, Techniques and Applications", Butterworth-Heinemann, 1995, 101-118.

Velocity and mass flow rate profiles of dry powders in a gravity conveyor using an electrodynamic tomography system.

R G Green, M F Rahmat, K Dutton, K Evans, A Goude, M Henry.

Abstract

This paper describes measurements made on a gravity drop conveyor using two arrays of axially spaced electrodynamic sensors to measure axial velocities close to the wall of the conveyor and velocity profiles of both flowing sand and plastic beads. The level of correlation obtained using pixels is investigated. The velocity profile is combined with a tomographic concentration profile to estimate the mass flow profile, which is summed over the measurement cross-section to estimate the mass flow rate. A calibration of tomographically determined mass flow rate versus actual mass flow rate is presented.

1. Introduction

Pneumatically conveyed solids generate electrical charge which can be detected using electrodynamic sensors [King 1973]. This paper describes the use of electrodynamic sensor arrays for velocity measurement [Featherstone et al 1983, Yan et al 1995]. The velocity measurements use cross correlation to determine transit times, which are then converted to velocities. Two velocities may be calculated from the collected data; the peripheral velocity and the velocity profile.

The peripheral velocity is obtained by cross correlating the data from an upstream electrodynamic sensor with that from a downstream sensor. In this paper only corresponding upstream and downstream sensors are correlated, because the measurements are made in a gravity drop system. With a pneumatic conveyor, the possibility of axial swirl flow can be investigated by correlating an upstream sensor with several of the downstream sensors and determining which combination of sensors provided the greatest correlation coefficient. The velocity profile within the measurement section is determined using tomographic techniques [Williams and Beck 1995] from the upstream and downstream concentration profiles. Both these methods are described in greater detail in section 3.

The velocity profile is used, in combination with the concentration profile to determine the solids mass flow rate through individual pixels and summed to provide the mass flow rate through the measurement section.

2. The measurement system

The measurement system consists of two axially spaced arrays of electrodynamic sensors mounted on an 81 mm diameter steel pipe (figure 1). The separation between upstream and downstream sensors is set, as a compromise, to 50 mm so the sensor outputs can be correlated adequately. A low separation produces a high correlation coefficient, but requires very high speed data capture and processing, a large separation results in a low correlation coefficient [Beck and Plaskowski 1987].
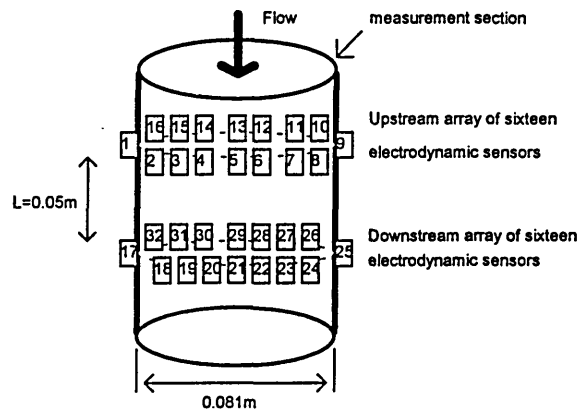
Figure 1. Arrangement of the thirty two electrodynamic sensors.

The sensor [Green et al 1996] consists of an electrode 3 mm diameter, connected to the transducer electronics. Charged particles falling in the pipe induce charge in the electrode. The induced charge is converted into a voltage, which is then amplified approximately five hundred times. The amplified voltages from all thirty two sensors are sampled by a proprietary data acquisition system and processed off-line. Measurements are made by energising all thirty two sensors and monitoring the sensor outputs. This was done for several solid flow rates using the data acquisition system to obtain three hundred and twelve samples from each sensor in each case. Usually the measurements are made by sampling each sensor output at a frequency of 1 kHz.

The flow rig is shown in figure 2. Solid material is fed from the hopper into the down pipe via the variable speed screw feeder at controlled rates. The solid particles are accelerated under gravity. Their velocity as they pass through the measurement section is estimated, neglecting feeder effects, collisions and bouancy as:
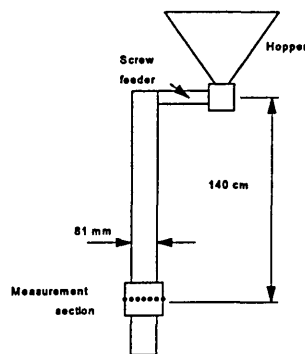
$$v = \sqrt{2gs}$$

$$= 5.24 m/s$$

Figure 2. The gravity flow rig

Two solid materials were used in the investigation; sand and plastic beads. The sand has a nominal size of 600 μm and the plastic chips are approximately 3 mm cubes. For sand, the sensor output voltages were measured at flow rates ranging from 30 to

255 g/s. For plastic beads, the sensor output voltages were measured at flow rates ranging from 14 to 84 g/s.

3. Peripheral velocity determination

The peripheral velocity measurements were made using a Hewlett Packard Dynamic Signal Analyser, model 3566A, by cross correlating signals from upstream and downstream sensors. The electrodynamic sensors posses a localised sensitivity (Green et al 1996) to the flowing charged particles which results in a transit time related to the movement of the particles closest to the wall where the electrode is mounted. The results for each channel can be plotted as functions of time, and typical signals for upstream and downstream sensors are shown for sand (figure 3) and plastic beads (figure 6).

3.1 Sand flow

The correlogram obtained by cross correlating upstream sensor number 5 with downstream sensor number 21 is shown in figure 4.
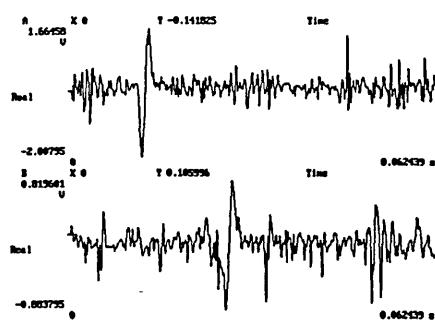

Figure 3. Typical sensor output signals: sensor 5 (upstream) and sensor 21 (downstream), sand flow rate of 103 g/s
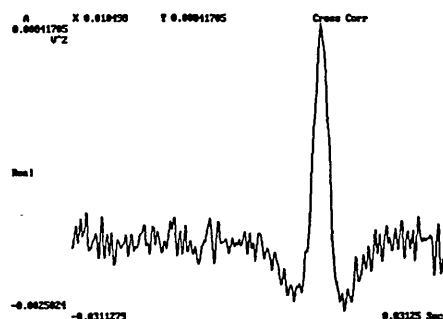

Figure 4. Cross correlation by HP Signal Analyser: sand flow rate 103 g/s.

The peak of the correlogram occurs at a transit time 10.50 ms, corresponding to a velocity of 4.76 m/s.

3.2 Plastic beads flow

The same procedure for measuring velocity with sand flow was repeated with plastic beads.
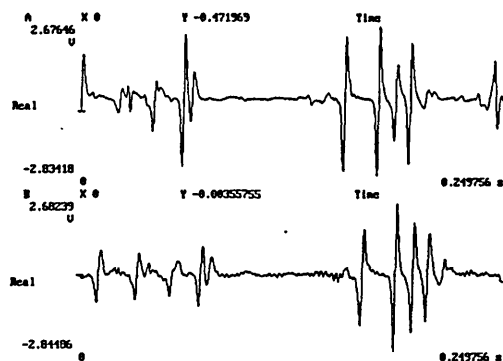
Figure 5. A typical dynamic output signal from sensor 3 (upstream) and sensor 19 (downstream) for plastic beads: flow rate 14 g/s.

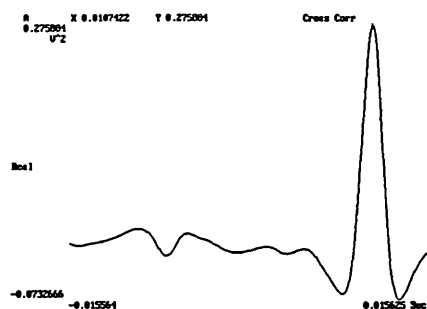The resulting correlogram is shown in figure 6.

Figure 6. Correlogram for plastic beads: flow rate 14 g/s.

The peak value of the correlogram occurs at a transit time of 10.7 ms, corresponding to a velocity of 4.66 m/s.

The small differences in measured velocity are probably due to the greater density of the sand compared to that of the plastic, though drag due to surface finish may be relevant.

3.3 Pixel concentration time series cross correlation

This measurement determines the velocity profile within the measurement cross-section. Three hundred and twelve sets of data (limited by the data acquisition system), each consisting of thirty two measurements obtained by sampling all the sensors in sequence, are collected. Each data set is captured in 1 ms and processed using a linear back projection algorithm (Green et al 1996) to generate an upstream and a downstream concentration profile. The electrodynamic sensors detect charge, so the resulting concentration must relate to the total amount of charge being detected. However, in tests, for specific materials it is assumed that all particles carry a similar charge, as the particles are of similar size and shape (Shackleton 1981). In the case of the gravity drop system the concentration output is calibrated against solids mass flow rate, because the particles have approximately the same velocity. In general, the concentration should be expressed in terms of number of particles within the measurement volume per unit time.

The concentration profile is represented by the concentration of individual pixels mapped onto the pipe cross-section (figure 7) and the positions of the individual pixels are identified by row and column. For example the upstream pixel in the fourth row and fifth column counting from the top left hand corner is written $PU_{4,5}$ (figure 7). Associated with this pixel is a numerical concentration value, identified as $CU_{4,5}]_1$ representing the concentration calculated from the first data set for the i,j th upstream pixel. The general upstream pixel is identified as $PU_{i,j}$ and the associated concentration $CU_{i,j}]_1$, the corresponding downstream pixel and concentrations are $PD_{4,5}$ and $CD_{i,j}]_1$ respectively.
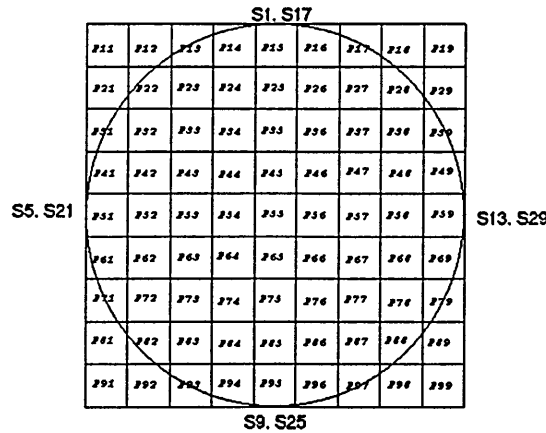

Figure 7. Pixel position identification, $P_{4,5}$ is the pixel in row 4 and column 5.

The concentration profiles are calculated for all three hundred and twelve upstream and downstream data sets. Consider a pixel, $PU_{i,j}$. The calculations result in three hundred and twelve values of concentration for it $(CU_{i,j}]_1$, $CU_{i,j}]_2$, $CU_{i,j}]_{312})$ occurring in a times series spaced at 1 ms intervals. These values of concentration are plotted against time to produce an upstream pixel concentration time function. These time functions are generated for all upstream and downstream pixels. An upstream and a downstream time series may be cross correlated to estimate the transit time between the two measurement arrays relating to the flowing solid particles. If corresponding upstream ($PU_{i,j}$) and downstream ($PD_{i,j}$) pixel concentrations are correlated the axial velocity component of the flow may determined, however, if non-corresponding ones are correlated non axial velocity components may be investigated. (This was not done in this investigation since there is little, if any, swirl with the gravity drop system.)

The cross correlations of the upstream and downstream concentrations was performed using MATLAB software in order to find the peak of the correlogram.

3.3. 1 Preliminary tests

Before attempting to produce velocity profiles an investigation was carried out to determine how the correlation coefficient varied for different positions in the measurement cross section relative to the pipe axis. Three pixels were considered: $P_{5,1}$, $P_{5,3}$, and $P_{5,5}$. To ensure optimum conditions for correlation the data was sampled at the higher rate of 3 kHz (sampling time of 0.33 ms per data set).

Typical graphs of concentration versus time are shown for upstream and downstream pixel, $P_{5,1}$ in figure 8 and the correlogram of the two time histories in figure 9. It should be observed that figure 8 is very similar in character to figures 3 and 5.
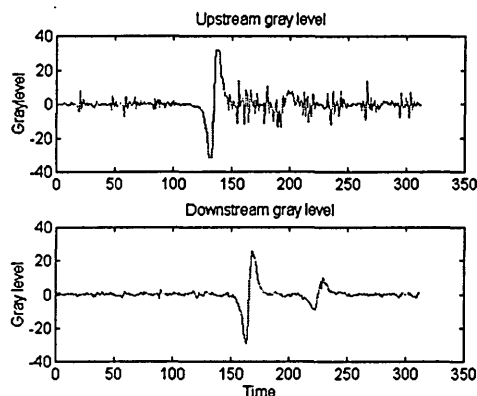

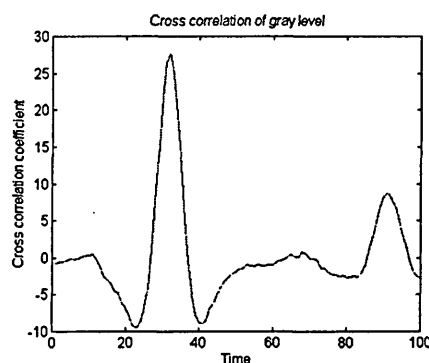Figure 8. Concentration versus time for upstream and downstream pixel$_{5,1}$.

Figure 9. Cross correlation of concentration time series for pixel$_{5,1}$.

The peak amplitude of the correlogram shown in figure 9 is 27.5 at a parametric time of 32, corresponds to a transit time of 10.56 ms (velocity = 4.74 m/s). The measurements were repeated for pixels $P_{5,3}$, and $P_{5,5}$. The peak amplitudes were 0.031 and 0.0058 respectively. The transit times were the same at 10.56 ms. The results show that the amplitude of the correlogram is reduced as the pixel being considered moves closer to the pipe axis, but the correlograms all have well defined peaks and transit times are easily measured.

These tests were repeated using plastic beads. The results follow the same pattern as for sand, though the amplitudes of the correlograms were larger(pixel$_{5,1}$ 38.44, pixel$_{5,3}$ 1.52 and pixel$_{5,5}$ 0.65 respectively), and the velocity slightly lower (4.45 m/s)

4 Uniform velocity profiles

Tests were made using plastic beads at flow rates between 52 and 107 g/s and the data processed to produce pixel concentration time series as described in section 3.3. The time functions of an upstream and the corresponding downstream pixel were cross correlated, the transit time determined and the velocity calculated. This was repeated for all the pixels. The results are shown numerically in figure 10 and graphically in figure 11.

233

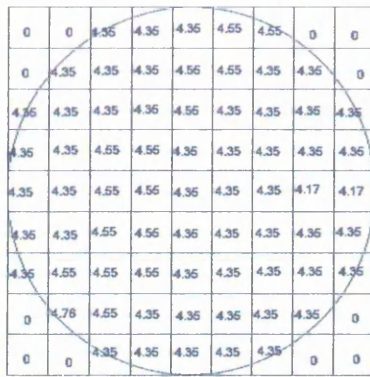| 0	0	4.55	4.36	4.36	4.55	4.55	0	0
0	4.35	4.35	4.36	4.56	4.55	4.35	4.36	0
4.36	4.35	4.35	4.36	4.56	4.35	4.35	4.36	4.35
4.36	4.35	4.55	4.56	4.36	4.35	4.35	4.36	4.56
4.35	4.35	4.55	4.55	4.36	4.35	4.35	4.17	4.17
4.36	4.35	4.55	4.56	4.36	4.35	4.35	4.36	4.35
4.36	4.55	4.55	4.55	4.36	4.35	4.35	4.36	4.35
0	4.76	4.55	4.35	4.36	4.36	4.35	4.35	0
0	0	4.35	4.36	4.36	4.35	4.35	0	0

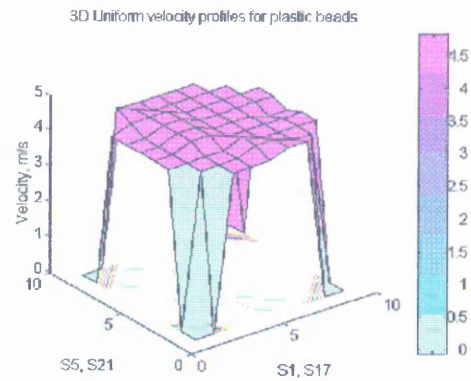Figure 10. Velocity profile for plastic beads at a flow rate of 52 g/s.

Figure 11. 3D velocity profile for plastic beads at a flow rate of 52 g/s.

The tests were repeated for a range of flow rates for sand. The velocity profiles all appeared very similar, which is expected since the main accelerating force is that of gravity. Further tests were carried out during which a non uniform velocity was produced.

5 Non uniform velocity profile

A flow of air was introduced into the gravity drop down pipe via a 3 mm bore plastic pipe connected to an air supply line, which was at a pressure of approximately 7 Bar. The air nozzle was positioned 10 cm above the upstream sensor. The flow of air was introduced to disturb the relatively uniform flow described in section 4, producing non-uniform velocities to see if the measurement system responded.

The tests described in section 4 were repeated and the velocity profiles determined. A typical result is shown in figures 12 and 13.

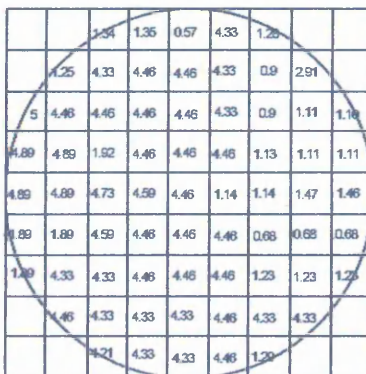|		1.34	1.35	0.57	4.33	1.2		
	1.25	4.33	4.46	4.46	4.33	0.9	2.91	
5	4.46	4.46	4.46	4.46	4.33	0.9	1.11	1.1
4.89	4.89	1.92	4.46	4.46	4.46	1.13	1.11	1.11
4.89	4.89	4.73	4.59	4.46	1.14	1.14	1.47	1.46
1.89	1.89	4.59	4.46	4.46	4.46	0.68	0.68	0.68
1.29	4.33	4.33	4.46	4.46	4.46	1.23	1.23	1.2
	1.46	4.33	4.33	4.33	4.46	4.33	4.33	
		1.21	4.33	4.33	4.46	1.2		

Figure 12. Non-uniform velocity profile for plastic beads at a flow rate of 52 g/s
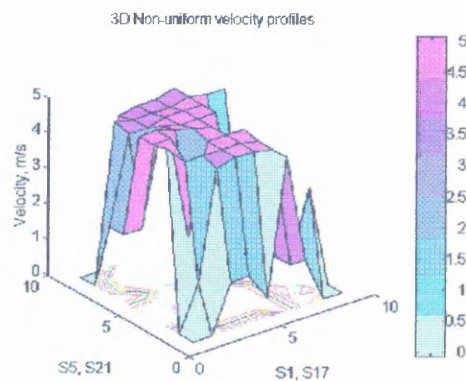
Figure 13. Non-uniform velocity profile for plastic beads at a flow rate of 52 g/s.

These results suggest the electrodynamic system is capable of determining non-uniform velocity profiles, though further testing in a pneumatic conveyor is planned.

6. Mass flow estimation

The mass flowrate, $\overset{\bullet}{m}$, through any pixel, P_{ij}, in the measurement cross section depends on the instantaneous concentration at time t associated with the pixel, $C_{i,j}\big]_t$, multiplied by the velocity associated with the pixel, v_{ij}:

$$\overset{\bullet}{m} = k \sum_{\substack{i=1 \\ j=1}}^{\substack{i=n \\ j=n}} C_{ij} v_{ij} \qquad (1)$$

Where k is a constant with appropriate units and n is the averaging interval. In practice the concentration will probably be varying more rapidly than the velocity, so either a rapidly changing mass flow profile may be generated or each pixel concentration may be averaged over some convenient time interval. These measurements are currently being investigated. A typical concentration multiplied by velocity profile ($C_{ij} v_{ij}$) is shown numerically in figure 14 and graphically in figure 15.

Figure 14. Numerical concentration multiplied by velocity profile: plastic beads
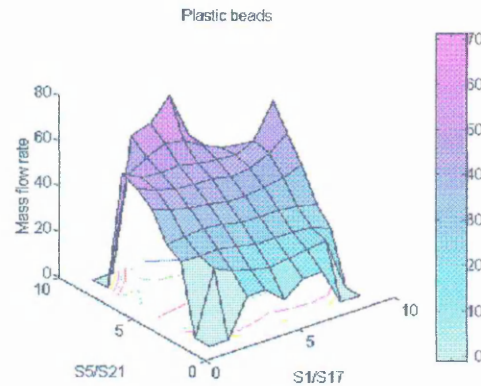

Figure 15. 3D concentration multiplied by velocity profile: plastic beads

These concentration multiplied by velocity flow rate measurements were repeated for a range of solid flow rates. Calculations were made using both the upstream and the down stream concentration profiles and summed over the cross-section to estimate the mass flow rate. The results are summarised in figure 16. For a mass flow rate meter the value of k in equation 1 is required. This can be estimated from the gradients of the upstream and downstream regression lines shown in figure 16. Ideally the upstream and down stream measurements should coincide, however errors arise due to the limited resolution in image reconstruction, velocity changes due to acceleration under gravity and the limitations of the data capture system. The intercept on the vertical axis has been used to compensate for the offset in the measurements due to noise, etc. The scaled results are shown in figure 17, along with the ideal calibration line.
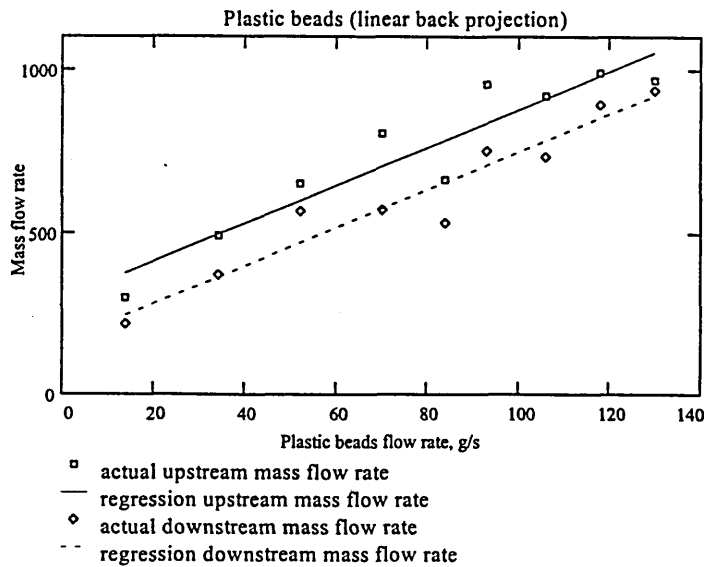
Figure 16. Summed unscaled concentration multiplied by velocity profile versus solid flow rate (plastic beads)
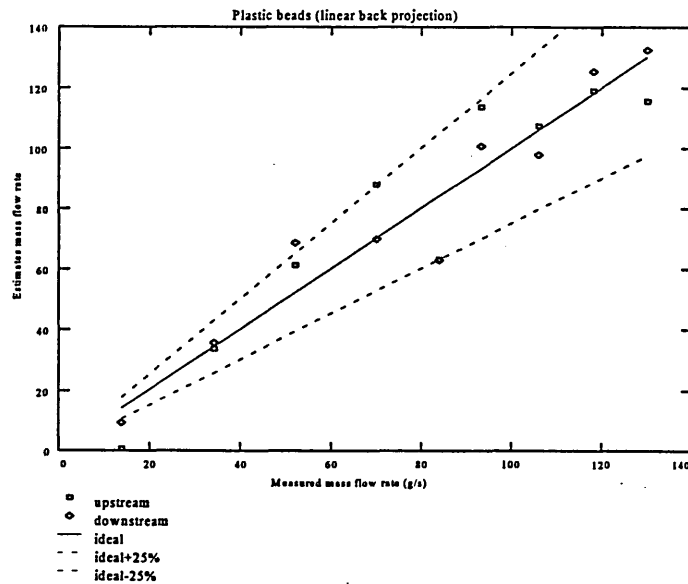

Figure 17. Scaled tomographically determined mass flow rate versus actual solid flow rate (plastic beads)

Figure 17 shows that for flow rates above 20 g/s all the measurements but one are within ± 25% of the measured value. However, further measurements, using a wide range of solid flow rates, solids velocities and flow profiles, are required to determine the repeatability and accuracy of this method of tomographic measurement.

7. Conclusions

Electrodynamic sensors are particularly suitable for applications of velocity measurement where the conveyed materials generate static electrical charge. Their sensitivity and high spatial frequencies enable them to be used to produce concentration profiles from an array of sensors. Two suitably positioned arrays enable the cross correlation of pixel concentration time histories to provide transit times and hence velocity profiles. Combination of velocity and concentration profiles on a pixel by pixel basis generates the mass flow rate profile. Summation of the mass flow rate

through each pixel provides a tomographic estimate of the solid mass flow rate with an estimated accuracy of approximately ± 25% of reading..

Further work is required to investigate the application of this measurement system in pneumatic conveyors to determine the range of velocities and concentrations for which it is suitable. Extended experimental work should enable the accuracy and repeatability of the system to be better defined.

8 References

Beck, M.S. and Plaskowski, A.B., "Cross correlation flowmeters: their application and design." Adam Hilger, 1987.

Featherstone, A M, Green, R G, Shackleton, M E, "Yarn velocity measurement." J. Phys. E: Sci. Instrum., Vol. 16, 1983, p 462-464.

Green, R.G., Rahmat, M.F., Evans, K., Goude, A., Henry, M., Stone, J.A.R., "Concentration profiles of dry powders in a gravity conveyor using an electrodynamic tomography system." ." Accepted Oct 1996, to be published, Meas. Sci. Technol..

King, P.W, "Mass flow measurement of conveyed solids, by monitoring of intrinsic electrostatic noise levels." 2nd. Int. Con. on the Pneumatic Transport of Solids in Pipes, Cranfield, 1973.

Shackleton, M.E., "Electrodynamic sensors for process measurement." M.Sc. Thesis, University of Bradford, 1981.

Williams, R A and Beck, M S, Ed "Process Tomography: Principles, Techniques and Applications", Butterworth-Heinemann, 1995, 101-118.

Yan, Y, Byrne, B, Woodhead, S, Coulthard, J, "Velocity measurement of pneumatically conveyed solids using electrodynamic sensors." Meas. Sci. Technol., Vol. 6, p 515-537, 1995.